The actin-binding protein Drebrin and its implications for Alzheimer's Disease using the model organism *C. elegans*

Dissertation zur Erlangung des akademischen Grades des
Doctor rerum naturalium (Dr. rer. nat.)

eingereicht im Fachbereich Biologie, Chemie, Pharmazie
der Freien Universität Berlin

vorgelegt von

Christian Gallrein
geboren in Halle (Saale)

2020

Die vorliegende Arbeit wurde am Leibniz Forschungsinstitut für molekulare Pharmakologie (FMP Berlin) im Zeitraum von 2016 – 2019 in der Arbeitsgruppe von Janine Kirstein angefertigt.

1. Gutachter: Prof. Dr. Janine Kirstein (Universität Bremen)

2. Gutachter: Prof. Dr. Stephan Sigrist (Freie Universität Berlin)

Disputation am 30. September 2020

Table of Contents

Summary

Patients of Alzheimer's Disease (AD) showed reduced levels of the actin-binding protein Drebrin in their neurons. The here presented work was set out to analyse the interaction between Drebrin and the disease-associated peptide Amyloid-β.

To analyse the interaction *in vivo* two novel models were designed, employing the nematode *C. elegans*. The Amyloid-β pathology was modelled by overexpressing the disease causing peptide pan-neuronally and employing a genetic sub-stoichiometric labelling method to be able to follow the aggregation *in vivo* and *in situ* in a non-invasive manner. A second model, expressing human Drebrin pan-neuronally was generated to analyse Drebrin stability, localization and phosphorylation as well as analysing the effect of Drebrin overexpression on the nematodes' vitality and fitness. The third project combined both generated models to obtain a genetic cross expressing $A\beta_{1-42}$ and Drebrin simultaneously. This model was sought to study the interaction between $A\beta_{1-42}$ and Drebrin.

I could show, that $A\beta_{1-42}$ aggregates with the progression of ageing and exhibits multiple disease phenotypes that can be correlated to observations obtained in murine neurons as well as observations of AD patients' brain tissues. Furthermore, I observed, that a distinct subset of head neurons of the anterior ganglion, the IL2 neurons, exhibits the first aggregates and that a cell-type specific suppression of $A\beta_{1-42}$ in IL2 neurons could delay the disease onset.

Drebrin was observed to be regulated by phosphorylation at Serine-647 by Ataxia telangiectasia mutated kinase and render nematodes more resistant towards chronic oxidative stress.

The genetic cross of $A\beta_{1-42}$ and Drebrin unravelled that overexpression of Drebrin can ameliorate $A\beta_{1-42}$ aggregation and toxicity and that this beneficial effect is dependent on phosphorylation of Drebrin-S647.

Zusammenfassung

Patienten, die an der Alzheimer'schen Krankheit leiden, weisen reduzierte Mengen des Aktinbindeproteins Drebrin in ihren Nervenzellen auf. Ziel der vorliegenden Arbeit war es, die Interaktion zwischen Drebrin und dem krankheitsassoziierten Peptid Amyloid-β zu untersuchen.

Für eine *in vivo* Analyse wurden zwei neue Modellsysteme im Fadenwurm *C. elegans* entwickelt. Die Amyloid-β-pathologie wurde durch panneuronale Überexpression des krankheitsinduzierenden Peptids nachgestellt. Zusätzlich wurde ein sub-stöchiometrischer Teil der Peptide genetisch markiert, um eine *in vivo* und *in situ* Nachverfolgung der Aggregation zu ermöglichen. Als zweites Modell wurde ein Stamm generiert, der humanes Drebrin panneuronal überexprimiert, um Drebrin-stabiliät, -lokalisation und -phosphorylierung, sowie den Einfluss auf die Vitalität und Fitness der Nematoden zu analysieren. Das dritte Projekt sollte die beiden zuvor generierten Modelle kombinieren. Eine genetische Kreuzung, die Drebrin und $A\beta_{1-42}$ simultan exprimiert, wurde generiert, um die Interaktion zwischen den beiden Proteinen zu analysieren. Ich konnte zeigen, dass $A\beta_{1-42}$-Aggregation mit fortschreitendem Altern der Nematoden einherging und verschiedene Krankheitsbilder damit korrelierten, welche in Experimenten mit murinen Neuronen, als auch in Experimenten an Gehirngewebsproben aus menschlichen Alzheimerpatienten nachgewiesen werden konnten. Darüber hinaus konnte ich zeigen, dass die ersten Aggregate in einer Subpopulation Kopfneurone des anterioren Ganglions, den IL2-Neuronen, auftreten, sowie, dass eine zellspezifische Inhibition der $A\beta_{1-42}$-expression in jenen IL2-Neuronen genügt, um die Aggregation in anderen Neuronen zu verzögern.

Es konnte gezeigt werden, dass Drebrin-Degradierung durch Phosphorylierung des Serin-647 durch die *Ataxia telangiectasia mutated* Kinase (ATM) reguliert wird und dass diese Phosphorylierung mit einer erhöhten Resistenz der Nematoden gegenüber chronischem oxidativen Stress einhergeht.

Die Kreuzung von $A\beta_{1-42}$ und Drebrin konnte schließlich zeigen, dass sowohl $A\beta_{1-42}$-Aggregation als auch Toxizität durch Drebrin-Überexpression abgeschwächt werden und dass dieser Effekt abhängig von der Phosphorylierung an Serin-647 ist.

Disclaimer

The here presented work was done under supervision of Prof. Dr. Janine Kirstein. The presented projects were cooperation projects, where certain experiments or parts of experiments were carried out or supported by colleagues.

For the 'Abeta project' (see chapter "Generation of a novel Alzheimer's Disease model") colleagues of the Kirstein lab participated. Manuel Iburg was a close associate that contributed to cloning (subcloning of $A\beta_{1-42}$ into pSUMO, cloning of the wrmScarlet-$A\beta_{1-42}$ fragment, subcloning of *klp-6p* into pPD95-GFP, subcloning of shRNA-$A\beta_{1-42}$::SL2 into pPD_*klp-6p*::GFP) and data collection (culture, lysis and performing western blots against $A\beta_{1-42}$, p62 and SQST-1; lifespan and paralysis assays of *klp-6p::*shRNA expressing nematodes; pathogen avoidance assays of JKM5 and shRNA expressing nematodes). Dmytro Puchkov and Diogo Feleciano contributed to TEM and CLEM imaging. Sara Maria Ayala Mariscal and Tanmoyita Nayak contributed to lifespan and thrashing data of *klp-6p::*shRNA expressing nematodes. Two students, Tim Michelberger and Alen Koçak, performed lifespan, progeny and cloning experiments under my supervision as assistants.

The 'Drebrin project' (see chapter "Generation and Characterization of a *C. elegans* model expressing human Drebrin") was carried out in close collaboration with the Eickholt lab. Reagents and protocols were shared regarding biochemical analysis of Drebrin expression. Certain western blot experiments (lysis, blot and detection) were carried out by Dr. Patricia Kreis.

Because of the conjoined and integrative character of the projects, some figures contain data from the aforementioned people, this is noted in the respective figure legends. Since these datasets are indispensable for understanding the context of the pursued experiments, they are presented in this thesis.

Introduction

Alzheimer's Disease

Alzheimer's Disease (AD) is a progressive neurodegenerative disorder that was first described more than one hundred years ago by Aloïs Alzheimer [1]. Despite the discovery of neurofibrillary tangles, amyloid plaques, astrogliosis and neuronal dystrophy as hallmarks of the disease we still do not fully understand the mechanisms leading to AD.

Currently, about 50 million people worldwide are suffering from dementia, including AD as the most common cause accounting for up to 70% of the cases [2–4]. Although, about 50 % of the AD patients display not only hallmarks of AD pathology but a mix with pathologies of other forms of dementia (*e.g.* synucleinopathies, fronto-temporalopathies) [5]. Together, they exhibit an enormous socio-economic burden for our society, bearing in mind the increasing amount of elderly people [6]. While coronary and heart diseases decrease, AD pathogenesis is accounted as the leading cause of death with an average survival time of eight years for those diagnosed at the age of 65 [7].

AD can be distinguished in a familial early-onset and a sporadic late-onset disease. Whereas, the familial early-onset AD represents less than 1% of all AD cases [8]. The familial AD is a result of a rare inherited autosomal dominant mutation, predominantly found in the genes for the amyloid-precursor protein (APP), Presenilin-1 and Presenilin-2 [8,9]. Such pathology driving mutations increase the production of the pathological amyloid-beta peptide (Aβ) or increase the fraction of the most toxic Aβ variant, the 42 amino acids long $A\beta_{1\text{-}42}$ [10–12]. The vast majority (> 95%) of AD cases are sporadic late-onset variants [8]. While genetic [13] and environmental factors contribute to increase the prevalence to develop AD, the most pronounced risk factor is ageing [14].

The first hallmarks of AD develop years before the first mild cognition defects manifest. The severity of the disease is then gradually increasing, impairing memory and cognitive capacity further and leading ultimately to neuronal lesions, neuron atrophy and death. These three phases can be considered a (1) biochemical phase, (2) a cellular phase and (3) a clinical phase [15].

The biochemical phase

The “biochemical phase” is characterized by the abnormal procession of the amyloid-precursor protein (APP), aggregation and oligomer formation of amyloid-beta peptides (Aβ), hyperphosphorylation and aggregation of tau protein, as well as spreading and seeding of aggregation. Protein misfolding and aggregation are hallmarks of AD as they are for most neurodegenerative diseases [16–19].

The aggregation prone Aβ peptides are released as by-products of an abnormal degradation of APP by the membrane-bound β- and γ-secretases (Fig.1.1) [20]. The most abundant forms are the less aggregation prone, 40 amino acids long, $A\beta_{1\text{-}40}$ and the more aggregation prone, more toxic, 42 amino acids long, $A\beta_{1\text{-}42}$. Shorter peptides are described, but because senile plaque are mostly composed of $A\beta_{1\text{-}42}$ they are thought to be more important for the disease phenotype [21–23]. APP can be cleaved by an α-secretase in a non-amyloidogenic pathway that competes with the abnormal processing, producing a neurotrophic and neuroprotective cleavage product (sAβPPα) [24,25]. Finally, healthy brains produce $A\beta_{1\text{-}42}$ in low picomolar concentrations, which are thought to affect synaptic plasticity and memory formation positively [26–28].

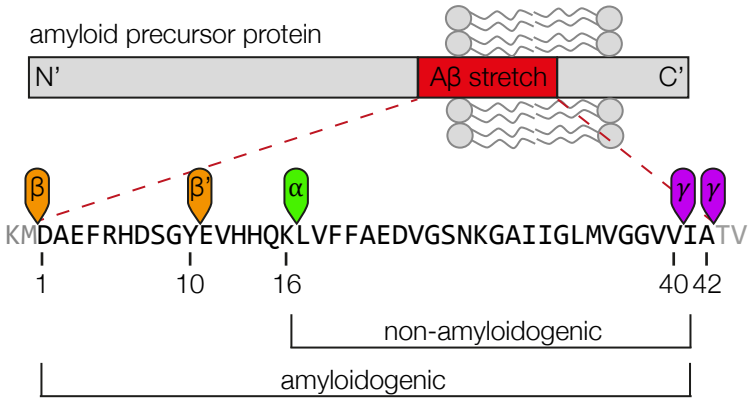

***Figure 1.1**: Schema of APP processing*

The amyloid precursor protein is processed by the combination of α-secretase and γ-secretase to retrieve non-amyloidogenic cleavage products or by β-secretase and γ-secretase to yield an amyloidogenic Aβ of 39 to 43 amino acids length. The cleavage-sites of the α-secretase (green), β-secretase (orange) and γ-secretase (violet) are indicated. The C’-terminal domain is located inside the cytoplasm, while the C’ terminal part of the Aβ stretch is located inside the plasma membrane. Adapted from Tan and Gleeson [29].

The rate limiting step for the amyloidogenic pathway is considered to be the cleavage by the β-secretase [30,31]. This first step occurs in multiple intracellular sites such as the Golgi, the endoplasmic reticulum (ER) or other endosomal compartments [32–35]. The second step, the cleavage by the γ-secretase complex, can occur throughout the whole protein trafficking as it is localized on the plasma membrane [36], the ER [37], the Golgi [38] and endosomes [36]. There is indirect evidence, that Aβ is also localized in the cytoplasm as it inhibits proteasomes that are cytoplasmic residents *in vivo* and *in vitro* [39–41].

This increase of pathogenic Aβ leads to the formation of oligomeric Aβ species followed by further progression of aggregation to form insoluble amyloid deposits. These large insoluble aggregates can be found in *post mortem* brain samples of AD patients and are termed amyloid plaques. This process of aggregation was correlated to toxicity and termed as "amyloid cascade hypothesis" [42,43]. Today, this hypothesis is more controversial than ever, as a multitude of other hypothesis have been proposed regarding the mechanism of toxicity in AD (see Fig.1.2).

The amyloid cascade hypothesis can be regarded as the most popular theory for the toxicity in AD and many other theories can be referred to as extensions of it (e.g. calcium-influx hypothesis [44,45]). Yet, it's most critical assumption, that the formation of large amyloid deposits / amyloid plaques leads to a series of toxic events in AD, has to be to questioned as clinical trials aiming to reduce the amyloid burden of AD patients did not yield success [46,47].

Today, it is believed that oligomeric Aβ species (AβO) are the most toxic agent in AD and inflicting the most damage ultimately leading to neuron death. The size of AβOs can vary and consist of three up to thirty or more monomers and there is no defined quaternary structure described [48–51]. There is evidence that Aβ plaques are not the major toxic species in AD. Synaptic loss was observed in APP transgenic mice models of AD while no plaque formation was observed [52], as well as intracellular Aβ could be correlated with cognitive dysfunction in several AD models in the absence of amyloid plaques [53,54]. Yet, it was shown that they could cause several aberrations: Amyloids can sequester other metastable proteins, induce protein misfolding thereby and give rise to potential toxic gain-of-function as well as loss-of-function by depletion of physiologically important proteins [17,55–58]. Furthermore, amyloid fibrils can cover plasma membrane surfaces and disrupt them mechanically [59,60]. Also, Aβ can complex and reduce metal-ions leading to increased formation of reactive oxygen species (ROS) [61–63]. Most

importantly, Aβ amyloids can induce secondary nucleation of Aβ monomers and therefore increase the amount of AβO formation and further aggregation in a feedforward loop manner [64–66]. Studies reasoning that AβO evoke the major toxic effects have gathered some strong evidence. Case studies have found that AβO abundance in AD patients correlated with the severity of cognitive impairment and neuronal lesion [48,67,68]. Furthermore, antibodies against AβOs were efficiently reversing cognition deficits in mouse models of AD [69,70].

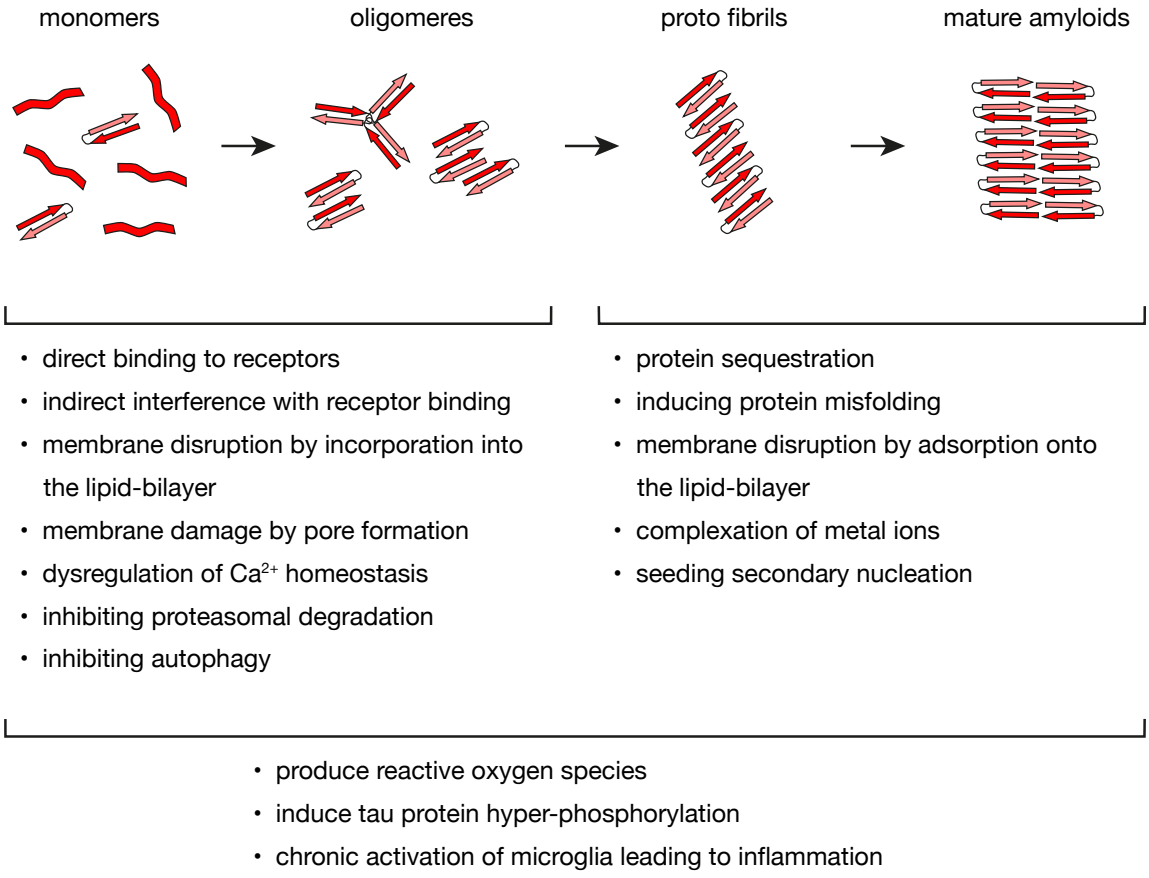

***Figure 1.2**: The Amyloid Cascade Hypothesis*

Schema containing the 'Amyloid Cascade Hypothesis', extended by features of the 'toxic-oligomer hypothesis', the 'Ca^{2+} influx hypothesis' and the 'cellular phase hypothesis'. Depicted is the progression of amyloid formation starting with unfolded (red stripe) or misfolded monomeric $A\beta_{1-42}$ (red forward arrow linked to light-red reversed arrow), that continue to condense to larger structures. Listed below are observed effects that are correlated to the indicated Aβ-species.

The spectra of observed perturbations by AβOs range from direct receptor binding, to membrane integrity perturbation and perturbation of intraneuronal proteostasis. Among the interaction with receptors, the most interesting ones are the activities on N-methyl-D-aspartate (NMDA) receptors and α-amino-3-hydroxy-5-methyl-4-isoxazolepropionic acid (AMPA) receptors that are decreasing long term potentiation (LTP) and enhancing long term depression (LTD), thereby interfering with memory formation and consolidation [71]. The binding of AβOs to the Insulin-like growth factor-1 receptor and the Insulin receptor is described to compromise signalling and therefore enhance neurodegeneration in AD [72]. Monomeric and small oligomeric Aβ can be incorporated into plasma membranes and affect membrane fluidity and lipid composition [73] by which mechanism also raft domains containing α7nACh receptors are perturbed. The lipid microenvironment is particularly important for the proper function of α7nACh receptors even though it is not known, if membrane fluidity or the lipid identity is responsible for the functionality [74,75]. The perturbation of this particular microenvironment by Aβ may pose a major perturbance for α7nACh receptor activity [76,77].

The incorporation of Aβ into plasma membranes can also induce Aβ pore formation or ion-channel formation [78]. Ca^{2+} entry through such channels perturbs ion homeostasis generally and poses a problem for maintaining neuronal membrane potential [44]. Secondly, such pores are hypothesized to be foundations for further fibril growth and subsequent lipid clustering around the growing aggregate, leading to major damage at the affected membrane [79–81].

As already mentioned, Aβ species can also enter the cytoplasm and provoke perturbation of the proteostasis machinery, by sequestering chaperones [82–84], inhibiting proteasomes [39,41] and by perturbing autophagy [85–87].

The second signature of the proteotoxic phenotype is the hyperphosphorylation and aggregation of the microtubule-associated protein tau (Tau) into amyloids termed ‘neuro fibrillar tangles’ (NFT) [88]. NFTs were found to correlate with AD severity [89–91] and their composition included a high ratio of hyperphosphorylated Tau compared to not phosphorylated Tau [92–94]. Tau-pathology and Aβ-pathology are tightly connected, as was shown by studies that observed that Aβ presence would increase the pathologic relevant hyperphosphorylation of Tau [95,96]. Studies have been conducted to identify kinases evoking Tau hyperphosphorylation and found CDK5 and GSK3β as strong candidates [97–99]. Those

kinases are regulated by Calpain, a Ca^{2+}-dependent cysteine protease [100,101]. Taken together, this is an interesting correlation to the Aβ-pathology that disturbs Ca^{2+} homeostasis by ion channel formation and previous studies observed an induction of Tau hyperphosphorylation by $Aβ_{1-42}$ [102,103].

While most of the described perturbations affect neurons at a single cell level primarily, some are thought to promote the disease to progress to a "cellular phase", impairing multiple cell-types and tissues alike. One of these effects is the increased production of reactive oxygen species in AD brains. Previous studies observed, that $Aβ_{1-42}$ not only elicits proteotoxic stress, but also oxidative stress by the direct production of ROS as well as by interfering with mitochondria's functional integrity [104–106]. Furthermore, Aβ induces microglia activation and inflammation [107].

The cellular phase

The cellular phase of AD is characterized by the progression of perturbations, not only in neurons but in all adjacent cell types, resulting in a catastrophic accumulation of damage that ultimately leads to the disorchestration of neuronal signal processing.

Microglia are the phagocytic cells of the central nervous system and comprise 5 to 12 % of the cells in adult murine brains [108]. Previous studies observed a tight association between senile plaques and microglia [109]. As mentioned above, Aβ can activate microglia and induce inflammation [107]. Tasks of microglia cells include the detection and removal of cellular debris and extracellular protein aggregates, the removal of supernumerary neurons during normal brain development and synaptic pruning, the constant and iterative inspection of synapses to remove dysfunctional or unnecessary synapses [110–112]. Two studies found rare mutations in receptors expressed in microglia, that are correlated with an up to fivefold increased risk of late-onset AD [113,114]. Together, this highlights that microglial cells are affected from AD and may contribute to the disease phenotype.

Another cell type, that is particularly important for the function of the nervous system are the oligodendrocytes. This cell type synthesizes myelin to cover axons and therefore facilitates neuronal signal transduction as saltatory action potentials. Their breakdown is a hallmark of multiple sclerosis, an autoimmune-mediated neurodegenerative disorder [115]. Yet, also for AD patients demyelination was described, as well as a link between Aβ aggregates and local demyelination [116,117].

The third class of glia cells in the brain that plays a crucial role in fine tuning neurotransmission are the astrocytes. They are required for multiple different supportive activities (*e.g.* maintaining the blood-brain-barrier together with endothelial cells, feeding the neurons, buffering of pH and ion concentrations, *etc.*) [118]. Furthermore, they facilitate synapse formation, maintenance and even influence neurotransmission by secretion of gliotransmitters like ATP, glutamate or D-serine [119]. Therefore, they can be regarded as an integrative part for the computing function of the brain [119,120].

In experiments with AD mice, no significant reduction of astrocytes could be detected nor were such reductions detected in ageing human brains or AD brains [121,122]. Thus, the situation is much more complex and the role astrocytes play in AD neurodegeneration remains enigmatic. One possible synaptotoxic mechanism is the upregulation of NFκB by Aβ that induces the release of the complement C3 protein, that leads to alterations of dendritic morphology and can possibly trigger synapse pruning [123]. Another key feature of astrocytes is the removal and recycling of otherwise excitotoxic neurotransmitters from the synapses [124]. Impairment of this function swiftly translates into neurodegeneration. In late stages of AD, reactive astrocytes can form glial scar-like barriers around amyloid plaques and by this disrupt the specific architecture of non-reactive astrocytes in the neocortex [125].

At this stage, multiple malfunctions accumulate and lead to the characteristic AD symptoms of dementia, progressing from mild to severe. This may be referred to as “clinical phase”.

The clinical phase

The “clinical phase” of AD is characterized by the onset of mild dementia. Cellular mechanisms are no longer able to maintain homeostasis and compensatory mechanisms [126,127] that were maintaining neuronal plasticity or were providing a “cognitive reserve”, start failing. Recent studies suggest that the asymptomatic phase of AD may proceed the onset of mild cognitive impairment by up to 20 years [128]. Synaptic loss correlates with cognitive decline in many vulnerable regions (*e.g.* hippocampus, dentate gyrus, etc.), but not with all affected areas [129]. Indeed, decrease in synaptic density is more highly correlated to the AD pathology and cognitive impairment than amyloid burden or NFTs [129–131].

Synapse function and integrity is closely linked to the morphology of dendritic spines and hence to the underlying structure and organization of the filamentous actin cytoskeleton (F-actin) [132]. An intact actin

cytoskeleton is vital for activity-dependent modulation, long-term changes and memory consolidation of the nervous system [133]. On the other hand, cytoskeletal defects appear to underlie cognitive deficits associated with ageing and dementia [134,135]. Candidate regulators of F-actin stability involved in cognitive decline and synaptic loss have been identified [129–132,136], among them the *developmentally-regulated brain protein* (Drebrin).

The actin-binding protein Drebrin

Drebrin is a highly conserved actin-binding protein regulating actin filament organization, F-actin stability and turn-over. In particular, it is involved during the formation of neurites and protrusion of motile cells [137–139]. Therefore, it exists in two major isoforms, an embryonic isoform (Drebrin E) and an adult isoform (Drebrin A) (Fig. 1.3), that are produced by alternative splicing [140,141]. While Drebrin E exists in multiple types of motile cells, as well as in growing neurons [137–139], a precise switch to Drebrin A is described in neurons upon synapse formation [142], suggesting an important contribution of Drebrin A in orchestrating a necessary reorganization of the actin cytoskeleton at synapses. Drebrin A is enriched in dendritic spines, protrusions on the neuronal surface that receive most excitatory input, forming the post synaptic sites of synapses [143,144].

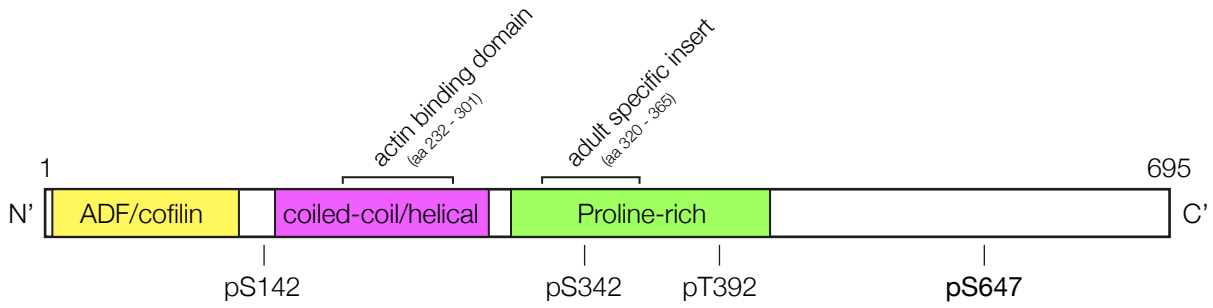

***Figure 1.3**: Domain organization of Drebrin*

Schema of Drebrin protein adult isoform domain organization consisting of an actin depolymerizing factor (ADF/Cofilin) homology domain, a coiled-coil domain followed by a helical domain and a proline-rich stretch. The actin-binding domain is indicated (amino acid 232 – 301). The adult specific insert of 44 amino acids (amino acid position 320 – 365) is characteristic for the 'adult isoform'. Four putative phosphorylation sites are indicated. pS647 (bold) is located in a putative unstructured domain and regulates Drebrin protein stability.

As already mentioned in the previous chapter, Drebrin is linked to both mild cognitive decline upon ageing as well as pathological decline in AD and Down's Syndrome (DS) [134,145]. In *post mortem* stainings of AD patient's brains a major loss of Drebrin was observed [145,146]. A reduction of Drebrin levels precedes pre-synaptic Synaptophysin loss in a mouse model of AD [147]. Further experiments with mouse models of AD could show, that a down-regulation of Drebrin aggravates AD toxicity [148], while overexpression of Drebrin alleviates the AD pathology [149]. A first mechanistic relationship between Drebrin degradation and concomitant loss of F-actin mediated by AD induced Calpain overactivation was shown by Chimura *et al.* [150].

Proper synaptic function relies on the highly regulated shape of dendritic spines, which in turn are dependent on continuous changes of the F-actin cytoskeleton. Drebrin A can bind up to two F-actin strands with its coiled-coil domain and adjacent helical domain (see Fig.1.3) [138,151]. Upon Drebrin decoration, the helical pitch of F-actin changes from 36 nm to 40 nm [152] and propagates this alteration also to undecorated F-actin parts. The Drebrin binding decreases F-actin depolymerisation rate and increases F-actin stability [153]. Furthermore, the two actin binding sites may bind two independent F-actin strands, enabling the formation of large bundles of F-actin by bridging Drebrin [139]. Experiments overexpressing Drebrin A in neuronal cell culture led to abnormally extended dendritic spines[154], while depletion of Drebrin was found to reduce the overall number of synapses drastically [155,156].

Beside its functional stabilization and bundling of F-actin, Drebrin A further contributes to synapse maturation by providing a diverse binding platform for different indispensable proteins that form the post synaptic density (*e.g.* Spikar directly accumulates by binding to Drebrin [157], PSD-95 likely accumulates via Drebrin interaction with Homer and Shank [158]).

Drebrin is not accumulated in all dendritic spines, but about 20% do not contain detectable amounts of Drebrin *in vivo* [159]. Yet, it was found, that Drebrin exits dendritic spines by a neuronal stimulus initiated process (see Fig. 1.4). NMDAR antagonists prevent the Drebrin exodus and it was thought that NMDAR activity is crucial for Drebrin translocation [160]. The artificial induction of chemical long term potentiation (cLTP) induces a transient Drebrin exodus comparable to the *in vivo* exodus [161]. NMDAR mediated Ca^{2+} influx into the post synapse activates Myosin II ATPase, thus resulting in the destabilization of Drebrin-F-actin complexes that promotes the Drebrin exodus [162,163]. After reduction of the stable F-actin pool, globular Actin (G-actin) can enter the spine by diffusion from the dendrite and facilitate F-actin

polymerization [164,165], therefore expanding the dendritic spine head size and enhancing the post synaptic density [166,167]. Finally, Drebrin re-enters the dendritic spines and stabilizes F-actin and therefore stabilizes the post synapse [168].

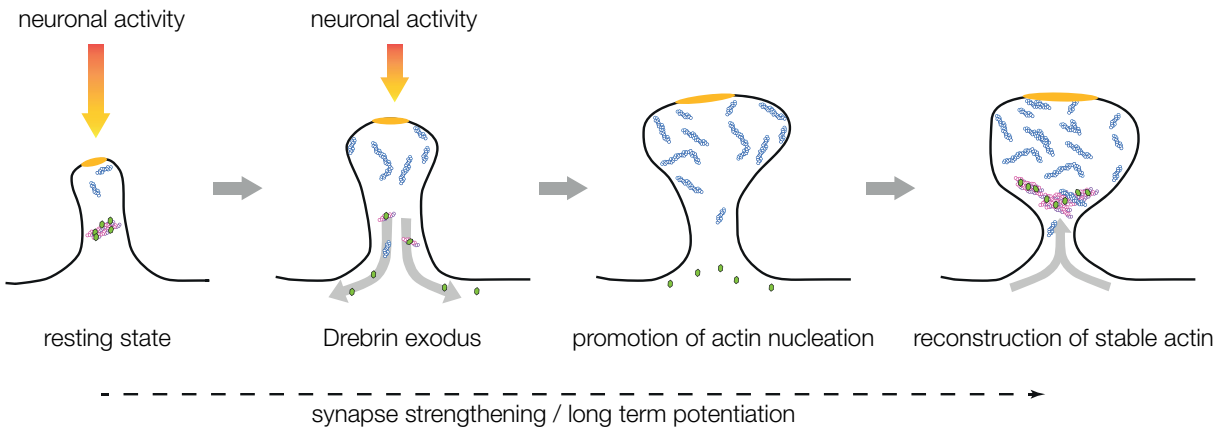

***Figure 1.4**: Drebrin exodus hypothesis*

Depicted is a schema of the Drebrin exodus hypothesis. Dendritic spines contain two pools of differently behaving F-actins, a dynamic pool (, blue circles) that undergoes swift treadmilling and is defining the spine shape, whilst a second pool is the Drebrin-bound stabilized pool (, magenta circles). Upon iterative neuronal inputs resting state spines can undergo synaptic strengthening leading to long term potentiation, enlarging the post synaptic density (, orange oval). Drebrin (, green hexagons) detaches from F-actin and evades from the spine head (exodus). Monomeric G-actin enters the spine and polymerizes to F-actin, bloating the spine head (promotion of nucleation) and enlarging the post synaptic density. Finally, Drebrin re-enters the spine and promotes F-actin bundling, stabilizing the dendritic spine. Adapted from Shirao *et al*. (2017) [169].

Drebrin is phosphorylated at multiple sites to fine tune actin binding activity, spine shape remodelling activity and protein stability. A number of phosphorylation sites has been identified by mass spectrometry of brain material and different cell lines [170–176], yet, only one site has been linked to a specific kinase [151,177] at the beginning of the thesis project.

While the phosphorylation sites from the ADF/Cofilin domain to the proline-rich domain are thought to influence actin-binding and spine remodelling, the focus was on the phosphorylation site pS647 as it is localized in a putative native disordered domain. Kreis *et al*. could show, that Phosphatase and Tensin homolog (PTEN) can dephosphorylate pS647, while neuronal activity leads to phosphorylation of Drebrin at S647 [178]. To this extent, one of the main findings of this cooperation project together with the

Eickholt Lab was, that S647 can be phosphorylated by the kinase Ataxia-telangiectasia mutated (ATM), a stress-induced kinase that activates DNA repair mechanisms upon DNA damage and that such phosphorylation of Serine-647 regulates Drebrin stability and turn-over [179–181].

Even though, reduced Drebrin levels correlate with decreased synapse count and mild cognitive impairment, Drebrin knockout brains have been observed to be healthy. It is a paradox that spine shape and synaptic function are not impaired [182], imposing that more factors contribute to mental deterioration.

Hence, to analyse multiple parameters that may cause Drebrin reduction as well as the complex effects induced by Drebrin reduction a model organism of fast ageing was sought that offers the possibility to analyse the Drebrin AD relationship in a quick and simple manner.

The nematode *C. elegans*

Caenorhabditis elegans (*C. elegans*) is a small, soil lived nematode whose suitability to become a model system for molecular biology, developmental biology, neuroscience, molecular ageing and many more fields was realized by Sidney Brenner nearly half a century ago [183].

Among all its benefits it is one simple, yet most important trait of *C. elegans* that it constitutes a whole organism, harbouring different tissues and cell types that cooperate and communicate in a complexly orchestrated way (Fig.1.5). *C. elegans* offers the benefit of being a complete animal that can be cultured in large quantities on the scale of tissue culture experiments [184].

C. elegans, a simple, yet powerful model system

C. elegans is a non-parasitic organism that feeds on bacteria and occurs in two sexes, hermaphrodites (being the majority with about 99.9 % abundance) and males, making it easy to culture genetically stable strains at low costs [183,185]. Furthermore, the nematodes are transparent, rendering them the ideal candidates for fluorescence microscopy studies. The complete genome was sequenced in 1998 and many genetic tools and models are available [186,187].

C. elegans has a generation cycle of 3.5 days (at 20°C), as it takes 3.5 days for a single nematode from hatching to grow into an egg-laying adult. One wild type hermaphrodite can have up to 300 progeny and live for up to four weeks.

Since the nematodes age, they are suitable models to analyse ageing related processes and the molecular mechanisms of ageing themselves [188–190]. Furthermore, the nematode's proteome contains approximately 80% human ortholog proteins and most of the signalling cascades are highly conserved between nematode and human (*e.g.* insulin / insulin-like pathway) [190–192].

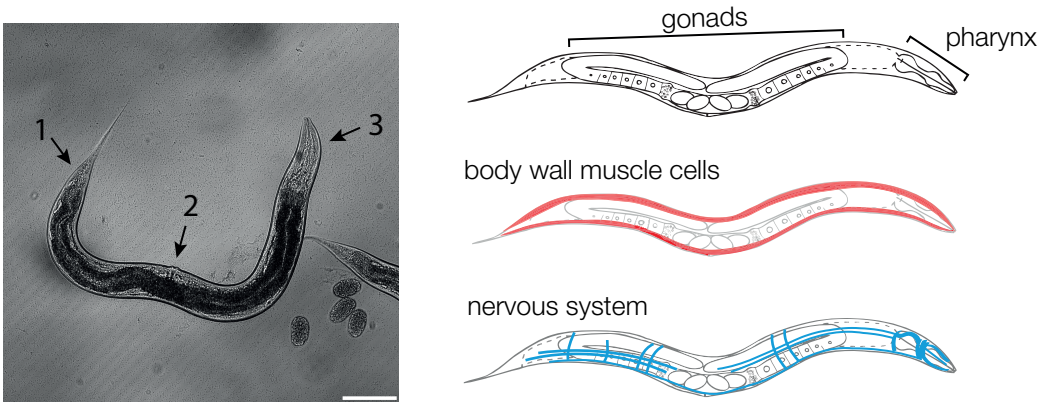

***Figure 1.5**: Anatomy of the nematode C. elegans*

The left image is a differential interference contrast (DIC) microscopy picture of an adult nematode exhibiting tail (1), vulva (2) and head (3). Scale bar is 100 µm. The right schema shows different tissue types, starting with the reproductive system and the pharynx on the top, followed by an outline of the body wall muscle cells (red) and the indicated nervous system (blue) on the bottom.

For my aims to study processes in neurons and the nervous system, another feature of the nematode is very useful: adult nematodes have a defined number of cells (959 in hermaphrodites and 1031 in males). Along with this, an adult hermaphrodite has exactly 302 neurons with specialist tasks, capabilities and fixed positions [193], a number high enough to enable complex interconnections and subsequent behaviours, but low enough to trace reactions back to single neurons or small subsets of neurons.

C. elegans as a model for neurodegenerative diseases

Modelling neurodegenerative diseases in *C. elegans* has a long and successful history. Malfunctional protein aggregation and subsequent neurodegeneration are hallmarks of most neurodegenerative diseases [19,194] and the expression of such proteotoxic proteins was conducted for many diseases and their disease-related proteins (*e.g*. overexpression of alpha-synuclein in dopaminergic neurons as a model of Parkinson's Disease [195]; overexpression of SOD1 [196,197], TDP-43 [198–200] or FUS [200,201] as models of amyotrophic lateral sclerosis; overexpression of poly-Q or Htt-Exon1 as models for Huntington's Disease [202,203]).

Also, disease models of AD were constructed in *C. elegans* by overexpressing Tau protein [204,205] or Aβ (see Table 1.1). This led to the identification of gene expression changes in the Aβ-pathology, such as increased levels of the small heat shock proteins Hsp-16.2 and Hsp-16.41 [206,207]. Screenings have been conducted to identify beneficial chemical compounds, as well as tests of known compounds for alleviation of the Aβ toxicity (*e.g.* ginkgolide, resveratrol) [208–210]. Despite those discoveries, the employed models were far from being flawless. Some of the most widespread models used to study AD in *C. elegans* express a truncated version of Aβ, one that consists of the amino acids 3 – 42, that was found to be less toxic than full length $A\beta_{1\text{-}42}$ [211]. Besides that, none of the available models that exhibited a disease phenotype was fluorescently tagged [212]. For localization studies or the *in situ* assessment of amyloid burden a fluorescence tag is indispensable. The first model that expressed an Aβ tagged with green fluorescent protein (GFP) was found to be aggregation-impaired, forming only oligomers *in vitro* and exhibiting no foci formation *in vivo* at all [213].

Table 1.1**:** *C. elegans amyloid-beta models*

List of Aβ variants expressing model strains. Some assays were not conducted or information is not available (n/a).

Strain	Aβ	Expression	Systemic Defects	Neurodegeneration	Aggregation
CL2006	3-42	body wall muscles	paralysis, reduced progeny	n/a	yes
CL2120	3-42	body wall muscles	paralysis, reduced progeny	n/a	yes
CL2355	3-42	pan-neuronal	reduced lifespan	impaired chemotaxis, impaired learning	yes
CL2621	3-42	body wall muscles	paralysis, reduced progeny	n/a	yes
CL2659	3-42	body wall muscles	paralysis, reduced progeny	n/a	yes
CL4176	3-42	body wall muscles	paralysis, reduced progeny	n/a	yes
GMC101	1-42	body wall muscles	paralysis	n/a	yes
GRU102	1-42	pan-neuronal	reduced lifespan, muscle defects, ATP depletion	n/a	yes
UA116	3-42	glutamatergic neurons	n/a	yes	n/a
pbLH98	n/a	cholinergic neurons	n/a	n/a	no
FDX25	3-42	ASE neurons	n/a	yes	n/a
CMD01	1-42	BAG neurons	no	perturbed signalling of BAG neurons	no

Objectives

(1) The generation of a novel model of Alzheimer's Disease in C. elegans

How can one trace amyloid formation in vivo in a non-invasive manner?

As stated before, so far, no *C. elegans* Aβ model was fluorescently tagged and detection of amyloids required fixation, permeabilization and staining, disabling an *in vivo* and *in situ* analysis of fibril formation. All models so far allowed only taking snap shots of the aggregation state and ignored that amyloids are highly dynamic structures that undergo changes with time. To analyse Aβ aggregation *in vivo* and *in situ* in a non-invasive manner I aimed to generate a novel model strain, that is fluorescently tagged and exhibits characteristic AD pathology.

***How is ageing affecting amyloid formation*?**

$A\beta_{1-42}$ is generated in low amounts already at young ages in human, yet cognitive decline and $A\beta_{1-42}$ aggregation are associated with elderly people (age 65+). This gave rise to the question, if $A\beta_{1-42}$ aggregation tendency and disease related toxicity would increase upon ageing in *C. elegans*.

To analyse this question, nematodes were analysed at different ages: **day 3** as last day of larval stage (L4-stage), **day 4** as first day of their fecund period (adult stage), **day 7** near the end of the fertile period and **day 10** for old nematodes in their post-fertile age.

What perturbations can be found in the novel AD model strain?

I was wondering to which extent *C. elegans* is impaired by the expression of $A\beta_{1-42}$ and what phenotypes one would be able to observe. Therefore, the models' general vitality, neurodegeneration and Aβ aggregation has been analysed.

How is the nervous system impaired?

Some features of direct neurodegeneration or perturbation of neuronal function were found in the previously established *C. elegans* models of AD. Hence, the focus was on the nature of

neurodegeneration and impairment of nervous systems functions [212,214]. The expression profiles of different neuron types differ significantly from each other and every neuron has an unique proteome to fulfil its functions [215,216]. Yet, this offers the possibility to detect differences in the vulnerability against Aβ and to uncover the molecular traits that lead to such increased susceptibility.

(2) A model system to analyse Drebrin regulation in vivo

What are the functions of C. elegans dbn-1?

The nematode *C. elegans* has a homolog of human Drebrin, Drebrin-like protein 1 (DBN-1, corresponding gene: *dbn-1*). Both proteins share a 54% sequence homology in the N'-terminal and a 53% sequence homology in the C'-terminal part. Previous studies observed actin-binding activity of DBN-1 in body wall muscle cells and intestinal cells [217,218]. Yet, I was interested how DBN-1 depletion would affect the nematode systemically and neuronally.

How is Drebrin regulated in C. elegans?

Human Drebrin can be phosphorylated at multiple sites modifying its binding to F-actin, its actin bundling activity and its stability. Since a majority of signalling pathways is highly conserved between human and nematode I wanted to analyse if nematode proteins can interact with human Drebrin in a cooperative manner and regulate Drebrin activity and turn-over. I was most interested in the phosphorylation of Serine-647 to corroborate results from our cooperation partners of the Eickholt lab that found pS647-Drebrin to exhibit a reduced turn-over in cell culture experiments compared to S647-Drebrin.

(3) The interaction of Aβ and Drebrin in vivo

Is Aβ aggregation affecting Drebrin abundance and localization?

Kaminski *et al.* showed that fluorescently labelled proteins, forming amyloid structures, exhibit a shifted fluorescence lifetime compared to monomeric species [219,220]. I wanted to employ fluorescence lifetime imaging (FLIM) to analyse $A\beta_{1-42}$ fibrilization and correlate Drebrin abundance/localisation using a genetically tagged version of Drebrin, a fusion with yellow fluorescent protein (YFP). Furthermore, I aimed to analyse lifespan and brood size as markers for systemic vitality.

Are Drebrin and Aβ directly interacting and co-aggregating?

I wanted to employ fluorescent tags on Drebrin and Aβ to analyse subcellular colocalization. A FLIM approach was thought to analyse the aggregation state of Drebrin and Aβ.

Can Drebrin overexpression attenuate Aβ fibrilization and phenotype?

Mouse models of AD showed, that Aβ toxicity is exacerbated upon Drebrin depletion, while overexpression of Drebrin attenuates the toxic phenotype [148,149]. I was wondering, if this phenotype could be corroborated in *C. elegans*.

Generation of a novel Alzheimer's Disease model

To analyse the sub-cellular localization and the progression of aggregation of $A\beta_{1-42}$ *in vivo* and *in situ* a novel model system was designed. Since the labelling of Aβ with GFP prevented Aβ from aggregation due to steric hindrances a model of sub-stoichiometric labelling was employed.

A bi-cistronic operon was designed under the control of either the pan neuronal *rgef-1* promoter or the body wall muscle promoter of *myo-3* (Fig. 2.1 A).

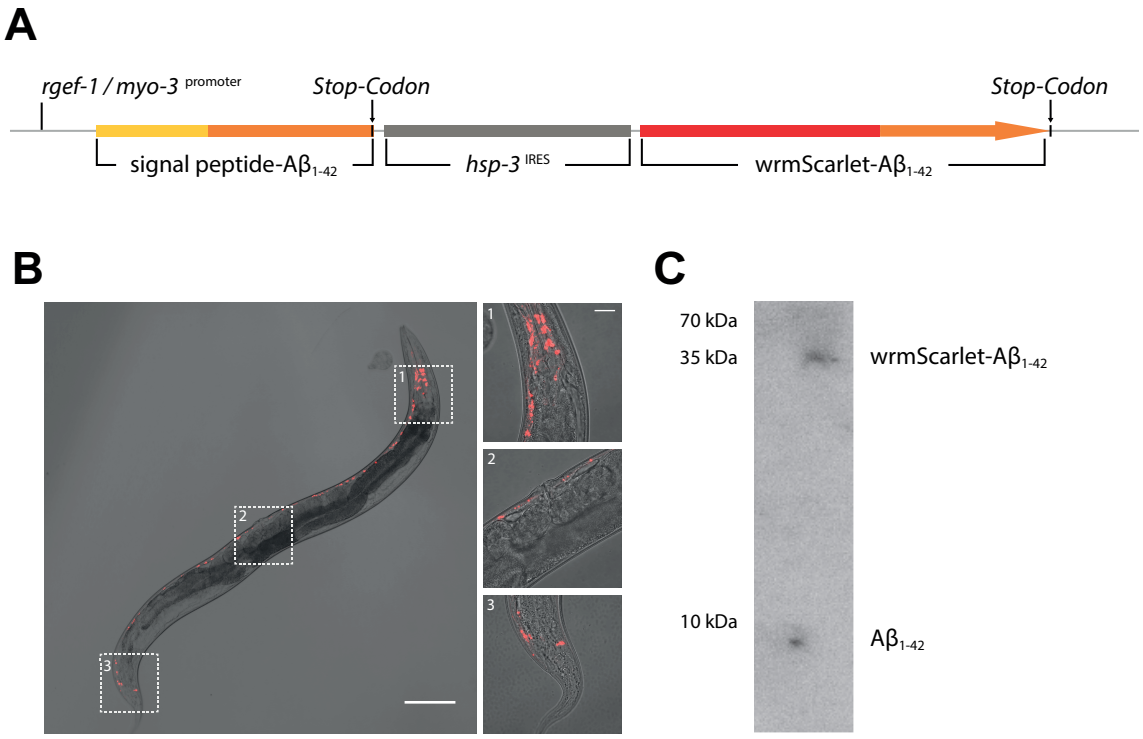

***Figure 2.1**: Operon for Aβ expression*

(A) Schema of the organization of the bi-cistronic 'Scabeta' operon to drive overexpression of human $A\beta_{1-42}$ and sub-stoichiometric expression of wrmScarlet-$A\beta_{1-42}$. **(B)** Confocal images (DIC + mScarlet fluorescence) of a JKM2 nematode expressing 'Scabeta' under control of the pan neuronal promoter *rgef-1* (100-fold magnification). Scale bar is 50 µm. Insets 1 – 3 show the respective close-ups of the head region (1), the mid body (2) and the tail (3) (630-fold magnification). Scale bar is 20 µm. **(C)** Representative western blot of total lysate of a non-synchronized population of JKM2 nematodes (yet, not older than day 5 of life). Detection with Mouse-anti-Aβ (6E10) and anti-Mouse-HRP. The migration of wrmScarlet-$A\beta_{1-42}$ and untagged $A\beta_{1-42}$ is indicated on the right. Kindly provided by Manuel Iburg.

The operon is transcribed into one mRNA that is differently translated: the 5' 'signal peptide-$A\beta_{1-42}$' sequence by highly efficient cap-dependent translation, while the translation of the following 3' 'wrmScarlet-$A\beta_{1-42}$' is driven by an internal ribosome entry site (IRES) that is less efficient. The signal peptide gets cleaved and the $A\beta_{1-42}$ peptide gets retro-translocated to the cytosol [208,221]. This results in a defined ratio of an excess of untagged Aβ that facilitates near-native fibril growth while sub-stoichiometric amounts of tagged wrmScarlet-Aβ are stochastically incorporated into the aggregates labelling them fluorescently. The efficient pan neuronal expression of the red fluorescent wrmScarlet-Aβ in the new strain JKM2 (nAβ) can be seen in the confocal image (Fig. 2.1 B). To ensure both variants, tagged and untagged Aβ are expressed, a western blot was performed (immunodetection with an anti-Aβ (6E10)) (Fig. 2.1 C). Two signals appeared, one band below the 10 kDa molecular weight marker corresponding to the untagged Aβ and a second band appeared at approx. 35 kDa, corresponding to wrmScarlet-Aβ. The net protein yield of the transgene in neurons is low as one can see in the fluorescence intensity (Fig. 2.1 B) as well as in the respective signal intensity in the western blot (Fig. 2.1 C).

To obtain a model that is suitable for biochemical analysis of protein-protein interactions, proteome changes or for the analysis of the cellular ultrastructure, a second model strain was generated, expressing the 'Scabeta' operon under the control of the body wall muscle promoter *myo-3p* (strain JKM7 (mAβ)) (Fig. 2.2). The expression in the body wall muscles yields a higher amount of transgenic protein than the pan neuronal expression. Therefore, the signals on the western blot of mAβ show both Aβ variants and are stronger than on the western blot of nAβ (compare Fig. 2.1 C and Fig. 2.2 B). The blot of mAβ also exhibits the intended difference in abundance of $A\beta_{1-42}$ (3 – 5 fold excess) and wrmScarlet-$A\beta_{1-42}$. To show that $A\beta_{1-42}$ and wrmScarlet-$A\beta_{1-42}$ interact with each other, an immunoprecipitation with an antibody against GFP was performed (Fig. 2.2 B right lane). Equal amounts of total protein were loaded in both lanes of the blot, yet an enrichment of wrmScarlet-Aβ and Aβ was observed. Most importantly, wrmScarlet-Aβ and Aβ co-precipitated upon pulldown with anti-GFP antibodies. I conclude, that both variants are interacting with each other, possibly forming amyloid fibrils together. For further validation of the model, the intracellular colocalization of $A\beta_{1-42}$ and mScarlet-$A\beta_{1-42}$ was analysed by immunohistochemistry. JKM2 (nAβ) and JKM7 (mAβ) nematodes were fixed and stained for $A\beta_{1-42}$ (Fig. 2.3 A and Supplemental Fig. 7.1 A).

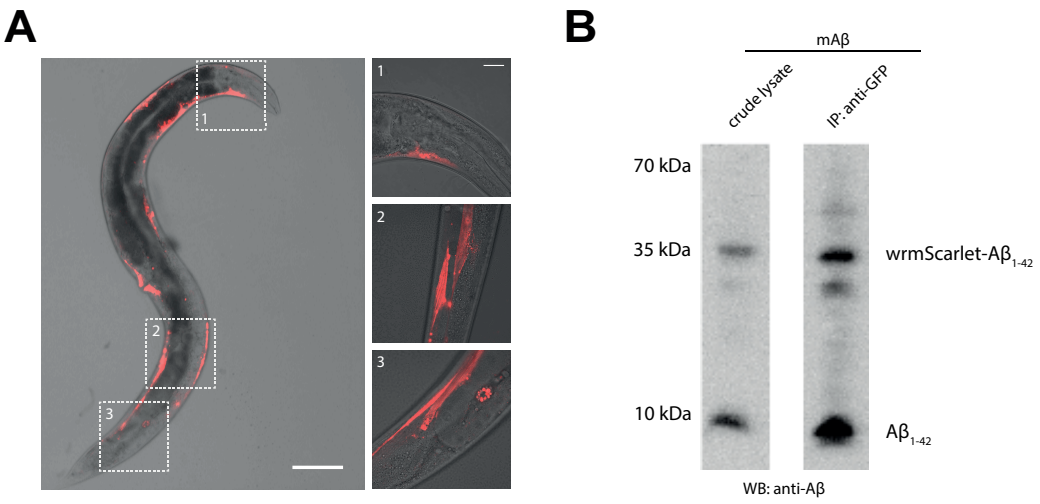

***Figure 2.2**: Expression of 'Scabeta' in body wall muscles*

(A) Confocal images (DIC + mScarlet fluorescence) of a JKM7 nematode expressing 'Scabeta' under control of the body wall muscle specific promoter *myo-3p* (100-fold magnification). Scale bar is 50 µm. Insets 1 – 3 show the respective close-ups of the head region (1), the mid body (2) and the tail region (3) (630-fold magnification). Scale bar is 20 µm. **(B)** Representative western blot of crude lysate (left lane) of a non-synchronized population of JKM7 nematodes (yet, not older than day 5 of life) and blot of immunoprecipitated material (with anti-GFP) (right lane). Detection with Mouse-anti-Aβ (6E10) and anti-Mouse-HRP. The migration of wrmScarlet-$A\beta_{1-42}$ and untagged $A\beta_{1-42}$ is indicated on the right. Kindly provided by Manuel Iburg.

$A\beta_{1-42}$ and mScarlet-$A\beta_{1-42}$ exhibited a strong colocalization (JKM2s Pearson's correlation coefficient = 0.64 ± 0.12, JKM7s Pearson's correlation coefficient = 0.77 ± 0.11) indicating that they interact *in vivo*. Most importantly, there are no foci composed of $A\beta_{1-42}$ alone that are devoid of mScarlet-$A\beta_{1-42}$.

This leads to the conclusion that mScarlet-$A\beta_{1-42}$ is not excluded from aggregation and fibril formation. Yet, I can confirm observations by Link *et al.* that $A\beta_{1-42}$ is localized intracellularly and cannot be found extracellularly by employing a protocol of fixation and staining as was described previously [221,222] and as was performed here. This observation does not negate that Aβ could spread outside of the expressing tissue, but rather that the detection method might simply be not sensitive enough.

To test if the novel model strains JKM2 and JKM7 exhibit amyloid formation, a staining with the amyloid-sensitive dye 'Thioflavin T' (ThT) was employed (Fig. 2.3 B and Supplemental Fig. 7.1 B). Upon binding to beta-sheet stacks, the structural motif of amyloid fibrils, ThT increases its fluorescence intensity by

a factor of ≈ 500 [223]. Yet, ThT staining of nematodes remains of poor quality and a strong autofluorescence was observed. Despite this obstacle, aggregates were detected exhibiting a strong fluorescence that clearly distinguishes from the autofluorescence (see white arrows in Fig. 2.3 B and Supplemental Fig. 7.1 B). Still, the staining efficacy varies among the nematodes of one batch stained with ThT. This makes ThT detection of aggregates erratic and unreliable for the attempt to quantify for aggregation. To overcome this issue, fluorescence lifetime microscopy was employed to assess and quantify the aggregation of $A\beta_{1-42}$ together with wrmScarlet-$A\beta_{1-42}$.

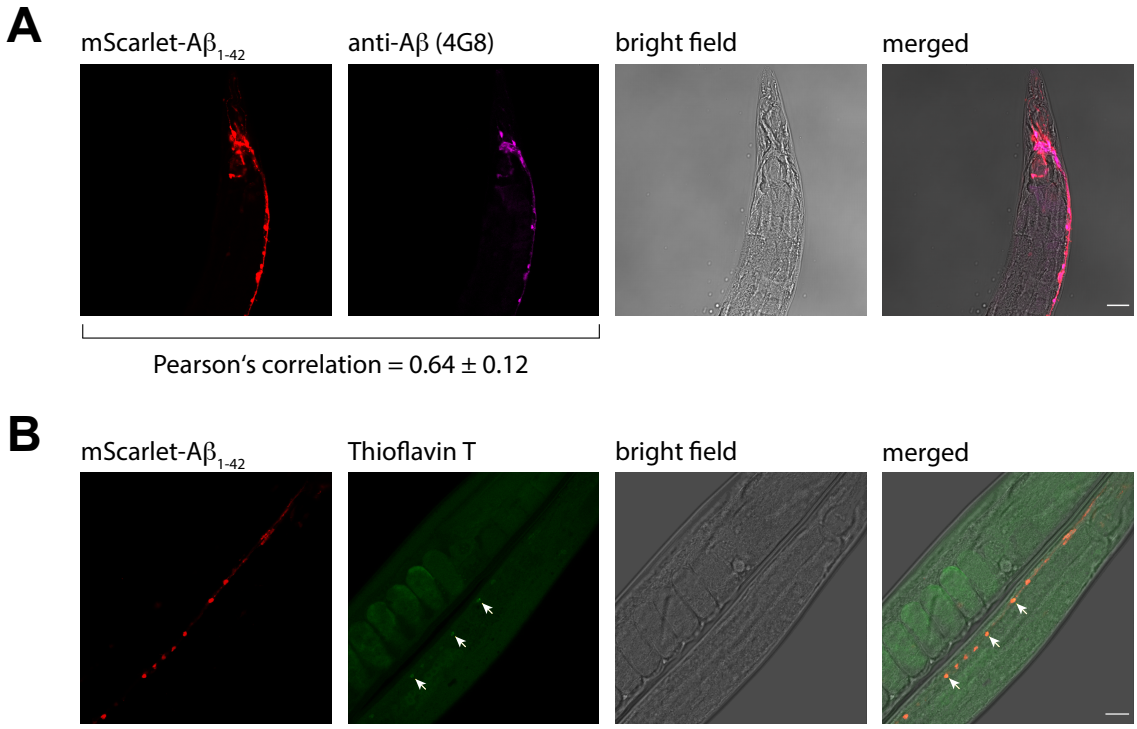

***Figure 2.3**: $A\beta_{1-42}$ and wrmScarlet-$A\beta_{1-42}$ are forming amyloids*

(A) Representative image of nAβ fixed with PFA and stained with anti-Aβ (6E10) + anti-mouse-IR680. Scale bar represents 20 µm. Colocalization of mScarlet fluorescence and IR680 fluorescence was analysed and Pearson's correlation coefficient was determined for all acquired images (n = 16), noted as mean ± SD. **(B)** Representative image of nAβ, fixed and stained with ThT. ThT-positive foci are marked with white arrows. Scale bar is 20 µm.

Aggregation of Aβ can be followed in vivo and in situ with the progression of ageing

Time-correlated single photon counting fluorescence lifetime microscopy (TCSPC-FLIM) was employed to measure the aggregation of Aβ in JKM2 and JKM7 nematodes *in vivo* and *in situ*. In theory, aggregation and incorporation of mScarlet-$A\beta_{1-42}$ into a growing amyloid fibril will lead to a quenching of the fluorophore that in turn reduces the apparent fluorescence lifetime [220]. The amyloid fibril serves as an acceptor for radiation free energy transfer, therefore long-lived photons have a high chance to be transferred instead of being emitted. The degree of short-lived photons that get emitted increases in relation to the long-lived photons, reducing the apparent fluorescent lifetime (τ). Thus, the reduction of the lifetime can be used as a proxy for the aggregation of $A\beta_{1-42}$ (Fig. 2.4). FLIM analyses are also independent of the expression level of the fluorophore [224], which is crucial when analyzing living animals that often exhibit reduced expression or stability of the transgenic protein with ageing.

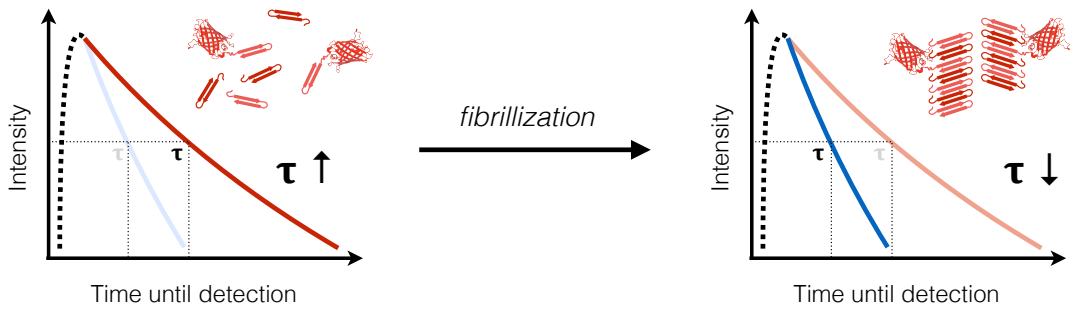

***Figure 2.4**: Schema of apparent fluorescence lifetime shift upon aggregation of $A\beta_{1-42}$*
Upon amyloid formation mScarlet-Aβ fluorophores get trapped into the growing amyloid fibrils and the apparent fluorescence lifetime (τ) is decreased.

The fluorescence lifetime is an intrinsic property of fluorophores and only dependent on the fluorophore and its microenvironment. Purified mScarlet exhibits a fluorescence lifetime of approx. 3.9 ns [225]. The fluorescence lifetime observed in young nematodes is already altered by the microenvironment of the cell, reducing the fluorescence lifetime of non-aggregated mScarlet in neurons to 2.9 ns and to 3.1 ns in muscle cells (Fig. 2.5). Only slight, yet not significant changes were observed in the progress of ageing in the control strains JKM3 and JKM8 expressing only mScarlet in neurons or muscles, respectively.

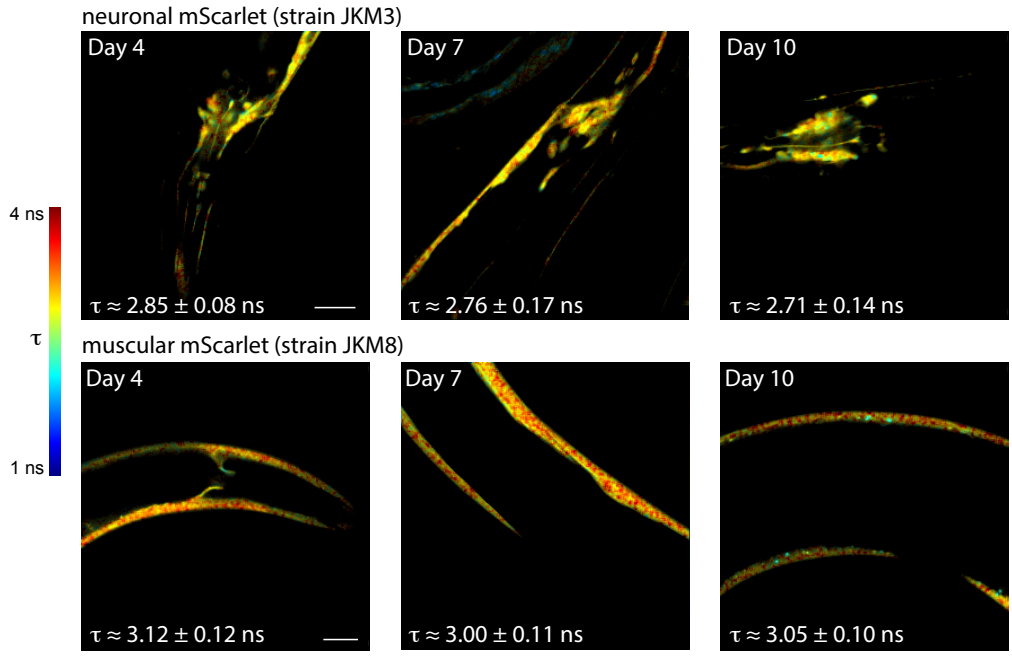

***Figure 2.5**: mScarlet does not aggregate upon ageing*

Representative TCPSC-FLIM images of neuronal/muscle mScarlet control (JKM3 and JKM8) on day 4, 7 and 10 alive. Fluorescence lifetime is false-coloured (from blue = low fluorescence lifetime to red = high fluorescence lifetime) and merged with the measured fluorescence intensity. Magnification was set to 630x and two to three cohorts of 10 to 15 nematodes per age were acquired. The average fluorescence lifetime of all recorded images per age is given as mean ± SD (τ). Scale bar represents 20 µm.

In the disease model strains JKM2 and JKM7 on the other hand, a progressive increase of aggregation was observed in an age dependent manner (Fig. 2.6). At day three of life, in the L4 stage, no foci formation nor reduced fluorescent lifetime pixels were visible and the histogram of the pixels exhibiting a certain fluorescence lifetime of JKM2 (nAβ; Fig. 2.6 A) overlapped to a great extent with the histogram of the control (JKM3, expression of mScarlet alone; black dashed line). On day four, the first foci appeared that show a decreased fluorescence lifetime (to about 2.0 to 2.4 ns), that can be referred to as aggregates (see white arrows in Fig. 2.6 A). The corresponding histogram for day four shows a clear shift to shortened fluorescence lifetimes. Previous studies have reported that on day four of life the proteostasis capacity of *C. elegans* starts to decline [19,226,227]. Interestingly, the first aggregates appeared reliably (in more than 90% of the observed JKM2 nematodes) in four to six head neurons of the anterior head ganglion around day 4 (Fig. 2.6 A, white arrows).

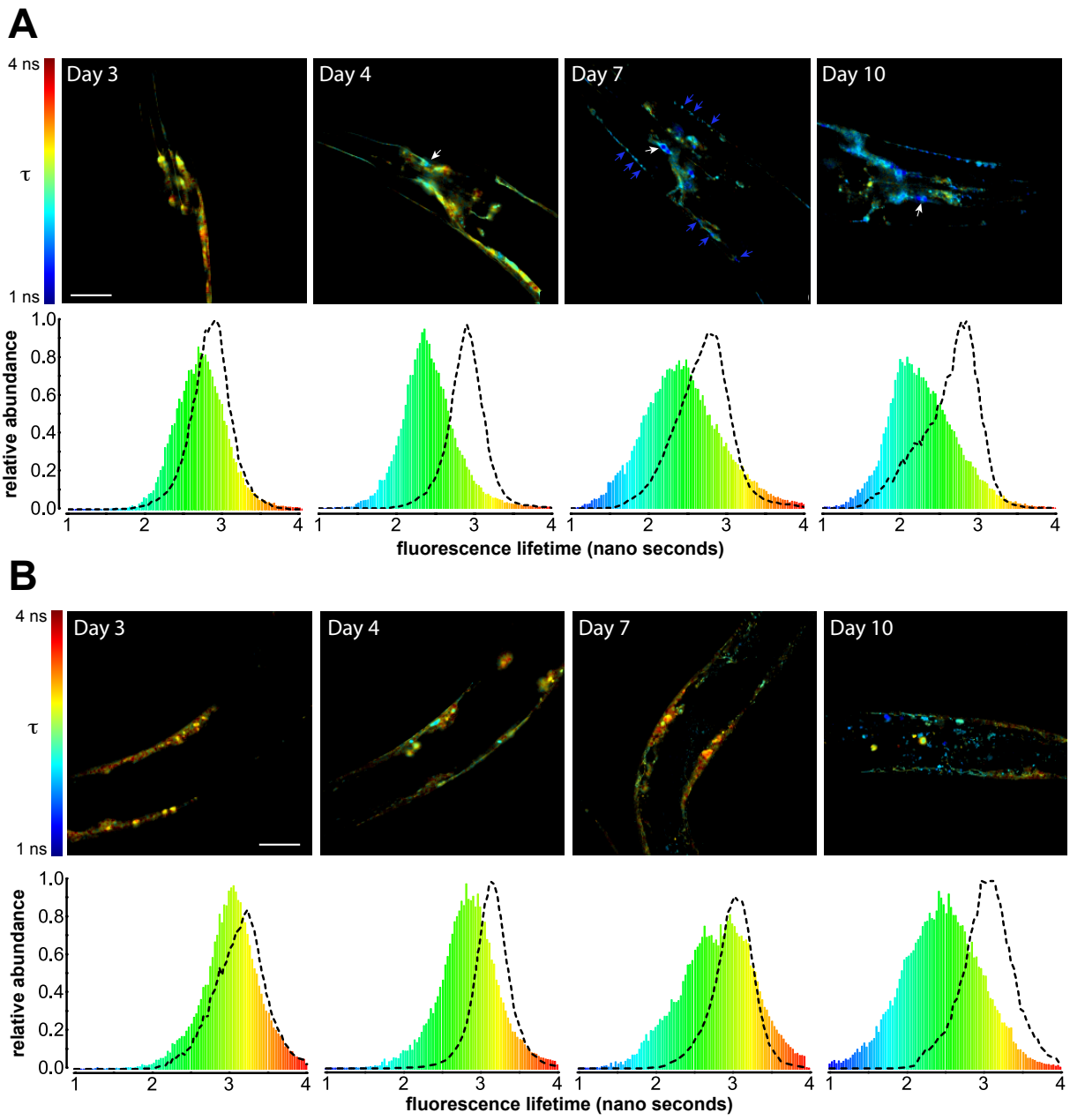

Figure 2.6: *Direct detection of the progression of aggregation of Aβ in neurons and body wall muscles using FLIM*

(A) Representative confocal TCSPC images of neuronal Aβ at different ages (day 3, 4, 7 and 10). Fluorescence lifetime is false-colored (from blue = low fluorescence lifetime to red = high fluorescence lifetime) and merged with the measured fluorescence intensity. 945-fold magnification, scale bar is 20 µm. The respective histograms depicted underneath each representative image of that particular age show the average occurrence of pixels exhibiting a certain fluorescence lifetime. $\mathbb{N}$ = 3 (cohorts), n = 10 - 15 (individual nematodes) per condition. Dashed black lines are outlining the shape of the histograms of control nematodes expressing only mScarlet in the neurons. **(B)** Representative confocal TCSPC images of muscle Aβ at different ages (day 3, 4, 7 and 10). Fluorescence lifetime is false-colored (from blue = low fluorescence lifetime to red = high fluorescence lifetime) and merged with the measured fluorescence intensity. 630-fold magnification, scale bar is 25 µm. The respective histograms depicted

underneath each representative image of that particular age show the average occurrence of pixels exhibiting a certain fluorescence lifetime. $\mathbb{N}$ = 3 (cohorts), n = 10 (individual nematodes) per condition. Dashed black lines are outlining the shape of the histograms of control nematodes expressing only mScarlet in the muscle cells.

At advanced age (day 7 – 10) more numerous and also smaller aggregates appeared that formed visible foci with a reduced fluorescence lifetime (1.8 ns to 2.4 ns; see blue arrows in Fig. 2.6 A). This trend continues on day 10 of life. The overall fluorescence intensity was decreased in the fraction that was not localized in foci, indicating a further decrease of soluble Aβ species, resembling in a strong shift of the τ-distribution in the corresponding day 10 histogram.

I observed a comparable, yet not identical behaviour in a model expressing $A\beta_{1\text{-}42}$ in the body wall muscle cells (JKM7, mAβ). I detected foci formation already from early larval stages on including L4 stage at day three (Fig. 2.6 B). Though, most of these foci did not display a reduced fluorescence lifetime. Such foci need to be regarded as "accumulates" rather than aggregates, as they are composed of non-aggregated, non-amyloidogenic material. The first shift towards reduced fluorescence lifetime was observed on day four but is less pronounced than the day 4 shift in nAβ. From day seven onwards, aggregation increases progressively. In contrast to the fluorescence intensity reduction observed in nAβ at day 10, no such decrease was found.

For quantification, the average fluorescence lifetime for all recorded images was plotted (Figure 2.7).

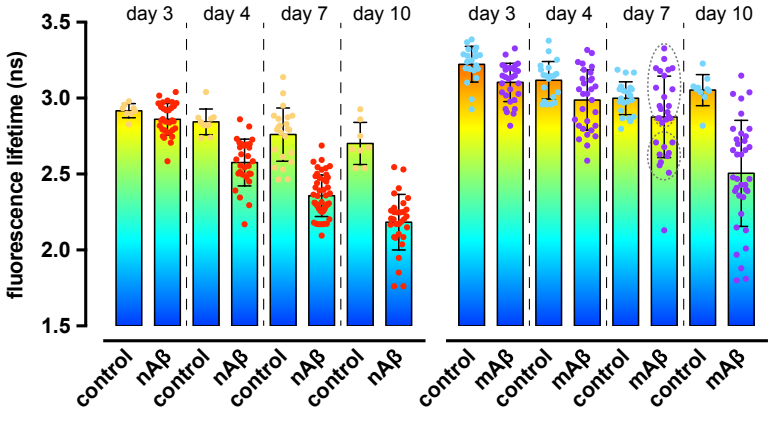

***Figure 2.7**: Scatter dot plot of the progression of aggregation in JKM2 and JKM7*

The average fluorescence lifetime of nAβ (red) and mAβ (violet) at different ages in comparison to their corresponding control expressing only mScarlet in neurons (yellow) or muscle cells (light-blue). Two populations exhibiting different life times (τ) were marked with dashed, grey circles. Every dot represents the mean fluorescence lifetime of a single image. Bars depict mean ± SD.

While only a minor, not significant decrease of the controls could be observed, the progressive nature of age dependent Aβ aggregation in both neuronal or muscular expression is clearly recognizable. Notably, despite the clear trend of the analysed cohorts, single animals exhibited differences in the mean fluorescence lifetime. This suggests that the observed variance is dependent on the individual fitness of every nematode analysed. Furthermore, this can also lead to the clustering of nematodes into sub-populations exhibiting different degrees of aggregate burden at the same day (see grey circle in Figure 2.7).

To test the hypothesis, that untagged $A\beta_{1-42}$ is necessary for aggregation in the generated model systems, a control strain that expresses mScarlet-$A\beta_{1-42}$ but no untagged $A\beta_{1-42}$ was generated (StopAβ, JKM5; see Supplemental Figure 7.2 A). Analysing the aggregation by FLIM revealed, that the fluorescence lifetime is, due to the microenvironment, already reduced on day four of life, but no further decrease in the progression of ageing was observed (Figure 2.8). Additionally, no characteristic foci formation was observed, suggesting that the untagged $A\beta_{1-42}$ is, indeed, required for native amyloid fibril formation. Using the amyloid specific dye ThT, no aggregation could be detected either (Supplemental Figure 7.2 B). Observations on *C. elegans* models that used only fluorescently labelled Aβ failed to detect fibrilization and thus further corroborate the conclusion that a moiety of untagged (naive) $A\beta_{1-42}$ is necessary to facilitate the aggregation of mScarlet-$A\beta_{1-42}$.

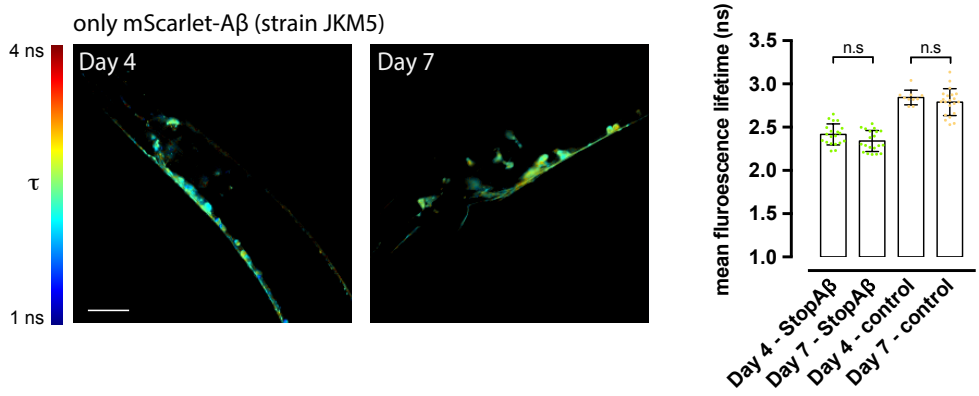

***Figure 2.8**: mScarlet-Aβ alone does not aggregate*

Representative TCSPC-FLIM images of StopAβ (JKM5) on day 4 and day 7 alive. Three cohorts of 10 - 15 nematodes each were analysed. Scale bar represents 20 µm. Scatter dot plot depicts mean ± SD, single dots represent the average fluorescence lifetime of one FLIM-image. JKM3 data, neuronal mScarlet control, was provided as reference.

The ultrastructure of Aβ aggregates is distorted

To analyse the ultrastructure and shape of amyloid fibrils *in vivo* would help to understand if and how amyloid spreading could work and if mechanic stress evokes toxicity. *In vitro* experiments with purified $A\beta_{1-40}$ or $A\beta_{1-42}$ showed a polar mode of fibril growth, and possible fibril lengths of several microns [228]. Stimulated emission depletion confocal microscopy (STED), transmission electron microscopy (TEM) and correlative light electron microscopy (CLEM) were employed to understand the shape of amyloids in the generated AD models *in vivo*.

STED extends the resolution of confocal microscopy beyond the diffraction barrier up to 40 nm. Fibrils of several microns could therefore be visible. Yet, no clearly distinguishable fibrils were observed (Figure 2.9). Most foci appeared thinner on STED images compared to the corresponding standard confocal images. Furthermore, foci that appeared as large, blurred spot in standard confocal microscopy were observed to be composed of several smaller foci that accumulated into one site (see Figure 2.9 close-up, green scales indicate size of apparent sub-foci). While detection of $A\beta_{1-42}$ fibrils in axial direction would be possible in theory, to discriminate between multiple axially aligned fibrils is not possible using STED. Furthermore, it is questionable if $A\beta_{1-42}$ fibrils would grow in a straight direction when they are affected from molecular crowding or if they would rather form tangles *in vivo* as surrounding proteins and structures could limit the straight growth and dictate fibril growth in the limited space available.

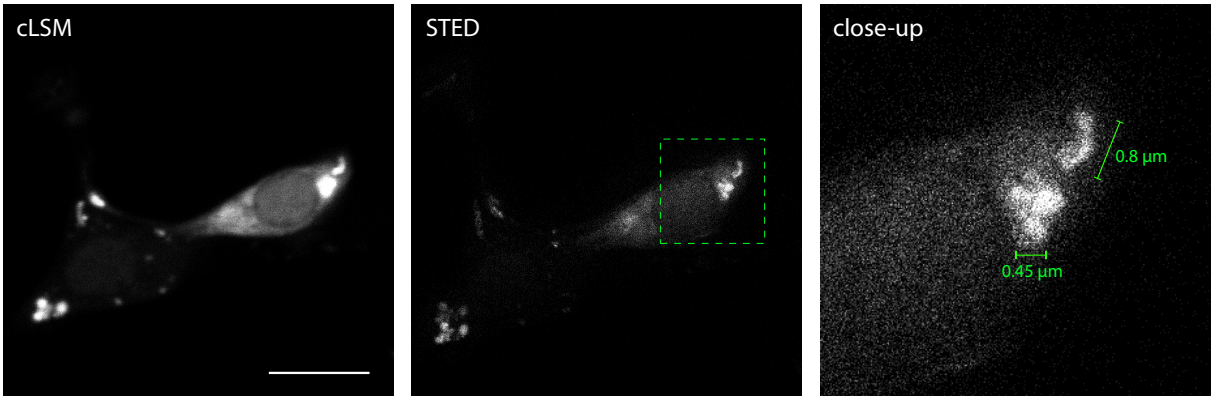

***Figure 2.9**: Confocal images of $A\beta_{1-42}$ foci do not reveal their underlying ultrastructure*
Representative stimulation emission depletion confocal image from a JKM2 nematode showing two neuron bodies from the retro-vesicular ganglion at 6000-fold magnification. Resolution-limited confocal image (cLSM) exhibits strong fluorescent, blurry foci. Scale bar represents 5 µm. STED image resolves few structures within the foci. Green scales indicate approximate size of corresponding objects.

Also, *in vivo* sheering forces and other perturbations due to cellular activities could shatter fibrils prematurely. Such shattered amyloids could induce secondary nucleation processes and increase aggregation and toxicity further. Yet, such disease relevant processes would not be detectable *in vitro* as only the unperturbed fibril growth is analysed.

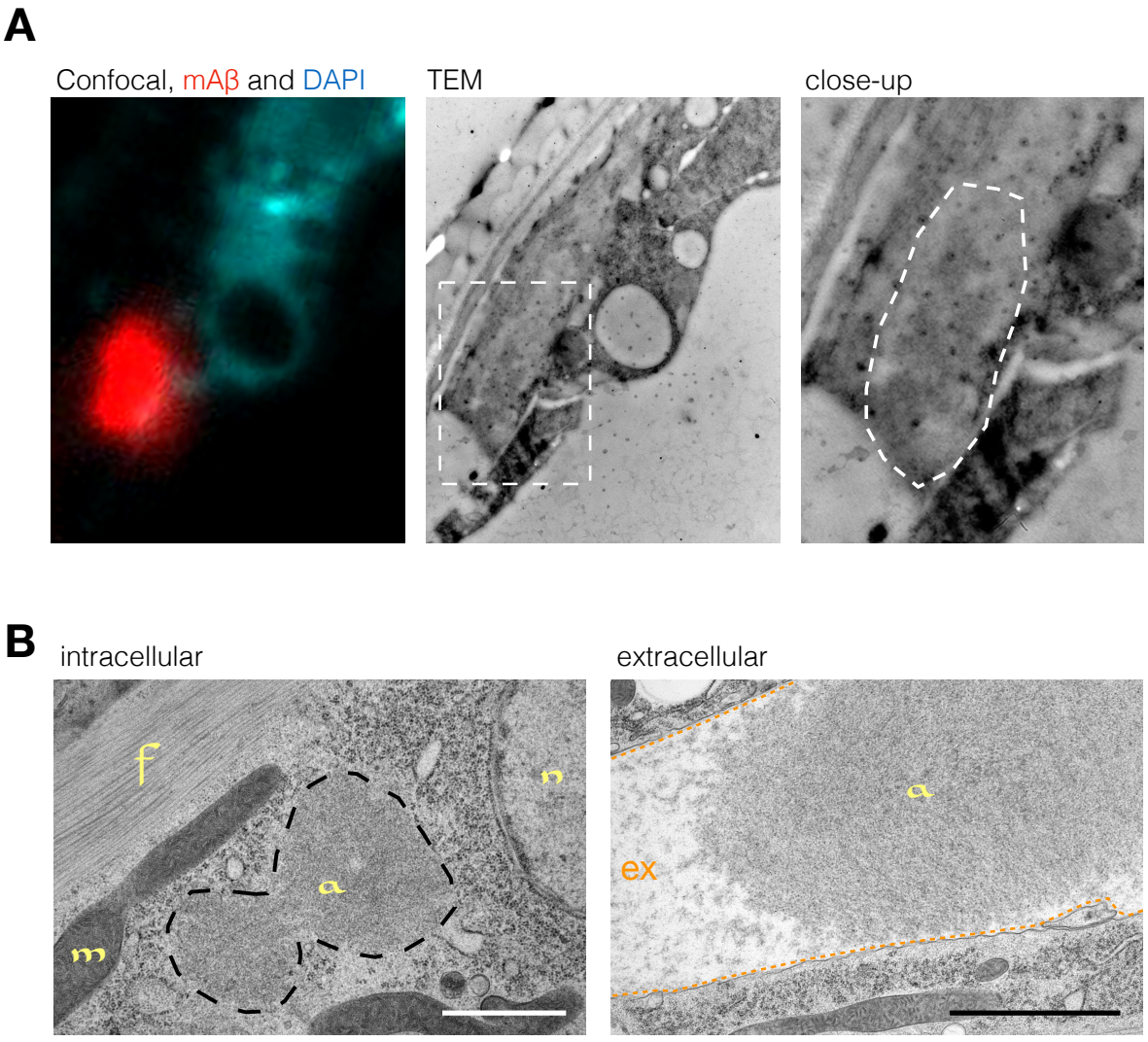

***Figure 2.10**: wrmScarlet-positive foci are composed of electron non-dense material*

(A) Correlative light-electron microscopy image of a JKM7 nematode embedded in HM20. wrmScarlet fluorescence (red) overlaps with material exhibiting altered electron density compared to the surrounding cytoplasm (see close-up, dashed white line). Kindly provided by Diogo Feleciano.

(B) Transmission electron microscopy of a JKM7 nematode embedded in Epoxy resin. The *left image* displays an intracellular region of a muscle cell, exhibiting an actin-myosin-fibre (f), mitochondria (m), a nucleus (n) and electron density altered material (black dashed line, a) at 30000-fold magnification. Scale bar is 1 µm. *Right image* displays extracellular space (ex) filled with some electron dense material (a). The cell membranes of the neighbouring cells are marked with a dashed, orange line. Image recorded at 20000-fold magnification. Scale bar represents 2 µm.

A technique with a higher resolution was employed: transmission electron microscopy (TEM). To detect aggregates, an approach combining light and electron microscopy was employed, correlated light electron microscopy (CLEM). DNA was stained with DAPI and used to align confocal and TEM images. Fluorescence of wrmScarlet-$A\beta_{1-42}$ was detected to colocalize with material that was slightly more electron dense than the surrounding cytoplasm (Figure 2.10 A). However, the quality of the TEM was too low, making it impossible to analyse the underlying ultrastructure. A second attempt of TEM was performed, using epoxy embedding that preserves the ultrastructure more reliably.

A cytosolic area containing presumably protein rich material, free from surrounding ribosomes and not delimited by a membrane was observed (Figure 2.10 B, left image, dashed black line, a). No halo around mitochondria and crisp cristae were detected as a sign for high quality freezing and fixation. The presumably protein rich material exhibited no striking underlying structures, yet the observed pattern was unique to $A\beta_{1-42}$ expressing nematodes. In wild type control nematodes, no such deposits could be found. Most interestingly, some deposits were detected in the pseudocoelom outside of the body wall muscle cells in mAβ but not in wild type nematodes (Figure 2.10 B, right image, a). This deposited material could be aggregated Aβ as well as endogenous aggregation prone material that got deposited upon increased proteotoxic stress elicited by $A\beta_{1-42}$ overexpression. Several proteins have been reported to aggregate in ageing nematodes [229,230], yet decreased proteoprotective capacity upon induced proteopathies (such as overexpression of $A\beta_{1-42}$) could accelerate these naturally occurring processes in a feedforward loop manner.

After amyloid formation and aggregate ultrastructure was observed and correlated to the progression of ageing I was wondering if toxicity would be elicited in $A\beta_{1-42}$ expressing nematodes.

Aggregation of Aβ elicits systemic defects

To characterize how the expression of $A\beta_{1-42}$ impairs the nematodes and to find possible read-outs for further hypothesis-driven experiments, several assays analysing the potentially systemic proteotoxicity have been conducted.

First, the lifespan of both nAβ and mAβ was analysed. nAβ nematodes exhibit a reduction of the median lifespan by 40% to 8.8 days and a decrease of the maximum life expectancy to 22 days (21% reduction) compared to wild type nematodes (Figure 2.11 left). The muscle expression strain mAβ exhibited a median lifespan reduction of 25% to 11 days and a decreased maximum life expectancy of 22 days (reduction of 21%) compared to wild type nematodes (Figure 2.11 right). The control strains expressing only wrmScarlet did not show any impairment of lifespan. Furthermore, the strain StopAβ (JKM5) did not show any lifespan reduction either (Supplemental Figure 7.2 C), correlating the observed toxicity in JKM2 and JKM7 to a progressive aggregation of $A\beta_{1-42}$. These data show, that $A\beta_{1-42}$ severely affects the lifespan, which is in contrast to previous studies where only moderate effects were reported [212,231].

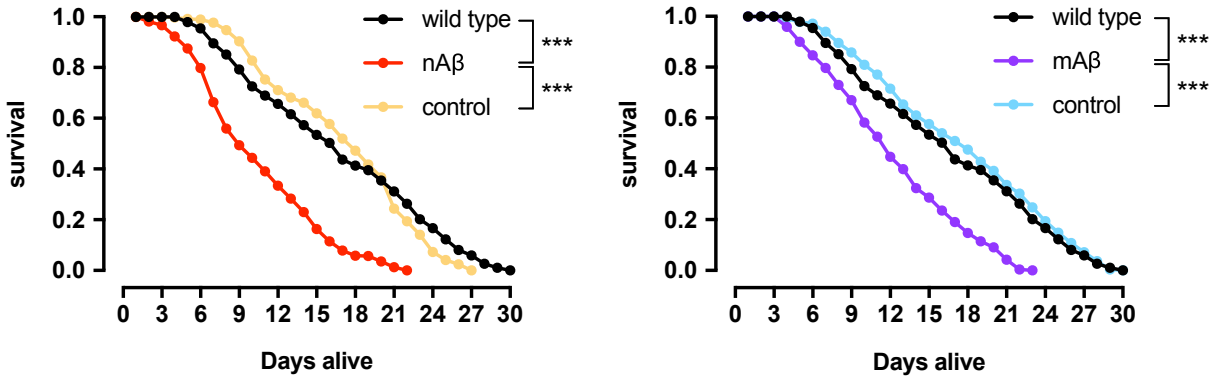

	wild type	neuronal $A\beta_{1-42}$	neuronal control	muscle $A\beta_{1-42}$	muscle control
median	16.1 ± 1.7	8.8 ± 1.1	17.9 ± 1.8	11.3 ± 1.2	17.2 ± 1.1
max	30	21	26	22	29

***Figure 2.11**: $A\beta_{1-42}$ expression reduces the nematodes lifespan*

Lifespan analysis of nAβ *vs.* N2 (wild type) *vs.* control (expression of mScarlet in neurons) and lifespan analysis of mAβ *vs.* N2 (wild type) *vs.* control (mScarlet expression in muscle). Shown is the mean cumulative survival probability versus age (days alive). Three cohorts of each 100 – 150 nematodes have been tested for nAβ, neuronal control and N2. One cohort of 120 nematodes has been tested for muscle Aβ and muscle control. A log-rank test was performed to test for significance (*** = $p < 10^{-6}$). The median and maximum lifespans for each strain are listed in the table below the graphs in days.

An additional read-out for organismal fitness is fecundity, which was measured by counting the viable offspring of $A\beta_{1-42}$ expressing nematodes (Figure 2.12 A). Both, nAβ and mAβ exhibited reduced brood sizes, while the wrmScarlet expressing controls did not show a reduction.

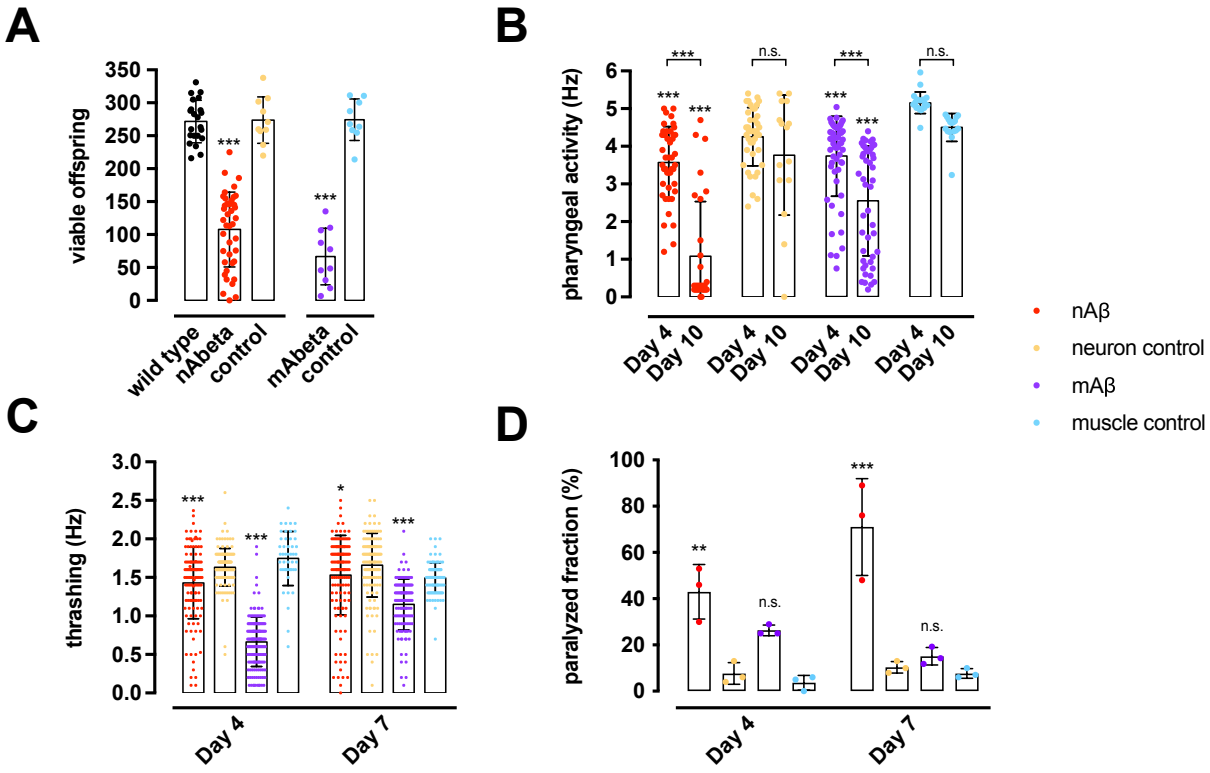

***Figure 2.12**: $A\beta_{1-42}$ expression impairs neuro muscular function*

(A) Scatter dot plot of a progeny assay for nAβ + control (JKM3), mAβ + control (JKM8) and wild type. Shown is the average number of viable offspring per nematode as mean ± SD. Three cohorts of 10 – 15 nematodes have been tested for N2 and nAβ. One cohort of 10 – 15 nematodes has been tested for neuronal control, muscle control and mAβ. Significance was assessed by one-way ANOVA + Bonferroni post hoc test (*** = $p < 0.001$) between the different strains and their respective controls. **(B)** Scatter dot plot of the pharynx pumping activity of nAβ (red) + control (yellow; JKM3) and mAβ (violet) + control (light-blue; JKM8) at day 4 and day 10 of life. Shown is the average pharyngeal activity as mean ± SD. In total, 20 to 60 nematodes have been tested per strain and day in cohorts of 10 – 15. Significance was tested with one-way ANOVA + Bonferroni post hoc test (*** = $p < 0.001$) between the different strains and their respective controls or between different ages of one strain. **(C)** Scatter dot plot of the thrashing capability of the same nematode lines as (B) swimming in M9 solution on day 4 and day 7 of life, respectively. Shown is mean ± SD. Three cohorts of 20 nematodes were recorded three times for 20 seconds as technical replicates. Significance was tested with two-way ANOVA + Bonferroni post hoc test (* = $p < 0.033$; *** = $p < 0.001$) between the different strains and their respective controls. **(D)** Scatter dot plot of the ability of the same nematode lines as (B) to swim in M9 solution for a period of 30 minutes. Paralyzed nematodes were counted and their fraction was plotted as mean ± SD from three cohorts of 20 – 30 nematodes per strain and day. The average of each cohort is represented by a dot in the graph. Nematodes were analyzed on day 4 and 7 of life, respectively.

The aggregation-impaired strain JKM5 did not exhibit a reduction in fertility, too, exemplifying the necessity of "$A\beta_{1-42}$ native" aggregation to exert toxicity (Supplemental Figure 7.2 D).

Next, the coordinated activity of neurons and muscles was tested by analyzing motility of the new disease model strains. Pharyngeal pumping was analyzed and found to be impaired compared to their respective controls and further aggravated upon ageing of the strains nAβ and mAβ (Figure 2.12 B).

To further test muscle activity, the swimming / thrashing of the nematodes in M9 medium was analyzed (Figure 2.12 C) and a strong reduction was observed for mAβ (≈ 60%), while a less pronounced, yet still significant, reduction was observed for nAβ (≈ 15%). Counterintuitively, the disease models performed better at older age. This is probably because of a survivorship bias: the most afflicted nematodes that perform poorly on day 4 die prematurely and are missing in the assay on day 7. This variance in population and the survivor effect was especially pronounced for mAβ as one could deduce from the observed phenotype and from the observed aggregation in the FLIM measurements (compare grey circles in Figure 2.7). To close the general characterization, a paralysis assay was performed, testing the swimming endurance in liquid medium. After 30 min swimming about 43% of the nAβ nematodes were not moving anymore nor reacting to prodding with an eye leash. Upon ageing this fraction increased to about 71%. mAβ was less affected, suggesting that neuronal activity is the limiting factor in this assay (Figure 2.12 D).

Aβ disturbs subcellular organelle organization and proteostasis

As JKM2 and JKM7 displayed severe systemic impairments, an analysis of subcellular and molecular perturbations was intended. Therefore, TEM images of $A\beta_{1-42}$ expressing nematodes were analyzed regarding subcellular organization and integrity (Figure 2.13). Major aberrations were found in both strains nAβ and mAβ body wall muscle cells, yet the exact occurrence differed. mAβ body wall muscle cells exhibited unnatural accumulations of probably defective endosomal, lysosomal and autophagosomal vesicles. These organelles were unfinished as their membranes were not closed, pointing towards defective membrane closure mechanisms (see red arrows in Figure 2.13 A). Yet, in the obtained images, all recorded muscle cells displayed accumulations of defective vesicles that engulfed each other in a matryoshka-like fashion, termed amphisomes. Since the neuronal $A\beta_{1-42}$ animals are also impaired in their motility I extended the EM analysis to $A\beta_{1-42}$ nematodes to see if this effect is

exclusively because of damaged motor neurons or if muscle cells themselves are damaged. Despite $A\beta_{1\text{-}42}$ was expressed in neurons, the adjacent muscle cells exhibited several abberations that were slightly different from those in mAβ nematodes. The endoplasmic reticulum (ER) was swollen (see green arrows in Figure 2.13 A). Amphisomes were detected, but they were not as abundant as in mAβ animals. The abundance of these perturbed structures was assessed by analysing the corresponding volume fraction as area of organelles *vs*. total cellular area (Figure 2.13 B). Amphisomes were enriched in mAβ, raising the hypothesis that these nematodes exhibit a strong perturbation of autophagy and possibly endo-lysosomal trafficking. The ER was significantly enlarged in nAβ compared to wild type, indicating defects in protein sorting.

Furthermore, ribosomes were observed to be reduced in mAβ and nearly completely depleted in nAβ (Figure 2.14). This matches previous findings, showing that both, the total amount of ribosomes as well as polysomes, are reduced in Aβ expressing nematodes [232]. This indicates defects in protein synthesis and evokes the hypothesis if other mechanisms maintaining proteostasis might by compromised, too.

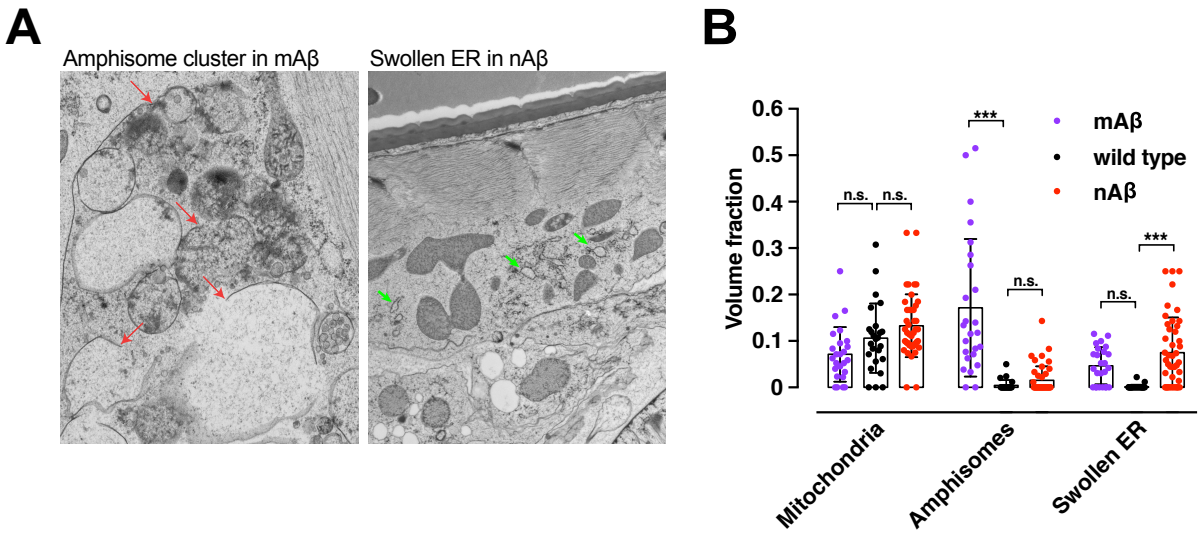

***Figure 2.13**: Cellular ultrastructure is damaged from $A\beta_{1\text{-}42}$ overexpression*

(A) Transmission electron microscopy (TEM) of epoxy embedded mAβ (JKM7) and nAβ (JKM2). Left, 20.000-fold magnification showing a close-up of a muscle cell. Red arrows show incomplete membranes from amphisome clusters (defective endosomal, lysosomal and/or autophagosomal structures). Right, 7000-fold magnification from nAβ displaying swollen ER (green arrows). **(B)** Scatter dot plot of total volume fractions of different organelles extracted from TEM images. mAβ (violet), nAβ (red) and wild type control (black) were plotted. 20 - 25 muscle cells from 5 - 6 nematodes were analysed. Significance was tested with two-way ANOVA + Bonferroni post hoc test (*** = $p < 0.001$).

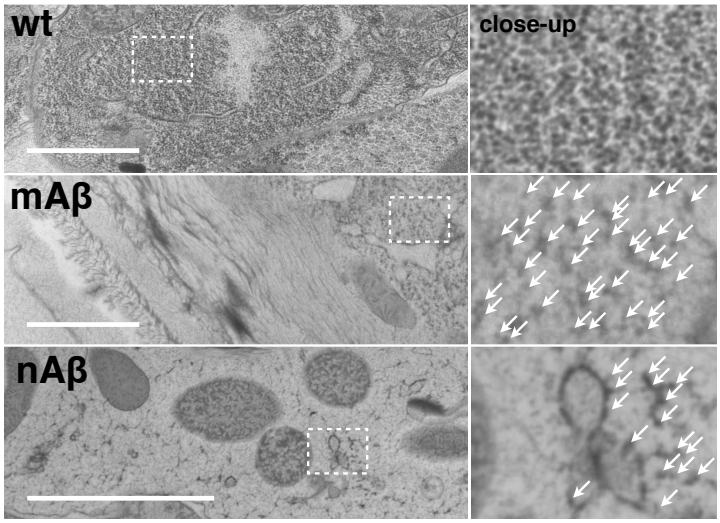

***Figure 2.14**: Ribosomes are depleted in $A\beta_{1-42}$ expressing nematodes*

Representative TEM images of wild type (wt, 12000-fold magnification), mAβ (12000-fold magnification) and nAβ (20000-fold magnification) nematodes with muscle cells displaying depletion of ribosomes. Scale bars represent 1 µm. Close-up images of indicated regions (dashed white box) displaying cytosol/ER with ribosomes (not indicated for wt, as there are too many; white arrows mark ribosomes in mAβ and nAβ).

Protein degradation is impaired in a model of AD

After observation of defects in membrane closure and amphisome enrichment, it was assumed that the endo-lysosomal / vesicular pathway could be impaired. Therefore, the protein degradation by autophagy as well as by the ubiquitin proteasome system (UPS) was assessed in $A\beta_{1-42}$ expressing nematodes. Day four old nAβ and mAβ nematodes were subjected to western blot analysis and SQST-1 (homolog of human p62) and LGG-1 (homolog of human LC-3) protein levels were assessed to analyse the autophagic flux (Figure 2.15 A). The levels of the adaptor and substrate protein SQST-1 were not affected by the $A\beta_{1-42}$ expression, suggesting that there is no turnover of SQST-1/p62. Yet, reduced levels of LGG-1 in mAβ animals were observed. LGG-1 is required to initiate phagophore construction and autophagosome maturation, rendering it an indispensable player for autophagy. Together with the TEM images that depict incomplete or disrupted membranous structures, this led to the conclusion that the autophagic flux is compromised in $A\beta_{1-42}$ animals.

The second major degradation pathway in eukaryotes, the UPS, is tightly connected with the regulation of autophagy and could be compromised in $A\beta_{1-42}$ expressing nematodes as previous studies observed [87]. Single proteins that are designated for degradation are marked by K48-linked-ubiquitin

chains and get subsequently processed by proteasomes. Proteasomes harbour three catalytic subunits that perform the proteolytic step. The most active of these catalytic sites has a chymotrypsin-like activity that can be tested in an *in vitro* assay using nematode lysates. The proteasomal activity of nAβ and control nematodes was tested regarding the progression of ageing (Figure 2.15 B). nAβ exhibited impaired proteasomal activity at advanced age (day 8) but not before. Thus, both major degradation pathways are compromised in $A\beta_{1\text{-}42}$ expressing nematodes.

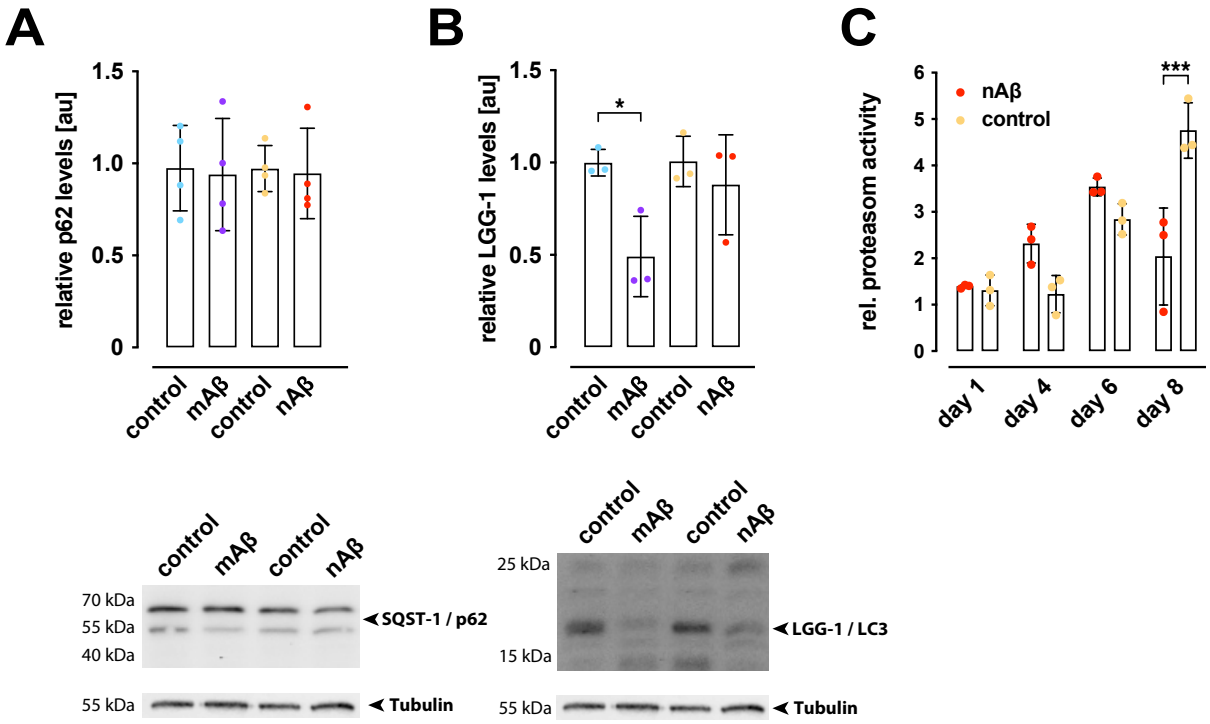

***Figure 2.15**: Autophagy and Proteasomes are inhibited*

(A) Quantification of the abundance of SQST-1 / p62 proteins in nAβ (red), neuronal control (yellow), mAβ (violet) or muscle control (light-blue) by western blot. Shown is mean intensity ± SD. Four cohorts were analysed. Significance was tested with one-way ANOVA + Bonferroni post hoc test. Image below is a representative western blot using anti-SQST-1 antibodies. Equal loading was checked by detection of α-Tubulin. Kindly provided by Manuel Iburg. **(B)** Quantification of the abundance of LGG-1 / LC3 proteins in nAβ (red), neuronal control (yellow), mAβ (violet) or muscle control (light-blue) by western blot. Shown is mean intensity ± SD. Three cohorts were analysed. Significance was tested with one-way ANOVA + Bonferroni post hoc test ($* = p < 0.033$). Image below is a representative western blot using anti-LGG-1 antibodies. Equal loading was checked by detection of α-Tubulin. Kindly provided by Manuel Iburg. **(C)** Scatter dot plot of proteasome activity test of nAβ *vs.* neuron control (JKM3). Three independent, age synchronized cohorts were harvested at the indicated age of 1, 4, 6 or 8 days and lysed. The proteasomal activity was measured in triplicates for each condition. Plotted is mean ± SD. Significance was tested employing two-way ANOVA + Bonferroni post hoc test ($*** = p < 0.001$).

Aβ$_{1-42}$ spreads to distant tissues

Since systemic toxicity and perturbed protein trafficking, synthesis and degradation were observed, I assumed a cell non-autonomous mechanism of pathogenicity, possibly involving spreading of Aβ$_{1-42}$ moieties. To analyse if Aβ$_{1-42}$ expressed in nAβ and mAβ can spread to distant tissues, a set of experiments was designed to address this major question. It was first tested, if Aβ$_{1-42}$ could be released from their expressing cells and migrate to the pseudocoelom, the central body cavity. Three pairs of coelomocytes are residing in the pseudocoelom and constantly filtering their surrounding medium. Yet, it was suggested that they serve immune, scavenging and hepatic functions [233]. In nAβ, red fluorescent wrmScarlet-Aβ$_{1-42}$ was found enriched in coelomocytes (Figure 2.16). Corresponding analysis of wrmScarlet control expression revealed only a small fraction of nematodes to exhibit enrichment of red fluorescent material in coelomocytes. While the fraction of nematodes exhibiting red fluorescence in the vacuoles of coelomocytes in control animals increased upon ageing slightly, there was no change observed for nAβ, yet a further increase seems to be hardly possible as already on day four 95% of the nematodes exhibited red fluorescent material in the coelomocytes. Hence, wrmScarlet-Aβ$_{1-42}$ seems to facilitate its release from neuronal cells and subsequently accumulate in the pseudocoelom and the coelomocytes. This may be an indication, that the deposited material found outside of cells in the TEM images could truly be Aβ$_{1-42}$.

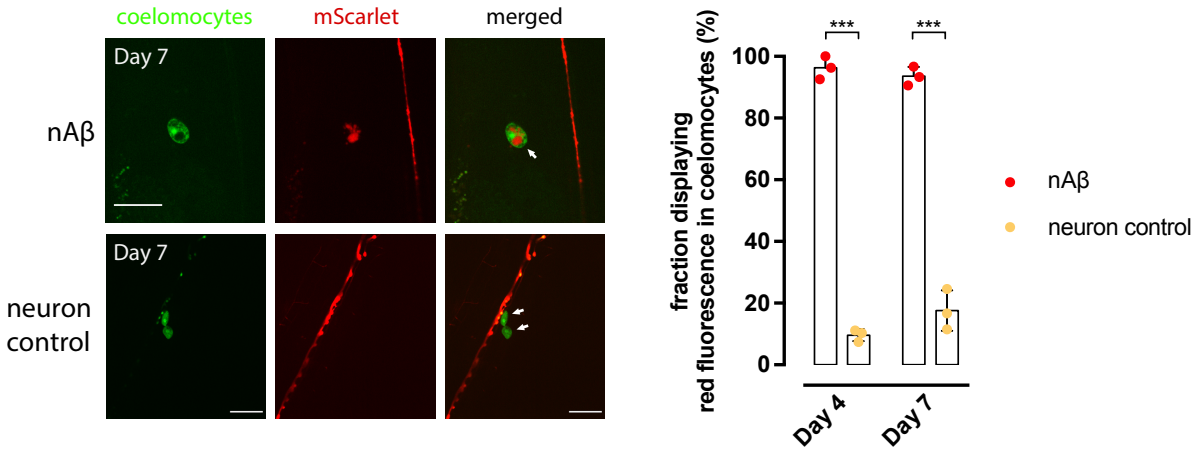

***Figure 2.16**: Aβ$_{1-42}$ accumulates in coelomocytes*

Representative confocal images of JKM2×ZIM1048 and JKM3×ZIM1048. Coelomocytes are labelled with GFP (*unc-122p*::GFP). wrmScarlet-Aβ$_{1-42}$ was found inside vacuoles of coelomocytes. Scale bars are 10 µm. Scatter dot plot to the right displays the fraction of nematodes exhibiting red fluorescence in coelomocytes at day 4 and 7 of life. Depicted is mean ± SD. Significance was tested with two-way ANOVA + Bonferroni post hoc test (*** = $p < 0.001$).

To test if $A\beta_{1-42}$ could be detected outside of cells, but not localized in coelomocytes, a second approach was employed by crossing JKM2 and JKM7 nematodes with nematodes expressing a pan neuronal YFP or body wall muscle GFP respectively. For both, nAβ and mAβ day 7 old nematodes wrmScarlet-$A\beta_{1-42}$ was observed outside of their respective expressing tissue (Figure 2.17 A, white arrows). No extrusion of wrmScarlet could be observed for the control nematodes JKM3 and JKM8 (crossed with nQ0 or mQ0 respectively Figure 2.17 B). This indicates that $A\beta_{1-42}$ is spreading. It was unclear if $A\beta_{1-42}$ was outside of cells at all or if it was able to invade other cell types and form deposits within them.

To test Aβ's ability to invade other cells, spreading was tested exemplarily to hypodermis. The hypodermis has a large surface and shares a close proximity to both, neurons and muscle cells. A hypodermally expressed GFP was employed to track wrmScarlet-$A\beta_{1-42}$ that was translocated into hypodermis (Figure 2.18 A). Indeed, colocalization of wrmScarlet-$A\beta_{1-42}$ derived fluorescence and hypodermal marker fluorescence was observed, both for neuronal and muscle cell origin (see blue arrows in Figure 2.18 A, Supplemental Figure 7.3). This clearly shows, that $A\beta_{1-42}$ is able to passage to other tissues, while wrmScarlet control is not able to intrude into the hypodermis.

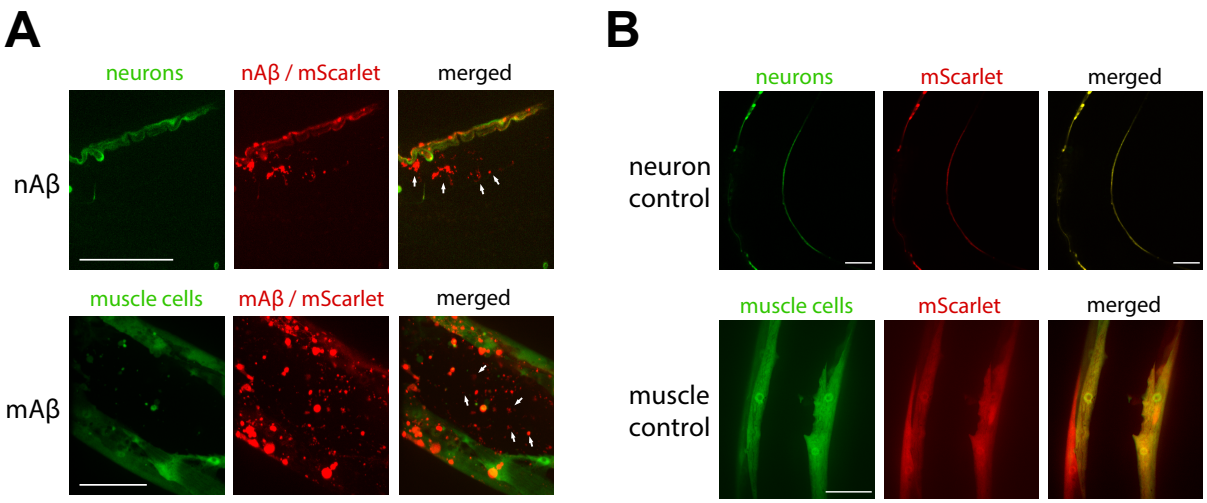

***Figure 2.17**: $A\beta_{1-42}$ escapes the expressing tissues*

(A) Representative confocal images of day 7 old JKM2×nYFP and JKM7×mGFP. Neurons or muscle cells are labelled with green fluorescence (respective YFP or GFP). Colocalization with red fluorescent wrmScarlet or wrmScarlet-$A\beta_{1-42}$ was analysed and non-colocalizing spots were marked with white arrows. **(B)** Representative confocal images of day 7 old JKM3×nYFP on the left side; and JKM8×mGFP on the right side. Scale bars are 20 µm.

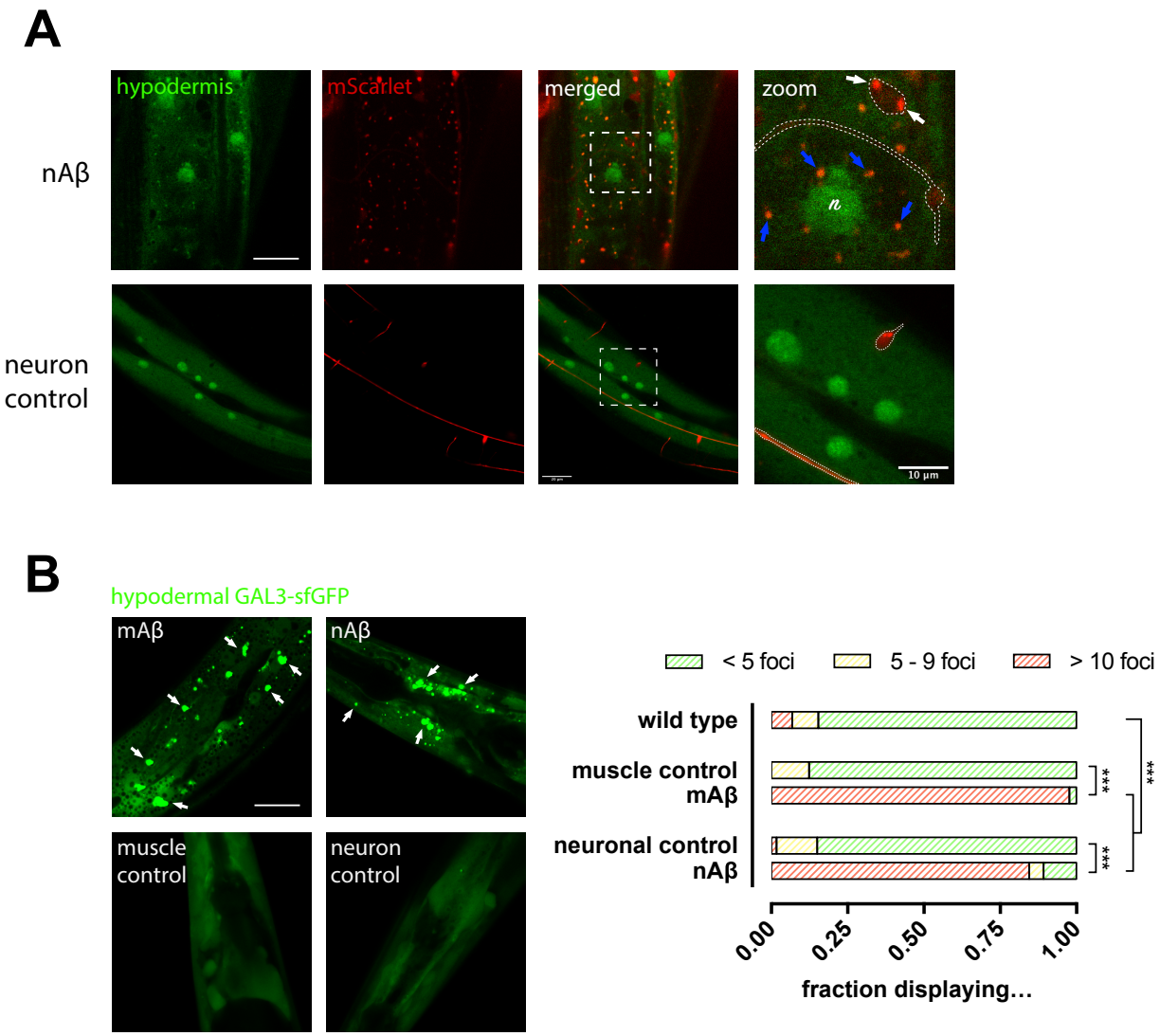

***Figure 2.18**: Hypodermal permeation by $A\beta_{1-42}$*

(A) Representative confocal images of nAβ×CS628 and JKM3×CS628 (expressing a hypodermal GFP marker). Scale bar represents 20 µm. Close-up (zoom) image of the indicated region exhibits wrmScarlet-$A\beta_{1-42}$ foci in hypodermis (blue arrows), as well as red fluorescence in neurons (white arrows). Position of neurons is indicated by dashed, white lines. A hypodermal nucleus is labelled (n). **(B)** Representative images of nAβ×BIJ34, mAβ×BIJ34, JKM3×BIJ34 and JKM8×BIJ34 exhibit green fluorescence from hypodermal LGALS3-sfGFP. Upon Ca^{2+} influx LGALS3 oligomerizes and forms visible foci (white arrows). Three independent cohorts, each of 10 – 20 nematodes were analysed in triplicates and the nematode fractions displaying certain number of foci are shown as bar plot (right). To test significance a two-way ANOVA + Bonferroni post hoc test was employed (*** = $p < 0.001$).

Although the mechanism that facilitates direct cell to cell transfer of Aβ is not known yet, an active transport and excretion/uptake mechanism could be involved in $A\beta_{1-42}$ spreading. Another possible mechanism could be passive transmission by disturbing membrane integrity.

To test this hypothesis, plasma membrane integrity was assessed indirectly, using a reporter strain expressing human Galectin-3::superfolderGFP (GAL3-sfGFP) in hypodermal cells. Galectin-3 oligomerizes upon binding to Ca^{2+}, indicating a leakage of Ca^{2+} into to cytoplasm and therefore compromised membrane integrity (Figure 2.18).

An abundant foci formation was observed in nAβ and mAβ (crossed with the Galectin reporter strain BIJ34) already in day four old nematodes. Nematodes expressing only the Galectin reporter or a combination with muscle / neuronal wrmScarlet did not show accumulation of GAL3-foci. This is a strong indication that membranes are permeated in $A\beta_{1-42}$ expressing nematodes resulting in Ca^{2+} influx from either the extracellular matrix or leakage from compromised endo-lysosomal compartment, or both. Yet, this observation substantiates the hypothesis of a potential passive spreading by direct membrane permeation.

Identification of a subset of aggregation prone neurons

Since strong indications of spreading behaviour of $A\beta_{1-42}$ were observed in the previously presented experiments, I assumed, that aggregation could occur unevenly distributed between different cell-types and spreading could induce seeding in distant, less-affected cell types. The aggregation propensity of $A\beta_{1-42}$ as well as other amyloidogenic proteins depends on a multitude of parameters whose identification and quantification are subject to current research. Yet, most factors remain elusive and both intrinsic (*e.g.* genetic predisposition) and extrinsic (*e.g.* environmental cues) ones can contribute to facilitate aggregation. Strikingly, nAβ nematodes exhibited the first aggregates consistently in a distinct subset of four to six head neurons of the anterior ganglion (approx. 90% of all analysed day four old nAβ nematodes were affected) (Figure 2.19 A, white arrows). The total amyloid burden remained low on day four of life and started to manifest in the complete nervous system more than one day later (Figure 2.6). The early aggregates were found in the neuronal soma. To identify these neurons, a confocal Z-stack (Figure 2.19 B) was recorded and I found that the cell bodies are located in the anterior

ganglion in close proximity to the metacorpus. They exhibited dendrites reaching to the tip of the nose, ending in potential sensory arrays and an axon directed into the central nerve ring. To identify the neurons, genetic crossings with animals expressing multiple neuronal markers were conducted.

First, the neurotransmitter identity was assessed by crossing nAβ nematodes with dopaminergic GFP expression marker (BZ555), glutamatergic GFP expression marker (OH10972) or cholinergic GFP expression marker (LX929) (Figure 2.19 C, Figure 2.20). The early aggregates occurred in cholinergic neurons. The relative position of individual neurons can vary between nematodes up to several lengths of one neuron body [193,234]. Together, shape, position and neurotransmitter identity led to the conclusion that the neurons exhibiting the first aggregates were either IL2 or URA neurons.

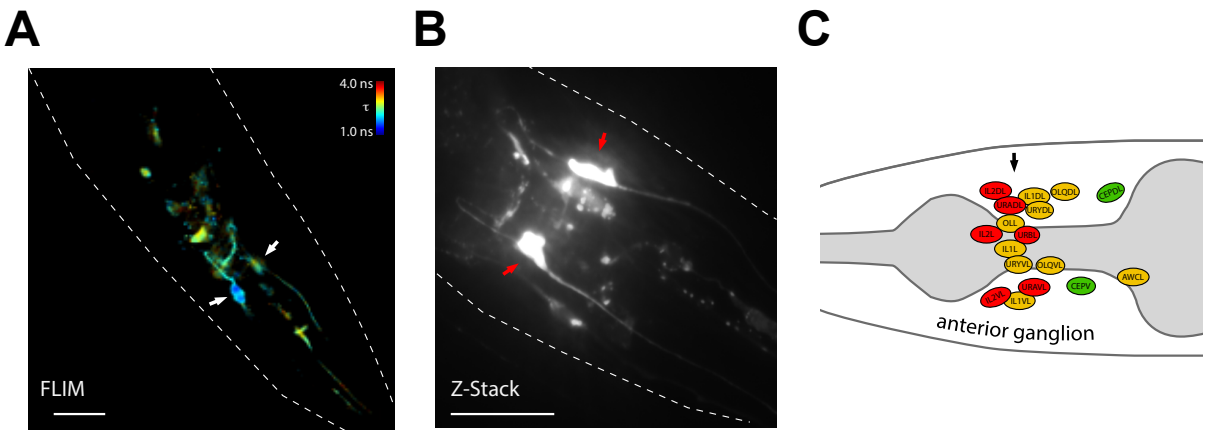

***Figure 2.19**: IL2 neurons exhibit the first aggregates*

(A) Representative FLIM image of a day four old nAβ nematode, exhibiting first aggregates in IL2 neurons (white arrows). Image is false-coloured to indicate fluorescence lifetime (from blue = low fluorescence lifetime to red = high fluorescence lifetime). Outline of the nematode is indicated by a dashed, white line. Scale bar is 20 µm. **(B)** Collapsed confocal Z-Stack (in 1 µm steps through the whole nematode head, ≈ 40 µm) of a representative day four old nAβ nematode. IL2 neurons are indicated (red arrows). Nematode is outlined by a dashed, white line. Scale bar is 20 µm. **(C)** Schema of relative position of the neuron bodies of head neurons of the anterior ganglion (left side). Relative position of the neurons exhibiting the first aggregates is indicated (black arrow). Neurons are coloured depending on neurotransmitter usage (red = Acetylcholine; yellow = Glutamate; green = Dopamine).

To identify the neurons, two additional markers were employed. First, the expression of *flp-22p::GFP* [235], localized in a subset of approx. 34 neurons, with the most anterior expression in URA neurons (Figure ***2.20***, blue arrows) was observed to display no colocalization with the early aggregating $A\beta_{1-42}$. Second, a marker expressed in IL2 neurons (*klp-6p::GFP* [236]) was employed that exhibited colocalization with the early aggregation (Figure 2.20, last panel). To exclude that the early onset of aggregation in IL2 neurons is only dose-dependent, FLIM images were analysed again regarding coincidence of intense fluorescence and aggregation (low fluorescence lifetime) (Supplemental Figure 7.4). Aggregation in IL2 was observed to be independent from expression levels, as no aggregates were detected in other neurons that exhibited an equivalent or even higher fluorescence intensity. Only a low amount of randomly occurring aggregates (regarding count and distribution) were found that were not localized in IL2 neurons (Supplemental Figure 7.4, yellow dashed arrows). This is in stark contrast to the aggregates in IL2 neurons that were reliably occurring in more than 90% of the analysed nAβ animals on day four of age.

BZ555 × JKM2

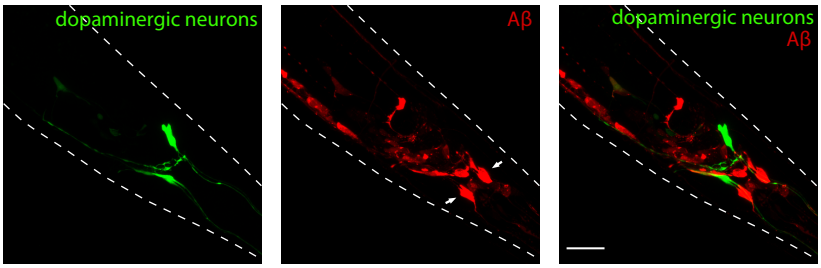

OH10972 × JKM2

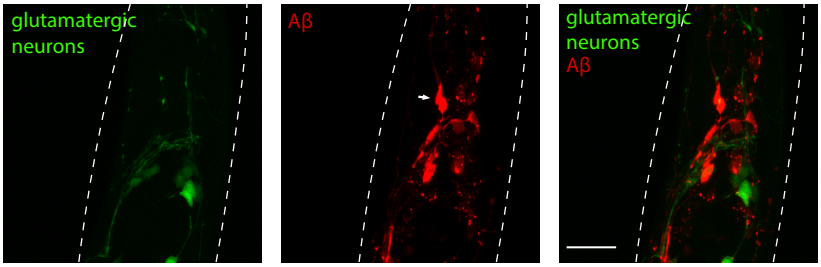

LX929 × JKM2

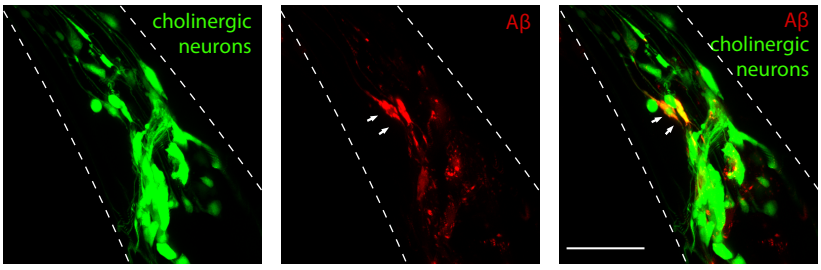

flp-22p::GFP × JKM2

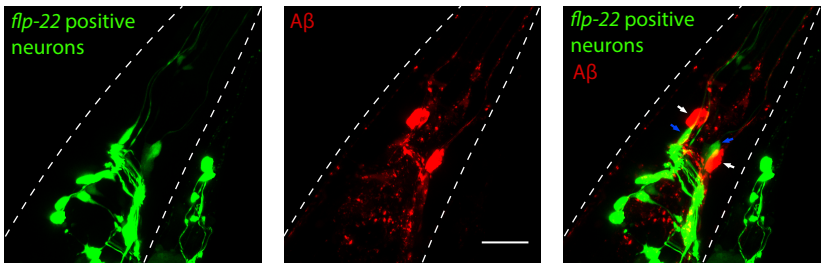

flp-22 expression: AIM, AIZ, ASG, AVA, AVG, AVL, CEP, CP neuron, PVD, PVW, RIC, RIV, SMD, **URA**, uv1

klp-6p::GFP × JKM2

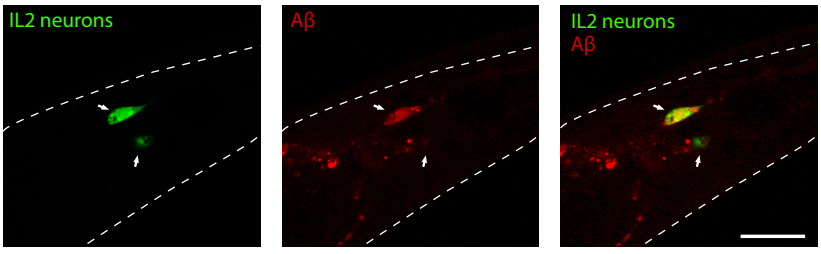

***Figure 2.20**: Identification of the neurons exhibiting the first aggregate as IL2 neurons*

Representative confocal images of crosses of the indicated strains were performed to assess neurotransmitter identity of the neurons exhibiting the first aggregates (cross with strains BZ555, OH10972 and LX929). Fluorescence of GFP markers and wrmScarlet-$A\beta_{1-42}$ was measured and analysed for colocalization. Crosses with strains expressing *flp-22p::GFP* (expression in a subset of ≈ 34 neurons) or *klp-6p::GFP* (hermaphrodite expression in IL2 neurons only) were performed to exactly identify IL2 neurons as the neurons exhibiting the first aggregates. Nematodes are outlined with dashed, white lines. Scale bars are 20 µm. White arrows point to the neurons with the first aggregates / IL2 neurons; blue arrows point to URA neurons. *klp-6p::GFP* × JKM2 cross and image kindly provided by Manuel Iburg.

Aβ$_{1-42}$ aggregation causes neurodegeneration and impairs neuronal function

Based on the observed systemic toxicity of neuronal Aβ$_{1-42}$ expression it was hypothesised that nAβ could exhibit visible neurodegeneration. Thus, the integrity of neurons was analysed using a fluorescent marker in a subset of neurons (under control of *tol-1* promoter). *tol-1p* expression is mainly found in the four URY neurons (ventral-left/right and dorsal-left/right) that belong to the anterior ganglion and are in close vicinity of the IL2 neurons. Z-stack images of nAβ × *tol-1p::GFP* nematodes were recorded on day 4, day 7 and day 10 of life. The fractions of nematodes displaying damaged neurites *vs*. intact neurites were quantified (Figure 2.21). On day seven of life 67% of the analysed nAβ nematodes showed damaged URY neurons compared to 35% of control nematodes. Upon ageing (day 10) this phenotype became more severe: 78% of the Aβ$_{1-42}$ expressing nematodes displayed damaged URY neurons, while still only 35% of the wild type animals displayed damage.

To complement this observation, the functionality of the URY neurons in nAβ was evaluated: their ability to sense certain pathogenic bacteria and provoke an avoidance behaviour.

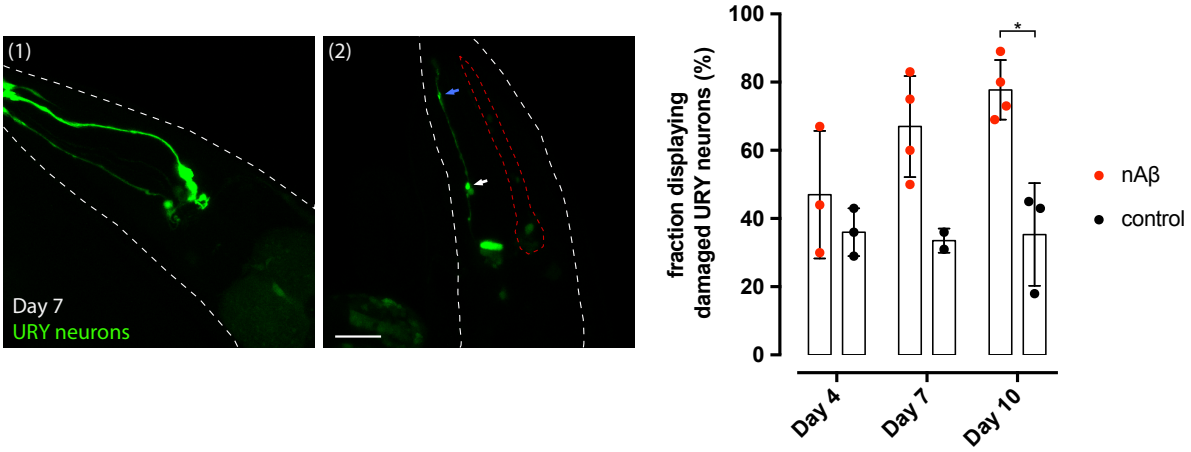

***Figure 2.21**: URY neurons suffer from progressive deterioration in nAβ*

Collapsed confocal Z-Stack of nAβ × *tol-1p::GFP* nematodes representative for healthy (1) or afflicted state (2) are shown. Nematodes were counted as damaged if they exhibited five or more blebs (blue arrow), two or more spheres or outgrowing branches (white arrow), and/or complete ablation / necrosis of URY neurons (dashed red line). Nematodes are outlined (dashed, white line). Scale bar represents 20 µm. The scatter dot plot to the right shows the quantification nAβ *vs.* wild type control animals as mean ± SD. Three to four individual cohorts of 8 - 16 nematodes each were analysed. Significance was tested with two-way ANOVA + Bonferroni post hoc test (∗ = $p < 0.033$).

A previously established pathogen avoidance assay was adapted [237], employing *E. coli* OP50 (common food source) as control and *Serratia marcescens* Db11 (pathogenic bacterial strain), as well as *S. marcescens* Db1140 (attenuated strain) to test avoidance. Wild type nematodes evade pathogenic Db11 bacteria. The *tol-1* receptor gene is particularly important for this reaction and a *tol-1* mutant strain (IG10) does not exhibit pathogen avoidance towards Db11. All analysed nematode strains dwell on non-pathogenic OP50 bacteria, but display a differentiated behaviour towards pathogenic Db11 bacteria. Wild type nematodes avoided Db11, while *tol-1* mutant nematodes did not avoid Db11. Notably, nAβ nematodes did not show any avoidance behaviour, compared to control nematodes JKM3 (neuronal wrmScarlet) and JKM5 (StopAβ, aggregation impaired) (Figure 2.22 A, Supplemental Figure ***7.2*** E).

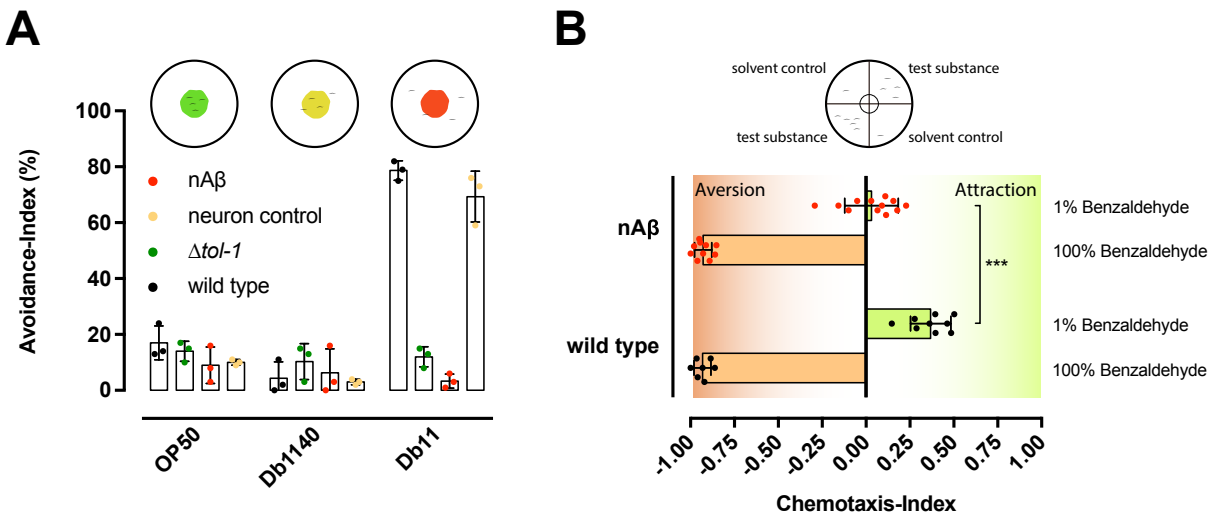

Figure 2.22*: nAβ exhibits impaired pathogen avoidance and chemotaxis*

(A) Scatter dot plot of a pathogen avoidance assay showing nematodes' reaction to different bacteria. Non-pathogenic *E. coli* strain OP50 was used to show nematodes' lawn dwelling. Pathogenic *Serratia marcescens* strain Db11 and attenuated *S. marcescens* strain Db1140 were employed to test avoidance reactions. Wild type (N2; black) served as positive control for avoidance reaction and *tol-1* mutant strain (IG10; green) served as negative control. nAβ animals are represented by red dots and neuronal control animals by yellow dots. Three independent experiments consisting of 3 - 5 cohorts of 10 - 15 nematodes were measured four times in 5 min intervals for their behaviour after being exposed to the respective bacteria for 48 h. **(B)** Scatter dot plot of a chemotaxis assay. Three independent experiments with each 2 - 4 cohorts of 50 - 100 nematodes (day 4/5 adults) were analysed regarding the distribution of nematodes between test and control quadrants, exposing them to odorants or solvent controls. Chemotaxis-Index was calculated. Significance was tested with two-way ANOVA + Bonferroni post hoc test (*** = $p < 0.001$).

The analysis of avoidance was performed from day four to day six of life. Hence, neuronal impairment occurs before macroscopic aberrations of neuronal structures become visible (compare starting degeneration from day 7 onwards, Figure 2.21).

To further investigate neuronal function that relies on the activity of other neurons, a chemotaxis assay was employed to analyse the nematodes' behaviour to volatile odorants. Diluted benzaldehyde (1% v/v) was tested for the induction of attraction behaviour. In wild type nematodes diluted benzaldehyde is sensed by AWC neurons, a class of chemotactic neurons located in the lateral ganglion and induces an attraction behaviour [238]. As expected, wild type nematodes are attracted towards 1% benzaldehyde. nAβ nematodes on the other hand are not attracted, therefore seem to be chemotactically impaired in either detecting the odorant or reacting to it. Both nematode strains are, on the other hand, repelled by pure benzaldehyde. Hence, $A\beta_{1-42}$ impaired certain neuronal functions, yet some functions appeared as preserved.

Suppression of $A\beta_{1-42}$ aggregation in IL2 neurons can delay amyloid pathology systemically

After I observed that $A\beta_{1-42}$ was indeed eliciting neurodegeneration I was wondering if spreading would play a role in this process and if prevention of spreading could alleviate neurodegeneration. Yet, the major question was if IL2 neurons, that exhibited the first aggregates, were especially vulnerable or unprotected towards $A\beta_{1-42}$ aggregation. This also offers the possibility that an inhibition of Aβ aggregation specifically in IL2 neurons could delay the aggregation systemically and lead to an alleviation of the AD phenotype.

To address this question, a cell-type specific knockdown by expressing a short hairpin construct site-specifically in IL2 neurons was employed (Figure 2.23 A). As a control, the same construct was expressed in a subset of other neurons with the major expression in URY neurons (driven by *tol-1p*). These constructs were crossed with nAβ animals (Figure 2.23 B) and tested for aggregation and systemic impairment. First, the specificity of the hairpin construct was evaluated by testing a specific phenotype in nAβ + $shRNA^{URY}$: pathogen avoidance (Supplemental Figure 7.5). Avoidance from

pathogenic *S. marcescens* Db11 bacteria was rescued partially by the expression of the short-hairpin construct in URY neurons, while the chemotaxis towards diluted benzaldehyde, that requires AWC neuron activity, remained impaired. I conclude that the designed short-hairpin expression system induces indeed cell-type specific RNAi. To assess the impact on the $A\beta_{1\text{-}42}$ aggregation, fluorescence lifetime measurements were conducted on nAβ with or without the co-expression of the short-hairpin constructs in IL2 neurons or URY neurons (Figure 2.24 A). Indeed, a systemic reduction of aggregation was observed for day four old nematodes upon $A\beta_{1\text{-}42}$ knockdown in IL2 neurons, yet not for a knockdown specifically in URY neurons (Figure 2.24 A, C). Also, a reduction of IL2 neurons harbouring aggregates was observed upon IL2-specific knockdown underlining the specificity of the employed site-specific knockdown approach (Figure 2.24 B). Given that a reduction of amyloid burden in IL2 neurons reduced neuronal $A\beta_{1\text{-}42}$ aggregation systemically, it was hypothesised that it may also alleviate toxicity in the nervous system and even on an organismal level.

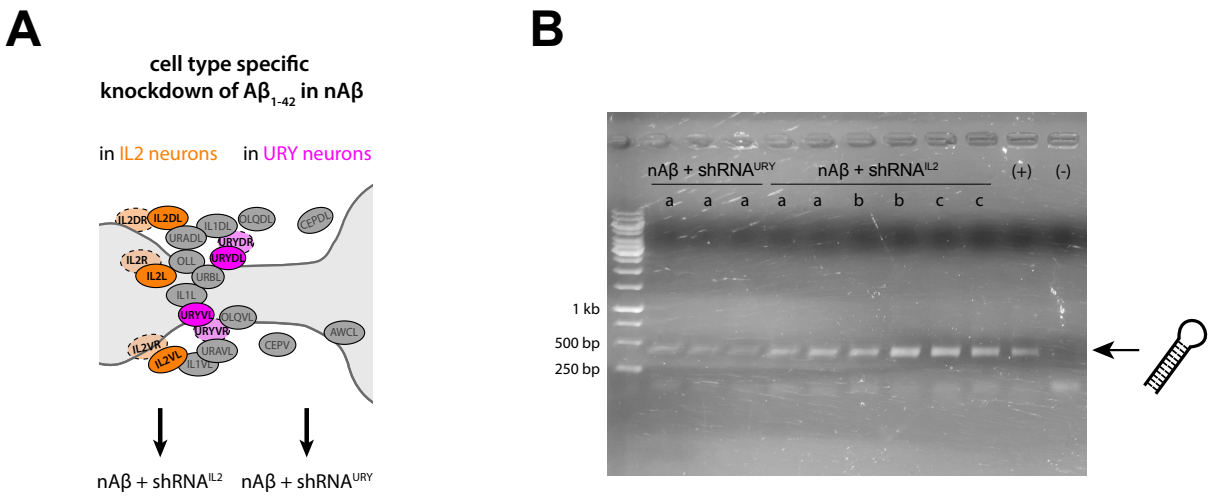

***Figure 2.23**: Expression of a short-hairpin construct for $A\beta_{1\text{-}42}$-knockdown*

(A) Schema depicting the strategy for cell type specific knockdown in neurons of the anterior ganglion. A short-hairpin construct against $A\beta_{1\text{-}42}$ is expressed in either IL2 neurons (using *klp-6* promoter sequence) or URY neurons (using *tol-1* promoter sequence). View on the left side of the head, affected IL2 and URY neurons on the right side of the head are light coloured and have dashed lines. Unaffected neurons for orientation are shown for the left side only and are grey coloured. **(B)** Agarose gel electrophoresis of a genotyping PCR for the short-hairpin construct (400 bp band) in transgenic nematode strains. One isolate was tested as triplicate for nAβ + $shRNA^{URY}$, three isolates were tested for nAβ + $shRNA^{IL2}$ in duplicates. The vector used for transgenesis was used as positive control (+) and wild type gDNA was used as negative control (-).

To this end, the general vitality of these nematodes was assayed by lifespan, swimming and paralysis assays. nAβ, +shRNA^{IL2}, +shRNA^{URY} and wild type nematodes were incubated in M9 medium swimming for 30 min and the fraction of paralyzed nematodes was assessed afterwards (Figure 2.25 A).

The co-expression of the hairpin construct in IL2 neurons reduced the fraction of paralyzed day 4 old nematodes compared to nAβ (+shRNA^{IL2}: 18% vs. nAβ: 43%) or the control, expressing the hairpin construct in URY neurons, significantly (+shRNA^{IL2}: 18% vs. +shRNA^{URY}: 57 %).

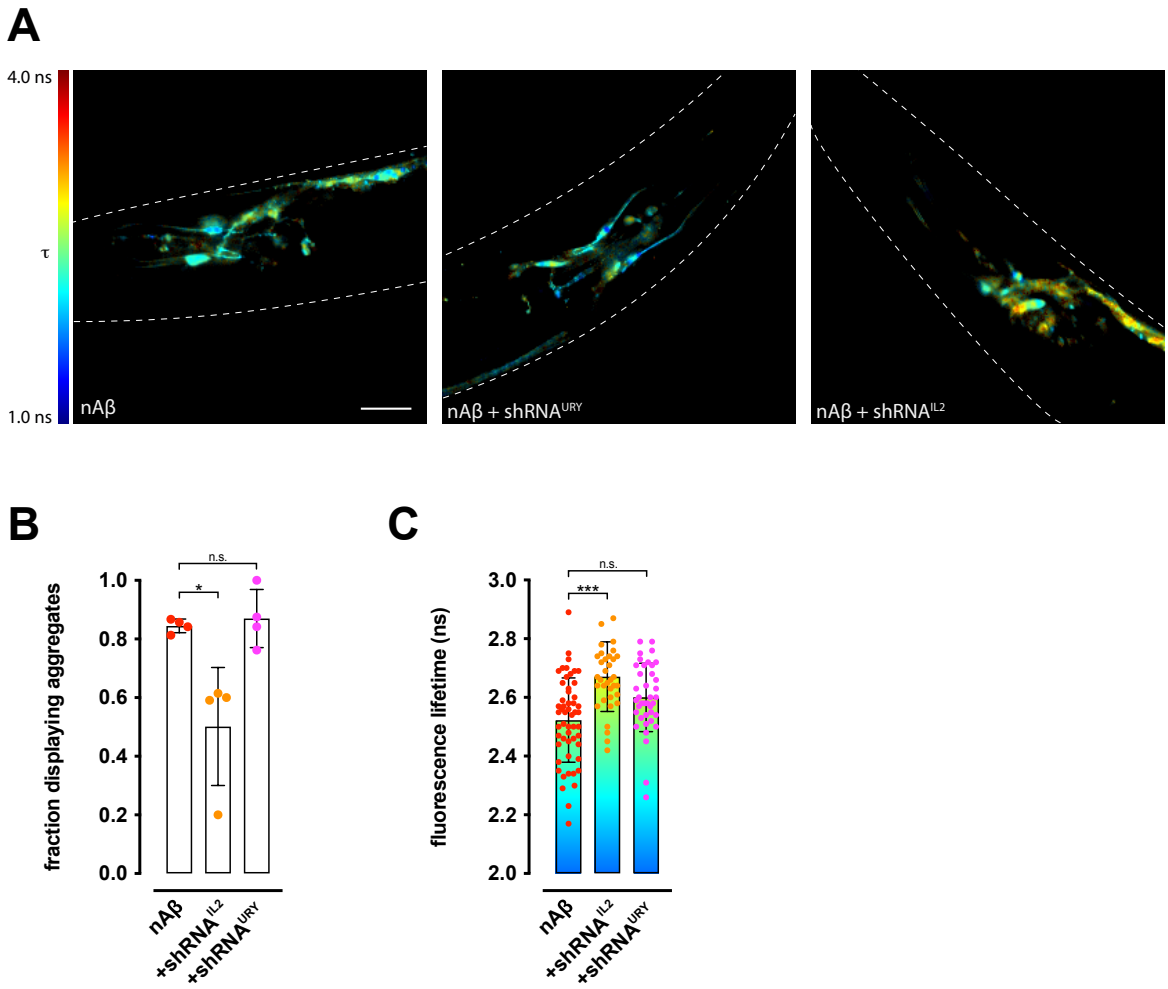

***Figure 2.24**: Knockdown of Aβ$_{1-42}$ in IL2 reduces amyloid burden*

(A) Shown are representative TCSPC-FLIM images of nAβ, +shRNA^{URY}, +shRNA^{IL2} in false-colours (from blue = low fluorescence lifetime to red = high fluorescence lifetime). Nematodes are outlined with dashed white lines. Scale bar represents 20 µm. **(B)** Scatter dot plot of the fraction of IL2 neurons displaying aggregates in nAβ, +shRNA^{URY}, +shRNA^{IL2} on day four of life. Aggregate evaluation was performed on FLIM images. Four cohorts of 8 – 12 nematodes each were analysed and mean ± SD is displayed. Significance was tested with one-way ANOVA + Bonferroni post hoc test (∗ = $p < 0.033$). **(C)** Scatter dot plot of the mean fluorescence lifetime of nAβ, +shRNA^{URY}, +shRNA^{IL2} on day four of life. Four cohorts of 8 – 12 nematodes each were analysed and mean ± SD is displayed. Significance was tested with one-way ANOVA + Bonferroni post hoc test (∗∗∗ = $p < 0.001$).

There was no significant difference between nAβ and nAβ + shRNA^{URY}, as well as there was no significant difference between the wild type and the rescue strain nAβ + shRNA^{IL2}. Hence, a reduction of nAβ$_{1-42}$ aggregation in the early onset of aggregation IL2 neurons seemed to reduce overall neuronal aggregation and importantly was beneficial for the organismal fitness. To complement this, thrashing was analysed and a significant rescue was observed for IL2-specific knockdown, but not for control knockdown or an untreated control (Figure 2.25 B).

To analyse if the knockdown provides a lasting benefit for the AD pathology, lifespan was assessed for nAβ and nAβ + shRNA^{IL2}. The knockdown increased the median lifespan by 27% (+shRNA^{IL2}: 9.0 days *vs.* nAβ: 7.1 days), but did not extend the maximum life expectancy (both strains: 18 days, Figure 2.25 C). This observation suggests that the IL2-specific knockdown delayed the onset of aggregation in other neurons, but could not completely suppress the progression of aggregation.

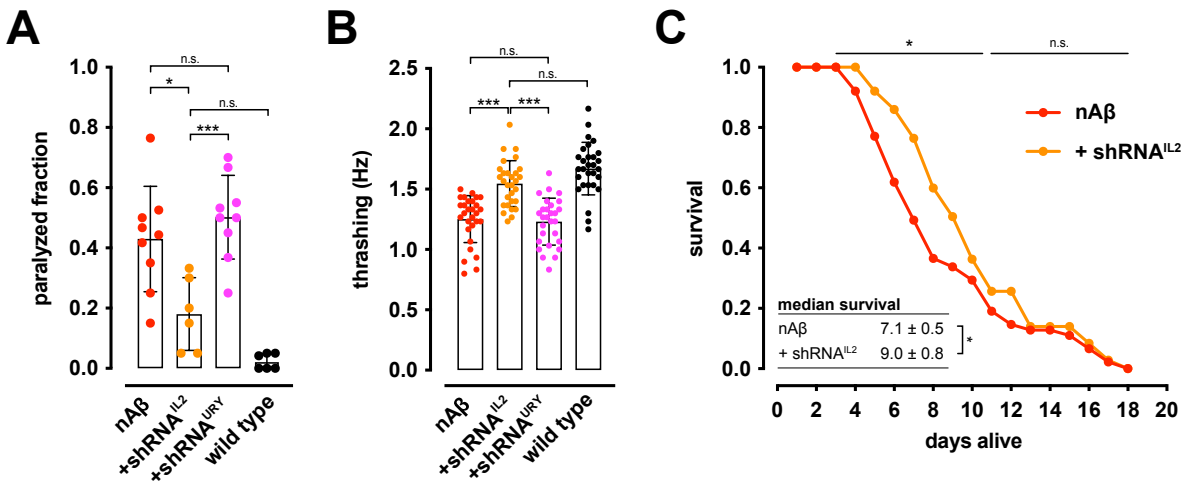

***Figure 2.25**: Knockdown of Aβ$_{1-42}$ in IL2 neurons alleviates AD toxicity temporarily*

(A) Scatter dot plot of the ability of nAβ, +shRNA^{URY}, +shRNA^{IL2} or wild type nematodes (day 4 old) to swim for 30 min in M9 medium. Paralyzed nematodes were counted and their fraction plotted as mean ± SD from six - nine cohorts of 10 – 20 nematodes each per strain. Significance was tested with one-way ANOVA + Bonferroni post hoc test (∗ = $p < 0.033$; ∗∗∗ = $p < 0.001$). Data were acquired in cooperation with Manuel Iburg. **(B)** Scatter dot plot of the thrashing activity of nAβ, +shRNA^{URY}, +shRNA^{IL2} or wild type nematodes (day 4 old) swimming in M9 medium. 38 – 40 individual nematodes were recorded for 30 sec in triplicates, plotted is mean ± SD. Significance was tested with one-way ANOVA + Bonferroni post hoc test (∗∗∗ = $p < 0.001$). Kindly provided by Tanmoyita Nayak. **(C)** Shown is the Kaplan-Meier plot of the cumulative survival probability of nAβ, +shRNA^{IL2}. 95 – 105 nematodes were analysed. Significance was tested for the indicated ranges with a log-rank test (∗ = $p < 0.01$). The inset table displays the median survival ± SD from three cohorts of 30 - 35 nematodes each per strain. Significance was tested with Student's t-test (∗ = $p < 0.033$). Kindly provided by Sara Maria Ayala Mariscal and Manuel Iburg.

Generation and Characterization of a *C. elegans* model expressing human Drebrin

The actin-binding protein Drebrin was observed to be depleted from AD brains in *post mortem* analyses and depletion experiments in AD mouse models observed increased severity of AD phenotypes. Yet, an analysis of human Drebrin in *C. elegans* as a comprehensive model to analyse multiple parameters in a fast manner (*e.g.* ageing studies, compound testing, *etc.*) was pursued.

To analyse human Drebrin in living nematodes, the utilization of a model, lacking the *C. elegans* endogenous ortholog DBN-1, was intended. DBN-1 shares sequence homology to two human proteins, Drebrin (DBN1) and Drebrin-like protein (DBNL). To exclude interference of the nematode DBN-1, a knockout strain lacking *dbn-1* (RB1004) was employed (Figure 2.26).

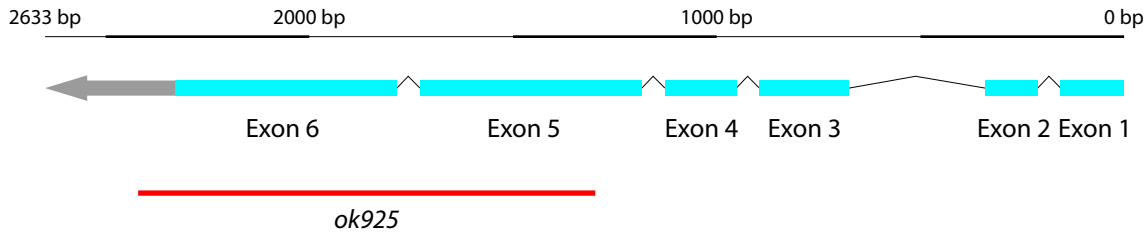

***Figure 2.26**: Schema of the dbn-1 locus*
The *dbn-1* locus (sequence K08E3.4) consists of six exons (cyan) and a 3'UTR (grey) spanning over 2633 base pairs and is located on the antisense strand of chromosome III. The deletion mutant strain RB1004 (variation *ok925*) lacks 1146 base pairs of exons 5 and 6.

First, the general vitality was assayed to find potential impairments due to the knockout of *dbn-1*. Yet, no apparent dysfunction was detected. Brood size and larval development were not impaired (Figure 2.27), both being general vitality markers. For the *dbn-1* mutant strain 285 ± 39 vivid progenies per nematode were counted. This did not differ significantly from the 292 ± 29 progeny per nematode that were counted for wild type nematodes. The obtained larvae aged and developed well, reaching L4 stage within three days at 20°C and reaching young adult stage at day 4, where they started to lay eggs on their own. There was no interference observed in the unstressed steady state, invoking the idea, that *dbn-1* could serve functions in acute stress response.

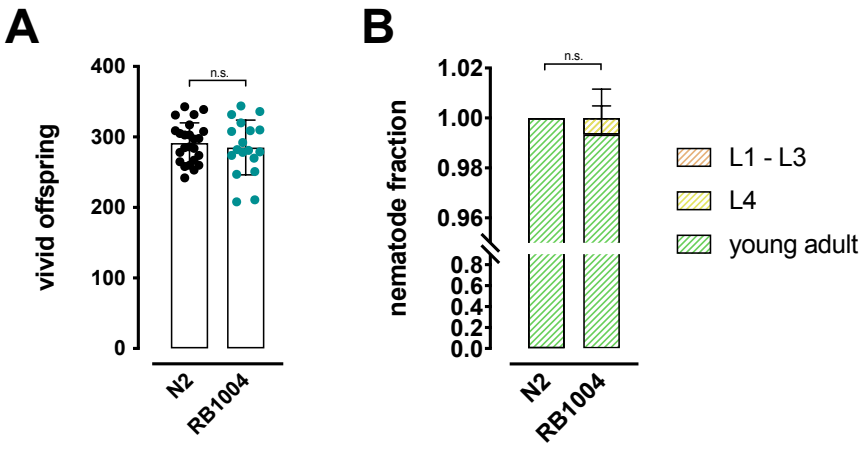

***Figure 2.27**: dbn-1 deletion does not impair fecundity or larval development*

(A) Scatter dot plot of the vivid offspring per nematode. Three cohorts of 10 – 15 wild type (N2) and *dbn-1* (RB1004) nematodes each were analysed and mean ± SD plotted. Significance was tested with Student's t-test. **(B)** Stacked bar plot of the development of an age synchronised cohort after four days. Three independent cohorts of 50 – 150 nematodes each were analysed, plotted is mean ± SD. Significance was tested by two-way ANOVA + Bonferroni post hoc test.

Analysis of oxidative stress in dbn-1 nematodes

To test if DBN-1 was involved in stress response, nematodes were challenged with oxidative stress using Paraquat. Paraquat can uncouple electrons from mitochondria and transfer them to oxygen molecules converting them to superoxide free radicals.

Lifespan analysis of wild type and *dbn-1* nematodes revealed that ageing under unstressed conditions is not affected in *dbn-1* animals (Figure 2.28). Yet, a significant effect was observed upon challenging with oxidative stress. Counterintuitively, wild type nematodes exhibited a stronger lifespan reduction (maximum life expectancy N2: 18 days *vs.* RB1004: 23 days). It was expected, that DBN-1 would be beneficial under stress conditions and that a depletion would subsequently aggravate damage under such conditions. The found results were an indication that either the hypothesis was wrong or that the model system employed was inappropriate.

Indeed, Butkevich *et al.* [217] analysed phenotypic traits of DBN-1 to muscle cells and generated an antibody against DBN-1. They observed that the *ok925* variation in RB1004 leads to an incomplete knockout of *dbn-1*, still producing a truncated variant of DBN-1 of 35 kDa. Hence, this N-terminal fragment could exhibit some unregulated functionality as actin-binding and remodelling are mainly driven by the N-terminal part of the protein.

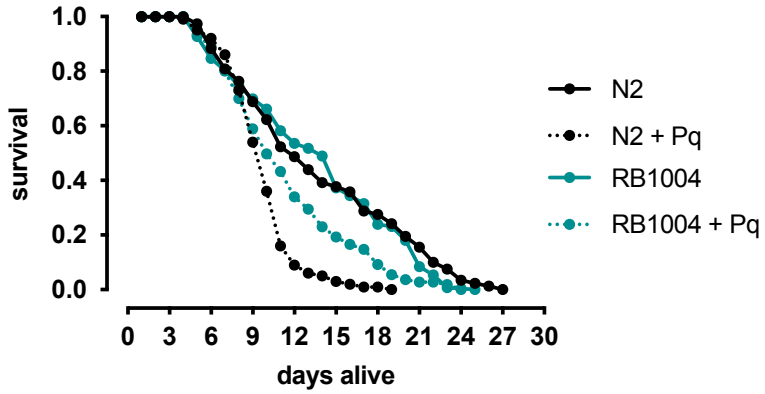

***Figure 2.28**: dbn-1 mutant nematodes are more resistant to oxidative stress*
Kaplan-Meier plot displaying the cumulative survival probability of wild type (N2) and *dbn-1* (RB1004) nematodes. One cohort for each strain was challenged with 2 mM Paraquat from L4 stage on (+ Pq / dotted line). Each cohort consisted of 100 – 150 nematodes.

Generation of a total knockout of dbn-1

To avoid interference by a truncated DBN-1, two approaches to overcome this obstacle have been tested. First, RNAi was performed with a small interfering RNA (siRNA) against *dbn-1* transcript in both, wild type and *dbn-1* mutant strain and second, a complete knockout strain was generated by CRISPR/Cas9 (Figure 2.29). In total, four guide RNAs have been employed, two binding at the beginning of *dbn-1* exon one and two binding the end of the corresponding exon six. One strain was obtained that exhibited the desired deletion in a genotyping PCR (Figure 2.29 B). This strain (experimental name "green 7.4") was sequenced at the *dbn-1* locus and a major deletion was observed leaving merely 83 base pairs from the *dbn-1* gene (Figure 2.29 C). The strain was named JKM1 and DBN-1 abundance was assessed by western blot. The detection with a DBN-1 specific antibody did neither show the full-length protein (≈ 130 kDa) nor a truncated variant of any size (Figure 2.29 D and E). To test, if RNAi would be appropriate to reduce DBN-1 levels, a western blot was employed, too. Yet, the truncated DBN-1 variant was observed for RB1004 and a clear reduction by approx. 60% was detected upon siRNA treatment of the nematodes (Figure 2.29 D). Even though, the knockdown is incomplete, the effects on the phenotype can be immense up to the extent, to yield results that are indistinguishable from the total knockout. To further validate knockdown and knockout, lifespan and brood size were analysed as read-outs for general vitality.

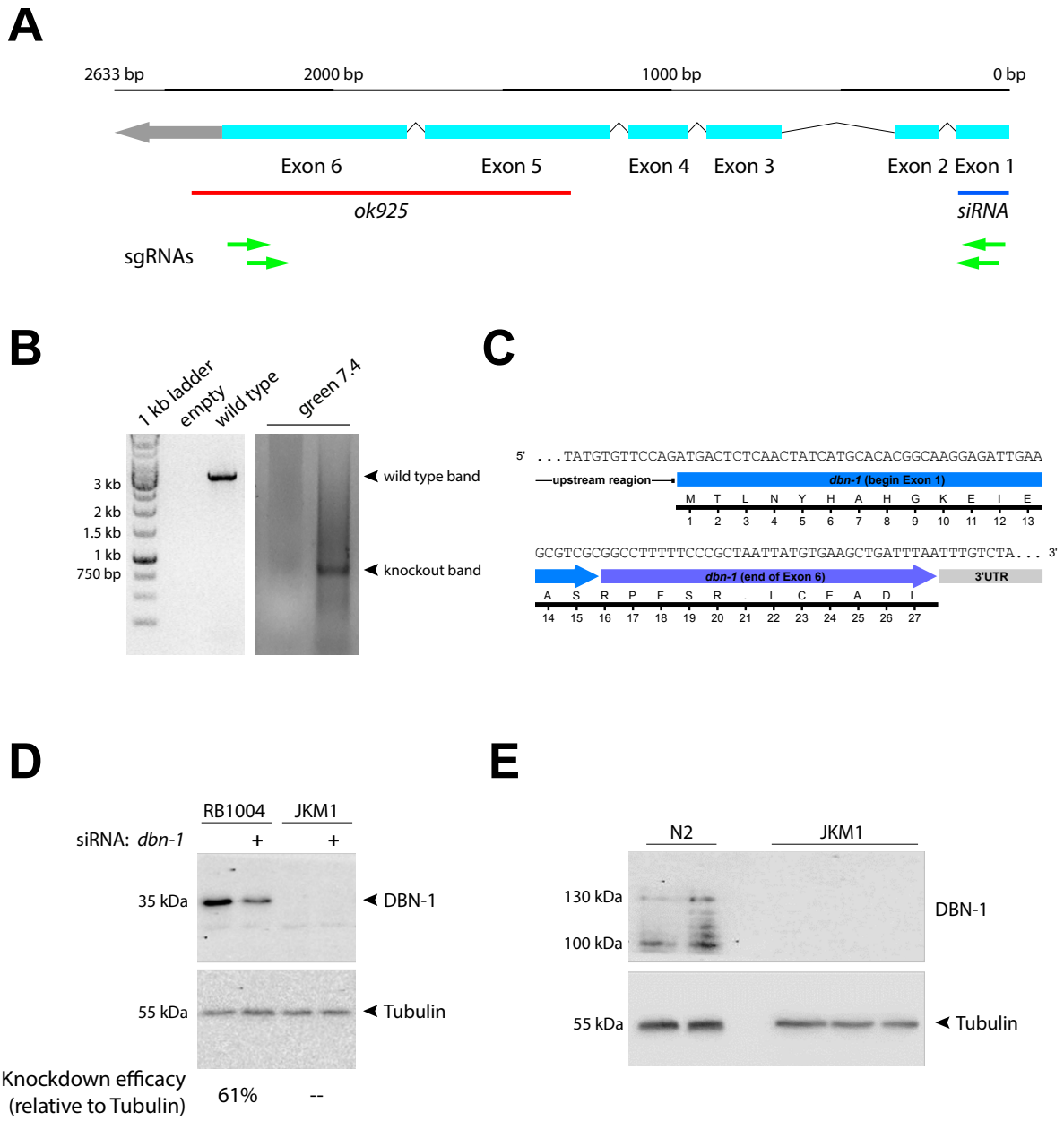

***Figure 2.29**: Knockdown and knockout of dbn-1*

(A) Schema of the *dbn-1* locus, deletion variant *ok925* of strain RB1004 (red), the position of a used siRNA (blue) and the position of four used sgRNAs (green) to generate a total knockout strain are indicated. **(B)** Agarose gel electrophoresis of genotyping of the *dbn-1* locus in wild type nematodes exhibiting a 3.3 kb band and in CRISPR/Cas9 treated strain "green 7.4" (coined JKM1) that exhibits a total *dbn-1* knockout (knockout band of 920 bp). **(C)** Sequencing of the *dbn-1* locus in JKM1, displaying a deletion of the major part of exons 1 and 6 and a complete deletion of the exons 2 – 5. The corresponding translation is indicated. **(D)** Western blot of RB1004 and JKM1 treated with an siRNA against *dbn-1* (+) or control siRNA ( ), exhibiting truncated DBN-1 protein at 35 kDa. DBN-1 antibodies and Tubulin antibodies were employed. Knockdown efficacy was calculated after densitometric assessment of DBN-1 bands over corresponding Tubulin bands. **(E)** Western blot of wild type (N2) and *dbn-1* total knockout (JKM1) nematodes detected with anti-DBN-1. Tubulin was detected as loading control. Two replicates of wild type and three replicates of Δ*dbn-1* were performed.

A small, yet significant reduction of brood size was observed for the total knockout (JKM1) compared to wild type (N2) or incomplete knockout (RB1004) (Figure 2.30 A), implicating that the presence of a truncated DBN-1 variant in RB1004 was enough to compensate for the observed progeny reduction. Furthermore, such progeny reduction could be achieved to the same extent in wild type or partial knockout lines by siRNA application. This offers the possibility to exploit knockdown in further experiments rather than using the complete knockout.

The lifespan of the total knockout (JKM1), wild type (N2) and incomplete knockout (RB1004) strain was analysed and no significant differences were found under non-stressed conditions. Upon induction of oxidative stress, the lifespan of the total knockout was significantly decreased compared to wild type (Figure 2.30 B), what is in stark contrast to the previous experiments where the alleged knockout strain (RB1004) was found to be more long-lived under oxidative stress compared to wild type.

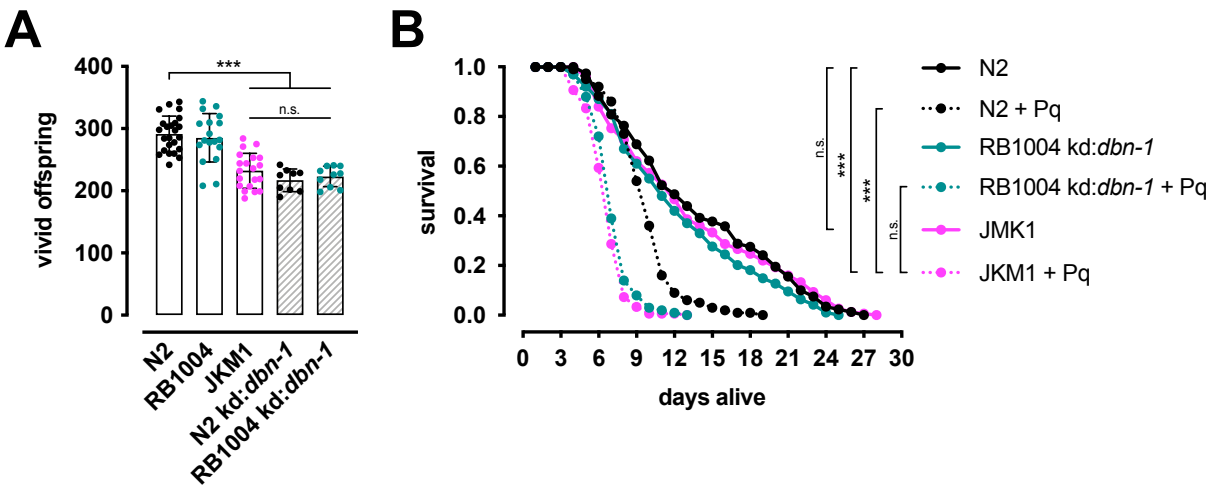

***Figure 2.30**: Complete dbn-1 deficiency renders nematodes sensitive to oxidative stress*

(A) Scatter dot plot of wild type (N2), *dbn-1* partial knockout (RB1004) and Δ*dbn-1* total knockout (JKM1) shown as mean ± SD. 10 - 30 nematodes have been analysed per strain, indicated strains have been treated with siRNA against *dbn-1* (kd: *dbn-1*). Significance was tested by one-way ANOVA + Bonferroni post hoc test (*** = $p < 0.001$) **(B)** Kaplan-Meier plot of wild type (N2), *dbn-1* partial knockout (RB1004) and Δ*dbn-1* total knockout (JKM1) nematodes cumulative survival probability was measured. Strain RB1004 was treated with siRNA against *dbn-1* to deplete also the truncated DBN-1. To test survival under oxidative stress, one cohort of each strain of 100 – 150 nematodes was treated with 2 mM Paraquat (dashed lines; + Pq) from L4 stage on. Control cohorts of 100 – 150 nematodes were treated with solvent control (water) from L4 stage on (continuous lines). Significance was tested with log-rank test (*** = $p < 10^{-6}$).

Upon application of siRNA to RB1004, the lifespan decrease under oxidative stress was observed to be similar to JKM1 under oxidative stress. This confirms that the truncated DBN-1 interfered with the conducted experiments and that a solid depletion is detrimental to the following experiments that are designed to analyse the effects of human Drebrin in *C. elegans.*

Generation of a humanized C. elegans model expressing human Drebrin

The endogenous *dbn-1* promoter was cloned from genomic DNA together with human Drebrin-YFP to analyse the *dbn-1* expression pattern *in vivo.* Confocal fluorescence microscopy revealed, that *dbn-1* was expressed in multiple tissues (Figure 2.31). A strong expression was observed in pharyngeal tissue (Figure 2.31, blue arrow head) and in a subset of head neurons. Further expression was observed in other neurons (Figure 2.31, white arrows). Previous studies described *dbn-1* expression in body wall muscle cells, too [217]. Yet, this expression pattern could not be confirmed nor rebutted by the generated model as the extrachromosomal array expression was too variable. Even though the expression pattern remained unclear to a certain extent, the implication for the following experiments was to employ a different promoter. To analyse DBN1 activity in neurons, a promoter that drives expression selectively pan-neuronally was employed (*rgef-1p*), thereby circumventing off-target effects from DBN1 expressed otherwise in non-neuronal tissue if *dbn-1* promoter would have been used.

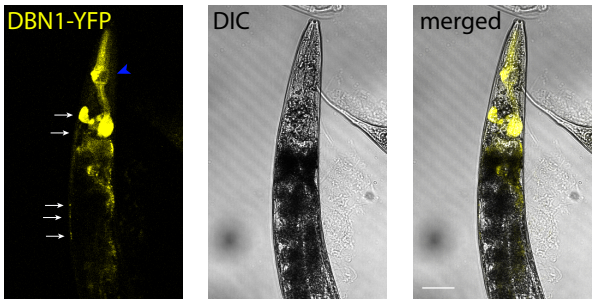

Figure 2.31*: Endogenous dbn-1 is expressed in multiple tissues*
Representative confocal images of a nematode expressing DBN1-YFP under control of the endogenous *dbn-1* promoter (*Ex* [*dbn-1p::*DBN1-YFP]). Fluorescence of YFP and differential interference contrast (DIC) were recorded. Scale bar represents 50 µm. White arrows point to DBN1-YFP signals in neurons. Blue arrow head points to DBN1-YFP expressed in pharyngeal muscle cells.

To corroborate results from our cooperation partners of the Eickholt Lab, Drebrin phosphorylation variants were cloned to mimic phosphorylation (substitution of selected amino acid by Aspartate) or constitutive dephosphorylation (substitution of selected amino acid by Alanine). The Serine-647 that was observed to regulate Drebrin turn-over in an *ex vivo* neuron model [179] was replaced by either Aspartate or Alanine to analyse the regulation of Drebrin turn-over in *C. elegans* neurons and the influence of putatively stabilized Drebrin on stress resistance. Drebrin-YFP fusion variants (wt S647, S647A and S647D) were expressed in JKM1 or RB1004 nematodes pan-neuronally (Figure 2.32).

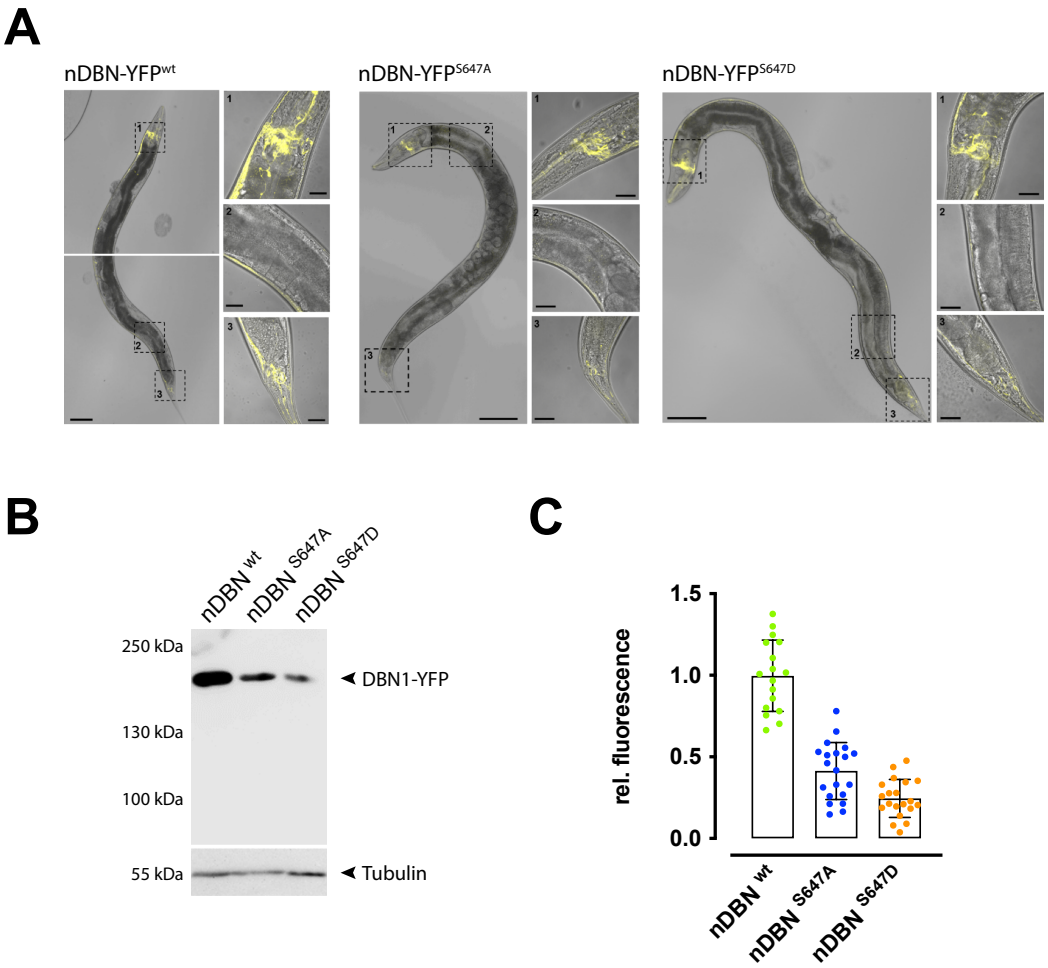

***Figure 2.32**: Neuronal expression of DBN1-YFP variants*

(A) Representative confocal images (merged DIC + YFP fluorescence) of nDBN^{wt} (Δ*dbn-1*[Ex1-Ex6] + *rgef-1p*::DBN1A^{wt}-YFP), nDBN^{S647A} (*ok925* + *rgef-1p*::DBN1A^{S647A}-YFP) and nDBN^{S647D} (*ok925* + *rgef-1p*::DBN1A^{S647D}-YFP). Magnification of images is 100x - 200x, scale bars represent 50 µm. Insets at 630x magnification, corresponding scale bars represent 20 µm. **(B)** Representative western blot of lysed nematodes (see A) detected with DBN1 specific antibody (M2F6) and with a Tubulin specific antibody as loading control. Kindly provided by Patricia Kreis (Eickholt lab, Charité Universitätsmedizin Berlin). **(C)** Scatter dot plot displaying the quantification of the fluorescence intensity of the employed nematode strains (see A). Fluorescence intensity was analysed by Fiji and mean ± SD are plotted.

The pan-neuronal expression was verified by confocal microscopy. YFP fluorescence was observed throughout the nervous system, including head, mid body and tail neurons (Figure 2.32 A). The expression levels after stable integration into genomic DNA were assessed by immunodetection on western blots and additionally by fluorometric measurement of total YFP fluorescence (Figure 2.32 B and C). Both, western blot and fluorometry exhibited similar abundances. The DBN1 wild type variant was most strongly expressed (99 ± 22%) compared to dephospho-mimicry S647A (41 ± 17%) or phospho-mimicry S647D (25 ± 12%). This quantification is particularly important for the evaluation of the following experiments, to exclude dose-dependent effects by differential expression levels.

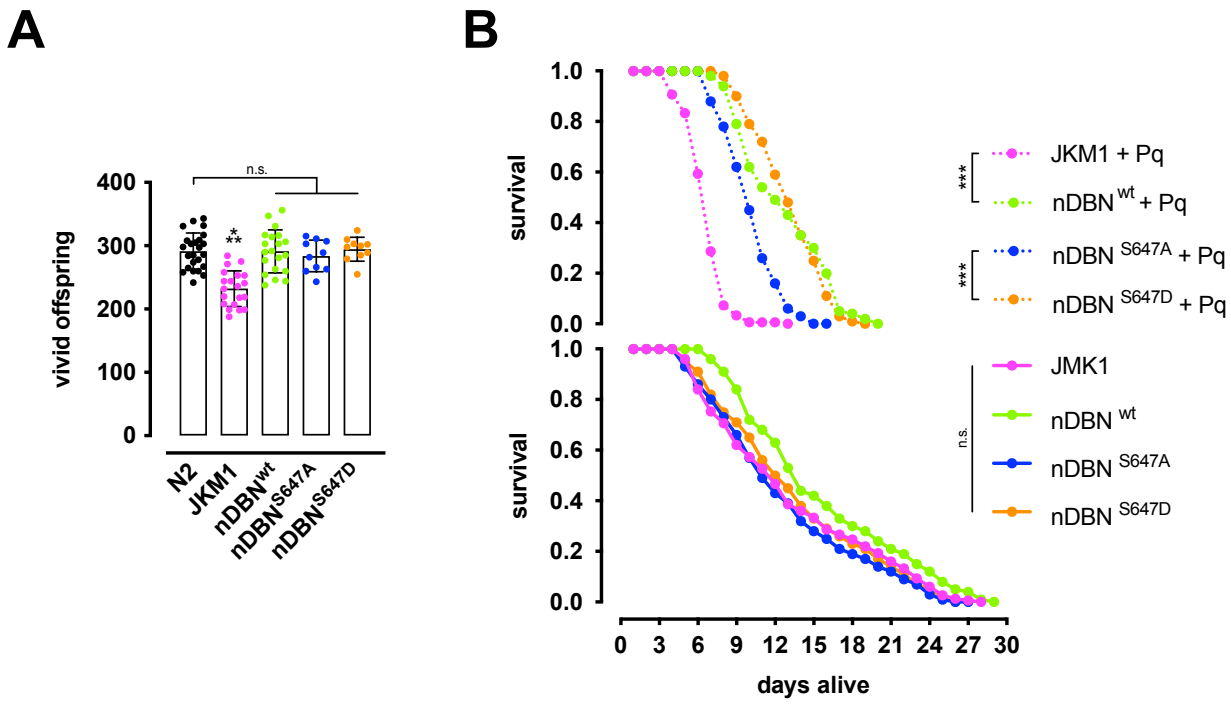

***Figure 2.33**: Human Drebrin rescues dbn-1 depletion partially*

(A) Scatter dot plot displaying the progeny per nematode of N2 (wild type), JKM1 (Δ*dbn-1*[Ex1-Ex6]), nDBN^{wt} (Δ*dbn-1*[Ex1-Ex6] + *rgef-1p*::DBN1A^{wt}-Dendra2), nDBN^{S647A} (Δ*dbn-1*[Ex1-Ex6] + *rgef-1p*::DBN1A^{S647A}-Dendra2) and nDBN^{S647D} (Δ*dbn-1*[Ex1-Ex6] + *rgef-1p*::DBN1A^{S647D}-Dendra2) strains. Significance was tested with one-way ANOVA + Bonferroni post hoc test, JKM1 was significantly different from all other tested strains (*** = $p < 0.001$). **(B)** Kaplan-Meier plots displaying the cumulative survival probability of JKM1 (Δ*dbn-1*[Ex1-Ex6]), nDBN^{wt} (Δ*dbn-1*[Ex1-Ex6] + *rgef-1p*::DBN1A^{wt}-YFP), nDBN^{S647A} (*ok925* + *rgef-1p*::DBN1A^{S647A}-YFP) and nDBN^{S647D} (*ok925* + *rgef-1p*::DBN1A^{S647D}-YFP) strains under constant knockdown of *dbn-1* by siRNA. Upper panel shows additional treatment with 2 mM Paraquat from L4 stage on, lower panel untreated control. Three independent cohorts of 100 – 150 nematodes per strain and condition were recorded and mean value plotted. Significance was tested by log-rank test (*** = $p < 10^{-6}$).

The general vitality and the reaction to oxidative stress were assessed by analysing the progeny per nematode and the lifespan. While the total deletion, as well as the RNAi induced depletion, led to reduced brood sizes compared to wild type (reduction by ≈ 20%) (Figure 2.30 A). The pan neuronal expression of DBN1 variants restored full brood size in Δ*dbn-1* nematodes (knockout as well as knockdown) (Figure 2.33 A). Therefore, human Drebrin exhibits a protective effect in the nematodes in a systemic manner. Since the depletion of *dbn-1* led to a sensitisation to oxidative stress, resulting in lifespan reduction upon Paraquat treatment, I hypothesized that human Drebrin could compensate this phenotype. A lifespan assay was performed inducing oxidative stress in nDBN variant strains (under depletion of endogenous *dbn-1* by knockout and knockdown) (Figure 2.33 B). Without oxidative stress, no significant difference was observed between any of the analysed strains. Yet, oxidative stress generated by Paraquat led to a decrease in lifespan in all analysed strains with different efficacy. JKM1 (Δ*dbn-1* control) exhibited the strongest reduction among the compared strains (by 54% to a maximum life expectancy of 13 days, median of 8.3 days). The expression of nDBN variants was beneficial for the lifespan under oxidative stress. The dephospho mimicry variant nDBN^{S647A} exhibited to smallest improvement (41% reduction to a maximum life expectancy of 16 days, median of 9.7 days). nDBN^{wt} and nDBN^{S647D} exhibited similar results and improved lifespan under oxidative stress compared to *dbn-1* knockout (nDBN^{wt}: 29 % reduction to maximum life expectancy of 20 days, median of 11.8 days; nDBN^{S647D}: 27% reduction to maximum life expectancy of 19 days, median of 11.8 days). This indicates, that human Drebrin was able to exert a protective function in the nematode neurons and thereby stabilize the whole nematode's health under oxidative stress and consequently rescue the lifespan. Furthermore, the rescue was dependent on the phosphorylation of Serine-647, as the reduced efficacy of the constitutive dephospho variant displayed.

The regulation of Serine-647 phosphorylation site was subject to further studies to understand how it affects Drebrin and subsequently remodels stress resistance. Our cooperation partners of the Eickholt lab were addressing this question in cell based models and *ex vivo* neuronal culture models [179]. I set out to corroborate their results in the nematode and could demonstrate that the differential regulation of Drebrin induces true physiological effects in a living animal.

Influence of ATM-1 on Drebrin phosphorylation

Previous studies showed that Drebrin gets phosphorylated at Serine-647 by a previously uncharacterised kinase in response to neuronal membrane depolarisation following neuronal activity [178]. The examination of the amino acid sequence of Drebrin revealed a putative consensus motif at Serine-647 for the Serine/Threonine kinase Ataxia telangiectasia mutated (ATM) [239]. Our cooperation partners could show that ATM phosphorylates S647-Drebrin indeed in response to oxidative stress and that this may be an adaption to increased ROS levels in neurons due to neuronal activity [179,240].

To test if ATM is involved in DBN function in nematodes, the impact of ATM inhibition on lifespan using the specific ATM inhibitor KU-55933 was analysed. Prior to the analysis, the ability of KU-55933 to inhibit *C. elegans* ATM-1 was validated. Nematodes expressing nDBN^{wt} were treated with KU-55933 and phosphorylation at Serine-647 was analysed on a western blot by employing a pS647-Drebrin-specific antibody (Figure 2.34 A). A significant reduction of pS647-Drebrin signal was observed, suggesting that KU-55933 is able to inhibit *C. elegans* ATM-1 indeed.

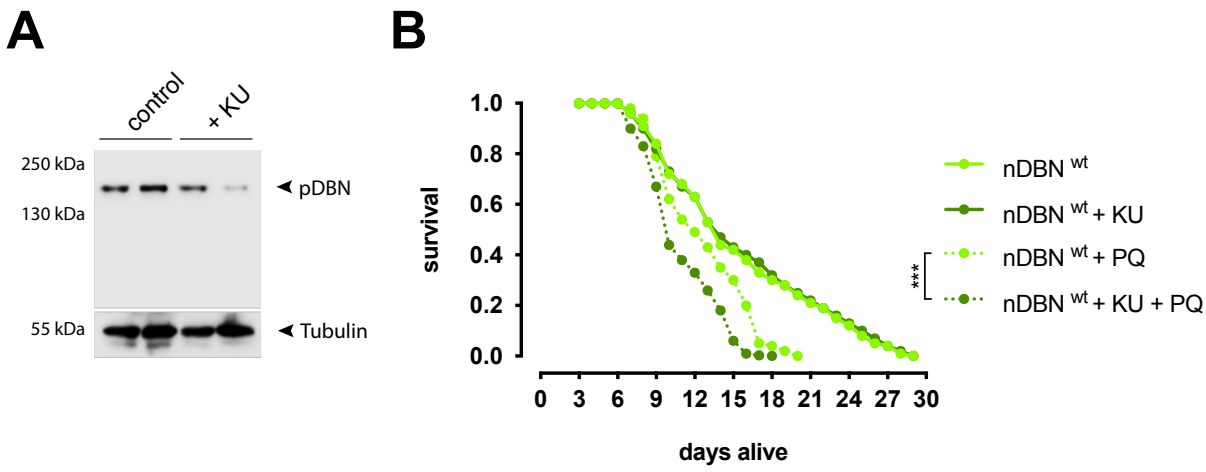

***Figure 2.34**: ATM-1 inhibition aggravates lifespan reduction upon oxidative stress*

(A) Representative western blot detecting pS647-DBN1 over Tubulin. Two cohorts of nDBN^{wt} (Δ*dbn-1*[Ex1-Ex6] + *rgef-1p*::DBN1A^{wt}-YFP) nematodes were treated with ATM kinase inhibitor KU-55933 (+ KU) or with DMSO solvent control (control). Lysis and blot were performed by Patricia Kreis (Eickholt lab). **(B)** Kaplan-Meier plot showing the cumulative survival probability of nDBN^{wt} (Δ*dbn-1*[Ex1-Ex6] + *rgef-1p*::DBN1A^{wt}-YFP) treated with KU-55933 (+ KU) or DMSO solvent control. Additionally, cohorts were challenged with 2 mM Paraquat to induce oxidative stress from day 4 of life on (+ PQ). Three independent cohorts of 100 – 120 nematodes each per condition were tested and the mean plotted. Significance was tested by log-rank test (*** = $p < 10^{-6}$).

The lifespan reduction of nDBN^{wt} strain was tested upon chronic oxidative stress ± ATM inhibitor. The KU-55933 treated cohorts exhibited a significantly decreased lifespan compared to unstressed condition (PQ + KU: 38% reduced lifespan, median 9.7 days *vs.* PQ + ctrl: 29% reduced lifespan, median 11.8 days). This suggested that loss of ATM-1 function exacerbated the effect of oxidative stress. To prove that this effect is due to altered phosphorylation at Serine-647, lifespan assay and KU-55933 treatment were conducted with the phospho and dephospho mimicry variant expressing nematodes (nDBN^{S647D} and nDBN^{S647A}). Since both strains are in the *ok925* (incomplete *dbn-1* deletion) background, the nematodes were cultured with constant siRNA treatment to induce an effective depletion of *dbn-1*. There was no significant difference between KU-55933 treated and untreated nematodes of the strains nDBN^{S647A} (median lifespan + KU: 13.1 days *vs.* ctrl: 13.0 days) and nDBN^{S647D} (median lifespan + KU: 15.5 days *vs.* ctrl: 14.0 days) (Figure 2.35 lower panel). Under chronic oxidative stress there was no effect of ATM-1 inhibition either (nDBN^{S647A} median lifespan + PQ + KU: 9.6 days *vs.* + PQ + ctrl: 9.7 days; nDBN^{S647D} median lifespan + PQ + KU: 11.7 days *vs.* + PQ + ctrl: 11.8 days) (Figure 2.35 upper panel).

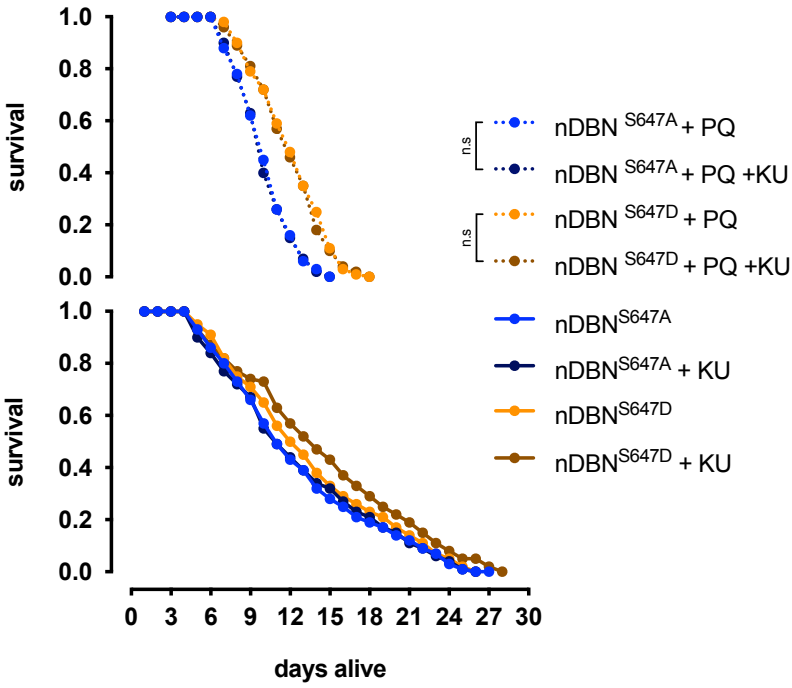

***Figure 2.35**: ATM-1 inhibition has no influence on DBN de/phospho variants lifespan*

Kaplan-Meier plots displaying the cumulative survival probability of three independent cohorts of 100 - 120 nematodes per strain and condition tested as mean. All strains were treated with siRNA against *dbn-1*.
The upper panel shows the strains that were treated with 2 mM Paraquat from day 4 of life on, the lower panel shows the controls without oxidative stress. Influence of ATM1 kinase inhibitor KU-55933 was tested (+ KU). The controls (all other strains) were treated with DMSO as solvent control. Significance was tested by log-rank test.

Since both de-/phospho mimicry variants alter lifespan during oxidative stress independent from ATM-1 function, S647-Drebrin presents an important ATM substrate in this response. Taken together, these results demonstrate DBN phosphorylation at Serine-647 as an integral mechanism involved in Drebrin mediated stress resistance towards oxidative stress.

As Drebrin was observed to be depleted in Alzheimer's Disease, the two established models were thought to be combined to analyse Drebrin-$A\beta_{1-42}$ interaction.

Interaction between human Drebrin and $A\beta_{1-42}$ in *C. elegans*

To analyse the interaction between Drebrin and $A\beta_{1-42}$ *in vivo,* the Drebrin expressing strains $nDBN^{wt}$, $nDBN^{S647A}$ and $nDBN^{S647D}$ were crossed with nAβ. Crossed strains that were triple homozygous (for the Drebrin variant, neuronal $A\beta_{1-42}$ expression and Δ*dbn-1*[Exon1-Exon6]) as well as a double homozygous nAβ-Δ control strain (nAβ + Δ*dbn-1*[Exon1-Exon6]; JKM2-Δ) were isolated.

In the following chapter the crossed strains are named: $nDBN^{wt}$, $nDBN^{S547A}$, $nDBN^{S547D}$ and nAβ-Δ / JKM2-Δ, the corresponding genotype is provided in Table 2.1.

***Table 2.1**: C. elegans strains, names and genotypes used in the following chapter*

Strain	Genotype
JKM2-Δ-nDBN ($nDBN^{wt}$)	*rgef-1p*::$DBN1A^{wt}$-Dendra2 + *rgef-1p*::SigPep-$A\beta_{1-42}$::IRES::wrmScarlet-$A\beta_{1-42}$ + Δ*dbn-1*[Exon1-Exon6] III
JKM2-Δ-$nDBN^{S647A}$ ($nDBN^{S647A}$)	*rgef-1p*::$DBN1A^{S647A}$-Dendra2 + *rgef-1p*::SigPep-$A\beta_{1-42}$::IRES::wrmScarlet-$A\beta_{1-42}$ + Δ*dbn-1*[Exon1-Exon6] III
JKM2-Δ-$nDBN^{S647D}$ ($nDBN^{S647D}$)	*rgef-1p*::$DBN1A^{S647D}$-Dendra2 + *rgef-1p*::SigPep-$A\beta_{1-42}$::IRES::wrmScarlet-$A\beta_{1-42}$ + Δ*dbn-1*[Exon1-Exon6] III
JKM2-Δ (nAβ-Δ)	*rgef-1p*::SigPep-$A\beta_{1-42}$::IRES::wrmScarlet-$A\beta_{1-42}$ + Δ*dbn-1*[Exon1-Exon6] III

First, the expression levels of both $A\beta_{1-42}$ and Drebrin variants were analysed by fluorometry to ensure equal protein abundance. There was no significant difference of $A\beta_{1-42}$ expression detected in $nDBN^{wt}$, $nDBN^{S647A}$, $nDBN^{S647D}$ and JKM2-Δ (Figure 2.36 A). Since $A\beta_{1-42}$ aggregation propensity is correlated to $A\beta_{1-42}$ abundance among other factors, a dose-dependent effect evoking changes of aggregation behaviour and subsequent toxicity can be excluded. All possibly detectable effects should therefore be the result of secondary effects that are independent from $A\beta_{1-42}$ abundance.

The expression of DBN^{S647A} and DBN^{S647D} did not exhibit a significant difference, yet their expression was approximately twice as strong as DBN^{wt} expression (Figure 2.36 B). Since the expression of the phospho and the dephospho variant are equal, the effect of Serine-647 phosphorylation can be evaluated correctly.

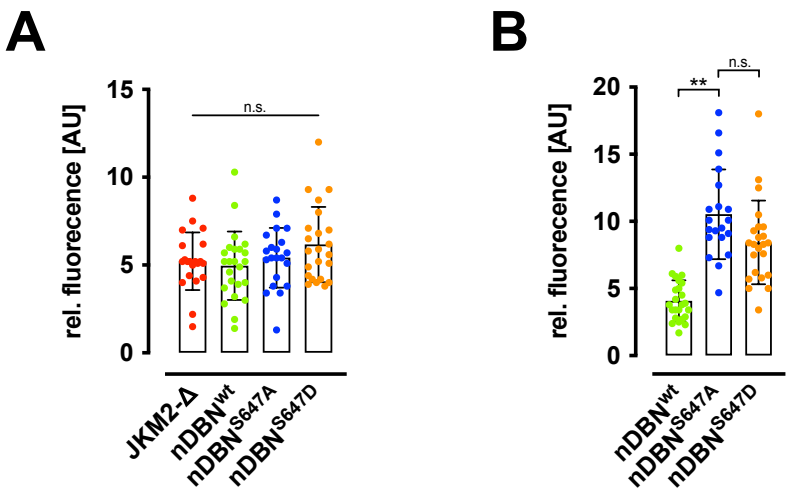

***Figure 2.36**: Expression levels of nDBN × nAβ*

(A) Scatter dot plot displaying the quantification of the fluorescence intensity of wrmScarlet-Aβ$_{1-42}$ in nDBN variants crossed with nAβ. Three independent cohorts of 10 - 20 nematodes each were analysed. Shown is mean ± SD. Significance was tested with one-way ANOVA + Bonferroni post hoc test. **(B)** Scatter dot plot displaying the quantification of the fluorescence intensity of DBN-Dendra2 in nDBN variants crossed with nAβ. Three independent cohorts of 10 - 20 nematodes each were analysed. Depicted is mean ± SD. Significance was tested with one-way ANOVA + Bonferroni post hoc test (** = $p < 0.01$).

Drebrin and Aβ$_{1-42}$ can colocalize

Both, Aβ$_{1-42}$ and Drebrin are expressed in neurons and localise mainly in the cytosol (Figure 2.37 A). To assess if Aβ$_{1-42}$ and Drebrin interact with each other, fluorescence microscopy studies were conducted. Aβ$_{1-42}$ formed foci in the cytoplasm of neurons and was able to sequester Drebrin, resulting in a colocalization (Figure 2.37 A, white arrows). Furthermore, the presence of Aβ$_{1-42}$ induced Drebrin foci formation without direct interaction, resulting in Drebrin foci that were devoid of Aβ$_{1-42}$ (Figure 2.37 A, green arrows). Such foci formation was not observed in nematodes expressing only Drebrin variants but no Aβ$_{1-42}$. Also, Aβ$_{1-42}$ foci appeared that were devoid of Drebrin, a phenomenon commonly observed in JKM2 nematodes. Hence, Aβ$_{1-42}$ could sequester Drebrin into foci and even induce Drebrin foci formation by secondary effects (*e.g.* reduced proteostatic capacity). Still, the majority of Drebrin remained soluble and evenly distributed in the cytosol as depicted in Figure 2.37 A.

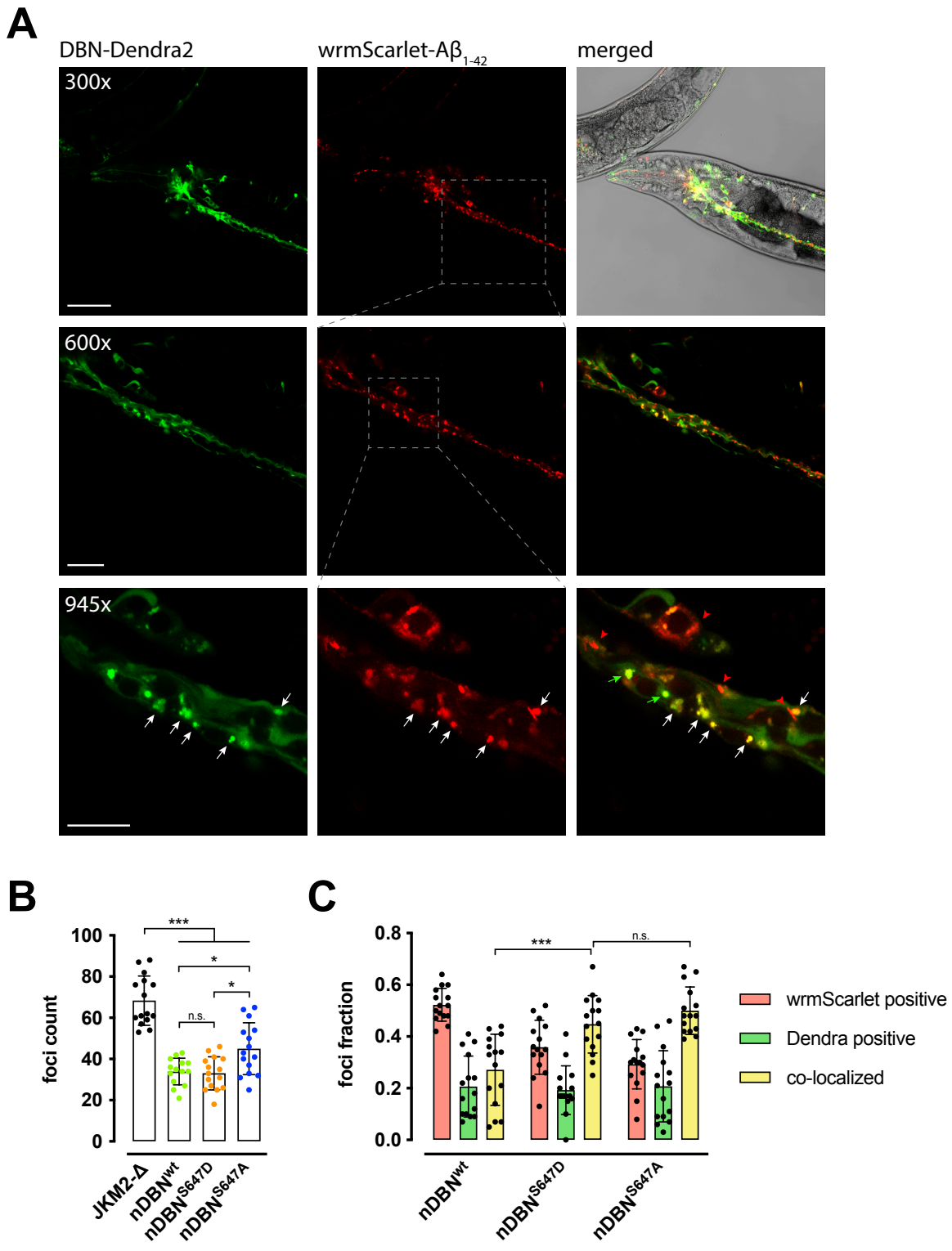

***Figure 2.37**: Drebrin and Aβ1-42 colocalize foci-wise*

(A) Representative confocal images of nDBN^{wt}×JKM2-Δ display fluorescence of DBN1-Dendra2 and fluorescence of wrmScarlet-Aβ1-42. Magnification was successively increased from 300x (scale bar is 50 µm; merge includes Dendra2 and wrmScarlet fluorescence + DIC) to 600x (scale bar is 20 µm), to 945x (scale bar is 10 µm) to zoom on the retrovesicular ganglion. White arrows point to foci exhibiting colocalization, red arrow heads point to wrmScarlet-Aβ1-42-only foci and green arrows point to DBN-

Dendra2-only foci. **(B)** Scatter dot plot showing the total foci count of Dendra2 and wrmScarlet positive foci as mean ± SD for n = 15 nematodes recorded per strain. To test significance one-way ANOVA + Bonferroni post hoc test was employed (∗ = $p < 0.33$, ∗∗∗ = $p < 0.001$). **(C)** Scatter dot plot depicting the distribution of Dendra and wrmScarlet fluorescent foci and their colocalization as fraction from total. Shown is mean ± SD from n = 15 analysed nematodes per strain. Significance was tested by two-way ANOVA + Bonferroni post hoc test (∗∗∗ = $p < 0.001$).

The total foci formation was reduced in nDBN^{wt} and nDBN^{S647D} compared to nDBN^{S647A}. Additionally, all Drebrin expressing variants exhibited reduced foci formation compared to nAβ-Δ strain, expressing only $Aβ_{1-42}$ (Figure 2.37 B). This is an indication, that the presence of Drebrin alters $Aβ_{1-42}$ aggregation behaviour in a potentially beneficial way. Yet, foci number should not be directly correlated to aggregate burden, as accumulation of material and amyloid formation constitute two different moieties. To further evaluate the contribution of DBN-pS647, the number of foci exhibiting colocalization between $Aβ_{1-42}$ and the respective Drebrin variant was scored (Figure 2.37 C). There were minor differences in the number of colocalizing foci between the analysed strains, yet there was no clear trend observed. Individual nematodes exhibited drastic variations in colocalization, giving rise to the hypothesis, that Drebrin sequestration by $Aβ_{1-42}$ may be independent of pSerine-647.

Drebrin does not aggregate despite foci formation

To analyse if Drebrin, that was trapped in $Aβ_{1-42}$ foci, was co-aggregated, DBN-Dendra2 aggregation was assessed by fluorescence lifetime microscopy of the crossed strains. The strain nDBN^{S647A} was employed as it exhibited the highest foci count of the crossed Drebrin variants.

Previous studies have described a fluorescence lifetime of 3.3 ns for Dendra2 (in its non-converted state) [241]. Nevertheless, expressed in *C. elegans* neurons and fused to Drebrin, a fluorescence lifetime of 3.0 to 3.1 ns was measured. nDBN^{S647A} nematodes exhibited an even distribution of Dendra2 fluorescence as well as an even fluorescence lifetime distribution (Figure 2.38 A, FLIM: Dendra2). Foci of Drebrin-Dendra2 as well as foci of colocalized $Aβ_{1-42}$ and Drebrin-Dendra2 did not exhibit a decreased fluorescence lifetime for Drebrin-Dendra2 (see white arrows in Figure 2.38 A).

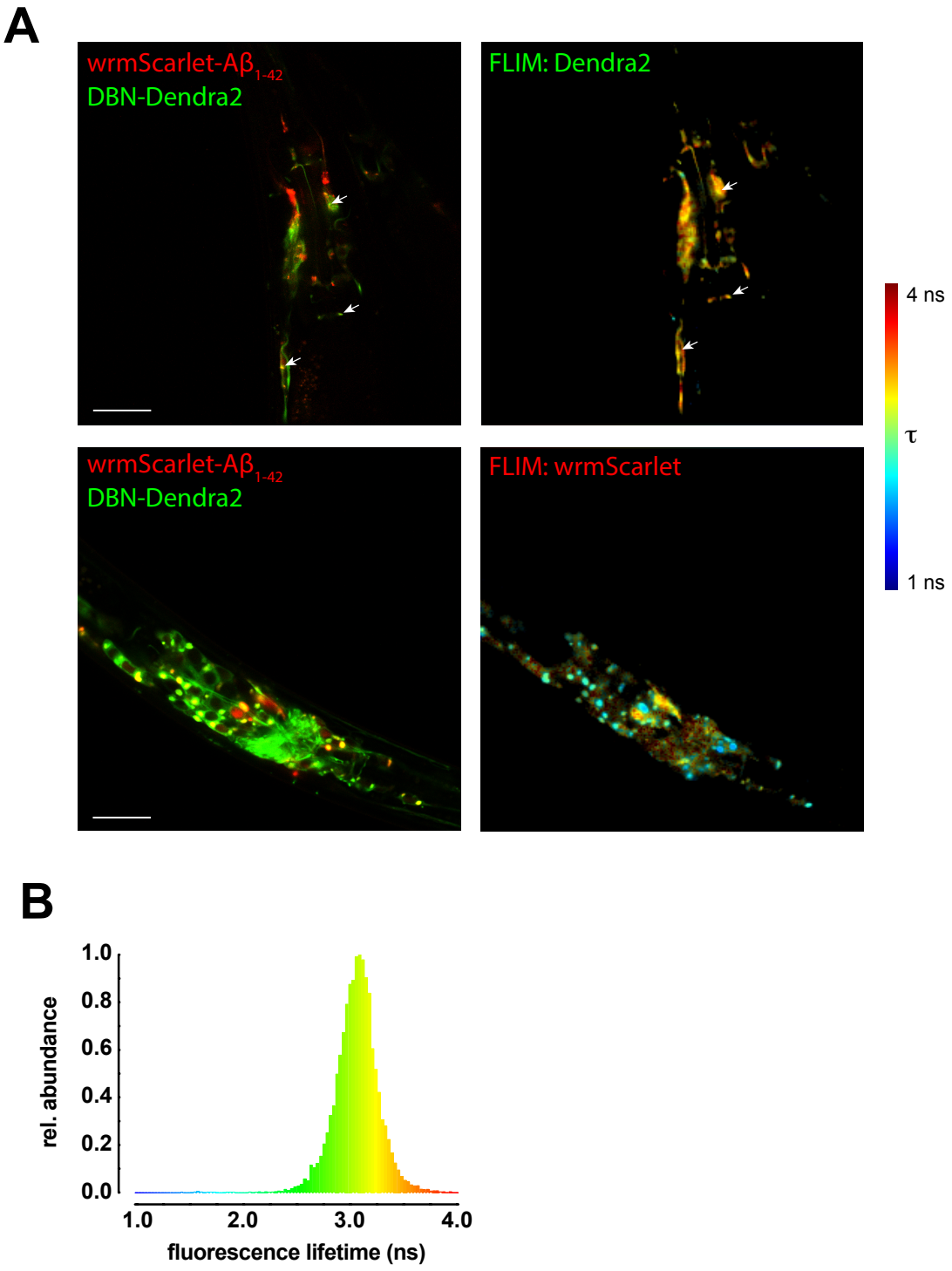

***Figure 2.38**: DBN-Dendra2 does not show fluorescence lifetime reduction in the presence of Aβ1-42*

(A) Both left panels display representative confocal images of day 4/5 old nDBN^{S647A} nematodes. Dendra2 and wrmScarlet fluorescence are merged and the scale bar represents 20 µm. On the right, the corresponding FLIM images are shown of either Dendra2 or wrmScarlet fluorescence. White arrows point to Drebrin-Dendra2 positive foci. **(B)** Histogram showing the average fluorescence lifetime distribution of the Dendra2 signal of nDBN^{S647A} obtained from the analysed FLIM images (n = 7).

The corresponding histogram displaying the abundance of certain fluorescence lifetime pixels, exhibited a bell-shaped curve with its peak at approx. 3.1 ns, accounting for a single species of probably monomeric Drebrin-Dendra2 (Figure 2.38 B).

wrmScarlet-$A\beta_{1-42}$ foci on the other hand exhibited reduced fluorescence lifetime, accounting for aggregated material (Figure 2.38 A, FLIM: wrmScarlet). Interestingly, the majority of observed foci that were colocalized with Drebrin, exhibited aggregated $A\beta_{1-42}$. In FLIM experiments with JKM2 nematodes, foci formation was observed to be independent from aggregation – not all observed foci exhibited a reduced fluorescence lifetime. Yet, it seems that DBN^{S647A} drives $A\beta_{1-42}$ aggregation upon colocalization. Since a quantification was not performed, I cannot reject nor verify this hypothesis at the moment.

Drebrin overexpression ameliorates $A\beta_{1-42}$ aggregation

To analyse the influence of Drebrin overexpression on $A\beta_{1-42}$ aggregation and to evaluate the impact of pSerine-647, FLIM analyses of $nDBN^{wt}$, $nDBN^{S647A}$, $nDBN^{S647D}$ and JKM2-Δ have been performed on days 3, 4, 7 and 10 of life. Thus, the change of aggregation over time could be resolved starting with a young animal in L4 larval stage (day 3) to an old animal after its fecund period (day 10) (Figure 2.39 and Figure 2.40).

No differences were observed for day 3 old nematodes. Nearly all $A\beta_{1-42}$ was evenly distributed throughout the cytosol of the analysed neurons, not forming foci nor exhibiting aggregates (Figure 2.39). The average fluorescence lifetime was equal for all analysed strains at approx. 2.7 ns (Figure 2.40). No change of fluorescence lifetime was detected compared to day 4, yet IL2 neurons exhibited the first aggregates in more than 85% of the analysed $nDBN^{S647A}$ and JKM2-Δ nematodes, whilst less than 70% of the analysed $nDBN^{S647D}$ and $nDBN^{wt}$ nematodes exhibited the early aggregates in IL2 neurons (see white arrows and indicated fraction of IL2 neurons bearing aggregates in Figure 2.39).

A significant increase of aggregation was observed in $nDBN^{wt}$, $nDBN^{S647A}$ and JKM-Δ on day 7 of life (Figure 2.40). Only in $nDBN^{S647D}$, the Serine-647 phospho mimicry variant, the aggregation was significantly ameliorated. There was no change from day 4 to day 7 detected in $nDBN^{S647D}$. Nevertheless, on day 10 of life all nematodes regenerated apparently. I assume that a major survivorship bias occurred skewing the day 10 data towards lower aggregate burden.

Therefore, day 10 data were omitted from further contemplation. Considering the reduced early-onset aggregation on day 4 of life and the overall reduced amyloid burden in nDBN^{S647D} nematodes at day 7 of life, one can assume that phosphorylation at Serine-647 contributes to amyloid formation regulation by Drebrin.

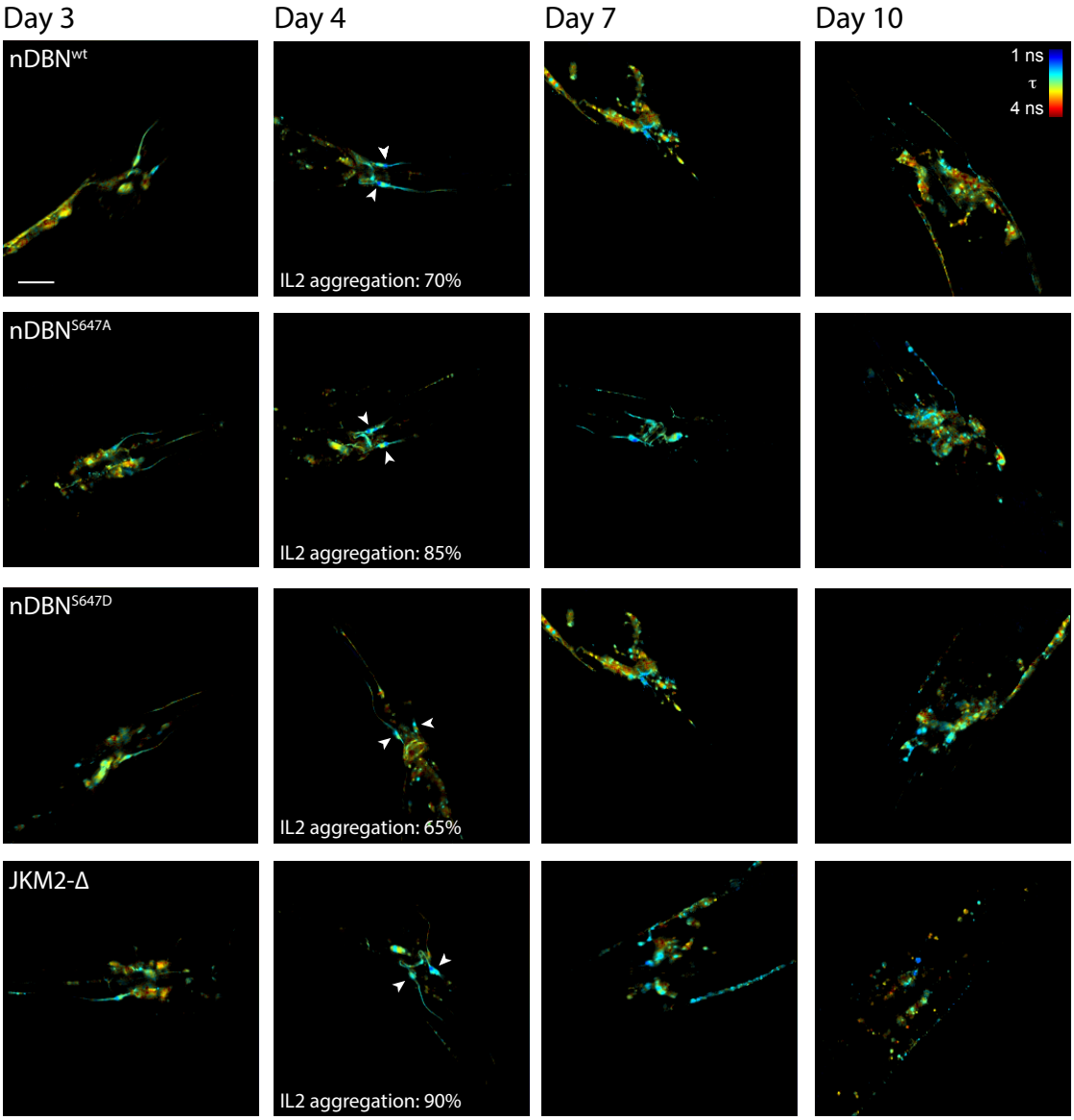

***Figure 2.39**: Drebrin overexpression ameliorates Aβ$_{1-42}$ aggregation*

Representative FLIM images of nDBN variants crossed with nAβ were recorded on days 3, 4, 7 and 10 of life. White arrows point to IL2 neurons exhibiting the first aggregates on day 4 of life. Fraction of nematodes exhibiting first aggregates is provided as rounded values (IL2 aggregation). One to three independent cohorts of 10 - 15 nematodes each were imaged per strain and day. Scale bar represents 20 µm.

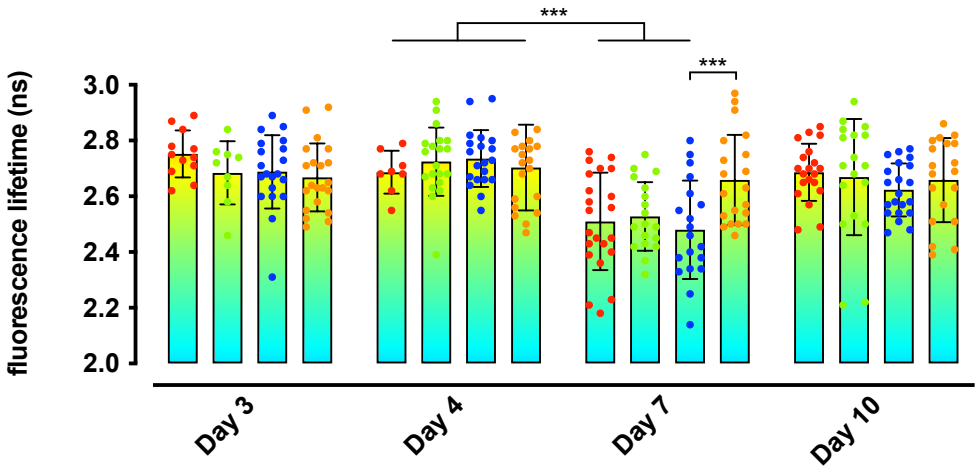

***Figure 2.40**: Aβ$_{1-42}$ aggregation is modulated by Drebrin*

Scatter dot plot displaying the fluorescence lifetime of wrmScarlet-Aβ$_{1-42}$ in JKM2-Δ (red), nDBN^{wt} (green), nDBN^{S647A} (blue) and nDBN^{S647D} (orange) on days 3, 4, 7 and 10 of life. One - three individual cohorts of 10 - 15 nematodes each were recorded. Mean ± SD is displayed. Significance was tested with two-way ANOVA + Bonferroni post hoc test (*** = $p < 0.001$).

Alleviation of Aβ$_{1-42}$ toxicity is regulated by DBN-pS647

After the evaluation of aggregation in the Drebrin variant strains crossed with nAβ, a characterization of systemic impairments and neurological defects was intended to correlate the progression of aggregation and toxicity. As read-out for general organismal fitness the brood size as well as the lifespan of nDBN^{wt}, nDBN^{S647A}, nDBN^{S647D} and JKM2-Δ have been analysed.

Previous experiments have shown that neuronal expression of Aβ$_{1-42}$ reduces the number of vivid progeny per nematode significantly (Figure 2.12 A; nAβ/JKM2: 108 ± 57). A rather moderate, yet significant reduction was observed for the depletion of endogenous *dbn-1* (Figure 2.30 A; Δ*dbn-1*/JKM1: 232 ± 28). The crossing of both strains, JKM2-Δ, exhibited a, compared to wild type, reduced brood size of 136 ± 46 progeny per nematode (Figure 2.41 A). It appeared that both genotypes combined do not work in a synergistic way. Yet it is difficult to evaluate, because the relative reduction of brood size of JKM1 is hardly larger than the standard deviation of the corresponding reduction of JKM2.

The expression of wild type Drebrin led to a slight improvement of progeny count, whilst both, phospho and dephospho mimicry variants did not lead to any rescue. To this point, Drebrin is possibly influencing

two different mechanisms that are maybe loosely, possibly not at all connected: brood size reduction due to a still unknown mechanism directly triggered by DBN-1 depletion and brood size reduction due to increased proteotoxic / oxidative stress by $A\beta_{1-42}$ overexpression. The overexpression of human Drebrin de/phospho mimicry variants seem to be not able to rescue any of these possible mechanisms and therefore, the fecundity remains reduced.

The lifespan was analysed as a second read-out of organismal fitness (Figure 2.41 B). Yet, depletion of DBN-1 did not reduce the lifespan under unstressed conditions in previous experiments (Figure 2.30 B). The lifespan of JKM2-Δ (maximum life expectancy: 20 days, median survival: 9.2 days) was significantly reduced compared to wild type (maximum life expectancy: 30 days, median survival: 18.2 days). The expression of dephospho mimicry Drebrin ($nDBN^{S647A}$) in nAβ nematodes did only have a subtle, not significant effect rescuing lifespan (maximum life expectancy: 22 days, median survival: 9.8 days). $nDBN^{wt}$ prolonged maximum life expectancy (25 days) and median survival (12.5 days) significantly compared to JKM2-Δ. An even stronger increase of lifespan was observed for $nDBN^{S647D}$ (maximum life expectancy: 30 days, median survival: 16.7 days). Hence, Drebrin overexpression seems beneficial for the nematodes by possibly counteracting proteotoxic and oxidative stress induced by $A\beta_{1-42}$. I assume, that phosphorylation of Serine-647 plays a key role in regulating the stress compensation, as both, wild type Drebrin (that can become phosphorylated upon stress) and the phospho mimicry Drebrin, significantly alleviate lifespan reduction as well as ameliorate the aggregate burden, as was shown in the FLIM experiments (Figure 2.39 and Figure 2.40). Therefore, a direct correlation between amyloid burden and lifespan reduction can be concluded that is regulated by Drebrin-S647 phosphorylation.

To further analyse if Drebrin exerts also benefits towards neuroprotection *in vivo*, chemotaxis to volatile odorants and pathogen avoidance were tested. Avoiding pathogenic *S. marcescens* is mediated mainly by URY neurons and a defective reaction, hence, indicates neuronal defects. nAβ as well as JKM2-Δ exhibited impaired pathogen avoidance towards *S. marcescens* (Figure 2.22 A and Figure 2.42 A). The overexpression of Drebrin variants did improve pathogen avoidance slightly, yet a significant benefit was only observed for $nDBN^{S647D}$. The constitutive phosphorylation mimicry was also significantly more repelled by the pathogenic bacteria than the dephospho mimicry nematodes.

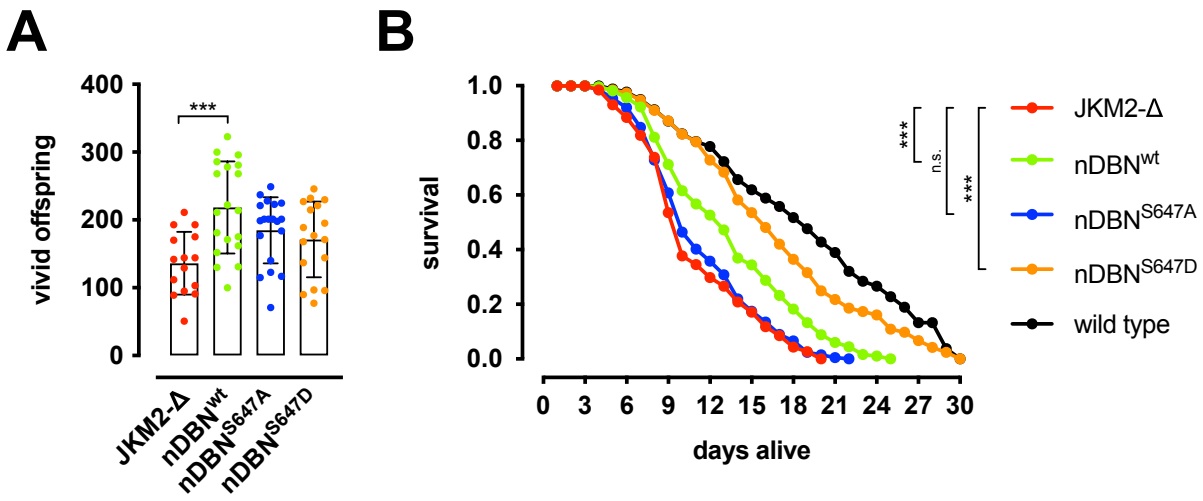

***Figure 2.41**: Drebrin overexpression has systemic beneficial effects on Aβ$_{1-42}$ expressing nematodes*
(A) Scatter dot plot displaying the progeny count per nematode of the indicated strains as mean ± SD. 15 - 20 nematodes were analysed per strain. Significance was tested by one-way ANOVA + Bonferroni post hoc test (*** = $p < 0.001$). **(B)** Kaplan-Meier plot of the cumulative survival probability of JKM2-Δ (red), nDBN^{wt} (green), nDBN^{S647A} (blue) and nDBN^{S647D} (orange) and wild type (N2; black) nematodes is displayed. 95 - 105 nematodes were analysed per strain. Significance was tested by log-rank test (*** = $p < 10^{-6}$).

Detection of volatile odorants such as Benzaldehyde, Diacetyl or diverse alcohols are vital functions for free living nematodes to find food, evade toxic environments *etc.*. Yet, these detections rely on a whole array of sensory neurons. Among them, AWC neurons are suitable to detect Benzaldehyde and resolve an attraction behaviour response. In previous experiments, overexpression of Aβ$_{1-42}$ in neurons was observed to negate the nematode's ability to sense diluted Benzaldehyde (Figure 2.22 B).

The depletion of endogenous DBN-1 did not alter this phenotype, as JKM2-Δ nematodes exhibited no attraction behaviour towards diluted Benzaldehyde (Figure 2.42 B). The co-expression of Drebrin nevertheless, was able to rescue attraction behaviour to certain extent. nDBN^{S647A} induced a minor response that was exceeded by the response observed in nDBN^{wt} and nDBN^{S647D}. Between nDBN^{wt} and nDBN^{S647D} there was no significant difference, yet both strains exhibited a solid attraction towards diluted Benzaldehyde. All analysed strains reliably avoided pure Benzaldehyde, exhibiting a not impaired neurologic function.

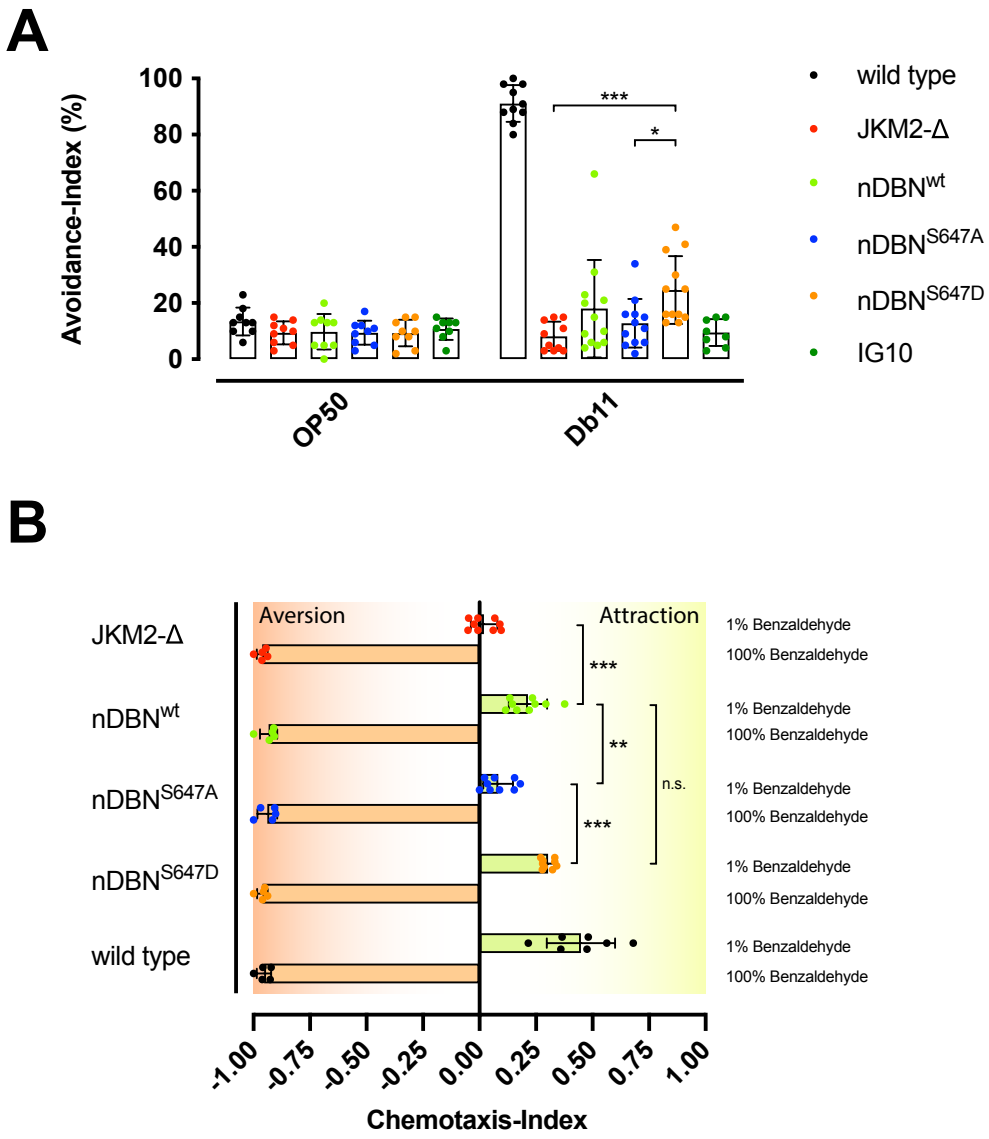

***Figure 2.42**: Drebrin overexpression improves neuronal function in nAβ*

(A) Scatter dot plot displaying the avoidance reaction index of JKM2-Δ (red), nDBN^{wt} (green), nDBN^{S647A} (blue), nDBN^{S647D} (orange), wild type (N2; black) and IG10 (*tol-1*; dark green) nematodes towards OP50 or Db11 bacteria. Three independent cohorts with 3 - 5 replicates of 10 - 15 nematodes each were analysed per strain and condition. Plotted is mean ± SD. Significance was tested with two-way ANOVA + Bonferroni post hoc test (* = $p < 0.334$, *** = $p < 0.001$). **(B)** Scatter dot plot displaying the chemotaxis index of the indicated strains towards pure Benzaldehyde (100%) or diluted Benzaldehyde (1%). Three independent cohorts with 3 - 5 replicates of 50 - 100 nematodes each per strain and condition were analysed. Plotted is mean ± SD. Significance was tested with two-way ANOVA + Bonferroni post hoc test (** = $p < 0.01$, *** = $p < 0.001$).

Drebrin overexpression appeared to be generally beneficial for the preservation of neuronal functions, yet the degree of rescue remained different for all analysed functions. Diverse factors that might influence the degree of rescue for certain neurons or certain functions remain elusive and need further research. Even though the discrepancies between the three employed Drebrin variants (wild type, S647A and S647D) was miniscule for some of the analysed phenotypes (*e.g.* pathogen avoidance assay) a general trend was observed, that Serine-647 phosphorylation was a vital part of Drebrin regulation and that phosphorylation was associated with an alleviation of AD toxicity in the here presented, novel model of $A\beta_{1-42}$ pathology.

Discussion

In the following chapters the three presented projects shall be discussed separately. Yet, I would like to emphasize that they are tightly connected to each other. Drebrin plays a vital role in the regulation of synapse stability that is compromised in Alzheimer's Disease. Still, the regulation of Drebrin itself and especially the mechanisms leading to its depletion in AD patients' brains remain enigmatic.

The Aβ pathology elicits toxicity affecting a myriad of cellular processes that ultimately lead to neurodegeneration (Figure 3.1), yet I would like to discuss some of them, involving Drebrin, in the following chapters in further detail.

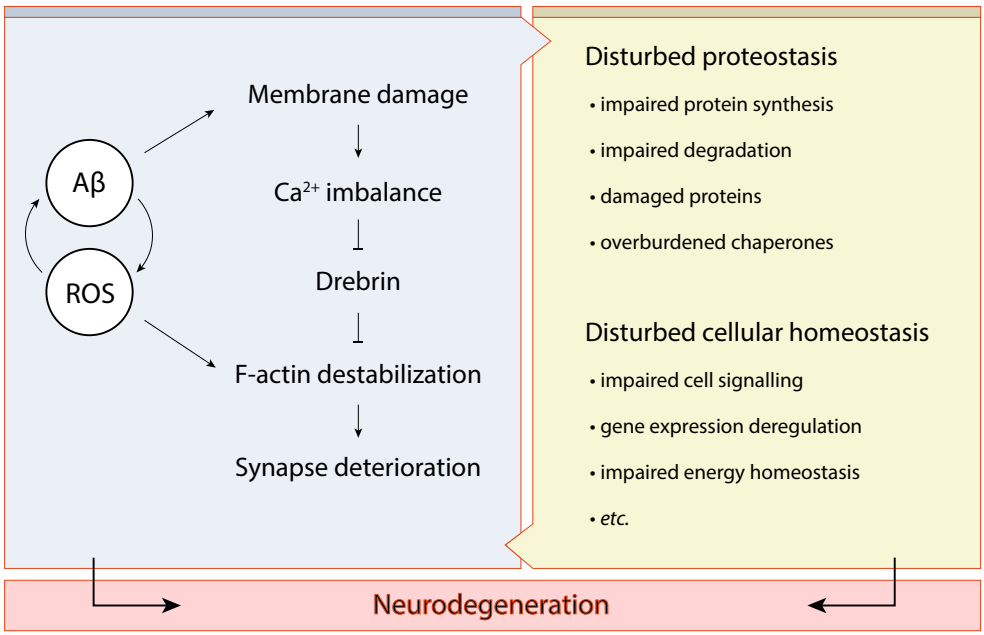

***Figure 3.1**: AD perturbs multiple layers of cellular integrity*

Schematic overview depicting a selection of dysregulations evoked by Alzheimer's Disease. The blue box contains a proposed mechanism how $A\beta_{1-42}$ aggregation and Drebrin depletion contribute to neurodegeneration. Aβ and reactive oxygen species (ROS) are affecting each other in a feed forward loop increasing pathogenicity. Both elicit multiple disturbances (*e.g.* damaging of membranes, damaging of F-actin fibres). Damaged membranes are leaking Ca^{2+} that in turn induces a Drebrin exodus from dendritic spines, followed by a destabilization of F-actin. Yet, Drebrin regulation is more complex than indicated here and Ca^{2+} imbalance is only one factor affecting Drebrin localisation and activity.

The yellow box contains a list of other dysregulations evoked by AD. The processes in the blue and in the yellow box are complexly interlaced which is indicated by overlapping of the boxes. All listed processes contribute to a yet unknown degree to neurodegeneration.

A novel model for studying Alzheimer's Disease *in vivo*

The present thesis presents a novel *C. elegans* model of Alzheimer's Disease that overcomes several obstacles of previous models. The strain JKM2 is the first AD model in *C. elegans* that exhibits $A\beta_{1-42}$ derived toxicity and enables non-invasive, *in vivo* and *in situ* analysis of aggregates by employing fluorescence microscopy.

A set of most widespread AD models in C*. elegans* expresses a truncated version of Aβ of only 40 amino acids length that is described as being less toxic than full length $A\beta_{1-42}$ [211,222]. Furthermore, only mild toxicity was observed in those models while JKM2 (neuronal expression of $A\beta_{1-42}$) and JKM7 (body wall muscle expression of $A\beta_{1-42}$) exhibit a multitude of disease related phenotypes (*e.g.* median lifespan reduction: JKM2 - 51% *vs.* CL2355 - 20% [231]). Yet most importantly, JKM2 and JKM7 are fluorescently labelled in a sub-stoichiometric manner that does not perturb native fibril growth while previous models that aimed to establish Aβ-GFP fusions were only forming oligomers *in vitro* and did not form foci *in vivo* at all [213].

"Native" aggregation of fluorescently labelled $A\beta_{1-42}$

One of the main questions of this project was how I could trace amyloid formation *in vivo* in a non-invasive manner. For this purpose, I have conceived a model of sub-stoichiometric expression, where the majority of untagged $A\beta_{1-42}$ can fibrilize into "native" amyloids unperturbed, while a seamlessly, sub-stoichiometric incorporation of fluorescently tagged wrmScarlet-$A\beta_{1-42}$ labels those fibrils. For amyloid *in vitro* studies sub-stoichiometric labelling by employing a defined ratio of fluorescently tagged and untagged moieties is a well-accepted method [228,242]. To translate this approach *in vivo*, the less efficient translation initiation by an internal ribosome entry site on a bicistronic expression vector was exploited [243,244]. By expressing wrmScarlet-$A\beta_{1-42}$ with and without excess $A\beta_{1-42}$ I could show, that the overexpression of an untagged variant is a prerequisite for amyloid formation as well as for $A\beta_{1-42}$ derived toxicity in the nematodes. On one hand, this is a confirmation of previous studies [213], on the other hand it is a clear extension of previous models that failed to generate $A\beta_{1-42}$ amyloids and toxicity.

Aβ$_{1-42}$ aggregation and toxicity aggravate in the progression of ageing

The second question was how ageing would affect amyloid formation. Yet, I could observe that aggregation increased in the progression of ageing forming more and more widespread aggregates.

Age-dependent decline of proteostasis capacity is regarded as a major driver of cellular dysfunction and degeneration [19,245,246]. The exact reasons why proteostasis capacity becomes reduced in mammals upon ageing remains unknown, yet one assumption is that lack of evolutionary pressure beyond the fertile phase gives rise to mutations limiting an organism's health- and lifespan.

This is fundamentally different in *C. elegans*, where a major reorganization of proteostatic capacity occurs on day 4 of life, reducing proteostasis in favour of fecundity [226,227]. The observation that both JKM2 and JKM7 exhibit their first aggregates at day 4 of life confirms previous studies and is also an indication, that failing proteostasis is a key mechanism leading to amyloid growth *in vivo.*

To further address this, genetic variations of slow or fast ageing (*daf-2*, *age-1*, *daf-16 etc.)* could be crossed with the Aβ$_{1-42}$ expressing strains to further analyse how Aβ$_{1-42}$ aggregation propensity is altered due to the programmed proteostasis collapse. Furthermore, a genetic deletion of the master regulator of this programmed decline (*cbd-1*) can be employed to untangle Aβ$_{1-42}$ intrinsic aggregation propensity and additional aggregation propensity due to reduced proteostasis capacity [247].

Aβ$_{1-42}$ elicits systemic defects and spreading toxicity

I hypothesized that progressive aggregation of Aβ$_{1-42}$ would elicit multiple disease related phenotypes that could be observed in the novel nematode model. Previous model strains could only show a subset of mild disease phenotypes.

I observed a multitude of disease related phenotypes in both JKM2 and JKM7 nematodes, ranging from systemic defects to neuron-specific impairments as well as perturbations of the cellular ultrastructure (see overview Figure 3.2). Despite the mainly intracellular localization of the expressed Aβ$_{1-42}$, these novel models, JKM2 and JKM7, are appropriate to analyse the traits that lead to AD, as well as to support studies in finding key players in aggregation regulation *etc..* For one, there is evidence that Aβ$_{1-42}$ can be localized in neurons despite its secretion into the intercellular space [32,69,248] and interact with the intracellular proteome. Furthermore, Aβ$_{1-42}$ was observed to inhibit proteasomes *in vivo* and it

was concluded to be localized inside the cytosol [39–41]. JKM2 and JKM7 therefore can serve as tools to analyse $A\beta_{1-42}$–protein interactions in the cytosol.

One AD related phenotype that was observed in both $A\beta_{1-42}$ expressing model strains, but was most prominent in the muscle expression strain, was the accumulation of amphisomes. The ultrastructure of neurons of AD patient brain slices were analysed by TEM and immune-gold labelling in previous studies and multivesicular bodies were enlarged [85] or found to exhibit striking similarity to pre-lysosomal autophagic vacuoles [249]. In the present study, I can confirm this phenotype, yet found in muscle cells expressing $A\beta_{1-42}$. I hypothesized that iterative induction of autophagophores and subsequent failing of membrane closure could be a reason for the detected dysfunctional autophagy and result in the observed matryoshka-like amphisome clusters. It was previously reported that increased autophagy induction in CA1 neurons of AD hippocampi overburdens lysosomal degradation machinery [86]. Yet, the data suggest that the underlying mechanism of $A\beta_{1-42}$-induced perturbation of autophagy is cell-type independent or works in such a general way that multiple cell types (*e.g.* neurons, muscle cells) can be affected alike.

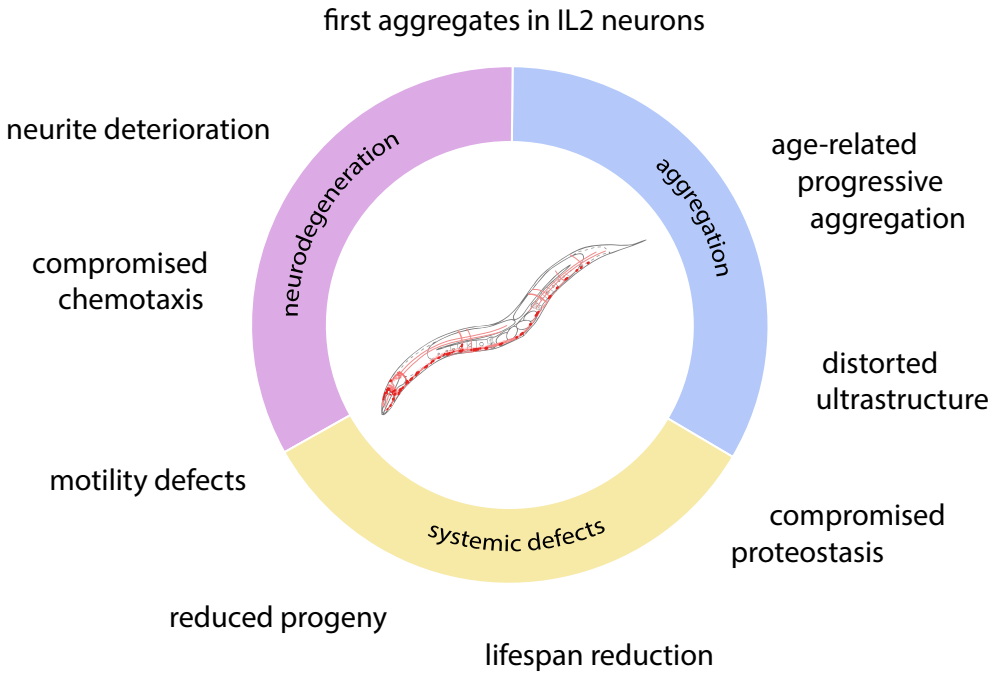

***Figure 3.2**: Schema of the observed phenotypes in the novel AD model strains*
Listed phenotypes belong to the indicated categories, some of them are at the conjunction of categories to indicate that they are relevant for both.

Furthermore, deregulation of the protein degradation machinery together with depletion of protein synthesis, poses a major threat for maintaining proteostasis. I assume that chaperones are either target for deregulation too or that they are overwhelmed by possible client abundance. Hence, analysis of the different chaperone systems (*e.g.* Hsp-70/J/110, Hsp-90, *etc.*) pose a promising approach to understand the mechanisms underlying the deregulation as well as finding drug target candidates that could ameliorate the AD toxicity.

I could show that $A\beta_{1-42}$ leaves its tissue of expression and gets excreted into the pseudocoelom by a yet unknown mechanism. There, it can travel through the whole nematode and possibly evoke damage at distant sites. Also, coelomocytes accumulate $A\beta_{1-42}$ in phagocytic vacuoles. This active uptake can be regarded as a proto clearance mechanism (a primordial clearance system that may have changed and improved due to evolution) and could possibly be employed as a model for $A\beta_{1-42}$ uptake, as was observed for glial cells of the human brain. Furthermore, $A\beta_{1-42}$ was observed to damage membranes and compromise membrane integrity by employing a hypodermal Ca^{2+} leakage marker, corroborating results described by Julien *et al*. who observed that $A\beta_{1-42}$ is able to incorporate into membranes and form pore-like structures that cause a permeation and challenge cellular repair mechanisms [103].

Furthermore, I could demonstrate that $A\beta_{1-42}$ can be transmitted to distant tissues (*e.g.* hypodermis) by a yet unknown mechanism. Since membrane damage and crossing over single membranes could be observed, I reason that $A\beta_{1-42}$ transmission works in a cell non-autonomous way. Yet, I cannot exclude that besides the passive membrane rupture/crossing mode a second or even further transmission modes exist that may require cellular machineries to facilitate transport (*e.g.* endosomal trafficking, endo- and exocytosis). For instance, such transport was described for another proteotoxic protein, alpha-synuclein, the pathogenic protein forming 'Lewy bodies' termed aggregates in Parkinson's Disease [250].

Yet, the discovery of $A\beta_{1-42}$ spreading in a nematode model paves the way for more detailed analysis of $A\beta_{1-42}$ transport and transmission compared to the more static analysis in other model systems that cannot be subjected to *in vivo* and *in situ* analysis by microscopy studies.

Upon analysing the characteristics of the new model systems, an interesting divergence in population fitness was observed. I hypothesized that there is a survivorship bias occurring. Nematodes that were more strongly affected by $A\beta_{1-42}$ expression had a high chance to die prematurely (with a median of 8.8 days, nearly half of the population of JKM2 would have died by day 7 when the assay was performed), therefore the apparent mean was increased. I suspect a mechanism of Darwinian selection of the fittest to evoke the observed divergence. Nematodes that acquired a mutation lowering the $A\beta_{1-42}$ expression or aggregation propensity would achieve an improved fitness compared to their cohort and would subsequently pass these mutations on to the next generation. Such adaptions can arise spontaneously with a rate of 2.2×10^{-7} per gene and generation by diverse mechanisms [251–253]. Furthermore, overexpression of Aβ induces constant oxidative and proteotoxic stress [104–106], that in turn may increase mutation rates due to oxidation of nucleobases [254–256]. Eventually, mutations can arise that allow nematodes to cope with the proteotoxic stress by $A\beta_{1-42}$.

Such selection processes can occur in all thinkable nematode models, yet, JKM2 and JKM7 are fluroescently tagged, enabling a consequent counterselection approach by selecting only nematodes exhibiting a constant level of fluorescence. On the other hand, the fluorescence intensity is a phenotypic marker that is easiliy detectable and quantifiable, rendering the model suitable for mutation screening approaches to identify new beneficial mutations.

IL2 neurons harbour the first aggregates and could serve as starting point for disease spreading

I was assuming that neurologic impairments would occur in the novel AD model strains, yet it was unclear to which extent single neurons would be affected.

The first $A\beta_{1-42}$ aggregates that appeared in JKM2 nematodes occurred reliably in a distinct set of head neurons of the anterior ganglion, the IL2 neurons. Furthermore, the onset of aggregation in the IL2 neurons preceded the aggregation in other neurons.

Two questions arose from this observation: (1) are those neurons more susceptible to proteotoxic stress and harbour therefore the first aggregates and (2) are amyloids spreading from those neurons, triggering aggregation at distant sites? I could show that an IL2 specific knockdown of $A\beta_{1-42}$ led to not only an

expected reduction of aggregation inside IL2 neurons themselves, but also decreased aggregation systemically. In consequence, this resulted in a temporary alleviation of AD toxicity. Yet, the knockdown could not completely prevent disease progression, but delayed the onset systemically. Also, it is not clear yet if a direct transmission of $A\beta_{1-42}$ from IL2 to other neurons was responsible for initiating an aggregation cascade or whether a signalling pathway was activated in IL2 neurons that led to modulation of aggregation propensity in other neurons. With respect to the observation of $A\beta_{1-42}$ spreading to the hypodermis I assume that neuron-neuron spreading might contribute to AD progression in the generated model strain JKM2.

The question remained if IL2 neurons were more susceptible to proteotoxic stress than other neurons and if so, what factors contribute to this predisposition. Previous experiments and studies on other disease related amyloid proteins (*e.g.* polyQ, Tau or alpha-synuclein) have led to the identification of differently affected tissues and cell types. Alpha-synuclein for instance, was described as mainly affecting dopaminergic neurons and causing dopaminergic neuron degeneration, being a hallmark of Parkinson's Disease [195]. The aggregation of huntingtin in Huntington's Disease is affecting multiple regions of the brain, ultimately leading to degeneration of the striatum and death by respiratory paralysis. A simple model that expressed only the aggregation-prone poly-glutamine stretch of huntingtin in different tissues revealed motor neurons as primarily affected from aggregation and aggregation-derived toxicity, yet, without further discrimination of distinct neurons [257]. The expression of FTDP-17 as model for tauopathies led to the discovery of a uniform pan neuronal aggregation in *C. elegans* [204]. Thus, the affected cells and brain areas seem to be inherently dependent on the nature of the amyloid protein on the one hand. Furthermore, a high enough detection sensitivity and resolution is crucial to uncover early onset aggregation, as could be shown for IL2 neurons in JKM2. I assume that the early onset of $A\beta_{1-42}$ aggregation in IL2 neurons reflects a specific pattern of aggregation and pathology.

The IL2 neurons have been described as polymodal/mechano-/chemo-sensory neurons in the dauer stage, where they mediate nictation, a dauer-specific dispersal behaviour [258]. In adult nematodes their function is still unknown [259,260]. They belong to the cholinergic neurons, employing acetylcholine as neurotransmitter and harbouring a homologous nicotinic acetylcholine receptor as well as neuropeptide Y like receptors [261–263]. The cholinergic system was described as one of the targets of

Alzheimer's Disease pathology in the human brain, where presynaptic cholinergic markers of the cerebral cortex were observed to be depleted [264,265]. The nucleus basalis of Maynert in the basal forebrain belongs to the major sources of cortical cholinergic innervation and was found to be severely affected from neurodegeneration in AD patients [266,267]. Further experiments showed, that cholinergic agonists (such as acetylcholine esterase inhibitors) were beneficial for patients suffering from AD demonstrating a strong correlation between the function of cholinergic innervation and AD induced neurodegenerative effects [268,269].

C. elegans possesses 159 cholinergic neurons (neurons positive for *unc-17* cholinergic marker [270]) out of 302 neurons in total. Yet, I cannot pinpoint what renders IL2 neurons particularly vulnerable for the aggregation of $A\beta_{1-42}$. IL2 neurons are discussed to participate in chemotaxis and olfaction what is an interesting parallel to observations of AD patients that suffer from anosmia and mouse experiments that analyse chemotactic neurons of the olfactory bulb. A volume reduction of the olfactory bulb was demonstrated in AD patients by brain imaging techniques and the loss of olfaction capacity preceded clinical AD pathologies [271–273]. Recent studies have observed, that $A\beta_{1-42}$ can be transported anterogradely and retrogradely through axons of neurons, corroborating some results described in this thesis, that $A\beta_{1-42}$ can passage across membranes and be transported along dendrites and neurons. In mouse experiments it could be shown that $A\beta_{1-42}$ oligomers that were injected into the olfactory bulb were actively taken up by the surrounding neurons and transported alongside the axons to distant brain regions, providing an efficient dispersal mechanism [274–276]. Hence, such mechanisms could be studied employing JKM2 or by refining the expression by limiting it to IL2 neurons and follow $A\beta_{1-42}$ spreading and disease progression.

Concluding remarks and limitations

Taken together, the novel model systems JKM2 and JKM7 provide a platform to analyse key features of the $A\beta_{1-42}$ pathology. Many characteristic aberrations that occur in AD patients or experiments with murine tissue were observed and can be correlated to the progressive aggregation of $A\beta_{1-42}$. Furthermore, the ability to track amyloid growth *in vivo* and *in situ* was a prerequisite to identify IL2 neurons as particularly vulnerable to $A\beta_{1-42}$ aggregation and may further represent an initiation site for amyloid spreading or a yet unknown, transcellular signalling, eliciting amyloid formation in distant neurons.

Yet, the generated models focus on the $A\beta_{1-42}$ pathology and do not reflect on the dynamic nature of different Aβ species of different lengths. Previous studies suggested that $A\beta_{1-42}$ poses the major toxicity in the AD pathology and other species, among them $A\beta_{1-40}$, could be negligible [21–23]. Also, the generation of different Aβ-species as well as tau pathology were not considered. Yet, this simplifies analysis because many cross reactions that would otherwise occur, are excluded.

Furthermore, reactivity with different cell-types can be analysed, yet the nematode's nervous system architecture differs in multiple ways from the human brain. For instance, glia cells exist and serve certain functions (*e.g.* promotion of directed neurite growth, promotion of synapse formation, modulation of synapse activity, *etc.*) they share with human glia cells, while other functions do not exist in nematodes (*e.g.* myelination of axons, supplying nutrients to neurons).

Yet, these limitations also offer possibilities to analyse certain interactions in a simple way without perturbing exceedingly complex interactions as are found in mammalian brains.

A humanized model of Drebrin overexpression in *C. elegans*

The actin-binding protein Drebrin was thought to stabilize F-actin filaments, bundle them and protect synapses by this process. Interestingly, Drebrin knockout mice exhibited no physiological changes to its neurons, brain or behaviour (personal communication Dr. Till Mack, 2019). Only after induction of a further stressor (*e.g*. oxidative stress) a stronger synapse deterioration could be observed, indicating that Drebrin loss sensitized the affected neurons to oxidative stress [179]. Multiple layers of regulation are influencing Drebrin activity and I was interested, if nematode signalling pathways could regulate Drebrin in a similar way.

C. elegans DBN-1 protein shares structural homology with two human proteins serving different functions and occurring in different tissues: Drebrin (DBN1) in neuronal and motile cells and Drebrin-like protein (DBNL) in immune and other motile cells. It is tempting to speculate if DBN1 and DBNL are paralogs that originate from an ancestral gene like *C. elegans dbn-1* but diverged in the progression of evolution to fulfil different, yet homologous functions. My results amend previous studies observing that *dbn-1* is expressed in multiple tissues, among them body wall muscle cells, pharyngeal muscle cells and neurons (see Figure 2.31) [217,218]. Since I was most interested in the effects of Drebrin in neurons, I decided to employ the *rgef-1* promoter to achieve pan neuronal expression rather than employing the endogenous *dbn-1* promoter to exclude cross reactivity through Drebrin overexpression in other tissues.

The following part is dedicated as complementation and corroboration of work done by our cooperation partners of the Eickholt lab that were analysing Drebrin overexpression in neuronal cell culture.

Drebrin turn-over is regulated by pSerine-647

Since Drebrin depletion sensitized neurons to oxidative stress and led to reduced number of dendritic spines, while overexpression of Drebrin ameliorated oxidative stress and led to an increase in Dendritic spines, it was assumed, that Drebrin protein level may play a pivotal role in actin orchestration and stabilization to prevent synapse loss in response to oxidative stress. Our cooperation partners of the

Eickholt lab observed that phosphorylation of Serine-647 is crucial for the regulation of Drebrin turn-over by proteasomal degradation [178,179].

Wild type Drebrin was observed to have a half-life of approximately 3 days (75 ± 8 h) while DBN^{S647A} exhibited an increased protein turn-over (39 ± 3 h). DBN^{S647D} exhibited a yet not significant slower turn-over (97 ± 16 h) [179]. I could not corroborate these observations in nematodes. The protein turn-over rates vary between individual neurons. Yet a major discrepancy was observed between head and tail neurons. Complete degradation of a marked protein pool was observed in head neurons after 24 h, while the degradation in tail neurons was much faster, removing the same, marked protein pool in merely 3 h (personal communication Dr. Diogo Feleciano, 2018). Due to these obstacles, a quantification of Drebrin degradation *in vivo* would require a focused approach, where only a subset of neurons one after the other is analysed to generate a neuronal degradation map of Drebrin. Yet, a faster approach would be the expression of Drebrin-Dendra2 limited to neurons that are interesting for the study of AD in nematodes (*e.g.* IL2 neurons + URY neurons for control).

Drebrin-S647 is a target for ATM-1 phosphorylation

Previous studies observed Drebrin-S647 phosphorylation upon neuronal stimulation [178] and predicted a phosphorylation site for ATM kinase [239]. Yet, experiments employing activated ATM kinase and purified Drebrin could demonstrate an efficient phosphorylation of Drebrin-S647 *in vitro*, furthermore purified Drebrin could be phosphorylated at Serine-647 employing mouse brain extract [179]. The phosphorylation of Drebrin-S647 could be efficiently blocked in both experiments, *in vitro* and *ex vivo*, by employing the specific ATM kinase inhibitor KU-55933 [277], exemplifying that ATM was the kinase phosphorylating Serine-647 as well as, that ATM was present and active in postnatal brain tissue.

ATM was reported to mediate cellular adaptions in response to DNA double-strand breaks, yet, recent studies identified a cytosolic ATM pool regulating redox signalling in response to oxidative stress [278]. Neurons are highly metabolically active cells that produce reactive oxygen species by their normal activity [240]. *Ex vivo* neuronal cell culture experiments employing agents to increase the synaptic activity were able to activate ATM as well as to increase the amount of Drebrin-pS647 [179].

To corroborate these results *in vivo* I employed a humanized nematode model expressing Drebrin pan-neuronally ($nDBN^{wt}$). The induction of constitutive oxidative stress by Paraquat application reduced the

nematode's lifespan, yet this reduction was ameliorated by the overexpression of wild type Drebrin. Additional application of the specific ATM kinase inhibitor KU-55933 in turn, negated the benefits of Drebrin overexpression to rescue lifespan under oxidative stress conditions. Furthermore, western blot experiments showed that application of KU-55933 reduced the phosphorylation of Drebrin-S647, therefore KU-55933 was able to inhibit ATM-1 (the nematode homolog of ATM) activity at least partially. Drebrin-S647 phosphorylation appeared as an integral part of the stress response to ROS in neuronal cell culture [179] and the nematode experiments suggest that the basic stress response pathway remained conserved between nematode and human.

Together with the data of de/phospho mimicry variants, this indicates, that the beneficial effect of Drebrin under sustained oxidative stress is mediated by Serine-647 phosphorylation. This is in turn dependent on ATM-1 kinase activity in nematodes as demonstrated by the inhibition of ATM-1 that did reduce Drebrin-pS647 levels and negated lifespan rescue, whilst phospho and dephosphy mimicry variants were uncoupled from ATM-1 regulation. Furthermore, ATM-1 inhibition in nematodes did not affect other players that would interfere with lifespan reduction under sustained oxidative stress.

Proposed model for Drebrin regulation and its limitations

Summarizing data from the literature and recent observations presented in this thesis, a model was proposed for the sequential mechanism of Drebrin dependent neuroprotection (Figure 3.3).

Reactive oxygen species induce ATM kinase activation [278] that phosphorylates, among other proteins, Drebrin-S647 (Figure 2.34,[179]). Drebrin turn-over gets reduced and the Drebrin pool stabilized [179], leading to stabilization of F-actin filaments [152,153]. Finally, this leads to protection of synapses in cell culture experiments [155,156,179,279] and exerts in nematodes systemically beneficial effects on lifespan (Figure 2.33).

Yet, the observed stabilization of Drebrin due to phosphorylation at Serine-647 by ATM kinase poses only one layer of controlling Drebrin activity. Levels of Drebrin-pS647 are closely linked to dephosphorylation by PTEN [178]. Previous studies observed that PTEN gets translocated upon NMDA receptor activation into dendritic spines in close association with PSD-95 being a major regulator of long-term depression [280]. Further studies could show, that inhibition of PTEN in a mouse model of Alzheimer's Disease could rescue normal synaptic function, yet this function was traced back to the localization change of PTEN to dendritic spines upon NMDAR activity [281]. This is an appealing

observation towards Drebrin function and could, together with the results presented in this thesis and the corresponding publication by Kreis, Gallrein, Puente *et al.* [179], be a foundation to further investigate the $A\beta_{1-42}$ - PTEN - Drebrin relationship.

Besides Drebrin turn-over regulation by Serine-647, several other phosphorylation sites were observed by mass spectrometry experiments suggesting functions in regulating F-actin binding properties and activities contributing towards dendritic spine remodelling (*e.g.* Serine-142, a target of CDK-5 kinase, regulates F-actin bundling by specific binding of pS142-Drebrin to parallel F-actin filaments [151]).

Hence, several putative upstream signalling processes regulating Drebrin activity and turn-over may influence synaptic stabilization and neuronal health also under neurodegenerative conditions.

On the other hand, the downstream activities evoked by Drebrin contribute to manifold processes, among them the regulation of F-actin dynamics that pose a crucial role for neuronal plasticity. Furthermore, adaption of cytoskeletal dynamics in stress or disease conditions may be a fundamental principle relevant during healthy ageing, development and regeneration after injury [240,282–284].

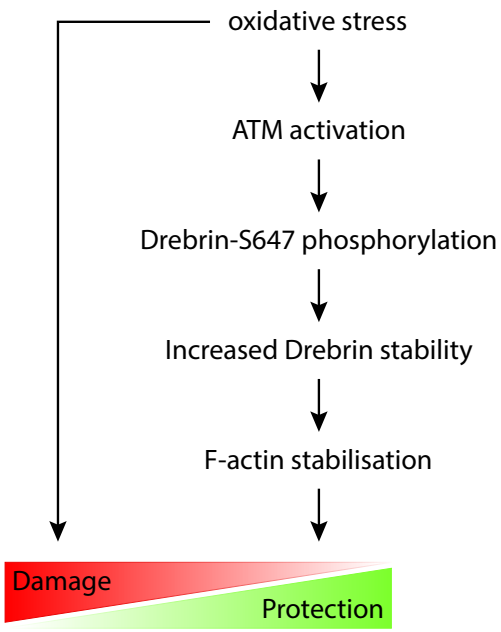

***Figure 3.3**: Proposed model of Drebrin activity*

Oxidative stress induces ATM activation leading to increased Drebrin-S647 phosphorylation. The Drebrin pool gets stabilised and subsequently stabilises the F-actin filament leading to increased resilience towards oxidation damage

In vivo interaction between Drebrin and $A\beta_{1-42}$

Drebrin was observed to be depleted from human brains and cell culture experiments analysing both mild cognitive dementia and AD [145,146]. To this point, a functional relationship between Drebrin and $A\beta_{1-42}$ was described for an AD mouse model, where a depletion of Drebrin led to a more severe AD phenotype, while an overexpression of Drebrin alleviated AD toxicity [148,149]. Still, the description of a causal relationship between Drebrin and $A\beta_{1-42}$ requires more research. Previous experiments observed that an increased activity of histone deacetylases induced by Aβ oligomers led to reduced Drebrin levels that could be rescued by the application of histone deacetylase inhibitors [285]. Another study described a correlation between AD severity and decreased Drebrin mRNA expression [286]. Yet, a clear link between Drebrin and AD or more specific, between Drebrin and $A\beta_{1-42}$ remains elusive.

Drebrin and $A\beta_{1-42}$ can form foci

Since $A\beta_{1-42}$ can cross membranes and accumulate in the cytosol of neurons [53,54], this opens the possibility of a direct protein-protein interaction with Drebrin. In this study, I observed that Drebrin and $A\beta_{1-42}$ could colocalize in micron-sized foci, yet the majority of Drebrin remained soluble and dispersed throughout the cytoplasm. Notably, the $A\beta_{1-42}$-foci formation was reduced upon Drebrin co-expression but the amount of foci composed of aggregated $A\beta_{1-42}$ was increased. Two different mechanism could induce such phenotype: (1) Drebrin could actively drive $A\beta_{1-42}$ aggregation or (2) Drebrin could prevent accumulation of $A\beta_{1-42}$ to a certain degree and therefore reduce the apparent foci load, yet being unable to prevent aggregation, leading to a changed ratio between foci consisting of aggregated material and foci consisting of non-aggregated material. Further experimentation would be necessary to prove the one or the other, yet it is tempting to speculate whether Drebrin could interact with $A\beta_{1-42}$ monomers or oligomers via its natively disordered C-terminal domain and induce or prevent $A\beta_{1-42}$ aggregation. Besides its actin-binding activity Drebrin can bind several other synaptic proteins to orchestrate construction of the post synaptic density [157,158] and thereby manipulate the close-by microenvironment. Yet, I cannot pinpoint how and by what mechanism Drebrin might alter $A\beta_{1-42}$ foci formation in neurons of *C. elegans.* It could therefore be of particular interest to set up *in vitro* experiments to analyse a possible Drebrin-$A\beta_{1-42}$ binding mode.

Drebrin overexpression alleviates Aβ$_{1-42}$ pathology

Despite the lack of a molecular mechanism, I could show that Drebrin overexpression is generally beneficial for Aβ$_{1-42}$ expressing nematodes (Figure 2.40, Figure 2.41 and Figure 2.42). Both, general vitality (analysed by lifespan and progeny count) as well as neurologic integrity (analysed by chemotaxis and pathogen avoidance) were alleviated upon Drebrin overexpression.

The foci formation in IL2 neurons was reduced in Drebrin expressing nematodes, with a stronger reduction for wild type and S647D-Drebrin compared to S647A-Drebrin or Aβ-Δ control. For all analysed phenotypes but one (brood size) a correlation between phosphorylation at Drebrin-S647 and improved behaviour was observed (see Table 3.1 for overview). Hence, regulation of brood size seems to be independent from the mechanism that alleviates the other analysed phenotypes. A similarly regulated mechanism might evoke the other analysed phenotypes dependent on phosphorylation of Drebrin-S647.

***Table 3.1*:** *Overview of the observed Drebrin-induced Aβ-toxicity alleviations*

Summary of the observed phenotypes of nDBN variant strains crossed with nAβ (Δ*dbn-1*[Ex1-Ex6] background). Arrows indicate up and down regulation respectively, bold arrows indicate strong up/down regulation.

	S647A	***S647 – wild type***	***S647D***
Aggregation	-	-	**↓**
IL2 foci formation	-	↓	**↓**
Lifespan	-	↑	**↑**
Progeny	-	↑	-
Chemotaxis	-	↑	**↑**
Pathogen avoidance	-	↑	**↑**

Drebrin-S647 phosphorylation was observed to regulate Drebrin turn-over in neuronal cell culture experiments [179], showing such regulation for nematodes would require further studies. Yet, it would pose a plausible mechanism by which Drebrin is regulated and how it positively affects cellular functions compromised by Aβ$_{1-42}$. Ultimately, the stabilization of the actin cytoskeleton could be one of the key processes leading to an alleviation of the toxicity in context of AD.

$A\beta_{1-42}$ alleviation is regulated by Drebrin-S647 phosphorylation

The actin cytoskeleton plays a key role in many cellular processes ranging from protein trafficking, cell growth, structural organisation to cell motility and synaptic plasticity in neurons (reviewed by Svitkina [287] and Sekino *et al.* [288]). Modifiers of actin organization, treadmilling and connection are of pivotal importance for the regulation of diverse processes, as is Drebrin for organization and maturation of the post-synapse [289].

Drebrin is depleted from neurons in AD patients, yet it is still unknown if aggregation of $A\beta_{1-42}$ induces Drebrin-depletion or if an initial Drebrin-depletion paves the way for extensive $A\beta_{1-42}$ aggregation. Most likely it is a coupled feedforward loop of mutual amplification of Drebrin-loss and AD toxicity.

Previous studies could show that overexpression of Drebrin in a mouse model of AD led to a rescue of cognitive capacity and an alleviation of other disease related disabilities [149]. The results presented in this thesis are corroborating those previous findings in a much simpler model system. Using the nematode certain questions should be easier to answer, for instance how the actin cytoskeleton is affected by AD and if Drebrin could be beneficial in this disease context.

F-actin disassembly was observed as a major phenotype correlated with AD and thought to be crucial for synapse deterioration due to $A\beta_{1-42}$ toxicity [280,281,290,291]. Yet, multiple mechanisms are assumed involving endocytosis of neurotransmitter receptors, deregulation of actin-binding proteins and direct damaging of actin bundles by oxidation (Figure 3.4). Oxidation events at Cys-374 were observed to be initiated by NADPH oxidase contribution as a defined regulation of F-actin dynamics, decreasing polymerization rates and weakening filaments [292,293]. Another regulator of F-actin dynamics exploiting oxidation is the [F-actin]-monooxygenase MICAL1. MICAL1 oxidizes Actin-M44 and Actin-M47 and thereby reduces polymerization rate and induces F-actin disassembly from both ends [294–296].

Since the excessive generation of reactive oxygen species is a hallmark of the $A\beta_{1-42}$ pathology such oxidation-dependent regulation mechanisms could turn into weak points paving the way for oxidation events evoking critical toxicity.

F-actin stability regulating proteins can become deregulated in an AD context leading to a severe destabilization of filaments (*e.g.* ADF/Cofilin gets activated in AD in a Calcineurin dependent fashion and promotes F-actin destabilization [297–299]). Drebrin is one of those proteins that are depleted in AD by a yet elusive set of interactions. PTEN phosphatase could be one part of this, getting translocated into

dendritic spines in $A\beta_{1-42}$ treated neurons [280,281], inducing a close proximity to one of its putative targets, Drebrin-pS647 [178]. A Drebrin dephosphorylation at Serine-647 increases its degradation by the ubiquitin-proteasome system and thereby destabilizes synapses.

Drebrin-S647 phosphorylation could be shown to have effects on most observed phenotypes in this study (Table 3.1). Hence, the regulation of Serine-647 phosphorylation poses a strong candidate for external interference.

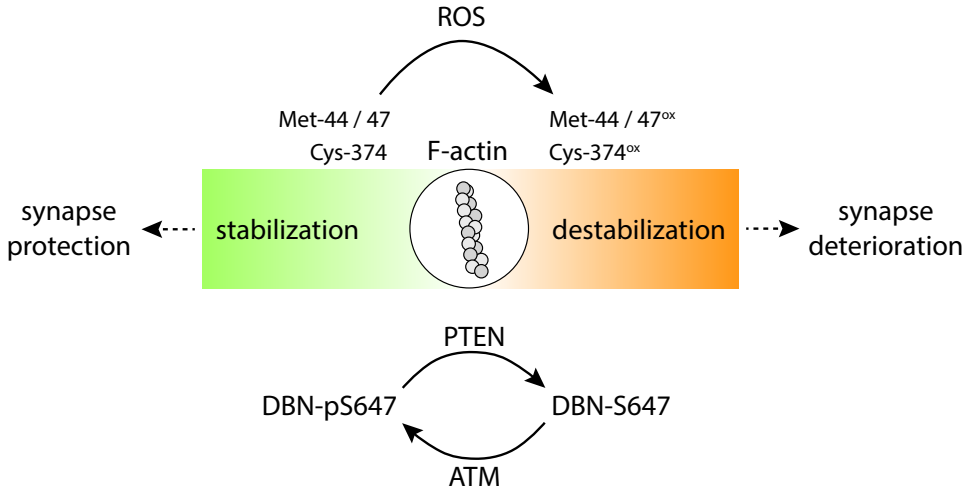

***Figure 3.4**: Actin cytoskeleton is crucial for synapse integrity*

F-actin plays a central role in both synapse integrity and synaptic plasticity being regulated by manifold players. Reactive oxygen species (ROS) can oxidize exposed residues and induce F-actin destabilization, while actin-binding proteins like Drebrin can bind to F-actin filaments and stabilize them. Yet such proteins are regulated by upstream factors, as is Drebrin by phosphorylation by Ataxia telangiectasia mutated (ATM) and dephosphorylation by Phosphatase and Tensin homolog (PTEN).

Targeted activation of ATM or selective inhibition of PTEN could be promising drug targets for treating AD. The nematode model presented in this study could serve as a testing platform for compound screening or RNAi screening. Both identified regulators, PTEN and ATM could be addressed in the nematode as there are orthologues *daf-18* for PTEN and *atm-1* for ATM. RNAi or CRISPR-based screenings could be employed to identify upstream regulators of Drebrin signalling.

Conclusion and Outlook

A novel model to study Alzheimer's Disease

Taken together, a novel Alzheimer's Disease model was generated to analyse key features of the $A\beta_{1-42}$ pathology that enabled me to identify many characteristic aberrations occurring in AD patients or that were observed in experiments with murine neurons. This new model provides insight into amyloid aggregation *in vivo* and *in situ* in a non-invasive manner. Furthermore, it allowed me to identify the IL2 neurons as particularly vulnerable to $A\beta_{1-42}$ aggregation and may further represent an initiation site for amyloid spreading or a yet unknown, transcellular signalling cascade, eliciting amyloid formation in distant neurons or evoking proteostasis imbalances in distant cells.

This model can serve for manifold succeeding experiments including analysis of signalling cascades, dysregulation of proteostasis or even large-scale screening approaches to identify yet unknown players. A few questions arose during this project that could not be answered yet.

What are the mechanisms of amyloid spreading? I could present evidence, that $A\beta_{1-42}$ can spread to distant tissues, yet without knowing the exact mechanisms behind. One possibility was addressed by the analysis of membrane integrity, that was found to be compromised, being a passive $A\beta_{1-42}$ migration by passaging directly through membranes. Yet, I cannot exclude any mechanism that works in a cell dependent manner.

Further studies addressing this question should consider analysis of subcellular compartment alterations, with special regard to endo/lysosomal vesicle transportation. Furthermore, analysing motor proteins (*e.g.* dynein, kinesin, non-muscle myosin) driving intracellular protein trafficking, as well as, regulators of protein transport.

Why are IL2 neurons more vulnerable to $A\beta_{1-42}$ aggregation? To address this question, it seems to become necessary to generate even more AD model strains that exhibit differential expression (*e.g.* limited to cholinergic/glutamatergic/dopaminergic *etc.* neurons or limited to smaller subsets of

neurons). Expression profiles of IL2 neurons *vs.* other neurons could be generated to analyse clusters of altered gene expression that could induce vulnerability, that could be subsequently tested in other neurons.

Is $A\beta_{1-42}$ spreading from IL2 neurons towards other neurons? To answer this question, it would be the easiest to generate a new model strain expressing $A\beta_{1-42}$ (and sub-stoichiometric amounts of fluorescently tagged $A\beta_{1-42}$) only in IL2 neurons and observe fluorescence dispersion. Furthermore, if labelled with a not-red fluorescent fluorophore and crossed with the initial JKM2 model (to combine wrmScarlet derived red fluorescence in all neurons and a different fluorescence in IL2 neurons), spreading from IL2 neurons could be correlated with the onset of aggregation in distant neurons.

How are proteostasis mechanisms contributing to pathogenicity or prevention of pathogenicity?
All aforementioned questions are connected to this fourth question, as the proteostasis regulation is vital for proper function of all cellular processes. Chaperones safeguard the proteome on all levels from protein biosynthesis to degradation and their functionality is essential to keep protein misfolding and aggregation in check. Yet, proteinopathies like AD are overwhelming chaperone capacities by various mechanisms.
To analyse how the presence or absence of certain chaperones are contributing to disease progression and spreading, knockdown experiments could be performed to test a set of known chaperones (Hsp-70s, J-proteins *etc.*). Furthermore, promising candidates that were alleviating or aggravating the Aβ toxicity could be overexpressed to complement the analysis.

A model to study human Drebrin in the context of a living animal

In the presented study, a humanized nematode line was presented that expresses human Drebrin pan neuronally that could compensate to a certain extent for the loss of endogenous *dbn-1*. Furthermore, Drebrin is regulated by phosphorylation of Serine-647 residue and can render the nematodes more resistant to oxidative stress.

How is Drebrin further regulated? Multiple other phosphorylation sites have been identified or predicted to regulate Drebrin (*e.g.* Serine-142, Threonine-392 *etc.*) that are controlled by kinases and phosphatases of well conserved signalling pathways. Most of them with orthologues in the nematode that enable specific manipulation by depletion or overexpression of those regulatory proteins.

How is Drebrin interacting with the actin cytoskeleton? Drebrin can bind F-actin and bundle single strands to compact fibres, a pivotal mechanism of dendritic spine maturation and plasticity. Yet, the postsynaptic structures in nematode neurons do not exhibit dendritic spines, but patches that cluster proteins of the postsynaptic density. F-actin organization and regulation by Drebrin should be analysed in the nematode to understand, if they are comparable and follow conserved mechanisms for increasing and decreasing synaptic strength and therefore be a suitable tool to analyse synaptic plasticity and memory consolidation in the nematodes.

A model to study the interaction of Drebrin and Amyloid-β

A conjoined analysis of Drebrin and $A\beta_{1-42}$ was carried out in the nematode model system. Yet, Drebrin overexpression could ameliorate $A\beta_{1-42}$ toxicity with pSerine-647 dependent efficacy. A direct interaction between Drebrin and $A\beta_{1-42}$ was observed as foci wise colocalization, but the majority of Drebrin was detected to not interact with $A\beta_{1-42}$ aggregates.
Yet, this study sets a starting point for future analyses of the Drebrin - $A\beta_{1-42}$ interaction to address many more questions.

Most of the questions that arose during the analysis of $A\beta_{1-42}$ alone, as well as Drebrin alone, could be subject for further studies in conjunction with the respective other protein. Yet, most interestingly would be the question, how $A\beta_{1-42}$ expression alters the neuronal proteome and gene expression profile and if certain gain- or loss-of-function alterations could be candidate modifiers of Drebrin regulation.

Material

Chemicals

Standard chemicals were purchased from Carl Roth (Karlsruhe, Germany) and Merck (Darmstadt, Germany).

Chemical	Company
Agar-Agar Kobe 1	Carl Roth, Karlsruhe, Germany
Agarose	Bio+Sell, Nürnberg, Germany
Ampicillin	Carl Roth, Karlsruhe, Germany
APS	Carl Roth, Karlsruhe, Germany
Bacto™ Pepton	BD Biosciences, New Jersey, USA
Benzaldehyde	Alfa Aesar, Heysham, UK
Beta-mercaptoethanol	Carl Roth, Karlsruhe, Germany
Bromphenol blue	Carl Roth, Karlsruhe, Germany
BSA	Carl Roth, Karlsruhe, Germany
Cholesterol	Sigma Aldrich, St. Louis, USA
cOmplete™ Protease inhibitor cocktail	Roche Diagnostics, Mannheim, Germany
Coomassie Brilliant Blue R-250	Carl Roth, Karlsruhe, Germany
DAPI	Carl Roth, Karlsruhe, Germany
Diacetyl	Sigma Aldrich, St. Louis, USA
Digitonin	Sigma Aldrich, St. Louis, USA
DMSO	Carl Roth, Karlsruhe, Germany
dNTP Mix 100 mM	Thermo Fisher Scientific, Waltham, USA
DTT	Carl Roth, Karlsruhe, Germany
Formaldehyde (37%)	Carl Roth, Karlsruhe, Germany
Gold powder 0.3-3 micron / 99.9%	Chempur, Karlsruhe, Germany
IPTG	Thermo Fisher Scientific, Waltham, USA
Isoamyl alcohol	Carl Roth, Karlsruhe, Germany
Kanamycin	Carl Roth, Karlsruhe, Germany
KU-55933 (ATM kinase inhibitor)	Sigma Aldrich, St. Louis, USA
LB agar	Serva, Heidelberg, Germany
LB medium	Carl Roth, Karlsruhe, Germany
Levamisole	AppliChem GmbH, Darmstadt, Germany
Methanol	Fisher Scientific, Schwerte, Germany
Methyl viologen dichloride hydrate (Paraquat)	Sigma Aldrich, St. Louis, USA
Milk powder	Carl Roth, Karlsruhe, Germany
Nuclease free water	Carl Roth, Karlsruhe, Germany

PMSF	Sigma Aldrich, St. Louis, USA
Polyvinylpyrrolidone	Sigma Aldrich, St. Louis, USA
RedSafe™ nucleic acid staining solution	iNtRON Biotechnology, Freiburg, Germany
Rotiphorese® Gel 30 (Acrylamid/Bisacrylamid Mix)	Carl Roth, Karlsruhe, Germany
Sodium azide	Sigma Aldrich, St. Louis, USA
Sodium hypochloride solution	Fisher Scientific, Schwerte, Germany
Spermidine	Sigma Aldrich, St. Louis, USA
Streptomycin	Carl Roth, Karlsruhe, Germany
TEMED	Carl Roth, Karlsruhe, Germany
Tetracycline	Carl Roth, Karlsruhe, Germany
Thioflavin T	Sigma Aldrich, St. Louis, USA
Triton X-100	Carl Roth, Karlsruhe, Germany
Tween 20	Carl Roth, Karlsruhe, Germany
VECTASHIELD® mounting medium with DAPI	Vector Laboratories, Inc., Burlingame, USA

Markers and loading dyes

Product	**Company**
DNA loading dye (6x)	Thermo Fisher Scientific, Waltham, USA
GeneRuler™ 1kb	Thermo Fisher Scientific, Waltham, USA
GeneRuler™ 50bp	Thermo Fisher Scientific, Waltham, USA
PageRuler™ Plus Prestained Protein Ladder	Thermo Fisher Scientific, Waltham, USA

Enzymes

Restriction Enzyme	**Company**
AgeI-HF (+CutSmart buffer)	New England Biolabs, Ipswich, USA
BamHI-HF (+CutSmart buffer)	New England Biolabs, Ipswich, USA
ClaI-HF (+CutSmart buffer)	New England Biolabs, Ipswich, USA
EcoRI-HF (+CutSmart buffer)	New England Biolabs, Ipswich, USA
KpnI-HF (+CutSmart buffer)	New England Biolabs, Ipswich, USA
NheI-HF (+CutSmart buffer)	New England Biolabs, Ipswich, USA
SpeI-HF (+CutSmart buffer)	New England Biolabs, Ipswich, USA
SphI-HF (+CutSmart buffer)	New England Biolabs, Ipswich, USA
XhoI-HF (+CutSmart buffer)	New England Biolabs, Ipswich, USA
XmaI-HF (+CutSmart buffer)	New England Biolabs, Ipswich, USA

Other Enzyme	Company
Collagenase (Type IV)	Sigma-Aldrich, St. Louis, USA
FastAP Alkaline Phosphatase	Thermo Fisher Scientific, Waltham, USA
Phusion Polymerase	Kirstein Lab
Proteinase K	Roche Diagnostics GmbH, Mannheim, Germany
T4 Ligase + buffer	Thermo Fisher Scientific, Waltham, USA

Antibodies

Primary antibodies

Antibody	Origin	Dilution	Source
α-Abeta (4G8)	Mouse	1:1000 (WB), 1:100 (IHC)	BioLegend, San Diego, USA
α-Abeta (6E10)	Mouse	1:1000 (WB), 1:100 (IHC)	BioLegend, San Diego, USA
α-DBN-1	Rabbit	1:1000 (WB)	Klopfenstein Lab
α-Drebrin (M2F6)	Mouse	1:2000 (WB)	Enzo Life Sciences, Farmingdale, USA
α-GFP (B34)	Mouse	1:2000 (WB)	Enzo Life Sciences, Farmingdale, USA
α-alpha-Tubulin	Mouse	1:2500 (WB)	Sigma Aldrich, St. Louis, USA
α-LGG-1	Rabbit	1:1000 (WB)	Kirstein Lab (Pineda Antikörper-Service, Berlin, Germany)
α-SQST-1	Rabbit	1:1000 (WB)	Kirstein Lab (Pineda Antikörper-Service, Berlin, Germany)

Secondary antibodies

Antibody	Origin	Dilution	Source
Goat-Anti-Mouse IR 680	Goat	1:1000 (IHC)	LI-COR, Lincoln, USA
Pierce®-Goat-Anti-Mouse IgG + IgM (H+L) Peroxidase Conjugated	Goat	1:2000 – 1:5000 (WB)	Thermo Fisher Scientific, Waltham, USA
Pierce®-Goat-Anti-Rabbit IgG (H+L) Peroxidase Conjugated	Goat	1:2000 – 1:5000 (WB)	Thermo Fisher Scientific, Waltham, USA

Kits

Product	Name	Company
ECL Detection Kit	Pierce ECL Western Blot Substrate	Thermo Fisher Scientific, Waltham, USA
Gel extraction	Qiaquick	Qiagen, Hilden, Germany
Gibson cloning	Gibson Assembly®	New England Biolabs, Ipswich, USA
Plasmid isolation for cloning and sequencing	NuceloSpin Plasmid Mini	Macherey-Nagel, Düren, Germany
Plasmid isolation for micro injections	ZR Plasmid Miniprep™-Classic	Zymo Research Europe GmbH, Freiburg, Germany
Western blot	Trans-Blot® Turbo™ Mini PVDF Transfer Packs	BioRad, Hercules, USA

Primer

All sequences are given in 5'-end --> 3'-end direction.

Primer for cloning

Primer working concentration stocks were 10 mM; 200 - 400 nM were used for PCRs.

Primer name	Sequence
k_ceDBNProm - f	CTCAAGTCTAGAACGCTGTGAGCACTGGTGAC
k_ceDBNProm - r	CTCAGGATCGATCTGGAACACATACAATATAGGGTTC
k_ClaI-DBN-YFP - f	CTCAAATCGATATGGCCGGCGTCAGCTTC
k_NheI-DBN-YFP - f	CTAAGCTAGCATGGCCGGCGTCAGCTTC
k_DBN-YFP-EcoRI - r	CTCCAGAATTCTTACTTGTACAGCTCGTCCATGC
k_hDrebrin-AgeI--rev	CTCACCGGTATCACCACCCTCGAAGCCCTC
k_SphI-B3.3Pr long - f	CTCAAGGCATGCCGTTTCCGATACCCCCTTATATC
k_ceF25B3.3Prom-NheI - r	CTCAAGGCTAGCCGTCGTCGTCGTCGATGC
Dendra-EcoRI-rev	CTCCAGAATTCCTTACCACACCTGGCTGGG
AgeI-Dendra-for	CTCAAGACCGGTATGAACACCCCGGGAATTAAC
k_hDrebrin-AgeI--rev	CTCACCGGTATCACCACCCTCGAAGCCCTC
k_cdc-42_KpnI	CGAATCGGTACCAAACTTGTCTCCTGATCAGCT
k_cdc-42_SpeI	CGATAGACTAGTTACTGTGACGGCGTAATTGT
k_AgeI/NheI-Abeta - f	cagtcaaccggtcagtcagctagcGATGCAGAATTCCGACATGAC
k_Abeta-XhoI - r	ataagaatctcgagctaCGCTATGACAACACCGCCCACC
k_AgeI/XbaI-wrmScarlet -f	cagtcaaccggtcagtcatctagaATGGTCAGCAAGGGAGAGGC

k_NheI-wrmScarlet - r	ataagaatgctagcCTTGTAGAGCTCGTCCATTCC
k_SphI-rgef1p -f	cagtcagcatgcCAAGACTAATTTTCGATTAACC
k_rgef1p-ClaI/AgeI -r	ataagaatatcgatataagaataccggtCGTCGTCGTCGTCGATGCCGTC
O_SigPep-DA for	gttttgctggcactgttctttatctttctggcaccagcaggtaccGACGCG
O_SigPep-DA rev	CGCGTCggtacctgctggtgccagaaagataaagaacagtgccagcaaaac
k_Fusion SigAb rev	CATGTCGGAATTCTGCATCCGCGTCGGTACCTGCTGG
k_Fusion SigAb for	CCAGCAGGTACCGACGCGGATGCAGAATTCCGACATG
k_ClaI-SigPep for	CTATAGATCGATGCATAAGGTTTTGCTGGCACTGTTC
k_Abeta-AgeI rev	TCATCGACCGGTTTACGCTATGACAACACCGCC
k_AgeI-IRES - f	CCTATGACCGGTTGCTCTCCCTTCACCACTCC
k_IRES-XbaI	GGATACTCTAGAGCCCAACAAGAATAAGGTCTTCATA
k_XmaI-SigPep for	CTAACTCCCGGGATGCATAAGGTTTTGCTG
k_XmaI-IRES rev	TGACTGCCCGGGTGAGCCCAACAAGAATAAGGTC
k_mScarlet_ext - f	GATTAGCTAGCATGAAGACCTTATTCTTGTTGG
k_mScarlet_stop - r	GACTAGAATTCCTACTTGTAGAGCTCGTCCATTCC
k_AgeI-myo-3 - f	GCTGAACCGGTAGTGATTATAGTCTCTGTTTTCGTTAAT
k_myo-3-NheI - r	GATTAGCTAGCCATTTCTAGATGGATCTAGTGGTCG
Gib_f1_myo3p-Sb - r	GCAAAACCTTATGCATCCCGGTCGTCATTTCTAGATGGATCTAGTGGTCGTG
Gib_f1_Sb-myo3p - f	CTTGGAAATGAAATAAGCTTGCATGAGTGATTATAGTCTCTGTTTTCGTTA
Gib_f2_myo3p-Sb - f	CACGACCACTAGATCCATCTAGAAATGACGACCGGGATGCATAAGGTTTTGC
Gib_f2_Sb-myo3p - r	TAACGAAAACAGAGACTATAATCACTCATGCAAGCTTATTTCATTTCCAAG
k_AgeI-myo-3p - f	GCTGAACCGGTAGTGATTATAGTCTCTGTTTTCGTTAAT
k_myo-3p-NheI - r	GATTAGCTAGCCATTTCTAGATGGATCTAGTGGTCG
Gib_SigP-mTrq --f	CTTTCTGGCACCAGCAGGTACCATGGTGAGCAAGGGCGAGGAGC
Gib_mTrq-IRES --r	GTGGTGAGGGAGAGCAACCGGTTACTTGTACAGCTCGTCCATGCCG
Gib_mTrq-IRES --f	CGGCATGGACGAGCTGTACAAGTAACCGGTTGCTCTCCCTCACCAC
Gib_SigP-mTrq --r	GCTCCTCGCCCTTGCTCACCATGGTACCTGCTGGTGCCAGAAAG
k_MetAbeta-AgeI-for	GCATTACCGGTATGGATGCAGAATTCCGACATG
k_MetAbeta-AgeI-rev	GAGCAACCGGTTTACGCTATGAC
o_ProxyStop-in-AgeI-top	CCGGATGGGTGCATAAGCATAAC
o_ProxyStop-in-AgeI-bot	GGCCGTTATGCTTATGCACCCAT
k_Abeta-SphI-rev	GCATTGCATGCGCTATGACAACACCGCC
k_SphI-Abeta-for	GCATTGCATGCGATGCAGAATTCCGACATGAC
k_BamHI-Abeta-for	GCATTGGATCCGCTATGACAACACCGCC
k_Abeta-NheI-rev	GCATTGCTAGCGATGCAGAATTCCGACATG
k_NheI-SL2-for	GCATTGCTAGCGCTGTCTCATCCTACTTTCAC
k_SL2-AgeI-rev	GCATTACCGGTGATGCGTTGAAGCAGTTTC
k_Abeta-KpnI/SphI-f	GGATTGGTACCGCATGCGATGCAGAATTCCGAC

k_SL2-AgeI/KpnI-r	GCATTGGTACCGGTGATGCGTTGAAGCAG
pklp-6f	cagtcagcatgcGTTGGAAAGTTTGGTAAGTTGC
pklp-6r	ataagaatggtaccatGGTATTCTGAAAAGTTCAAC
AbetaSL2f	ataagaataccggtGATGCAGAATTCCGACATGAC
AbetaSL2r	ataagaatctcgagGATGCGTTGAAGCAGTTTCC

Primer for genotyping

Primer name	Sequence	Expected fragments
GT_dbn-1ko 3 f	GCCGCTCAACTACCGTAACT	wt-band: 3315 bp
GT_dbn-1ko 3 r	CAGGAAGTGGGAGAATGGGAG	ko-band: 800 – 1000 bp

Primer for mutagenesis

The modified base pairs are underlined and highlighted in green.

Primer name	Sequence
m_DBN(S647A)_1938 - F	GGTACTTCAGTCAAGCACAGGAGGAGGAG
m_DBN(S647A)_1938 - R	CTCCTCCTCCTGTGCTTGACTGAAGTACC
m_DBN(S647D)_1938-40 - F	GGTACTTCAGTCAAGACCAGGAGGAGGAG
m_DBN(S647D)_1938-40 - R	CTCCTCCTCCTGGTCTTGACTGAAGTACC
m_DBN-wt f	GGTACTTCAGTCAATCACAGGAGGAGGAG
m_DBN-wt r	CTCCTCCTCCTGTGATTGACTGAAGTACC
mut_AgeI-rgef-SigPep - F	GACGACGACGACCGGTATGCATAAGG
mut_AgeI-rgef-SigPep - R	CCTTATGCATACCGGTCGTCGTCGTC

Primer for sequencing

Primer name	Sequence
Seq_Scarlet-1-rev	GGATGTCCCAGGAGAATGG
Seq_Scarlet-2-rev	TCGTGTCCGTTCATGGATC
Seq_DBN - 1 -- r	GCTTGAGGTCATCGGAGCC
Seq_DBN - 2 --f	GAGGCGGTTGAAGGAGCAG

Seq_DBN - 3 -- r	GGGTTGTCAGGCCGCTGG
Seq_DBN - 4 --f	GCCGCCACCAGCCTCATTG
Seq_YFP - 1 --f	GCGCACCATCTTCTTCAAG
Seq_YFP - 2 -- r	CCAGGATGTTGCCGTCCTC
Seq_rgef-1-end-for	CGCATCCGAGAATTGAAAC
Seq_M13R	CAGCTATGACCATGATTACGCC
Seq_GFP-1r	AGTGACAAGTGTTGGCTG
Seq_GFP-2r	CCTTCGGGCATGGCACTC
Seq_wrmScarlett - f (NheI)	GATTAGCTAGCATGGTCAGCAAGGGAGAGG

Oligonucleotides for CRISPR/Cas9

Oligonucleotide name	**Sequence**
o_sgRNA1 - f	tcttgCAACTATCATGCACACGGCA
o_sgRNA1 - r	aaacTGCCGTGTGCATGATAGTTGc
o_sgRNA4 - f	tcttgTAGCGGGAAAAAGGCCTACG
o_sgRNA4 - r	aaacCGTAGGCCTTTTTCCCGCTAc
o_sgRNA5 - f	tcttgGATGGCTCTCTGGGACTACC
o_sgRNA5 - r	aaacGGTAGTCCCAGAGAGCCATCc
o_sgRNA7 - f	tcttgAGGAGATTGAAGCGTCGTAT
o_sgRNA7 - r	aaacATACGACGCTTCAATCTCCTc

Plasmids

Name	**Insert**	**Resistance**	**Origin**
pPD95_77	GFP	Amp	Fire Lab
L4440	2x T7-promoter	Amp	Fire Lab
pCFJ104	*myo-3p*::mCherry	Amp	Jorgensen Lab
pJJR50	sgRNA-empty	Amp	Boxem Lab
pMB67	*hsp-16.48p*::Cas9	Amp	Boxem Lab
IR98	*rps-0p*::hygR CeOpt	Cam	Chin Lab
pEYFP-N1-DBNA(WT)	DBN1A-YFP	Kan/Neo	Eickholt Lab
pSEM87	wrmScarlet–*twk-18*	Amp	Boulin Lab
pEY54	*klp-6p*::mNeptune2.5	Amp	Hobert Lab

pJB253	*tol-1p*::GFP	Amp	Ringstad Lab
pCR-flp-22	*flp-22p*::GFP	Amp	Li Lab
XW08	*unc-4p::*QF::SL2::mCherry	Amp	Shen Lab
pPD_DBN1A(wt)	*rgef-1p*::DBN1A^{wt}-YFP	Amp	this work
pPD_DBN1A(S647A)	*rgef-1p*::DBN1A^{S647A}-YFP	Amp	this work
pPD_DBN1A(S647D)	*rgef-1p*::DBN1A^{S647D}-YFP	Amp	this work
pPD_DBN-Dendra (wt)	*rgef-1p*::DBN1A^{wt}-Dendra2	Amp	this work
pPD_DBN-Dendra (S647A)	*rgef-1p*::DBN1A^{S647A}-Dendra2	Amp	this work
pPD_DBN-Dendra (S647D)	*rgef-1p*::DBN1A^{S647D}-Dendra2	Amp	this work
pJJR_sgRNA1	U6prom::guideSeq-1	Amp	this work
pJJR_sgRNA4	U6prom::guideSeq-4	Amp	this work
pJJR_sgRNA5	U6prom::guideSeq-5	Amp	this work
pJJR_sgRNA7	U6prom::guideSeq-7	Amp	this work
pPD_nScabeta	*rgef-1p*::SigPep-Abeta$_{1-42}$:: *hsp-3*^{IRES}::wrmScarlet-Abeta$_{1-42}$	Amp	this work
pPD_mScabeta	*myo-3p*::SigPep-Abeta$_{1-42}$:: *hsp-3*^{IRES}::wrmScarlet-Abeta$_{1-42}$	Amp	this work
pPD_StopAbeta	*rgef-1p*::ProxyStop::*hsp-3*^{IRES}:: wrmScarlet-Abeta$_{1-42}$	Amp	this work
pPD_nSca-ext	*rgef-1p*::wrmScarlet_ext	Amp	this work
pPD_mSca-ext	*myo-3p*::wrmScarlet_ext	Amp	this work
pPD_nTrq2_Scabeta	*rgef-1p*::SigPep-Trq2:: *hsp-3*^{IRES}::wrmScarlet-Abeta$_{1-42}$	Amp	this work
pPD_shAbeta(URY)	*tol-1p*::shAbeta::SL2::GFP	Amp	this work
pPD_shAbeta(IL2)	*klp-6p*::shAbeta::SL2::scramble	Amp	Kirstein Lab
pPD_klp-6::GFP	*klp-6p::*GFP	Amp	Kirstein Lab
pSUMO-Abeta42	T7prom::SUMO-Abeta	Amp	Kirstein Lab
pPD95-Prgef-1::GFP	*rgef-1p*::GFP	Amp	Kirstein Lab

Equipment

Device	Name	Company
Agarose gel electrophoresis system		Carl Roth, Karlsruhe, Germany
Centrifuge (1,5ml / 2ml)	Heraeus Fresco 17	Thermo Fisher Scientific, Waltham, USA
Centrifuge (15ml / 50ml)	3K12	SIGMA, Osterode am Harz, Germany
Table-top Centrifuge (PCR-tubes)	Ministar	VWR, Radnor, USA
Centrifuge (6x 1L)	Sorvall LYNX 6000, Rotor: F9-6x1000 LEX	Thermo Fisher Scientific, Waltham USA
Centrifuge	5417C, Rotor: F45-30-11 015999	Eppendorf, Hamburg, Germany

Confocal laser scanning microscope	ZEISS LSM-780	Carl Zeiss Microscopy GmbH, Jena, Germany
Confocal laser scanning microscope (for FLIM)	Leica SP5	Leica, Wetzlar, Germany
Confocal laser scanning microscope (for STED)	Leica SP8	Leica, Wetzlar, Germany
Fluorescence lifetime measurement microscopy	PicoHarp 300	PicoQuant, Berlin, Germany
Fluorescence microscope	M165FC	Leica, Wetzlar, Germany
Freezer (-80°C)	KM-DU73Y1E	Panasonic, Kadoma, Japan
Gamma irradiator	OB29	STS, Braunschweig, Germany
GeneGun		FMP work shop facility
Heating block incubator	HLC	Ditabis, Pforzheim, Germany
Homogenizer	Precellys® 24	Bertin instruments, Montigny-le-Bretonneux, France
Incubator (30°C and 37°C)	Heraeus Kelvitron	Thermo Fisher Scientific, Waltham USA
Incubator (15°C)	TC255	Lovibond Tintometer GmbH, Dortmund, Germany
Incubator (20°C)	TC255L	Lovibond Tintometer GmbH, Dortmund, Germany
Magnetic stirrer	RET basic	IKA, Staufen, Germany
Mass spectrometer	NanoLC-Esi-MSMS (Orbitrap Elite)	Thermo Fisher Scientific, Waltham, USA
Nanodrop	NanoVue Plus	GE Healthcare, Buckinghamshire, UK
pH meter		Mettler Toledo, Ohio, USA
Pipettes	Transferpette®	Brand, Wertheim, Germany
Pipettor	Pipetboy	Integra Bioscience, Bibertal, Germany
Plate reader	F200 Pro	Tecan, Männedorf, Switzerland
Power supply	PowerPac HC / Basic	Bio-Rad, Hercules, USA
SDS PAGE system	Mini-PROTEAN cell chambers	Bio-Rad, Hercules, USA
Shaker (4°C)	SM-30 control	Edmund Bühler GmbH, Hechingen, Germany
Shaker/Incubator	Innova 4230	New Brunswick Scientific / Eppendorf, Hamburg, Germany
Shaker/Incubator	Multitron Pro	Infors HT, Bottmingen, Switzerland
Sonication water bath	XUBA	Grant Scientific, Royston, UK
Stereo microscope	M165 FC	Leica, Wetzlar, Germany
Stereo microscope	SMZ 745	Nikon, Tokio, Japan
Thermocycler	Mastercyler Gradient	Eppendorf, Hamburg, Germany
Thermocycler	C1000 Touch	Bio-Rad, Hercules, USA
Tube roller	RS-TR-5	Phoenix Instrument, Garbsen, Germany
Vacuum pump		KNF Lab, New Jersey, USA
Vortex	Vortex-Genie® 2	Scientific Industries, Bohemia, USA

Westernblot detection system	Lumi-Imager F1	Boehringer Mannheim GmbH, Mannheim, Germany
Westernblot system (semi-dry)	Trans-Blot Turbo Transfer System	Bio-Rad, Hercules, USA
Westernblot system (wet)	MiniTrans-Blot® Cell	Bio-Rad, Hercules, USA

Consumables

Product	**Company**
Culture plates (35/60/100 mm)	Sarstedt, Nümbrecht, Germany
Falcon tubes (15 ml and 50 ml)	Sarstedt, Nümbrecht, Germany
Filter tips	Sarstedt, Nümbrecht, Germany
Glass vial / lid	Carl Roth, Karlsruhe, Germany
Glass cover slips (18 x 18 mm)	Carl Roth, Karsruhe, Germany
Glass slides (76 x 26 mm)	Carl Roth, Karsruhe, Germany
Kwik-Fil™ borosilicate glass capillaries	World Precision Instruments, Sarasota, USA
Lysing Kit tubes (0.5 and 2 ml)	Bertin instruments, Montigny-le-Bretonneux, France
MicroAmp ™ Fast optical 96-well reaction plate	Applied Biosystem by life technologies, Foster City, USA
MicroAmp ™ Fast optical adhesive film	Applied Biosystem by life technologies, Foster City, USA
Parafilm	Bemis, Neenah, USA
Pasteur pipettes (glass)	Carl Roth, Karsruhe, Germany
PCR tubes (single)	Sarstedt, Nümbrecht, Germany
PCR tubes (stripes)	Kisker Biotech GmbH & Co. KG, Steinfurt, Germany
Plates (96-well)	Sarstedt, Nümbrecht, Germany
Platinum wire (0.3 mm)	Carl Roth, Karlsruhe, Germany
Reaction tubes (1.5 ml and 2.0 ml)	Sarstedt, Nümbrecht, Germany
Roti®-Fluoro PVDF	Carl Roth, Karlsruhe, Germany
Scalpel	Carl Roth, Karlsruhe, Germany
Serological pipettes	Sarstedt, Nümbrecht, Germany
Table waste bags	Sarstedt, Nümbrecht, Germany
Tips	Sarstedt, Nümbrecht, Germany

C. elegans strains

Strain name	Genotype / description / state of integration		Source
BIJ34	jaaIs4 (hyp7p::sfGFP-LGALS3)	Is	Jäättelä Lab
BZ555	egIs1 (*dat-1p*::GFP)	Is	CGC
CS628	qcIs55 [*vha-7p*::GFP::*sma-3* + *rol-6*(su1006)]	Is	CGC
IG10	*tol-1* (nr2033) I	ko	CGC
JKM1	Δ*dbn-1* (Exon 1 – 6) III (CRISPR/Cas9-total knockout)	ko	this work
JKM2 (nAβ)	*rgef-1p*::SigPep-$A\beta_{1-42}$::*hsp-3*^{IRES}::wrmScarlet-$A\beta_{1-42}$ + *rps-0p*::hygR CeOpt	Is	this work
JKM2-Δ (nAβ-Δ)	[Δ*dbn-1* (Exon 1 – 6) III]; [*rgef-1p*::SigPep-$A\beta_{1-42}$::*hsp-3*^{IRES}::wrmScarlet-$A\beta_{1-42}$ + *rps-0p*::hygR CeOpt]	Is	this work
JKM2-Δ-nDBN (nDBN^{wt})	[Δ*dbn-1* (Exon 1 – 6) III]; [*rgef-1p*::SigPep-$A\beta_{1-42}$::*hsp-3*^{IRES}::wrmScarlet-$A\beta_{1-42}$ + *rps-0p*::hygR CeOpt]; [*rgef-1p*::hDBN1A^{wt}-Dendra2]	Is	this work
JKM2-Δ-nDBN^{S647A} (nDBN^{S647A})	[Δ*dbn-1* (Exon 1 – 6) III]; [*rgef-1p*::SigPep-$A\beta_{1-42}$::*hsp-3*^{IRES}::wrmScarlet-$A\beta_{1-42}$ + *rps-0p*::hygR CeOpt]; [*rgef-1p*::hDBN1A^{S647A}-Dendra2]	Is	this work
JKM2-Δ-nDBN^{S647D} (nDBN^{S647D})	[Δ*dbn-1* (Exon 1 – 6) III]; [*rgef-1p*::SigPep-$A\beta_{1-42}$::*hsp-3*^{IRES}::wrmScarlet-$A\beta_{1-42}$ + *rps-0p*::hygR CeOpt]; [*rgef-1p*::hDBN1A^{S647D}-Dendra2]	Is	this work
JKM2-BIJ34	[*rgef-1p*::SigPep-$A\beta_{1-42}$::*hsp-3*^{IRES}::wrmScarlet-$A\beta_{1-42}$ + *rps-0p*::hygR CeOpt]; jaaIs4 [hyp7p::GFP-LGALS3]	Is	this work
JKM2-CS628	[*rgef-1p*::SigPep-$A\beta_{1-42}$::*hsp-3*^{IRES}::wrmScarlet-$A\beta_{1-42}$ + *rps-0p*::hygR CeOpt]; qcIs55 [*vha-7p*::GFP::*sma-3* + *rol-6*(su1006)]	Is	this work
JKM2-JKM10	[*rgef-1p*::SigPep-$A\beta_{1-42}$::*hsp-3*^{IRES}::wrmScarlet-$A\beta_{1-42}$ + *rps-0p*::hygR CeOpt]^{het}; [*tol-1p*::GFP]^{het}	Is-het	this work
JKM2-LX929	[*rgef-1p*::SigPep-$A\beta_{1-42}$::*hsp-3*^{IRES}::wrmScarlet-$A\beta_{1-42}$ + *rps-0p*::hygR CeOpt]; vsIs48 [*unc-17p*::GFP]	Is	this work
JKM2-OH10972	[*rgef-1p*::SigPep-$A\beta_{1-42}$::*hsp-3*^{IRES}::wrmScarlet-$A\beta^{1-42}$ + *rps-0p*::hygR CeOpt]; otIs376 [*eat-4*(prom4)::GFP + *rol-6*(su1006)]	Is	this work
JKM2-shAbeta(IL2)	[*rgef-1p*::SigPep-$A\beta_{1-42}$::*hsp-3*^{IRES}::wrmScarlet-$A\beta^{1-42}$ + *rps-0p*::hygR CeOpt]; [*klp-6p*::shAbeta::SL2::Scramble + *myo-2p*::GFP]^{ex}	Is/Ex	this work
JKM2-shAbeta(URY)	[*rgef-1p*::SigPep-$A\beta_{1-42}$::*hsp-3*^{IRES}::wrmScarlet-$A\beta^{1-42}$ + *rps-0p*::hygR CeOpt]; [*tol-1p*::shAbeta::SL2::GFP]^{ex}	Is/Ex	this work
JKM2-ZIM1048	[*rgef-1p*::SigPep-$A\beta_{1-42}$::*hsp-3*^{IRES}::wrmScarlet-$A\beta^{1-42}$ + *rps-0p*::hygR CeOpt]; mzmIs4 (*unc-31p*::NLS-GCaMP5Kf + *unc-122p*::GFP); *lite-1* (*ce314*) X	Is	this work
JKM3	*rgef-1p*::wrmScarlet_ext + *rps-0p*::hygR CeOpt	Is	this work
JKM3-CS628	[*rgef-1p*::wrmScarlet_ext + *rps-0p*::hygR CeOpt]; qcIs55 [*vha-7p*::GFP::*sma-3* + *rol-6*(su1006)]	Is	this work

JKM3-ZIM1048	[*rgef-1p*::wrmScarlet_Ext + *rps-0p*::hygR CeOpt]; mzmIs4 (*unc-31p*::NLS-GCaMP5Kf + *unc-122p*::GFP); *lite-1* (*ce314*) X	Is	this work
JKM5	*rgef-1p*::ProxyStop::*hsp-3*^{IRES}::wrmScarlet-Aβ$_{1-42}$ + *rps-0p*::hygR CeOpt	Ex	this work
JKM6	*rgef-1p*::SigPep-mTurquois2::*hsp-3*^{IRES}::wrmScarlet-Aβ$_{1-42}$ + *rps-0p*::hygR CeOpt	Ex	this work
JKM7 (mAβ)	*myo-3p*::SigPep-Aβ$_{1-42}$::*hsp-3*^{IRES}::wrmScarlet-Aβ$_{1-42}$ + *rps-0p*::hygR CeOpt	Is	this work
JKM7-CS628	[*myo-3p*::SigPep-Aβ$_{1-42}$::*hsp-3*^{IRES}::wrmScarlet-Aβ$_{1-42}$ + *rps-0p*::hygR CeOpt]; qcIs55 [*vha-7p*::GFP::*sma-3* + *rol-6*(su1006)]	Is	this work
JKM7-jaaIs4	[*myo-3p*::SigPep-Aβ$_{1-42}$::*hsp-3*^{IRES}::wrmScarlet-Aβ$^{1-42}$ + *rps-0p*::hygR CeOpt]; jaaIs4 [hyp7p::GFP-LGALS3]	Is	this work
JKM8	*myo-3p*::wrmScarlet_ext + *rps-0p*::hygR CeOpt	Ex	this work
JKM8-CS628	[*myo-3p*::wrmScarlet_ext + *rps-0p*::hygR CeOpt]^{ex}; qcIs55 [*vha-7p*::GFP::*sma-3* + *rol-6*(su1006)]	Ex/Is	this work
JKM10	*tol-1p*::GFP	Is	this work
LX929	vsIs48 [*unc-17p*::GFP]	Is	CGC
N2	wild type (*C. elegans* var Bristol)	--	CGC
nDBN^{S647A}	*ok925*; *rgef-1p*::hDBN1A^{S647A}-YFP + *myo-2p*::RFP	Is	this work
nDBN^{S647A}-Dendra	Δ*dbn-1* (Exon 1 – 6) III; *rgef-1p*::hDBN1A^{S647A}-Dendra2	Is	this work
nDBN^{S647D}	*ok925*; *rgef-1p*::hDBN1A^{S647D}-YFP + *myo-2p*::RFP	Is	this work
nDBN^{S647D}-Dendra	Δ*dbn-1* (Exon 1 – 6) III; *rgef-1p*::hDBN1A^{S647D}-Dendra2	Is	this work
nDBN^{wt}	Δ*dbn-1* (Exon 1 – 6) III; *rgef-1p*::hDBN1A^{wt}-YFP	Is	this work
nDBN^{wt}-Dendra	Δ*dbn-1* (Exon 1 – 6) III; *rgef-1p*::hDBN1A^{wt}-Dendra2	Is	this work
OH10972	otIs376 [*eat-4*(prom4)::GFP + *rol-6*(su1006)]	Is	CGC
RB1004	*ok925* (Δ*dbn-1* Exon 5 – Exon 6)	ko	CGC
shAbeta(IL2)	*klp-6p*::shAbeta::SL2::Scramble + *myo-2p*::GFP	Ex	Kirstein Lab
shAbeta(URY)	*tol-1p*::shAbeta::SL2::GFP	Ex	this work
ZIM1048	mzmIs4 (*unc-31p*::NLS-GCaMP5Kf + *unc-122p*::GFP); *lite-1* (ce314) X	Is	Zimmer Lab

Bacterial strains and RNAi clones

Baterial strain – application	Genotype
E. coli DH5αZ1 – cloning	laci^{q}, PN25-tet^{R}, Sp^{R}, deo^{R}, supE44, Delta(lacZYA-argFv169), Phi80 lacZDeltaM15, hsdR17(rK- mK+), recA1, endA1, gyrA96, thi-1, relA1
E. coli HT115(DE3) – RNAi	F-, mcrA, mcrB, IN(rrnD-rrnE)1, rnc14::Tn10(DE3) lysogen: lavUV5 promoter -T6 polymerase
E. coli OP50 – food source	uracil auxotroph
S. marcescens Db11 – Pathogen Avoidance Assay	Kan^{R}, Tet^{R}, Strep^{R}
S. marcescens Db1140 – Pathogen Avoidance Assay	Kan^{R}, Tet^{R}, Strep^{R}, Protease 1 deficient, phage ΦJ^{R}

HT115 RNAi clones	Source
L4440–*dbn-1*	Ahringer Library
L4440–empty	Fire Lab

Software and online tools

Software	Name	Source
Confocal Microscopy	Zen 2010B SP1 v6.0	Zeiss, Oberkochen, Germany
Data analysis	Prism 8 for macOS	GraphPad Software Inc.
Documents	Word 2016	Microsoft
Figure composition	Adobe Illustrator	Adobe Systems Inc.
FLIM image analysis	FLIMfit (v4.12 and v5.1.1)	Warren et al.[300]
FLIM / STED Microscopy (microscopy setup)	Leica Application Suite Advanced Fluorescence 2.7.3.9723	Leica Microsystems CMS GmbH, Mannheim, Germany
FLIM Microscopy (TCSPC)	SymPhoTime 64	PicoQuant, Berlin, Germany
Image adjustment	Adobe Photoshop	Adobe Systems Inc.
Image analysis	Fiji v2.0	Schindelin et al.[301]
Image colocalization analysis	Fiji-plugin: EzColocalization	Stauffer et al.[302]
Nematode swimming analysis	Fiji-plugin: WrmTrck	Pedersen et al.[303]
Presentations	Keynote 9.1	Apple Inc.
Primer design	Primer3 v3	Untergasser et al.
Primer specificity	PrimerBLAST	NCBI, Bethesda, USA
sgRNA design	crispr.mit.edu	Zhang Lab
Spreadsheets	Excel 2016	Microsoft
Western blot detection	LumiAnalyst 3.0	Boehringer Mannheim

Methods

Molecular biological and biochemical methods

Polymerase chain reaction

For sequence specific amplification of DNA, polymerase chain reactions (PCR) were employed. In brief, a thermostable, engineered DNA polymerase amplifies a defined stretch of DNA in cycles, while the amplicon size is delimited by the binding of two primers defining the 5'- and 3'-end. Primers were designed to bind specifically to the gene of interest (GOI) and melting temperatures were arranged to be between 58°C and 67°C. For genomic DNA templates Primer3 was used to find specific primers (excluding off-targets in *C. elegans* and *E. coli*). All reactions were performed with Phusion polymerase. The reactions consisted of an initial denaturation step of 98°C for 3 min, followed by 30 to 36 cycles of denaturation (at 95-98°C for 30-45 sec), annealing (calculated annealing temperature of the primer pair for 30-45 sec) and elongation (at 72°C for 30 sec per kilo base for sequences up to 3 kb, additional 30 sec per kb after 3rd kb for templates longer than 3 kb). After cycling, a final elongation step is performed for 5 min per kb up to 30 min at 72°C.

To increase specific primer binding, a touch-down approach was employed. In brief, the annealing step temperature is gradually decreased every reaction cycle by 0.5 to 1 K, starting from a higher melting temperature to reach the calculated temperature by the 10th to 12th cycle. Afterwards, 20 to 24 reaction cycles are done with the calculated annealing temperature.

To increase specificity and yield of difficult-to-amplify sequences, nested PCR was employed. An additional primer pair was designed binding approx. 150 – 300 base pairs up- and downstream of the GOI. A second PCR amplifying the actual GOI is performed using the amplificate from the preceding PCR as template.

For restriction cloning, recognition sites of Type II restriction enzymes were added at the primers 5'-ends plus five to six random bases.

For Gibson Assembly, primers were designed to be complementary to the two sequences to ligate, therefore the designed primer's 5'ends are homologous to the 3'end of the respective upstream fragment.

For fusion PCR, two primer pairs are designed: two outer primers on different genes and two homologous primers, which are complementary to each other and bind on both genes to fuse on their respective 3'- and 5'-end. In total three PCRs are performed: two to amplify the two GOIs using their respective outer and homology primer. Following, the amplificates from the two preceding PCRs are used as templates and the outer primers are used to amplify and fuse the two GOIs.

Single worm PCR

For genotyping or to get fragments from the nematodes' genomic DNA a single worm PCR was performed. The PCR itself is performed as described before but 10 µl of proteinase K (ProtK) digested nematodes are used as template.

One to ten nematodes (best results with day 4 – day 6 old, gravid adults) are picked into 10 µl of ProtK lysis buffer and digested for 90 min at 65°C. ProtK enzymes are inactivated at 95°C for 30 min. The ProtK digested material can be stored at 4°C for up to a week.

For the PCR the 10 µl are topped-up with 15 µl Mastermix containing Phusion, Primers, dNTPs and additives in 1x PCR-Buffer I.

Mutagenesis

Mutagenesis is used to introduce defined point mutations in plasmid DNA. In brief, forward and reverse primers are designed to bind the sequence to mutate. The mutation is caused by mismatched bases. The mismatched bases are in the middle of the primers and the homologous flanking regions are at least 10 bp long.

The reaction is performed as following: Initial denaturation at 98°C. 18 cycles of denaturation (98°C for 45 sec), primer annealing (at 55°C for 1 min) and elongation (at 68°C for 1 min per kilo base). Final elongation at 68°C for 20 min.

After the PCR reaction is completed 20 U DpnI per 25 µl reaction volume are added and template vector is cleaved for 3 h at 37°C. DpnI enzymes are inactivated at 80°C for 30 min. 10 – 20 µl of the reaction are directly used to transform DH5α bacteria (see transformation). Finally, the mutation is verified by sequencing.

The plasmids pPD_DBN1A(S647A) and pPD_DBN1A(S647D) have been generated by mutagenesis from pPD_DBN1A(wt) employing the listed mutagenesis primers. Further, the plasmids pPD_DBN-Dendra(S647D) and pPD_DBN-Dendra(wt) have been generated by mutagenesis from pPD_DBN-Dendra(S647A).

The plasmid pPD_nScabeta was used as template for mutagenesis to restore the AgeI restriction site upstream of the signal peptide sequence, generating pPD_nScabeta(AgeI).

Molecular cloning

The backbone for all nematode expression plasmids was pPD95_77. All restriction reactions were performed with 10 U High Fidelity® enzymes in 1x CutSmart® buffer (NEB). The reaction volume was 20 µl. 800 ng - 1.2 µg DNA were cleaved for 30 - 45 min at 37°C (if any enzyme required a different temperature, temperature was selected following the manufacturer's instructions). Vector backbones were treated with 1 U FastAP (Thermo Scientific) simultaneously. The reactions were stopped by heat inactivating the enzymes at 65°C - 80°C for 15 min. Products were purified using a spin column only, or if necessary using extraction from an agarose gel (QIAquick Gel Extraction Kit, Qiagen).

Ligation reactions were performed in 10 µl reaction volume using 5 U T4 DNA Ligase (Thermo Scientific). 50 ng vector backbone and 20 – 100 ng insert were ligated for 2 h at RT. If colony yield was low, ligation was repeated at 16°C over night. 5 – 10 µl of the reaction volume were used for transformation of DH5α.

Drebrin-YFP containing plasmids. GFP was removed from pPD95_77 by SphI + EcoRI cleavage. Promoter region of *rgef-1* was amplified by PCR including SphI and NheI recognition sites (k_SphI-B3.3Pr long – f + k_ceF25B3.3Prom-NheI – r). DBN-YFP was amplified by PCR with NheI and EcoRI sites (k_NheI-DBN-YFP – f + k_DBN-YFP-EcoRI – r). Both fragments were simultaneously inserted to obtain pPD_DBN1A(wt).

Drebrin-Dendra containing plasmids. GFP was excised from pPD95 by AgeI + EcoRI treatment. Dendra2 was amplified by PCR from YD3 nematodes (Dendra-EcoRI-rev + AgeI-Dendra-for) and inserted to obtain pPD95_Dendra2. DBN1A(S647A) was amplified by PCR (k_NheI-DBN-YFP - f + k_hDrebrin-AgeI--rev) and inserted upstream of Dendra2 by using NheI + AgeI to obtain pPD95_DBN1A(S647A)-Dendra2. The promoter region of *rgef-1* was amplified (k_SphI-B3.3Pr long – f + k_ceF25B3.3Prom-NheI – r) and sub-cloned by using SphI + NheI to obtain pPD95_rgef-1p::DBN1A(S647A)-Dendra2 (listed as pPD_DBN-Dendra(S647A)).

guideRNA containing plasmids. The backbone pJJR50 was used. pJJR50 was cleaved with BbsI-HF. Forward and reverse oligonucleotides (see Oligonucleotides for CRISPR/Cas9) were annealed according to the Zhang Labs recommendations [304] and ligated into the cleaved pJJR50 vector to obtain the plasmids pJJR_sgRNA1/4/5/7.

Bicistronic operon for sub-stoichiometric expression of mScarlet-Aβ$_{1-42}$ and Aβ$_{1-42}$. Aβ$_{1-42}$ was amplified from pSUMO-Abeta42 (k_AgeI/NheI-Abeta - f + k_Abeta-XhoI - r) and replaced GFP in pPD95_77 (AgeI and XhoI). wrmScarlet, was amplified from pSEM87 (k_AgeI/XbaI-wrmScarlet -f + k_NheI-wrmScarlet -r) and inserted upstream of Aβ$_{1-42}$ (AgeI and NheI). The promoter sequence of *rgef-1* was amplified from pPD95_DBN1A(wt) (k_SphI-rgef1p -f + k_rgef1p-ClaI/AgeI -r) and inserted upstream of wrmScarlet (SphI and AgeI). Signalpeptide- Aβ$_{1-42}$ (SigPep-Abeta) was created by Fusion-PCR using a synthetic 50mer (O_SigPep-DA for + O_SigPep-DA rev) as first PCR template and k_ClaI-SigPep for plus k_Fusion SigAb rev as primers; second PCR template was pSUMO-Abeta42 and k_Fusion SigAb for plus k_Abeta-AgeI rev as primers. The subsequent Fusion-PCR was carried out with the products of the first and second PCR as templates (k_ClaI-SigPep for + k_Abeta-AgeI rev). Insertion between *rgef-1p* and wrmScarlet (ClaI and AgeI) resulted in a loss of 400 bp promoter sequence. The *hsp-3* IRES element was amplified from genomic DNA (k_AgeI-IRES – f + k_IRES-XbaI) and inserted between SigPep-Aβ$_{1-42}$ and wrmScarlet-Aβ$_{1-42}$ (AgeI and XbaI). The Signalpeptide-Aβ$_{1-42}$-IRES sequence was amplified (k_XmaI-SigPep for + k_XmaI-IRES rev) and inserted (XmaI and AgeI) into the intermediate plasmid pPD_rgef-1p::wrmScarlet-Aβ$_{1-42}$ to obtain the final pPD_nScabeta plasmid (*rgef-1p*::SigPep-Aβ$_{1-42}$::*hsp-3*^{IRES}::wrmScarlet- Aβ$_{1-42}$).

Control construct for neuronal expression of wrmScarlet. pPD95_77 was cleaved with SphI and EcoRI to remove GFP. The promoter sequence of *rgef-1* was amplified (k_SphI-rgef1p -f + k_rgef1p-ClaI/AgeI

-r) and cleaved with SphI + NheI. wrmScarlet_ext was amplified (k_mScarlet_ext - f + k_mScarlet_stop – r) and cleaved with NheI and EcoRI. All three fragments were ligated in one reaction to obtain pPD_nSca-ext

Bicistronic operon for body wall muscle expression. Because of the limitations of available restriction sites a restriction enzyme independent method was used: Gibson Assembly (NEB). The promoter sequence of *myo-3* was amplified from pCFJ104 with homologous overlaps to 'Scabeta' (Gib_f1_myo3p-Sb - r + Gib_f1_Sb-myo3p - f). The plasmid pPD_nScabeta was amplified by PCR to remove *rgef-1p* and to insert overlaps homologous to *myo-3p* (Gib_f2_myo3p-Sb – f + Gib_f2_Sb-myo3p - r). The Gibson Assembly was performed following the manufacturer's instructions. In brief, 2 µl of the unpurified PCR products were mixed, 6 µl water was added as well as 10 µl Gibson-Mastermix. The reaction was performed for 60 min at 50°C. 4 µl of the reaction mix were used to transform NEB5α cells provided with the Gibson Assembly kit.

Control construct for muscle expression of wrmScarlet. The promoter region of *myo-3* was amplified (k_AgeI-myo-3 – f + k_myo-3-NheI – r) and inserted into pPD_nSca-ext to replace *rgef-1p* using AgeI and NheI.

Signalpeptide-mTurqouis2 + wrmScarlet- Aβ$_{1-42}$. Because of the limitations of available restriction sites a restriction enzyme independent method was used: Gibson Assembly (NEB). Trq2 was amplified from pN1-Trq2 (Gib_SigP-mTrq --f + Gib_mTrq-IRES --r). pPD_nScabeta was amplified removing the first Aβ$_{1-42}$ and introducing homology arms (Gib_mTrq-IRES --f + Gib_SigP-mTrq --r). Gibson Assembly was performed following the manufacturer's instructions.

Proxystop construct for expression of wrmScarlet-Aβ$_{1-42}$ only. SigPep-Aβ$_{1-42}$ was removed from pPD_nScabeta(AgeI) using AgeI. 100 pmol of two oligonucleotides (o_ProxyStop-in-AgeI-top + o_ProxyStop-in-AgeI-bot) were phosphorylated using 5 U T4-polynucleotide kinase and gradually annealed, starting with an initial denaturation for 5 min at 95°C followed by subsequent lowering of the temperature over 15 min to 25°C. The annealed oligonucleotide was ligated into the AgeI site of pPD_nScabeta(AgeI), replacing SigPep-Aβ$_{1-42}$ and giving pPD_StopAbeta.

Short-hairpin construct against Aβ$_{1-42}$ in URY neurons. Aβ$_{1-42}$ was amplified (k_Abeta-SphI-rev + k_SphI-Abeta-for) and inserted into pPD95_77 using SphI to obtain pPD_AbetaFOR. By sequencing a plasmid containing forward Aβ$_{1-42}$ was selected for further cloning. Two fragments were cloned, reversed Aβ$_{1-42}$

(k_BamHI-Abeta-for + k_Abeta-NheI-rev) and the splice leader 2 sequence from *gdp-2* (k_NheI-SL2-for + k_SL2-AgeI-rev). These fragments were cleaved (BamHI, NheI and AgeI) and inserted into pPD_AbetaFOR using BamHI and AgeI restriction sites to obtain pPD_AbetaFOR-REV::SL2. The obtained AbetaFOR-REV::SL2 sequence was amplified (k_Abeta-KpnI/SphI-f + k_SL2-AgeI/KpnI-r) and inserted into KpnI site of pPD_tol-1p::GFP to obtain pPD_shAbeta(URY).

Agarose gel electrophorese

To check the size of DNA fragments agarose gel electrophoresis was employed. 0.7 – 2.0 % (w/v) agarose were solved in 1x TAE buffer and boiled, 1x SafeRed™ was added and a gel was cast in a horizontal chamber. After solidifying, 5 – 10 µl DNA samples were mixed with loading dye (to 1x final concentration) and loaded onto the gel. Electrophoresis was performed for 30 - 60 min at 85 - 100 V. DNA was visualized using a G:Box Syngene System.

Transformation

For DNA synthesis *E. coli* strain DH5α was used, for RNAi by feeding *E. coli* strain HT115 was used. A fresh aliquot of chemo competent bacteria was thawed on ice and DNA was added (maximum 10% (v/v)). After 25 min incubation on ice bacteria were heat shocked for 45 s at 42°C (HT115 bacteria were heat shocked at 37°C). After heat shock they were put on ice for 2 min immediately. 1 ml LB-medium (without antibiotics) was added and bacteria were incubated for 1 h at 37°C, shaking at 450 rpm. Afterwards, bacteria were pelleted and pellet was resuspended in 100 µl LB-medium. 50 µl resuspended bacteria were plated on LB-agar plates (containing appropriate antibiotics).

Nematode lysis

Nematodes were grown under desired conditions to the desired age and harvested by rinsing the plates with M9 medium and collecting the nematodes in solution into 15 ml tubes. Nematodes were allowed to settle by gravity and supernatant was removed. Nematodes were washed three times this way. Afterwards, the nematodes were washed with HMK-buffer once and pelleted again. The pellet was resuspended in 100 - 500 µl HMK-buffer + inhibitors and transferred to lysis tubes with ceramic beads

(Precellys® Lysing Kit). Lysis was performed in a homogenizer (Precellys®24) using the following program: (1) homogenize for 30 sec at 6000 rpm, (2) 10 sec break, (3) homogenize for 30 sec at 6000 rpm, (4) remove from homogenizer and cool on ice for 60 sec, (5) homogenize for 30 sec at 6000 rpm, (6) 10 sec break and (7) homogenize for 30 sec at 6000 rpm.

The homogenate was transferred to low binding tubes and centrifuged for 15 min at 4°C and 12000 rpm. The supernatant was transferred to fresh low binding tubes and used for further experiments.

Bradford-Assay

To quantify the protein concentration of nematode lysates, Bradford-Assay was employed. In brief, Bradford reagent (Roti-Quant) was prepared following the manufacturer's instructions and 200 µl were filled in wells of a clear 96-well plate. A calibration curve was prepared from BSA (covering a range from 0 to 10 mg/ml). For each sample, 1 µl was pipetted into the prepared reagent employing triplicates. After mixing, samples were incubated for 5 min at RT. Afterwards, absorption was measured at 595 nm in a plate reader (Tecan). Protein concentration was calculated using the calibration curve.

Immunoprecipitation

To precipitate proteins of interest (POI) and interacting proteins, immunoprecipitation was performed. 25 µl Protein A/G coated, magnetic beads (Pierce) were resuspended with 125 µl 1x TBST. A magnetic rack was employed to pellet the beads and the supernatant was removed. 1 ml TBST was added to wash and pellet the beads twice. 10 µl monoclonal antibody (anti-GFP or anti-Aβ) + 1 ml TBST were added to the beads. The bead and antibody solution was rotated (20 rpm) for 2 h at 4°C. After bead-antibody-binding, the beads were washed with TBST once, followed by two washing steps with 1 ml HMK-buffer.

500 µl nematode lysate of the strains JKM2 or JKM7 was used to identify proteome alterations upon $A\beta_{1-42}$ overexpression. As control lysates of JKM3 or JKM8 were employed. These experiments have been conducted as biological triplicates.

To analyse alterations upon overexpression of DBN1A-YFP nematode strain nDBN was used for the co-IP experiment. 500 µl of nDBN lysate were used.

The lysates were mixed with the antibody-coated beads (anti-Aβ for JKM2, JKM3, JKM7 and JKM8; and anti-DBN1 for nDBN) and rotated (20 rpm) for 3 h at 4°C. After binding, the beads were washed three times with TBST and the supernatant was removed completely. The beads were resuspended in 2x SDS sample buffer and proteins were eluted by boiling for 10 min at 95°C.

Following this, the samples were incubated with 15 mM chloroacetamide for 30 min at 55°C as preparation for mass spectrometry. For simple analysis by SDS-PAGE, samples were not further treated.

For western blotting to identify Aβ and wrmScarlet-Aβ , nematodes were lysed in RIPA buffer and anti-GFP antibody was used for detection.

SDS-polyacrylamide gel electrophoresis

SDS-polyacrylamide gels were cast in a commercial system (BioRad) in two succeeding steps, first a separation gel was cast (12.5 % acrylamide or gradient of 5 to 20 % acrylamide following the method of Tal Lorberbaum, Columbia University) and overlaid with isopropanol. After solidifying the isopropanol was removed and the stacking gel was cast. Recipe for two 0.75 mm gels or one 1.5 mm gel:

***Table 4.1**: SDS-PAGE recipe*

Components	**Separation gel (12.5%)**	**Stacking gel (4%)**
Rotiphorese® Gel 30 (37.4:1)	3.33 ml	1.5 ml
Separation gel buffer	2 ml	--
Stacking gel buffer	--	2.5 ml
H_2O	2.67 ml	6 ml
APS	80 µl	100 µl
TEMED	8 µl	10 µl

Samples were mixed in 1:1 ratio with 2x SDS sample loading buffer and denatured for 10 min at 95°C. The cast gel was placed in a vertical electrophoresis chamber (Mini-Protean Tetra) and running buffer was added to cathode and anode reservoirs. Samples were loaded and gel run was performed at a constant current of 25-35 mA per gel.

Afterwards, the gel was stained using Coomassie staining solution for 30 min at RT. Coomassie was removed and gel washed with water. Destaining was conducted with destaining buffer until protein

bands were clearly visible and background was transparent. For all staining and destaining steps, the added volume of solution was chosen so that the gel was able to float in liquid.

Western blot

To identify proteins and analyse their abundance semi quantitatively, western blots were employed. For small proteins (< 65 kDa) a semi dry blot approach (Trans-Blot® Turbo™) was employed preferably, for larger proteins (> 65 kDa) a wet blot system (Mini Trans-Blot® Cell) was employed.

In brief, an SDS-PAGE was performed and the gel was equilibrated in transfer buffer for 5 min. A PVDF-membrane was activated in methanol for 1 min and also equilibrated in transfer buffer. Whatman® paper were soaked with transfer buffer and a Whatman-gel-membrane-Whatman sandwich was assembled together with the wet blot systems components (two meshes and a cassette). Blotting was performed at 90 V for 90 min cooled by ice or overnight at 4°C using 45 V. For blotting $A\beta_{1-42}$ transfer was limited to 60 min.

After blotting, the membrane was blocked for 60 min at RT in 5% (w/v) milk powder TBST. For detection of endogenous DBN-1, 10% (w/v) milk powder TBST was used instead. For detection of $A\beta_{1-42}$ 4% (w/v) BSA was used instead. Blocking solution was removed and primary antibody (dilution is indicated in 'Material' section) was added in 3% (w/v) milk powder TBST or 1x Roti Block (anti-Aβ antibody) for incubation over night at 4°C.

The membrane was washed four times with TBST for 10 min. Afterwards, secondary antibody (dilution as indicated) was added in 3% (w/v) milk powder TBST or 1x Roti Block (anti-Aβ antibody) for 60 min incubation at RT. The membrane was washed three times with TBST for 10 min and once with TBS for 15 min. Imaging was performed using ECL-reagent (Pierce) according to the manufacturer's instructions and a Lumi-Imager to measure chemiluminescence.

AMC-Assay / Proteasome activity assay

To measure the chymotrypsin-like activity of proteasomes in nematode lysate, an AMC-Assay was performed as previously described [305,306]. In brief, nematodes of defined age (days 3, 4, 6 and 8 old) were lysed and protein concentration of the cleared lysates was determined by Bradford assay. 25 µg

of total protein was incubated with 100 µM Suc-LLVY-AMC substrate (Enzo) in a clear 96-well plate. As inhibition control, one sample was pre-incubated with 50 µM MG-132 (Sigma), a potent proteasome inhibitor, for 30 min on ice. Fluorescence was measured in a plate reader (Tecan Safire) at 380 nm excitation and 460 nm emission every two minutes for 30 min at 25°C. Lysates were prepared as biological triplicates, measurements were performed using technical duplicates.

For analysis, the slope of the linear component of the curve was used to calculate relative activities.

Plasmid DNA preparation

Plasmid DNA was isolated from DH5α bacteria growing in their exponential phase using the kits 'NucleoSpin MiniPrep' (Machery-Nagel) for molecular cloning and sequencing, or using 'ZR Plasmid Miniprep' (Zymo) for microinjection. Preparation was performed following the manufacturer's instructions. In brief, plasmid containing bacteria were cultured in LB-medium containing appropriate antibiotics at 37°C and 165 rpm shaking for 15 - 18 h. Bacteria were pelleted by centrifugation for 3 min at 15000 g. Resuspension, lysis and extraction of DNA over a silica column was performed following manufacturer's instructions. Finally, DNA was eluted in ddH_2O and concentration was measured using a nanodrop reader (NanoVue Plus).

Gel extraction

To retrieve DNA fragments of a desired size after restriction digestion, DNA was used for agarose gel electrophoresis. Bands were checked using 354 nm UV light (low power settings) and exposure time was minimized to a few seconds. Bands were cut out using a scalpel and collected in tubes.

Extraction was performed using 'QIAquick Gel Extraction Kit' (Qiagen). In brief, Agarose blocks were resolved using 3x volume of chaotropic buffer, incubating for 15 - 30 min at 50°C, inverting every 5 min. After lysis, 1x volume isopropanol was added and the DNA agarose solution was cast over a silica column (following the manufacturer's instructions) and column was washed with 500 µl wash buffer. Final elution was carried out in 15 - 30 µl ddH_2O and concentration was determined using a nanodrop reader (NanoVue Plus).

Bacterial culture

OP50 food source

400 ml sterile LB-medium was inoculated with 10 µl *E. coli* OP50 from a frozen glycerol stock and grown over night at 37°C and 165 rpm shaking. Afterwards, the bacteria solution was aliquoted in 40 ml aliquots and stored at 4°C. Few drops of OP50 (about 2 cm^2) were plated on NGM-plates as food source of *C. elegans* and incubated at RT (seeded plates remained stable for up to two weeks).

DH5α for plasmid extraction

5 ml sterile LB-medium was mixed with the appropriate antibiotics and inoculated with plasmid bearing bacteria (by picking a single colony from a plate or by using 5 µl from a frozen glycerol stock). The bacteria were incubated for 12 – 16 h at 37°C shaking at 165 rpm.

Serratia marcescens for pathogen avoidance assay

Serratia marcescens bacteria were kept on LB-agar plates for up to three weeks at 4°C. To start a culture a fresh LB-agar plate was supplemented with Kanamycin, Tetracycline and Streptomycin and bacteria were streaked out from the old storage plate. The fresh plate was allowed to grow for 36 h at RT. Multiple colonies were used to inoculate 15 ml LB-medium supplemented with 50 µg/ml Kanamycin, 7.5 µg/ml Tetracycline and 25 µg/ml Streptomycin and incubated for 12 – 16 h at 25°C, shaking at 165 rpm.

HT115 bacteria for RNAi

5 – 10 ml LB-medium was supplemented with 100 µg/ml Ampicillin and 15 µg/ml Tetracycline and inoculated with 5 µl HT115 bacteria containing L4440-plasmid for RNAi from a frozen glycerol stock. Bacteria were grown over night at 37°C, shaking at 165 rpm. The next morning, IPTG (1 M stock) was added to a final concentration of 1 mM to induce siRNA expression and the culture was incubated for additional 2 h at 37°C, shaking at 165 rpm. Bacteria were directly used to seed plates or stored for up to 10 days at 4°C.

Mass spectrometry

Samples from IP experiments were subjected to SDS-PAGEs until they migrated approx. 2 cm into the separation gel. The individual lanes were excised, removing stacking gel and loading dye. A tryptic digestion was carried out as previously described [307]. LC-MS/MS was performed by the group of Dr. Fan Liu using an 'UltiMate 3000 RSLC nano LC system' coupled on-line to an 'Orbitrap Elite mass spectrometer' (Thermo Fisher Scientific). For reversed-phase separation an analytical column (self-packed Poroshell 120 EC.C18, 2.7 µm, Agilent Technologies) with a 120 min gradient was employed. First scan (MS1) was performed in the orbitrap using 60000 resolution, second scan (MS2) was recorded in the ion trap using an AGC target of 5E3 and a maximum injection time of 50 ms,

The label-free quantification was performed as previously reported [308]. Data were analysed with MaxQuant (v 1.6.1.0) software using following listed parameters. Results were reported at 1% false discovery rate at the protein level.

Type of search:	MS/MS Ion Search
Enzyme:	Trypsin/P
Variable modifications:	Oxidation (Met), Propionamide (Cys)
MS1 ion mass tolerance:	± 4.5 ppm
MS2 ion mass tolerance:	± 0.5 Da
Max. missed cleavages:	2
Database:	SwissProt, CAEEL (10/2016)

C. elegans methods

Maintenance

Nematodes were cultured on nematode growth medium (NGM) using established protocols [183,185]. Culture dish size was 60 mm, filled with 8 to 10 ml NGM. Temperature while culturing and during experiments was 20°C. Five to ten nematodes per strain were passaged to fresh plates every four days to preserve well fed and clean populations.

RNAi treatment

For selective gene knockdown, RNA interference (RNAi) was performed by feeding. HT115 bacteria containing L4440-target plasmids were used as food source, producing double stranded RNA (dsRNA). The uptake of these dsRNAs and subsequent processing to active siRNAs by the nematodes induces systemic RNAi. To induce siRNA synthesis in HT115 bacteria NGM-plates were supplemented with Ampicillin and IPTG. To cast RNAi-plates 100 µg/ml Ampicillin and 1 mM IPTG were added to NGM after cooling down just prior pouring the plates. The used bacterial strains were taken from the Ahringer library (Dr. Julie Ahringer, University of Cambridge).

Oxidative stress treatment

To induce oxidative stress, nematodes were cultured on NGM-plates supplemented with 0.1 - 2.0 mM 1,1'-Dimethyl-4,4'-bipyridinium (Paraquat). For Lifespan-Assays under oxidative stress, nematodes were grown to L4 stage and transferred to 2 mM Paraquat containing plates. For Development-Assays under oxidative stress, eggs were prepared by bleaching and transferred onto Paraquat plates with concentrations ranging from 0.1 to 0.5 mM.

Compound treatment / ATM-1 kinase inhibition

To reduce ATM-1 kinase activity chemically, a selective ATM-1 kinase inhibitor (KU-55933) was employed. nDBN (S647A / S647D / wt) nematodes were synchronized by bleaching and grown to L4 stage. The L4 larvae were washed off the plates with M9 medium, washed once with S-Basal and pelleted on ice. Approx. 150 nematodes were transferred into wells of a 12-well plate and topped up

with prepared S-Basal^{+} to a total volume of 3 ml. Test wells were supplemented with 500 µM KU-55933 (dissolved in DMSO) and control wells were supplemented with 1% (v/v) DMSO.

After 22 h incubation at 20°C nematodes were transferred to NGM-plates and used for life span assay (starting day = day 4) or nematodes were directly lysed for western blots to check DBN-1 phosphorylation.

Male generation

To generate male nematodes for crossing, up to five NGM-plates were colonized with five L4 to young adult stage nematodes. Nematodes were incubated at 30°C for 6 to 8 h and shifted back to 20°C. After three to five days, plates were screened for males and those found were transferred to a fresh plate. To maintain males, two L4 hermaphrodite nematodes were added to the male plate.

Alternatively, wild type males (generated using the protocol above) were cultured and crossed with other transgenic nematodes to obtain heterozygous males for crossing.

Crossing

To obtain hybrid nematode strains, two strains bearing different genetic features were crossed. Male nematodes of one strain were generated. For crossing, seven adult males were put on a plate and two L4 stage hermaphrodites of the other strain were added. After three to five days incubation at 20°C nematodes were checked for crosses (identifiable by phenotypic or fluorescent markers). First generation crosses (F1; definitely heterozygous for both features) were put on a fresh plate and grown for four to five days. Six second generation nematodes, positive for both markers (F2; potentially homozygous for one or both feature/s), were singled onto fresh plates. The resulting populations were checked for (double-)homozygote. If only one feature was homozygous, nematodes were singled and procedure was repeated until both genetic features were homozygous.

If one genetic feature was not coupled to a phenotypic or fluorescent marker, the genotype was controlled by PCR. The crossing strategy was slightly altered: Males were generated from the strain bearing a phenotypic/fluorescent marker. The crossing was set up as 7 male adults + 2 L4 hermaphrodites of the second strain (no marker). After crossing, young male nematodes bearing the

phenotypic/fluorescent marker were used to set up a second crossing: 7 males + 2 L4 hermaphrodites of the second strain (no marker). The resulting hybrid generation has a 50% chance to be homozygous for the second genetic feature (with no marker). F2 generation is cultured and genotyped. After the feature without marker is homozygous, the other feature with marker is selected to obtain double homozygous nematodes.

Synchronisation

For age synchronisation, three different methods were employed: bleaching, egg-laying or L4-picking. For bleaching, mixed populations of adult nematodes were harvested by washing them off the plates with M9 buffer. Nematodes were collected in a 15 ml tube and volume was topped up to 7.5 ml with H_2O. 500 µl NaOH (10 M) + 2 ml hypochlorite solution (20%) were added and nematodes were harshly mixed on a vortex mixer for 1 min. Afterwards, tubes were inverted until nematodes started to dissolve completely. To stop the reaction, nematodes were pelleted by centrifugation (1 min at 2500 rpm) and the supernatant was removed. The pellet was washed with H_2O, twice, and once with M9. The supernatant was removed a final time and pellet was resuspended in 500 µl M9. The eggs were incubated for 22 h at 20°C and L1-arrest was exploited to generate age synchronous L1 (= day 1) populations. Bleaching was not applicable for nematodes carrying $A\beta_{1-42}$ transgene.

For egg-laying, ten to twenty day 5/6 old nematodes were put on a fresh plate and allowed to lay eggs for 4 h. After egg laying the adults were removed and the plates incubated at 20 °C (= day 0). Egg-laying was not applicable for nematodes carrying $A\beta_{1-42}$ transgene as they tend to arrest in larval stages or develop at different speeds.

For L4-picking, a mixed population of nematodes was started approx. five days before picking. L4 nematodes were picked from the population and transferred to a fresh plate (= day 3). L4-picking was used for nematodes carrying $A\beta_{1-42}$ transgene; the preparation of a mixed population five days before made sure all picked L4 larvae have a similar development speed and chronological age.

Lifespan-Assay

To assess the lifespan of the different nematode strains 100 to 150 nematodes were age synchronized. Nematodes were transferred to fresh plates daily until the end of their fertile period, afterwards they were transferred every three days to fresh plates. Surviving and dead nematodes were scored every day and corpses were removed. If a nematode was not moving, survival was checked by first, tapping the agar beside the nematode to provoke a reaction. If tapping failed, the nematode was gently prodded with a platinum wire at head, tail and mid body region. If there was no reaction the nematode was removed and counted as dead. Nematodes that disappeared or died while transfer to a fresh plate were censored and removed from the analysis. To increase statistical significance, up to three independent cohorts were recorded. Lifespan was evaluated as cumulative survival probability. The fraction of survivors (q_i) was calculated as:

$$q_i = \frac{n_{i-1} - d_i}{n_{i-1}} \quad \text{(equation 1.1)}$$

n_i … count of living individuals at day i
d_i … dead individuals at day i

And the cumulative survival probability was calculated as:

$$survival_i = q_1 \cdot q_2 \cdot \ldots \cdot q_i \quad \text{(equation 1.2)}$$

q_i … fraction of survivors at day i

Significance was tested using Mantel-Cox-Test (LogRank-test).

Pharynx pumping-Assay

Nematodes were age synchronized and grown to day 4, day 7 and day 10 of life. Nematodes were transferred to a fresh plate and allowed to crawl onto the bacterial lawn. Pharynx pumping was counted three times for 30 s per nematode with 10 s break between counting.

Progeny-Assay

10 to 15 L4 stage nematodes were singled per strain and analysed. Each nematode was transferred to a fresh plate every day and laid eggs / L1 larvae were counted. Transferring the elder nematodes was done until no more eggs were laid (usually on day 9). To ease counting, assay plates were seeded with a drop of 50 µl OP50 and were put to 4°C immediately after drying. Before placing the nematodes on the plates, the plates were incubated at RT for 30 min.

Thrashing-Assay

To analyse the thrashing / swimming of nematodes in M9 medium, nematodes were synchronized and grown to day 4 or day 7. Nematodes were picked from plates and transferred to fresh M9 medium in 35 mm plates (liquid column 3 – 4 mm). Nematodes were moved with an eye leash to remove residual bacteria clumps and to disperse them evenly in the liquid. Nematodes were allowed to swim for 3 min before video acquisition.

Videos were recorded at 7.3x magnification, 5 frames per second, for three times 10 - 20 seconds per group of nematodes (5 to 10 nematodes) in triplicates. If nematodes touched each other, they were separated with an eye leash and video acquisition was repeated.

The videos were analysed using Fiji + Fiji-plugin: wrMTrck. First, they were converted into 8-bit grey scale images. The background was removed, AutoThreshold was applied and wrMTrck was run (script for automation and settings can be found in the appendix). The analysed data were saved as Excel files and further processed. Analysed objects with a size smaller than 0.04 mm^2 (area) were omitted, objects that were not present in all 100 frames (#frames) were omitted. The table was sorted by body bends per seconds (BBPS) and objects with more than 2 BBPS plus a moved distance less than 0.1 mm were re-checked in the videos if they were truly moving nematodes or just artefacts.

Swim-Exhaustion-Assay

Nematodes were synchronized and grown to day 4 or day 7. 20 – 50 nematodes were picked and transferred to M9 medium (3 – 4 mm liquid column in 3.5 mm plate). Nematodes were separated with an eye leash and non-moving nematodes were removed. Nematodes were incubated for 30 min at RT.

Moving and non-moving nematodes were counted. Non-moving nematodes were touched with an eye leash and reacting nematodes were counted. Fraction of paralyzed nematodes was calculated as number of non-moving divided by total count.

Chemotaxis-Assay

To assess the nematodes' behaviour towards volatile odorants, a four quadrant chemotaxis assay was employed [309]. In brief, unseeded NGM plates were divided into four quadrants by two perpendicular lines. The centre of the plate was marked with a circle (diameter ≈ 1 cm). 2 µl test substance was applied in two opposing quadrants, 2 cm from the central intersection. 2 µl of control substance was applied the same way to the remaining two quadrants. This preparation had been done approx. 5 min before starting the assay.

To prepare the test substances, NaN_3 (500 mM) was mixed in a 1:1 ratio with (a) pure benzaldehyde and (b) with prediluted benzaldehyde (2% v/v in water). To prepare the control substances, NaN_3 (500 mM) was mixed in a 1:1 ratio with the used solvent (water).

Nematodes were washed three times with M9 medium and collected in a 15 ml tube. Afterwards, the nematodes were incubated for 5 min in M9 and washed again, this was repeated once. Subsequently, the supernatant was removed again and 1 ml fresh M9 medium was applied. The nematodes were incubated for 30 min at RT to starve.

The assay was started by pipetting 4 µl nematodes (directly from the pellet) to the intersection of the prepared plates (there should be 80 to 120 nematodes per plate, if the count was too low, more nematodes were pipetted). The nematodes were allowed to crawl on the plates for 2 h, being incubated at 20°C in a dark environment. Afterwards, nematodes in test and control quadrants were counted and the chemotactic index (ci) was calculated as:

$$ci = \frac{(Test\_Quadrant\_1 + Test\_Quadrant\_2) - (Control\_Quadrant\_1 + Control\_Quadrant\_2)}{total\ nematode\ count} \quad \text{(equation 2)}$$

Pathogen-Avoidance-Assay

Pathogen avoidance assay was adopted after Pujol *et al.* [237]. The nematode's reaction to pathogenic *Serratia marcescens* bacteria was tested. *S. marcescens* was cultured as described above. Assay plates were seeded with exactly 150 µl bacteria five to seven days prior starting the experiment. The bacteria were spotted slowly to ensure a circular lawn. *E. coli* OP50 were used as control. An attenuated *S. marcescens* strain (Db1140) was used as negative control.

Nematodes were synchronized by L4-picking and grown for 16 h at 20°C to reach day 4 of life. Day 4 old nematodes were transferred to the prepared assay plates (approx. 50 - 75 nematodes per strain and bacteria tested). After 24 h incubation at 20°C nematodes were transferred to fresh assay plates (with the same bacteria they were exposed to) in groups of 10 to 15 nematodes, resulting in 4 - 5 groups per nematode strain and bacteria strain. After 24 h further incubation at 20°C nematodes were scored for dwelling on the bacterial lawn or staying away. Every group was counted four times, with at least 5 min intervals between counting. An avoidance index (ai) was calculated as:

$$ai = \frac{SUM(counted\ nematodes\ off\ lawn)}{SUM(counted\ nematodes\ off\ lawn + counted\ nematodes\ on\ lawn)} \quad \text{(equation 3)}$$

Three independent cohorts were analysed and the mean avoidance index was calculated.

Galectin-Punctae-Assay

To analyse membrane rupture and calcium influx into cytoplasm in hypodermal cells, the galectin punctae assay was employed after Aits *et al.*[310]. In brief, nematodes were crossed with the reporter strain BIJ34, carrying the integrated array jaaIs4 (hyp7p::sfGFP-Gal3).

Nematodes carrying jaaIs4 were grown to day 4 of life and used for confocal laser scanning microscopy. 10 - 20 individual nematodes were used and three images of different, randomly selected parts of the hypodermis were recorded. Three independent cohorts per strain were imaged.

Fluorescent foci with an area ≥ 1.0 µm^2 were counted per nematode and nematodes were categorized as harbouring "less then 5", "5 to 9" or "10 or more" foci. Fractions were calculated.

Colocalization of fluorophores

To assess subcellular colocalization of fluorescent molecules, images were acquired at a confocal laser scanning microscope in line mode, using a multi-pass dichroic to image two different fluorophores (mScarlet and IR-680) simultaneously. Analysis was performed in Fiji using the plug-in EzColocalization [302]. Colocalization was evaluated using Pearson's correlation coefficient. Approx. 20 individual nematodes were analysed per condition.

CRISPR/Cas9 for total knockout generation

To generate a full knockout of endogenous *dbn-1* CRISPR/Cas9 was employed. Four guide RNAs were designed using the web tool *crispr.edu.mit*. Guides were selected to be located within the first 50 base pairs of exon 1 and the last 50 base pairs of exon 6. Guide_1 exhibited 2 predicted off targets (score = 100%), Guide_4 exhibited 2 predicted off targets (score = 100%), Guide_5 exhibited 1 predicted off target (score = 100%), Guide_7 exhibited 0 predicted off targets (score = 100%). Guide_1 and Guide_7 were located in Exon 1, Guide_4 and Guide_5 were located in Exon 6. Guide sequences were ordered as oligo nucleotides and inserted into BbsI-cleaved pJJR50 after Cong *et al.* [304].

N2, wild type, nematodes were injected with an injection mix containing:

- 50 ng/µl pJJR50_sgRNA-1 (germ line expressed Guide_1+tracerRNA)
- 50 ng/µl pJJR50_sgRNA-4 (germ line expressed Guide_4+tracerRNA)
- 50 ng/µl pJJR50_sgRNA-5 (germ line expressed Guide_5+tracerRNA)
- 50 ng/µl pJJR50_sgRNA-7 (germ line expressed Guide_7+tracerRNA)
- 50 ng/µl pMB67 (heat shock inducible Cas9)
- 3 ng/µl Pmyo-2::mCherry (co-injection marker, pharyngeal red fluorescence)
- 5 ng/µl pCFJ104 (co-injection marker, body wall muscle red fluorescence)
- 1,5 ng/µl pIR98 (co-injection marker, hygromycin resistance)

A strain expressing all markers was selected and cultured in presence of hygromycin. 20 L4 stage to young adult stage nematodes were heat shocked at 34°C for 2 h. After 12 h recovery time nematodes were allowed to lay eggs for 6 h on a fresh NGM plate supplemented with hygromycin. Offspring was

grown to L4/young adult stage and treated the same way. This procedure was repeated a third time. 20 nematodes of the F3 generation were singled onto separate plates. Populations were tested for knockout using PCR (primer pair GT_dbn-1 ko 3 f + GT_dbn-1 ko 3 r) and populations with wild type bands of 3.3 kb were omitted. One population was found to exhibit a 900 bp band ("green 7"). 10 nematodes of this population were singled out and genotyped again to ensure homozygous appearance of the knock-out band ("green 7.4" = JKM1). PCR products were sequenced using the separate genotyping primer as sequencing primers.

Transgenic strain generation

Microinjection

One method to generate transgenic nematode strains with complex extra-chromosomal arrays is microinjection. GOIs are cloned together with promoter sequences into the nematode expression vector pPD95. Plasmids for microinjection were purified using ZR Plasmid Miniprep™-Classic (Zymo). Injection mixes were prepared in 15 µl total volume. GOI were added for final concentrations of 10 - 30 ng/µl in desired combination and amount. Co-injection markers were added if necessary in following concentrations: 1.5 ng/µl pIR98 (hygromycin resistance), 3 ng/µl Pmyo-2::mCherry (red pharynx marker), 3 ng/µl Pmyo-2::GFP (green pharynx marker), 5 ng/µl pCFJ104 (red body wall muscle marker). If the combined DNA of GOI and Marker were below 100 ng/µl, filler DNA was added (100 – 150 ng/µl, 50bp-Ladder, Thermo).

Injection mixes were centrifuged 11 min at 13000 rpm in a benchtop centrifuge prior to injection. Glass needles were drawn using a needle puller model P-97 (Sutter Instruments Co., with settings heat = 600, pull = 45, vel = 75, del = 90) and loaded with 1.8 µl injection mix. Agar pads for mounting the nematodes were prepared in advance, in brief, 2% agarose (w/v) was dissolved in water, boiled and one drop of liquid agarose was put on a coverslip. A second coverslip was placed on top to get an even texture and a diameter of < 1 mm. Agar pads were allowed to solidify and the top coverslip was removed. The agar pad sticking to the first coverslip was baked for 120 min on an 80°C heat block.

For injection, one to five nematodes (day 4 adults) were picked using halocarbon oil (type 700) and put onto a dried agar pad. The nematodes were arranged to expose their gonads to the sides using an eye leash. Few picolitres of injection mix were injected into both gonads using an FemtoJet (Eppendorf,

settings: p_i = 1905 hPa, t_i = 0.5, p_c = 51 hPa). The nematodes were recovered in M9 solution and placed in groups of 3 - 5 on fresh NGM plates. The nematodes were incubated at 20°C and positive transformants among the offspring were screened for every day.

Ballistic transformation – micro particle bombardment

The second employed method to generate transgenic nematode strains was micro particle bombardment. A gene gun was built by the FMP workshop following the documentation of the Schnabel lab [311].

Wild type nematodes were synchronized by bleaching and grown to day 4 of life. For the bombardment, gold particles (0.3 - 3 microns) were coated in a stepwise protocol with DNA.

1 mg particles were resuspended in 100 µl spermidine solution (50 µM) by sonication in a water bath sonicator. After 10 min incubation at RT and resuspending by flicking every 2 min, 10 µg of one plasmid were added (one additional marker could be added as 1 µg). After 10 min incubation at RT and resuspending by flicking every 2 min, H_2O was added to a total volume of 360 µl. After 10 min incubation at RT and resuspending by flicking every 2 min, 100 µl $CaCl_2$ (1 M) was added dropwise and the resulting solution was mixed on a vortex mixer for 30 sec. After 10 min incubation at RT and resuspending by flicking every 2 min, the particles were pelleted by centrifugation for 30 sec at 13000 rpm in a benchtop centrifuge. The supernatant was removed and the pellet was resuspended in 500 µl ethanol (absolute). This procedure was repeated twice. Afterwards, the supernatant was removed completely and the pellet was resuspended in 200 µl PVP-solution.

In between, nematodes were harvested in M9. Five shooter plates (unseeded 35 mm NGM plates) were seeded with 12 µl OP50 and let allowed to dry. The seeded shooter plates and nematodes were cooled on ice. 20 µl nematodes (directly taken from the pellet) were put on the shooter plates as one pile, directly in the centre.

22 µl coated particle PVP solution was loaded to the gene gun. One shooter plate was positioned in the shooting chamber and the chamber pressure was reduced by 0.4 bar. The shot was released with 8 bar pressure (using He gas) within < 150 ms. The nematodes of one shooter plate were recovered in M9, spread on two seeded 100 mm NGM plates and incubated at 15°C overnight. Afterwards, the nematodes were incubated at 20°C and plates were checked for positive transformants every day.

Integration

UV-Integration

To integrate extra-chromosomal DNA stably into genomic DNA, UV-integration was employed. In brief, 200 transgenic nematodes (day 4 old adults) were picked and washed five times with M9 to remove residual bacteria. The nematodes were placed on a not seeded NGM plates and irradiated with 30 mJ UV light of 251 nm (Stratalinker® 2400). The nematodes were transferred to 20 - 30 fresh NGM plates (seeded with OP50) in groups of five and incubated at 20°C for 6 - 8 days. Afterwards, nematodes have been starved and were chunked to fresh plates. Chunked nematodes were allowed to crawl off their former agar for 10 min. Positive L1/L2 larvae were singled to seeded 35 mm NGM plates, until approx. 300 nematodes per strain were singled.

The populations were grown at 20°C for up to a week and screened for successful integration (all progeny is positive for the transgene / the co-transformation marker).

Gamma-irradiation integration

Same procedure as above, but nematodes did not need to be washed. DNA double strand breaks and DNA damage repair are achieved by irradiation with 4000 rad of gamma rays instead of UV treatment.

Selection on Hygromycin

To enrich transgenic nematodes that carry the pIR98 cassette, 15 µl hygromycin (50 mg/ml stock) were resuspended in 150 µl H_2O and spread on one 60 mm NGM-plate (to get a final concentration of 0.08 – 0.1 mg/ml). If nematodes were placed onto these plates, only offspring carrying the hygromycin resistance would survive. If the hygromycin was applied to a mixed population, adult nematodes without the resistance gene would die within four days, hatched larvae without the resistance would arrest in dauer stage. Only nematodes carrying the resistance would expand.

Microscopy

Sample preparation

Alive and moving

To record time series of moving/swimming nematodes, M9 medium was filled into empty 35 mm plates, to reach a liquid column of 3 – 4 mm (2.25 ml) and nematodes were picked into the liquid. An eye leash was used to arrange them and to remove bacteria clumps.

Alive and anesthetized

To record images of living nematodes, 2.5% agarose pads were casted and nematodes mounted on them. For casting the agar pads, 2.5% (w/v) agarose was dissolved in water and boiled in a micro wave. 1 cm^2 drops of agarose were pipetted onto glass slides and directly sealed with a second slide on top. After solidifying, the second slide was removed and the flattened agar pad was used for mounting nematodes. 8 - 10 µl of 2 mM levamisole was pipetted onto the agar pad and up to 20 nematodes were picked into that drop. An eye leash was used to arrange the nematodes and a coverslip was applied. Alternatively, 250 mM NaN_3 were used, as a stronger anaesthetic (especially for FLIM). To prevent drying out, liquid agarose was used to seal the coverslip on the edges.

PFA fixation and immunostaining

Mixed populations of nematodes were harvested in M9 and washed three times. Nematodes were pelleted and supernatant was removed. 500 µl ice cold formaldehyde solution was added and nematodes were inverted every three seconds at 4°C overnight. After fixation, nematodes were washed three times with 1 ml PBS. Nematodes were incubated with 500 µl PBS + 2% (v/v) Tween-20 for 30 min at RT and washed three times with 1 ml PBST afterwards.

The nematodes were incubated for 24 h at 37°C in bME-solution. Afterwards, the pellets were washed three times with 1 ml PBST. The supernatant was removed and 100 µl Collagenase-solution was added followed by incubation at 37°C and violent shaking (> 3000 rpm) for 5 min. After 5 min, 10 µl were taken as sample for microscopy and the number of cracked nematodes was evaluated. Incubation at 37°C shaking was continued until > 20% of the nematodes were broken. The reaction was stopped by placing

the tube on ice and washing two times with 1 ml PBST. The pellet was washed once in 1 ml AbA solution.

For $A\beta_{1-42}$ detection, nematodes were incubated in 200 µl AbA solution + anti-Aβ (4G8 or 6E10) antibody in 1:100 dilution for 18 h at 4°C, rotating at 20 rpm. The supernatant was removed and nematodes were washed in 1 ml AbA solution three times for 2 h at RT, rotating at 20 rpm. Supernatant was removed and 200 µl AbA solution + 1:200 anti-Mouse-680 antibody was added, incubating over night at 4°C and rotating at 20 rpm.

The pellets were washed with 1 ml AbA solution three times for 2 h at RT, rotating at 20 rpm. The supernatant was removed and nematodes were mixed with 10 µl mounting medium + DAPI (VectaShield®). Nematodes were mounted on clean glass slides and sealed with cover slips and clear nail polish. Imaging was performed immediately or slides were stored at - 20°C until imaging.

PFA fixation and amyloid specific Thioflavin T staining

Fixation and permeabilization was done as described above, but Collagenase treatment was not performed. For specific staining of amyloid aggregates Thioflavin T (ThT) was employed.

Fixed and permeabilized nematode pellets were incubated with 500 µl 0.125% (w/v) ThT in 50% (v/v) ethanol for 2 min at RT. The supernatant was removed and the pellet sequentially washed with 50% / 75% / 90% (v/v) ethanol for 5 min at RT inverting twice a minute. Afterwards, the pellet was washed with water. 5 µl nematodes were mixed with 5 µl mounting medium + DAPI (VectaShield®) and put on clean glass slides, sealed with coverslips and clear nail polish. Imaging was performed immediately. Every step involving ThT, including transport of the final slides, was done in the dark or by covering the agents with aluminium foil.

Confocal laser scanning microscopy

Standard imaging

For confocal image acquisition a laser-scanning microscope (LSM-780 or LSM-710, Zeiss) was used. Objectives were ‘Plan-apochromat 100x/1.40 Oil DIC M27’, ‘Plan-apochromat 63x/1.40 Oil DIC M27’, ‘Plan-apochromat 20x/0.8 M27’ and ‘EC Plan-Neofluar 10x/0.3’ used in combination with a 10x magnification ocular. Used were Argon, HeNe, DPSS and diode lasers. DAPI was excited at 405 nm,

CFP was excited at 458 nm, GFP was excited at 488 nm, YFP was excited at 514 nm, RFP was excited at 561 nm, IR680 was excited at 633 nm. Laser power was set to 1 – 20% as required. Photomultiplier voltage was set to 550 – 650 V. Digital Gain was set to 1, only for non-quantitative measurements of weak signals digital gain was increased up to 2. Pin hole was set between 40 – 100 µm, usually at airy disk ratio = 1.0. For recording Z-Stack images, the pin hole was opened up to 200 µm. Emission was measured according to the used fluorophores.

Dendra2 conversion for protein turn-over measurements

To measure protein degradation *in vivo* the convertible fluorophore Dendra2 was expressed in *C. elegans.* Two to four nematodes were mounted on an agar pad using 0.5 mM Levamisole as anaesthetic. Neurons of interest were selected and a region for conversion was defined. GFP and RFP signal were recorded before and after conversion. Conversion was performed by scanning the selected region with 405 nm laser (set to 60% power) up to 20 times, or until GFP fluorescence was reduced to less than 40%.

The nematodes were immediately recovered in M9 medium and singled to seeded NGM-plates. After 3, 6 or 24 h the nematodes were imaged again and GFP and RFP signals were recorded applying the exact same settings as before. Per timepoint three independent cohorts of 10 nematodes were imaged. The fluorescence decay (RFP) was calculated.

Fluorescence lifetime measurement

To assess the aggregation state of $A\beta_{1-42}$ *in vivo,* the fluorescence lifetime was measured by time correlated single photon counting (TCSPC) using a confocal SP5 microscope (Leica) and PicoHarp300 FLIM unit (PicoQuant). mScarlet was excited at 565 nm using a super continuum pulsed laser (80 MHz pulse rate) and emission was measured from 575 - 625 nm. Photomultiplier voltage was set to 990 V.

Five to ten Nematodes were anesthetized with 250 mM NaN_3 and mounted on 2.5% agarose pads. Imaging was performed within 45 min after mounting. $nA\beta_{1-42}$ (JKM2) was imaged in the head region to get images from the anterior to the retrovesicular ganglion. Image recording was performed for up to 3 min or until 3500 counts on the brightest pixels were accumulated. The laser was set to 1 - 15% power and incoming signal rate was kept below 1% laser repetition rate. Magnification was 945fold

(63x/1.3 objective, 10x ocular, 1.5 fold zoom), pin hole was set to airy = 1.0 - 1.2. Neuronal control (JKM3) was acquired the same way.

mAβ_{1-42} (JKM7) was imaged at the body walls to image muscle cells. Image recording was performed for up to 3 min or until 2000 counts on the brightest pixels were accumulated. The laser was set to 1 - 15% power and incoming signal rate was kept below 1% laser repetition rate. Magnification was 630fold (63x/1.3 objective, 10x ocular), pin hole was set to airy = 1.0 - 1.2. Muscle control (JKM8) was recorded as JKM7.

An IRF was measured as scattering at the glass slide's surface for every day and at every excitation wavelength measurements were performed.

Data were analysed using FlimFit software. In brief, an integration value of 80 – 150 was defined to remove stray light and autofluorescence. The corresponding IRF was imported and aligned. Data points for fitting of the mono exponential decay were limited to 1100 ps to 4000 ps. If necessary, segmentation was used to remove autofluorescence that was still present.

Stimulated emission depletion

To generate confocal images with resolutions beyond the diffraction limit, gated stimulated emission depletion microscopy (STED) was performed on JKM2 and nDBN nematodes. Nematodes were mounted on agar pads and anesthetized. First, a conventional confocal image was acquired at 6000x magnification. Afterwards, the same region was imaged using STED. The depletion laser was set to 60% power at 592 nm.

Spinning disk microscopy

To record confocal time lapse images or to acquire Z-Stack images with high axial resolution (Z-dimension), Spinning disk microscopy was employed.

For fluorescence intensity quantification, nematodes were anaesthetized and immobilized on agar pads. Z-Stack images were acquired of the nematodes' heads in 1 µm steps at 400-fold magnification. Field of view was set such that the head fit from the tip of the mouth to the retrovesicular ganglion. Exposure time was set to 75 ms for nDBN-Dendra (all variants) and 30 ms for mScarlet-Aβ (all crosses and variants) for every image of the stacks. Laser power and sensor sensitivity were kept constant.

Quantification was done using Fiji by performing a 'max projection' + density measurement and subtracting of background density.

Light microscopy

To analyse the motility of large cohorts on nematodes, time lapse images of swimming nematodes in M9 were recorded using a transmission light microscope at 7.3-fold magnification.

Transmission electron microscopy

To analyse the ultrastructure of nematode tissues, transmission electron microscopy was performed on wild type, m$A\beta_{1-42}$ and n$A\beta_{1-42}$ day ten old nematodes.

Nematodes were cryofixed by high pressure freezing (in a HPM100 instrument) using bacteria as cryoprotectant. The nematodes were embedded in epoxy resin. First, the remaining water was freeze substituted by acetone + 1% (w/v) osmium + 0.1% (w/v) uranyl acetate + 0.1% (v/v) glutaraldehyde over a time course of 36 h from -90°C to 0°C. After freeze substitution, the nematodes were washed in 100% acetone and infiltrated by acetone-epoxy resin mix (ratio 2:1, 1:1, 1:2) followed by pure epoxy resin and polymerization at 60°C.

The polymerized blocks were trimmed and ultrathin sectioned onto hexagonal finder grids (Plano). The nematode sections were contrasted with uranyl acetate and lead citrate and imaged at a transmission electron microscope (Zeiss 900).

Cryofixation, freeze substitution, sectioning and contrasting was performed by Dmytro Puchkov. Image acquisition was performed together with Dmytro Puchkov.

For image analysis, images of nematode sections were stitched together manually using prominent landmarks (*e.g.* unique shapes, staining artefacts). To assess the volumetric abundance of mitochondria, amphisomes and bloated endoplasmic reticulum, a virtual grid was used as overlay (mesh size 2 µm x 2 µm squares). Intersections in muscle cells were counted as well as intersections in mitochondria, amphisomes and bloated ER of these muscle cells. The volume fraction was calculated.

Statistical analysis

ANOVA

One/Two-way ANOVA + Bonferroni post hoc test were performed using GraphPad Prism 8. P-values were selected as following: $*$ = $p < 0.0334$; $**$ = $p < 0.01$; $***$ = $p < 0.001$.

Log-Rank-Test

Log-rank tests were performed in Excel to test for significant differences of lifespan assays. For LS experiments with multiple analysed cohorts all cohorts were tested separately and the lowest significance value was displayed. P-values were selected as:

$*$ = $p < 10^{-2}$; $**$ = $p < 10^{-4}$; $***$ = $p < 10^{-6}$.

Student's t-test

Student's t-test was performed using GraphPad Prism 8. P-values were selected as following:

$*$ = $p < 0.0334$; $**$ = $p < 0.01$; $***$ = $p < 0.001$.

Buffers

AbA solution	
1x	PBS (pH 7.2)
0.5% (v/v)	Triton X-100
1% (w/v)	BSA
notes:	prepare freshly and store at 4°C
used for:	*Immunostaining*

b-ME solution	
125 mM	Tris-HCl (pH 7.4)
4% (v/v)	Triton X-100
5% (v/v)	beta-mercaptoethanol
notes:	prepare under fume hood!
used for:	*Immunostaining*

Collagenase solution	
100 mM	Tris-HCl (pH 7.4)
1 mM	$CaCl_2$
2 µg/ml	Collagenase
notes:	prepare freshly
used for:	*Immunostaining*

Coomassie staining solution	
2.5% (w/v)	Coomassie brilliant blue R-250
40% (v/v)	Methanol
10% (v/v)	Acetic acid
notes:	--
used for:	*SDS-PAGE*

Destainer	
40% (v/v)	Methanol
10% (v/v)	Acetic acid
notes:	--
used for:	*SDS-PAGE*

HMK-buffer (+ inhibitors)

30 mM	HEPES (pH 8.4)
100 mM	CH_3COOK
5 mM	$MgCl_2$
---	---
+ 5 mM	DTT [(1)]
+ 1 mM	PMSF [(1)]
+ 1x	cOmplete™ Protease inhibitor cocktail [(1)]
+ 100 µM	Digitonin [(1)]
notes:	sterile filter with 0.22 µm, (1) add directly before use
used for:	*Lysis, Immunoprecipitation*

1x LB-agar (+ antibiotics)

15 g/l	Agar
10 g/l	Tryptone
5 g/l	Yeast extract
5 g/l	NaCl
---	---
+ 100 mg/l	Ampicillin (optional) [(1)]
+ 50 mg/l	Kanamycin (optional) [(1)]
+ 15 mg/l	Tetracycline (optional) [(1)]
+ 50 mg/l	Streptomycin (optional) [(1)]
notes:	autoclave, (1) add after autoclaving
used for:	*Transformation, Bacterial growth*

1x LB-medium

10 g/l	Tryptone
5 g/l	Yeast extract
5 g/l	NaCl
notes:	autoclave
used for:	*Transformation, Bacterial growth*

10x M9

58 g/l	Na_2HPO_4
30 g/l	KH_2PO_4
5 g/l	NaCl
10 g/l	NH_4Cl_2
notes:	autoclave
used for:	*Lysis, Thrashing, Exhaustion, Chemotaxis*

NGM-Agar / RNAi-Agar

50 mM	NaCl
2.5 g/l	Bacto® Peptone
17 g/l	Agar-Agar Kobe 1
---	---
+ 1 mM	$CaCl_2$ (1)
+ 1 mM	$MgSO_4$ (1)
+5 µg/ml	Cholesterol (1)
+ 25 mM	KH_2PO_4 (pH 6.0) (1)
---	---
+ 100 µg/ml	Ampicillin (optional) (1), (2)
+ 1 mM	IPTG (optional) (1), (2)
notes:	autoclave, (1) add after autoclaving before casting, (2) for RNAi-plates
used for:	*Nematode culture, RNA interference*

10x PBS

120 mM	HPO_4^{2-} (pH 7.4)
1.37 M	NaCl
27 mM	KCl
notes:	sterile filter with 0.22 µm
used for:	*Immunostaining*

10x PBST

120 mM	HPO_4^{2-} (pH 7.4)
1.37 M	NaCl
27 mM	KCl
0.5% (v/v)	Tween-20
notes:	sterile filter with 0.22 µm
used for:	*Immunostaining*

10x PCR buffer I

100 mM	Tris-HCl (pH 8.8)
500 mM	KCl
20 mM	$MgCl_2$
1% (v/v)	Trition X-100
notes:	aliquot and freeze at -20°C.
used for:	*PCR, Single worm PCR, Mutagenesis*

ProtK lysis buffer	
1x	PCR buffer I
50 µg/ml	Proteinase K (10 mg/ml stock)
notes:	prepare freshly
used for:	*Single worm PCR*

PVP-solution	
100 mg/l	Polyvinylpyrrolidone
99.5% (v/v)	Ethanol
notes:	dissolve (10 mg) PVP in (500 µl) H_2O and add to (99.5 ml) ethanol
used for:	*Micro particle bombardment*

4x sample loading buffer	
100 mM	Tris-HCl (pH 6.8)
4% (w/v)	SDS
30% (v/v)	Glycerol
0.2% (w/v)	Bromophenol blue
100 mM	DTT
notes:	store at -20°C in small aliquots
used for:	*SDS-PAGE*

S-Basal / S-Basal$^+$	
100 mM	NaCl
6 mM	K_2HPO_4
44 mM	KH_2PO_4
5 mg/l	Cholesterol
---	---
+ 30 mM	$MgSO_4$ (1)
+ 30 mM	$CaCl_2$ (1)
+ 15 µg/l	Cholesterol (1)
+ 2×10^7 bacteria/ml	OP50 or HT115(L4400-*dbn-1*) (1) (2)
notes:	autoclave, (1) add after autoclaving, (2) for ATM-1 inhibition *dbn-1* knockdown was done
used for:	*Compound treatment*

SDS-PAGE running buffer	
25 mM	Tris-HCl (pH 8.8)
192 mM	Glycine
0.1% (w/v)	SDS
notes:	sterile filter with 0.22 µm
used for:	*SDS-PAGE*

Separation buffer

1.5 M	Tris-HCl (pH 8.8)
0.04% (w/v)	SDS
notes:	sterile filter with 0.22 µm
used for:	*SDS-PAGE*

Stacking buffer

0.5 M	Tris-HCl (pH 6.8)
0.04% (w/v)	SDS
notes:	sterile filter with 0.22 µm
used for:	*SDS-PAGE*

50x TAE

2 M	Tris
5.71% (v/v)	Glacial acetic acid
50 mM	EDTA
notes:	sterile filter with 0.22 µm
used for:	*Agarose gel electrophoresis*

10x TBS

200 mM	Tris
1.5 M	NaCl
notes:	sterile filter with 0.22 µm
used for:	*Western blot*

10x TBST

200 mM	Tris
1.5 M	NaCl
1% (v/v)	Tween 20
notes:	sterile filter with 0.22 µm
used for:	*Immunoprecipitation, Western blot*

Transfer buffer for western blot

192 mM	Glycine
25 mM	Tris
20% (v/v)	Methanol
notes:	sterile filter with 0.22 µm
used for:	*Western blot*

References

1. Alzheimer, A. Über eine eigenartige Erkrankung der Hirnrinde. *Allg Zeitschr f Psychiatr. u Psych-Gerichtl Med* **64**, 146–8 (1907).
2. Plassman, B. L. *et al.* Prevalence of dementia in the United States: The aging, demographics, and memory study. *Neuroepidemiology* **29**, 125–132 (2007).
3. Christina Patterson. World Alzheimer Report 2018 - The State of the Art of Dementia Research: New Frontiers; World Alzheimer Report 2018. *Alzheimer's Dis. Int.* 48 (2018). doi:10.1111/j.0033-0124.1950.24_14.x
4. Wimo, A. & Prince, M. World Alzheimer Report 2010. *Dementia* 96 (2010). doi:10.1111/j.0963-7214.2004.00293.x
5. Brenowitz, W. D. *et al.* Mixed neuropathologies and estimated rates of clinical progression in a large autopsy sample. *Alzheimer's Dement.* **13**, 654–662 (2017).
6. Gaugler, J., James, B., Johnson, T., Marin, A. & Weuve, J. 2019 Alzheimer's disease facts and figures. *Alzheimer's Dement.* **15**, 321–387 (2019).
7. Davis, M. *et al.* Estimating Alzheimer's Disease Progression Rates from Normal Cognition Through Mild Cognitive Impairment and Stages of Dementia. *Curr. Alzheimer Res.* **15**, 777–788 (2018).
8. Shao, W., Peng, D. & Wang, X. Genetics of Alzheimer's disease: From pathogenesis to clinical usage. *J. Clin. Neurosci.* **45**, 1–8 (2017).
9. Cruts, M., Theuns, J. & Van Broeckhoven, C. Locus-specific mutation databases for neurodegenerative brain diseases. *Hum. Mutat.* **33**, 1340–1344 (2012).
10. Bertram, L. & Tanzi, R. E. The genetics of Alzheimer's disease. *Prog. Mol. Biol. Transl. Sci.* **107**, 79–100 (2012).
11. De Strooper, B. *et al.* Deficiency of presenilin-1 inhibits the normal cleavage of amyloid precursor protein. *Nature* **391**, 387–390 (1998).
12. Tomiyama, T. *et al.* A new amyloid β variant favoring oligomerization in Alzheimer's-type dementia. *Ann. Neurol.* **63**, 377–387 (2008).
13. Karch, C. M. & Goate, A. M. Alzheimer's disease risk genes and mechanisms of disease pathogenesis. *Biol. Psychiatry* **77**, 43–51 (2015).
14. Ziegler-Graham, K., Brookmeyer, R., Johnson, E. & Arrighi, H. M. Worldwide variation in the doubling time of Alzheimer's disease incidence rates. *Alzheimer's Dement.* **4**, 316–323 (2008).
15. De Strooper, B. & Karran, E. The Cellular Phase of Alzheimer's Disease. *Cell* **164**, 603–615 (2016).
16. Dobson, C. M., Knowles, T. P. J. & Vendruscolo, M. The Amyloid Phenomenon and Its Significance in Biology and Medicine. *Cold Spring Harb. Perspect. Biol.* a033878 (2019). doi:10.1101/cshperspect.a033878
17. Hipp, M. S., Park, S.-H. & Hartl, F. U. Proteostasis impairment in protein-misfolding and -aggregation diseases. *Trends Cell Biol.* **24**, 506–514 (2014).
18. Knowles, T. P. J., Vendruscolo, M. & Dobson, C. M. The amyloid state and its association with protein misfolding diseases. *Nat. Rev. Mol. Cell Biol.* **15**, 384–96 (2014).
19. Labbadia, J. & Morimoto, R. I. The biology of proteostasis in aging and disease. *Annu. Rev. Biochem.* **84**, 435–464 (2015).
20. Haass, C., Kaether, C., Thinakaran, G. & Sisodia, S. Trafficking and proteolytic processing of APP. *Cold Spring Harb. Perspect. Med.* **2**, (2012).
21. Iwatsubo, T. *et al.* Visualization of Aβ42(43) and Aβ40 in senile plaques with end-specific Aβ monoclonals: Evidence that an initially deposited species is Aβ42(43). *Neuron* **13**, 45–53 (1994).
22. Lane, C. A., Hardy, J. & Schott, J. M. Alzheimer's disease. *Eur. J. Neurol.* **25**, 59–70 (2018).
23. Portelius, E. *et al.* Mass spectrometric characterization of brain amyloid beta isoform signatures in familial and sporadic Alzheimer's disease. *Acta Neuropathol.* **120**, 185–193 (2010).
24. Wang, Y. Q., Qu, D. H. & Wang, K. Therapeutic approaches to Alzheimer's disease through stimulating of non-amyloidogenic processing of amyloid precursor protein. *Eur. Rev. Med. Pharmacol. Sci.* **20**, 2389–2403 (2016).
25. Thornton, E., Vink, R., Blumbergs, P. C. & Van Den Heuvel, C. Soluble amyloid precursor protein α reduces neuronal injury and improves functional outcome following diffuse traumatic brain injury in rats. *Brain Res.* **1094**, 38–46 (2006).
26. Puzzo, D. *et al.* Picomolar amyloid-β positively modulates synaptic plasticity and memory in hippocampus. *J. Neurosci.* **28**, 14537–14545 (2008).
27. Puzzo, D. *et al.* Endogenous amyloid-β is necessary for hippocampal synaptic plasticity and memory. *Ann. Neurol.* **69**, 819–830 (2011).
28. Plant, L. D., Boyle, J. P., Smith, I. F., Peers, C. & Pearson, H. A. The production of amyloid β peptide is a critical requirement for the viability of central neurons. *J. Neurosci.* **23**, 5531–5535 (2003).
29. Tan, J. Z. A. & Gleeson, P. A. The role of membrane trafficking in the processing of amyloid precursor protein and production of amyloid peptides in Alzheimer's disease. *Biochim. Biophys. Acta - Biomembr.* **1861**, 697–712 (2019).
30. Thinakaran, G. & Koo, E. H. Amyloid precursor protein trafficking, processing, and function. *J. Biol. Chem.* **283**, 29615–29619 (2008).
31. Zhang, Y. W., Thompson, R., Zhang, H. & Xu, H. APP processing in Alzheimer's disease. *Mol. Brain* **4**, (2011).

32. Toh, W. H., Tan, J. Z. A., Zulkefli, K. L., Houghton, F. J. & Gleeson, P. A. Amyloid precursor protein traffics from the Golgi directly to early endosomes in an Arl5b- and AP4-dependent pathway. *Traffic* **18**, 159–175 (2017).

33. Chia, P. Z. C. *et al.* Intracellular itinerary of internalised β-secretase, BACE1, and its potential impact on β-amyloid peptide biogenesis. *Traffic* **14**, 997–1013 (2013).

34. Burgos, P. V. *et al.* Sorting of the Alzheimer's Disease Amyloid Precursor Protein Mediated by the AP-4 Complex. *Dev. Cell* **18**, 425–436 (2010).

35. Kinoshita, A. *et al.* Demonstration by FRET of BACE interaction with the amyloid precursor protein at the cell surface and in early endosomes. *J. Cell Sci.* **116**, 3339–3346 (2003).

36. Fukumori, A. *et al.* Presenilin-dependent γ-secretase on plasma membrane and endosomes is functionally distinct. *Biochemistry* **45**, 4907–4914 (2006).

37. Fassler, M., Li, X. & Kaether, C. Polar transmembrane-based amino acids in presenilin 1 are involved in endoplasmic reticulum localization, Pen2 protein binding, and γ-secretase complex stabilization. *J. Biol. Chem.* **286**, 38390–38396 (2011).

38. Réchards, M., Xia, W., Oorschot, V. M. J., Selkoe, D. J. & Klumperman, J. Presenilin-1 exist in both pre- and post-golgi compartments and recycles via COPI-coated membranes. *Traffic* **4**, 553–565 (2003).

39. Almeida, C. G., Takahashi, R. H. & Gouras, G. K. B-Amyloid Accumulation Impairs Multivesicular Body Sorting By Inhibiting the Ubiquitin-Proteasome System. *J. Neurosci.* **26**, 4277–4288 (2006).

40. Tseng, B. P., Green, K. N., Chan, J. L., Blurton-Jones, M. & LaFerla, F. M. Aβ inhibits the proteasome and enhances amyloid and tau accumulation. *Neurobiol. Aging* **29**, 1607–1618 (2008).

41. Oh, S. *et al.* Amyloid peptide attenuates the proteasome activity in neuronal cells. *Mech. Ageing Dev.* **126**, 1292–1299 (2005).

42. Hardy, J. A. & Higgins, G. A. Alzheimer's disease: The amyloid cascade hypothesis. *Science (80-.).* **256**, 184–185 (1992).

43. Hardy, J. & Allsop, D. Amyloid deposition as the central event in the aetiology of Alzheimer's disease. *Trends Pharmacol. Sci.* **12**, 383–388 (1991).

44. Kawahara, M. Neurotoxicity of β-Amyloid Protein: Oligomerization, Channel Formation and Calcium Dyshomeostasis. *Curr. Pharm. Des.* **16**, 2779–2789 (2012).

45. Pollard, H. B., Arispe, N. & Rojas, E. Ion channel hypothesis for Alzheimer amyloid peptide neurotoxicity. *Cell. Mol. Neurobiol.* **15**, 513–526 (1995).

46. Maia, M. A. & Sousa, E. BACE-1 and γ-secretase as therapeutic targets for alzheimer's disease. *Pharmaceuticals* **12**, (2019).

47. Puzzo, D., Gulisano, W., Arancio, O. & Palmeri, A. The keystone of Alzheimer pathogenesis might be sought in Aβ physiology. *Neuroscience* **307**, 26–36 (2015).

48. Lesné, S. E. *et al.* Brain amyloid-β oligomers in ageing and Alzheimer's disease. *Brain* **136**, 1383–1398 (2013).

49. Lesné, S. *et al.* A specific amyloid-β protein assembly in the brain impairs memory. *Nature* **440**, 352–357 (2006).

50. Ahmed, M. *et al.* Structural conversion of neurotoxic amyloid-B 1-42 oligomers to fibrils. *Nat. Struct. Mol. Biol.* **17**, 561–567 (2010).

51. Chen, Y. R. & Glabe, C. G. Distinct early folding and aggregation properties of Alzheimer amyloid-β peptides Aβ40 and Aβ42: Stable trimer or tetramer formation by Aβ42. *J. Biol. Chem.* **281**, 24414–24422 (2006).

52. Mucke, L. *et al.* High-level neuronal expression of Aβ(1-42) in wild-type human amyloid protein precursor transgenic mice: Synaptotoxicity without plaque formation. *J. Neurosci.* **20**, 4050–4058 (2000).

53. Leon, W. C. *et al.* A novel transgenic rat model with a full alzheimer's - Like amyloid pathology displays pre - Plaque intracellular amyloid -β- Associated cognitive impairment. *J. Alzheimer's Dis.* **20**, 113–126 (2010).

54. Iulita, M. F. *et al.* Intracellular Aβ pathology and early cognitive impairments in a transgenic rat overexpressing human amyloid precursor protein: A multidimensional study. *Acta Neuropathol. Commun.* **2**, (2014).

55. Knowles, T. P. J., Vendruscolo, M. & Dobson, C. M. The amyloid state and its association with protein misfolding diseases. *Nat. Rev. Mol. Cell Biol.* **15**, 384–396 (2014).

56. Olzscha, H. *et al.* Amyloid-like aggregates sequester numerous metastable proteins with essential cellular functions. *Cell* **144**, 67–78 (2011).

57. Hu, X. *et al.* Sortilin Fragments Deposit at Senile Plaques in Human Cerebrum. *Front. Neuroanat.* **11**, 1–19 (2017).

58. Kundra, R., Ciryam, P., Morimoto, R. I., Dobson, C. M. & Vendruscolo, M. Protein homeostasis of a metastable subproteome associated with Alzheimer ' s disease. *Mol. Psychiatry* 1–9 (2016). doi:10.1073/pnas.1618417114

59. Pepys, M. Amyloidosis. *Annu. Rev. Med.* (2006). doi:10.1146/annurev.med.57.121304.131243

60. Williams, T. L. & Serpell, L. C. Membrane and surface interactions of Alzheimer's Aβ peptide - Insights into the mechanism of cytotoxicity. *FEBS J.* **278**, 3905–3917 (2011).

61. Regland, B. *et al.* Treatment of Alzheimer's disease with clioquinol. *Dement. Geriatr. Cogn. Disord.* **12**, 408–414 (2001).

62. Ritchie, C. W. *et al.* Metal-Protein Attenuation with Iodochlorhydroxyquin (Clioquinol) Targeting Aβ Amyloid Deposition and Toxicity in Alzheimer Disease: A Pilot Phase 2 Clinical Trial. *Arch. Neurol.* **60**, 1685–1691 (2003).

63. Huang, X. *et al.* The Aβ peptide of Alzheimer's disease directly produces hydrogen peroxide through metal ion reduction. *Biochemistry* **38**, 7609–7616 (1999).

64. Törnquist, M. *et al.* Secondary nucleation in amyloid formation. *Chem. Commun.* **54**, 8667–8684 (2018).

65. Michaels, T. C. T. *et al.* Chemical Kinetics for Bridging Molecular Mechanisms and Macroscopic Measurements of Amyloid Fibril Formation. *Annu. Rev. Phys. Chem.* **69**, 273–298 (2018).

66. Cohen, S. I. A. *et al.* Proliferation of amyloid-β42 aggregates occurs through a secondary nucleation mechanism. *Proc. Natl. Acad. Sci. U. S. A.* **110**, 9758–9763 (2013).

67. Pham, E. *et al.* Progressive accumulation of amyloid-β oligomers in Alzheimer's disease and in amyloid precursor protein transgenic mice is accompanied by selective alterations in synaptic scaffold proteins. *FEBS J.* **277**, 3051–3067 (2010).

68. Lue, L. F. *et al.* Soluble amyloid β peptide concentration as a predictor of synaptic change in Alzheimer's disease. *Am. J. Pathol.* **155**, 853–862 (1999).

69. Billings, L. M., Oddo, S., Green, K. N., McGaugh, J. L. & LaFerla, F. M. Intraneuronal Aβ causes the onset of early Alzheimer's disease-related cognitive deficits in transgenic mice. *Neuron* **45**, 675–688 (2005).

70. Xiao, C. *et al.* Brain transit and ameliorative effects of intranasally delivered anti-amyloid-β oligomer antibody in 5XFAD mice. *J. Alzheimer's Dis.* **35**, 777–788 (2013).

71. Yamin, G. NMDA receptor-dependent signaling pathways that underlie amyloid β-protein disruption of LTP in the hippocampus. *J. Neurosci. Res.* **87**, 1729–1736 (2009).

72. Moloney, A. M. *et al.* Defects in IGF-1 receptor, insulin receptor and IRS-1/2 in Alzheimer's disease indicate possible resistance to IGF-1 and insulin signalling. *Neurobiol. Aging* **31**, 224–243 (2010).

73. Rondelli, V. *et al.* Amyloidβ Peptides in interaction with raft-mime model membranes: A neutron reflectivity insight. *Sci. Rep.* **6**, (2016).

74. Antollini, S. S. *et al.* Physical state of bulk and protein-associated lipid in nicotinic acetylcholine receptor-rich membrane studied by laurdan generalized polarization and fluorescence energy transfer. *Biophys. J.* **70**, 1275–1284 (1996).

75. Criado, M., Eibl, H. & Barrantes, F. J. Functional properties of the acetylcholine receptor incorporated in model lipid membranes. Differential effects of chain length and head group of phospholipids on receptor affinity states and receptor-mediated ion translocation. *J. Biol. Chem.* **259**, 9188–9198 (1984).

76. Barrantes, F. J. Lipid matters: Nicotinic acetylcholine receptor-lipid interactions (review). *Mol. Membr. Biol.* **19**, 277–284 (2002).

77. Lee, A. G. Lipid-protein interactions in biological membranes: A structural perspective. *Biochim. Biophys. Acta - Biomembr.* **1612**, 1–40 (2003).

78. Di Scala, C., Chahinian, H., Yahi, N., Garmy, N. & Fantini, J. Interaction of Alzheimer's β-amyloid peptides with cholesterol: Mechanistic insights into amyloid pore formation. *Biochemistry* **53**, 4489–4502 (2014).

79. Relini, A., Marano, N. & Gliozzi, A. Misfolding of amyloidogenic proteins and their interactions with membranes. *Biomolecules* **4**, 20–55 (2014).

80. Kotler, S. A., Walsh, P., Brender, J. R. & Ramamoorthy, A. Differences between amyloid-β aggregation in solution and on the membrane: Insights into elucidation of the mechanistic details of Alzheimer's disease. *Chem. Soc. Rev.* **43**, 6692–6700 (2014).

81. Engel, M. F. M. *et al.* Membrane damage by human islet amyloid polypeptide through fibril growth at the membrane. *Proc. Natl. Acad. Sci. U. S. A.* **105**, 6033–6038 (2008).

82. Yoo, B. C., Seidl, R., Cairns, N. & Lubec, G. Heat-shock protein 70 levels in brain of patients with Down Syndrome and Alzheimer's disease. *J. Neural Transm. Suppl.* 315–322 (1999). doi:10.1007/978-3-7091-6380-1_22

83. Wilhelmus, M. M. M. *et al.* Specific association of small heat shock proteins with the pathological hallmarks of Alzheimer's disease brains. *Neuropathol. Appl. Neurobiol.* **32**, 119–130 (2006).

84. Ojha, J., Masilamoni, G., Dunlap, D., Udoff, R. A. & Cashikar, A. G. Sequestration of Toxic Oligomers by HspB1 as a Cytoprotective Mechanism. *Mol. Cell. Biol.* **31**, 3146–3157 (2011).

85. Willén, K. *et al.* Aβ accumulation causes MVB enlargement and is modelled by dominant negative VPS4A. *Mol. Neurodegener.* **12**, (2017).

86. Bordi, M. *et al.* Autophagy flux in CA1 neurons of Alzheimer hippocampus: Increased induction overburdens failing lysosomes to propel neuritic dystrophy. *Autophagy* **12**, 2467–2483 (2016).

87. Feleciano, D. R. *et al.* Crosstalk between chaperone-mediated protein disaggregation and proteolytic pathways in aging and disease. *Front. Aging Neurosci.* **11**, (2019).

88. Kametani, F. & Hasegawa, M. Reconsideration of amyloid hypothesis and tau hypothesis in Alzheimer's disease. *Front. Neurosci.* **12**, (2018).

89. Gómez-Isla, T. *et al.* Neuronal loss correlates with but exceeds neurofibrillary tangles in Alzheimer's disease. *Ann. Neurol.* **41**, 17–24 (1997).

90. Bierer, L. M. *et al.* Neocortical Neurofibrillary Tangles Correlate with Dementia Severity in Alzheimer's Disease. *Arch. Neurol.* **52**, 81–88 (1995).

91. Arriagada, P. V., Growdon, J. H., Hedley-Whyte, E. T. & Hyman, B. T. Neurofibrillary tangles but not senile plaques parallel duration and severity of Alzheimer's disease. *Neurology* **42**, 631–639 (1992).

92. Wood, J. G., Mirra, S. S., Pollock, N. J. & Binder, L. I. Neurofibrillary tangles of Alzheimer disease share antigenic determinants with the axonal microtubule-associated protein tau (τ). *Proc. Natl. Acad. Sci. U. S. A.* **83**, 4040–4043 (1986).

93. Kosik, K. S., Joachim, C. L. & Selkoe, D. J. Microtubule-associated protein tau (τ) is a major antigenic component of paired helical filaments in Alzheimer disease. *Proc. Natl. Acad. Sci. U. S. A.* **83**, 4044–4048 (1986).

94. Grundke-Iqbal, I. *et al.* Abnormal phosphorylation of the microtubule-associated protein tau (tau) in Alzheimer cytoskeletal pathology. *Proc. Natl. Acad. Sci. U. S. A.* **83**, 4913–4917 (1986).

95. Grueninger, F. *et al.* Phosphorylation of Tau at S422 is enhanced by Aβ in TauPS2APP triple transgenic mice. *Neurobiol. Dis.* **37**, 294–306 (2010).

96. De Felice, F. G. *et al.* Alzheimer's disease-type neuronal tau hyperphosphorylation induced by Aβ oligomers. *Neurobiol. Aging* **29**, 1334–1347 (2008).

97. Liu, S. L. *et al.* The Role of Cdk5 in Alzheimer's Disease. *Mol. Neurobiol.* **53**, 4328–4342 (2016).

98. Hernandez, F., Lucas, J. J. & Avila, J. GSK3 and tau: Two convergence points in Alzheimer's disease. *J. Alzheimer's Dis.* **33**, (2013).

99. Mairet-Coello, G. *et al.* The CAMKK2-AMPK Kinase Pathway Mediates the Synaptotoxic Effects of Aβ Oligomers through Tau Phosphorylation. *Neuron* **78**, 94–108 (2013).

100. Nikkel, A. L. *et al.* The novel calpain inhibitor A-705253 prevents stress-induced tau hyperphosphorylation in vitro and in vivo. *Neuropharmacology* **63**, 606–612 (2012).

101. Kurbatskaya, K. *et al.* Upregulation of calpain activity precedes tau phosphorylation and loss of synaptic proteins in Alzheimer's disease brain. *Acta Neuropathol. Commun.* **4**, 34 (2016).

102. Zempel, H., Thies, E., Mandelkow, E. & Mandelkow, E. M. Aβ oligomers cause localized Ca2+ elevation, missorting of endogenous Tau into dendrites, Tau phosphorylation, and destruction of microtubules and spines. *J. Neurosci.* **30**, 11938–11950 (2010).

103. Julien, C. *et al.* In vivo induction of membrane damage by β-amyloid peptide oligomers. *Acta Neuropathol. Commun.* **6**, 131 (2018).

104. Allan Butterfield, D., Castegna, A., Lauderback, C. M. & Drake, J. Evidence that amyloid beta-peptide-induced lipid peroxidation and its sequelae in Alzheimer's disease brain contribute to neuronal death. *Neurobiol. Aging* **23**, 655–664 (2002).

105. Mark, R. J., Lovell, M. A., Markesbery, W. R., Uchida, K. & Mattson, M. P. A role for 4-hydroxynonenal, an aldehydic product of lipid peroxidation, in disruption of ion homeostasis and neuronal death induced by amyloid beta-peptide. *J Neurochem* **68**, 255–264 (1997).

106. Markesbery, W. R. Oxidative stress hypothesis in Alzheimer's disease. *Free Radic. Biol. Med.* **23**, 134–147 (1997).

107. Heneka, M. T. *et al.* Neuroinflammation in Alzheimer's disease. *Lancet Neurol.* **14**, 388–405 (2015).

108. Lawson, L. J., Perry, V. H., Dri, P. & Gordon, S. Heterogeneity in the distribution and morphology of microglia in the normal adult mouse brain. *Neuroscience* **39**, 151–170 (1990).

109. McGEER, P. L., ITAGAKI, S., TAGO, H. & McGEER, E. G. Occurrence of HLA-DR Reactive Microglia in Alzheimer's Disease. *Ann. N. Y. Acad. Sci.* **540**, 319–323 (1988).

110. Lieberman, O. J., McGuirt, A. F., Tang, G. & Sulzer, D. Roles for neuronal and glial autophagy in synaptic pruning during development. *Neurobiol. Dis.* **122**, 49–63 (2019).

111. Salter, M. W. & Beggs, S. Sublime microglia: Expanding roles for the guardians of the CNS. *Cell* **158**, 15–24 (2014).

112. Li, Y., Du, X. F., Liu, C. S., Wen, Z. L. & Du, J. L. Reciprocal Regulation between Resting Microglial Dynamics and Neuronal Activity In Vivo. *Dev. Cell* **23**, 1189–1202 (2012).

113. Jonsson, T. *et al.* Variant of TREM2 associated with the risk of Alzheimer's disease. *N. Engl. J. Med.* **368**, 107–116 (2013).

114. Guerreiro, R. *et al.* TREM2 variants in Alzheimer's disease. *N. Engl. J. Med.* **368**, 117–127 (2013).

115. Mahad, D. H., Trapp, B. D. & Lassmann, H. Pathological mechanisms in progressive multiple sclerosis. *Lancet Neurol.* **14**, 183–193 (2015).

116. Behrendt, G. *et al.* Dynamic changes in myelin aberrations and oligodendrocyte generation in chronic amyloidosis in mice and men. *Glia* **61**, 273–286 (2013).

117. Bartzokis, G. Alzheimer's disease as homeostatic responses to age-related myelin breakdown. *Neurobiol. Aging* **32**, 1341–1371 (2011).

118. Khakh, B. S. & Sofroniew, M. V. Diversity of astrocyte functions and phenotypes in neural circuits. *Nat. Neurosci.* **18**, 942–952 (2015).

119. Allen, N. J. Astrocyte Regulation of Synaptic Behavior. *Annu. Rev. Cell Dev. Biol.* **30**, 439–463 (2014).

120. Gittis, A. H. & Brasier, D. J. Astrocytes tell neurons when to listen up. *Science (80-.).* **349**, 690–691 (2015).

121. Pelvig, D. P., Pakkenberg, H., Regeur, L., Oster, S. & Pakkenberg, B. Neocortical glial cell numbers in Alzheimer's disease: A stereological study. *Dement. Geriatr. Cogn. Disord.* **16**, 212–219 (2003).

122. Olabarria, M., Noristani, H. N., Verkhratsky, A. & Rodríguez, J. J. Concomitant astroglial atrophy and astrogliosis in a triple transgenic animal model of Alzheimer's disease. *Glia* **58**, 831–838 (2010).

123. Lian, H. *et al.* NFκB-Activated Astroglial Release of Complement C3 Compromises Neuronal Morphology and Function Associated with Alzheimer's Disease. *Neuron* **85**, 101–115 (2015).

124. Schousboe, A., Bak, L. K. & Waagepetersen, H. S. Astrocytic control of biosynthesis and turnover of the neurotransmitters glutamate and GABA. *Front. Endocrinol. (Lausanne).* **4**, (2013).

125. Colombo, J. A., Quinn, B. & Puissant, V. Disruption of astroglial interlaminar processes in Alzheimer's disease. *Brain Res. Bull.* **58**, 235–242 (2002).

126. Dekosky, S. T. *et al.* Upregulation of choline acetyltransferase activity in hippocampus and frontal cortex of elderly subjects with mild cognitive impairment. *Ann. Neurol.* **51**, 145–155 (2002).

127. Honer, W. G. *et al.* Cognitive reserve, presynaptic proteins and dementia in the elderly. *Transl. Psychiatry* **2**, (2012).

128. Sperling, R., Mormino, E. & Johnson, K. The evolution of preclinical Alzheimer's disease: Implications for prevention trials. *Neuron* **84**, 608–622 (2014).

129. Scheff, S. W., Price, D. A., Schmitt, F. A. & Mufson, E. J. Hippocampal synaptic loss in early Alzheimer's disease and mild cognitive impairment. *Neurobiol. Aging* **27**, 1372–1384 (2006).

130. DeKosky, S. T. & Scheff, S. W. Synapse loss in frontal cortex biopsies in Alzheimer's disease: Correlation with cognitive severity. *Ann. Neurol.* **27**, 457–464 (1990).

131. Terry, R. D. *et al.* Physical basis of cognitive alterations in alzheimer's disease: Synapse loss is the major correlate of cognitive impairment. *Ann. Neurol.* **30**, 572–580 (1991).

132. Hotulainen, P. & Hoogenraad, C. C. Actin in dendritic spines: Connecting dynamics to function. *J. Cell Biol.* **189**, 619–629 (2010).

133. Lamprecht, R. & LeDoux, J. Structural plasticity and memory. *Nat. Rev. Neurosci.* **5**, 45–54 (2004).

134. Zhao, L. *et al.* Role of p21-activated kinase pathway defects in the cognitive deficits of Alzheimer disease. *Nat Neurosci* **9**, 234–242 (2006).

135. Benitez-King, G., Ramírez-Rodríguez, G., Ortíz, L. & Meza, I. The neuronal cytoskeleton as a potential therapeutical target in neurodegenerative diseases and schizophrenia. *Curr. Drug Targets. CNS Neurol. Disord.* **3**, 515–533 (2004).

136. Bishop, N. A., Lu, T. & Yankner, B. A. Neural mechanisms of ageing and cognitive decline. *Nature* **464**, 529–535 (2010).

137. Geraldo, S., Khanzada, U. K., Parsons, M., Chilton, J. K. & Gordon-Weeks, P. R. Targeting of the F-actin-binding protein drebrin by the microtubule plus-tip protein EB3 is required for neuritogenesis. *Nat. Cell Biol.* **10**, 1181–1189 (2008).

138. Hayashi, K. & Shirao, T. Change in the shape of dendritic spines caused by overexpression of drebrin in cultured cortical neurons. *J. Neurosci.* **19**, 3918–3925 (1999).

139. Shirao, T. *et al.* Formation of thick, curving bundles of actin by drebrin A expressed in fibroblasts. *Exp. Cell Res.* **215**, 145–153 (1994).

140. Shirao, T., Kojima, N. & Obata, K. Cloning of drebrin A and induction of neurite-like processes in drebrin-transfected cells. *Neuroreport* **3**, 109–112 (1992).

141. Kojima, N., Kato, Y., Shirao, T. & Obata, K. Nucleotide sequences of two embryonic drebrins, developmentally regulated brain proteins, and developmental change in their mRNAs. *Mol. Brain Res.* **4**, 207–215 (1988).

142. Hayashi, K., Suzuki, K. & Shirao, T. Rapid conversion of drebrin isoforms during synapse formation in primary culture of cortical neurons. *Dev. Brain Res.* **111**, 137–141 (1998).

143. Yuste, R. & Tank, D. W. Dendritic integration in mammalian neurons, a century after Cajal. *Neuron* **16**, 701–716 (1996).

144. Harris, K. M. & Kater, S. B. Dendritic Spines: Cellular Specializations Imparting Both Stability and Flexibility to Synaptic Function. *Annu. Rev. Neurosci.* **17**, 341–371 (1994).

145. Shim, K. S. & Lubec, G. Drebrin, a dendritic spine protein, is manifold decreased in brains of patients with Alzheimer's disease and Down syndrome. *Neurosci. Lett.* **324**, 209–212 (2002).

146. Harigaya, Y., Shoji, M., Shirao, T. & Hirai, S. Disappearance of actin-binding protein, drebrin, from hippocampal synapses in Alzheimer's disease. *J. Neurosci. Res.* **43**, 87–92 (1996).

147. Aoki, C., Mahadomrongkul, V., Fujisawa, S., Habersat, R. & Shirao, T. Chemical and morphological alterations of spines within the hippocampus and entorhinal cortex precede the onset of Alzheimer's disease pathology in double knock-in mice. *J. Comp. Neurol.* **505**, 352–362 (2007).

148. Liu, Y. *et al.* Down-Regulated Drebrin Aggravates Cognitive Impairments in a Mouse Model of Alzheimer ' s Disease. **1**, 1–17 (2017).

149. Liu, Y. *et al.* Effective expression of Drebrin in hippocampus improves cognitive function and alleviates lesions of Alzheimer's disease in APP (swe)/PS1 (ΔE9) mice. *CNS Neurosci. Ther.* **23**, 590–604 (2017).

150. Chimura, T., Launey, T. & Yoshida, N. Calpain-mediated degradation of drebrin by excitotoxicity in vitro and in vivo. *PLoS One* **10**, 1–18 (2015).

151. Worth, D. C., Daly, C. N., Geraldo, S., Oozeer, F. & Gordon-Weeks, P. R. Drebrin contains a cryptic F-actin-bundling activity regulated by Cdk5 phosphorylation. *J. Cell Biol.* **202**, 793–806 (2013).

152. Sharma, S., Grintsevich, E. E., Phillips, M. L., Reisler, E. & Gimzewski, J. K. Atomic force microscopy reveals drebrin induced remodeling of F-actin with subnanometer resolution. *Nano Lett.* **11**, 825–827 (2011).

153. Mikati, M. A., Grintsevich, E. E. & Reisler, E. Drebrin-induced stabilization of actin filaments. *J. Biol. Chem.* **288**, 19926–19938 (2013).

154. Mizui, T., Takahashi, H., Sekino, Y. & Shirao, T. Overexpression of drebrin A in immature neurons induces the accumulation of F-actin and PSD-95 into dendritic filopodia, and the formation of large abnormal protrusions. *Mol. Cell. Neurosci.* **30**, 149–157 (2005).

155. Takahashi, H., Mizui, T. & Shirao, T. Down-regulation of drebrin A expression suppresses synaptic targeting of NMDA receptors in developing hippocampal neurones. *J. Neurochem.* **97 Suppl 1**, 110–115 (2006).

156. Jung, G. *et al.* Drebrin depletion alters neurotransmitter receptor levels in protein complexes, dendritic spine morphogenesis and memory-related synaptic plasticity in the mouse hippocampus. *J. Neurochem.* **134**, 327–339 (2015).

157. Yamazaki, H. *et al.* Spikar, a novel drebrin-binding protein, regulates the formation and stabilization of dendritic spines. *J. Neurochem.* **128**, 507–522 (2014).

158. Shiraishi-Yamaguchi, Y. *et al.* Interaction of Cupidin/Homer2 with two actin cytoskeletal regulators, Cdc42 small GTPase and Drebrin, in dendritic spines. *BMC Neurosci.* **10**, (2009).

159. Aoki, C. *et al.* Drebrin A is a postsynaptic protein that localizes in vivo to the submembranous surface of dendritic sites forming excitatory synapses. *J. Comp. Neurol.* **483**, 383–402 (2005).

160. Sekino, Y. *et al.* Activation of N-methyl-d-aspartate receptor induces a shift of drebrin distribution: Disappearance from dendritic spines and appearance in dendritic shafts. *Mol. Cell. Neurosci.* **31**, 493–504 (2006).

161. Mizui, T., Sekino, Y., Yamazaki, H., Ishizuka, Y. & Takahashi, H. Myosin II ATPase Activity Mediates the Long-Term Potentiation-Induced Exodus of Stable F-Actin Bound by Drebrin A from Dendritic Spines. **9**, (2014).

162. Murrell, M. P. & Gardel, M. L. F-actin buckling coordinates contractility and severing in a biomimetic actomyosin cortex. *Proc. Natl. Acad. Sci. U. S. A.* **109**, 20820–20825 (2012).

163. Wilson, C. A. *et al.* Myosin II contributes to cell-scale actin network treadmilling through network disassembly. *Nature* **465**, 373–377 (2010).

164. Korn, E. D., Carlier, M. F. & Pantaloni, D. Actin polymerization and ATP hydrolysis. *Science (80-.).* **238**, 638–644 (1987).

165. Star, E. N., Kwiatkowski, D. J. & Murthy, V. N. Rapid turnover of actin in dendritic spines and its regulation by activity. *Nat. Neurosci.* **5**, 239–246 (2002).

166. Shirao, T. & Koganezawa, N. The role of drebrin-binding stable actin filaments in dendritic spine morphogenesis. *Cytoskelet. Heal. Dis.* **238**, 363–371 (2015).

167. Lynch, M. A. Long-Term Potentiation and Memory. *Physiol. Rev.* **84**, 87–136 (2004).

168. Fukazawa, Y. *et al.* Hippocampal LTP is accompanied by enhanced F-actin content within the dendritic spine that is essential for late LTP maintenance in vivo. *Neuron* **38**, 447–460 (2003).

169. Shirao, T. *et al.* The role of drebrin in neurons. *J. Neurochem.* **141**, 819–834 (2017).

170. Olsen, J. V. *et al.* Global, In Vivo, and Site-Specific Phosphorylation Dynamics in Signaling Networks. *Cell* **127**, 635–648 (2006).

171. Molina, H., Horn, D. M., Tang, N., Mathivanan, S. & Pandey, A. Global proteomic profiling of phosphopeptides using electron transfer dissociation tandem mass spectrometry. *Proc. Natl. Acad. Sci. U. S. A.* **104**, 2199–2204 (2007).

172. Vosseller, K. *et al.* Quantitative analysis of both protein expression and serine/threonine post-translational modifications through stable isotope labeling with dithiothreitol. *Proteomics* **5**, 388–398 (2005).

173. Tao, W. A. *et al.* Quantitative phosphoproteome analysis using a dendrimer conjugation chemistry and tandem mass spectrometry. *Nat. Methods* **2**, 591–598 (2005).

174. Rush, J. *et al.* Immunoaffinity profiling of tyrosine phosphorylation in cancer cells. *Nat. Biotechnol.* **23**, 94–101 (2005).

175. Chew, C. S., Okamoto, C. T., Chen, X. & Thomas, R. Drebrin E2 is differentially expressed and phosphorylated in parietal cells in the gastric mucosa. *Am. J. Physiol. - Gastrointest. Liver Physiol.* **289**, (2005).

176. Ballif, B. A., Villén, J., Beausoleil, S. A., Schwartz, D. & Gygi, S. P. Phosphoproteomic analysis of the developing mouse brain. *Mol. Cell. Proteomics* **3**, 1093–1101 (2004).

177. Sonego, M. *et al.* Drebrin regulates neuroblast migration in the postnatal mammalian brain. *PLoS One* **10**, (2015).

178. Kreis, P. *et al.* Phosphorylation of the Actin Binding Protein Drebrin at S647 Is Regulated by Neuronal Activity and PTEN. *PLoS One* **8**, 1–12 (2013).

179. Kreis, P. *et al.* ATM phosphorylation of the actin-binding protein drebrin controls oxidation stress-resistance in mammalian neurons and C. elegans. *Nat. Commun.* **10**, 1–13 (2019).

180. Canman, C. E. *et al.* Activation of the ATM kinase by ionizing radiation and phosphorylation of p53. *Science (80-.).* **281**, 1677–1679 (1998).

181. Shiloh, Y. & Ziv, Y. The ATM protein kinase: Regulating the cellular response to genotoxic stress, and more. *Nat. Rev. Mol. Cell Biol.* **14**, 197–210 (2013).

182. Willmes, C. G. *et al.* Investigation of hippocampal synaptic transmission and plasticity in mice deficient in the actin-binding protein Drebrin. *Sci. Rep.* **7**, 42652 (2017).

183. Brenner, S. The genetics of Caenorhabditis elegans. *Genetics* **77**, 71–94 (1974).

184. Altun, Z. F. & Hall, D. H. WormAtas Hermaphrodite Handbook - Introduction. *WormAtlas* (2006). doi:10.3908/wormatlas.1.1

185. Wood, W. B. The Nematode Caenorhabditis elegans. *Cold Spring Harb. Monogr. Arch. Vol. 17 Nematode Caenorhabditis elegans* (1988).

186. C. elegans Sequencing Consortium. Genome sequence of the nematode C. elegans: A platform for investigating biology. *Science (80-.).* **282**, 2012–2018 (1998).

187. Hillier, L. W. *et al.* Genomics in C-elegans: So many genes, such a little worm. *Genome Res.* **15**, 1651–1660 (2005).

188. Kenyon, C. J. The genetics of ageing. *Nature* **464**, 504–512 (2010).

189. Friedman, D. B. & Johnson, T. E. A mutation in the age-1 gene in Caenorhabditis elegans lengthens life and reduces hermaphrodite fertility. *Genetics* **118**, 75–86 (1988).

190. Dorman, J. B., Albinder, B., Shroyer, T. & Kenyon, C. The age-1 and daf-2 genes function in a common pathway to control the lifespan of Caenorhabditis elegans. *Genetics* **141**, 1399–406 (1995).

191. Lai, C. H., Chou, C. Y., Ch'ang, L. Y., Liu, C. S. & Lin, W. C. Identification of novel human genes evolutionarily conserved in Caenorhabditis elegans by comparative proteomics. *Genome Res.* **10**, 703–713 (2000).

192. Rubin, G. M. *et al.* Comparative genomics of the eukaryotes. *Science (80-.).* **287**, 2204–2215 (2000).

193. White, J. G., Southgate, E., Thomson, J. N. & Brenner, S. The structure of the nervous system of the nematode Caenorhabditis elegans. *Philos. Trans. R. Soc. London. B, Biol. Sci.* **314**, 1–340 (1986).

194. Morimoto, R. I. Proteotoxic stress and inducible chaperone networks in neurodegenerative disease and aging. *Genes Dev.* **22**, 1427–1438 (2008).

195. Lakso, M. *et al.* Dopaminergic neuronal loss and motor deficits in Caenorhabditis elegans overexpressing human α-synuclein. *J. Neurochem.* **86**, 165–172 (2003).

196. Wang, J. *et al.* An ALS-linked mutant SOD1 produces a locomotor defect associated with aggregation and synaptic dysfunction when expressed in neurons of Caenorhabditis elegans. *PLoS Genet.* **5**, (2009).

197. Oeda, T. Oxidative stress causes abnormal accumulation of familial amyotrophic lateral sclerosis-related mutant SOD1 in transgenic Caenorhabditis elegans. *Hum. Mol. Genet.* **10**, 2013–2023 (2001).

198. Ash, P. E. A. *et al.* Neurotoxic effects of TDP-43 overexpression in C. elegans. *Hum. Mol. Genet.* **19**, 3206–3218 (2010).

199. Liachko, N. F., Guthrie, C. R. & Kraemer, B. C. Phosphorylation promotes neurotoxicity in a Caenorhabditis elegans model of TDP-43 proteinopathy. *J. Neurosci.* **30**, 16208–16219 (2010).

200. Vaccaro, A. *et al.* Mutant TDP-43 and FUS cause age-dependent paralysis and neurodegeneration in C. elegans. *PLoS One* **7**, (2012).

201. Murakami, T. *et al.* Als mutations in FUS cause neuronal dysfunction and death in caenorhabditis elegans by a dominant gain-of-function mechanism. *Hum. Mol. Genet.* **21**, 1–9 (2012).

202. Morley, J. F., Brignull, H. R., Weyers, J. J. & Morimoto, R. I. The threshold for polyglutamine-expansion protein aggregation and cellular toxicity is dynamic and influenced by aging in Caenorhabditis elegans. *Proc. Natl. Acad. Sci. U. S. A.* **99**, 10417–10422 (2002).

203. Faber, P. W., Alter, J. R., Macdonald, M. E. & Hart, A. C. Polyglutamine-mediated dysfunction and apoptotic death of a Caenorhabditis elegans sensory neuron. *Proc. Natl. Acad. Sci. U. S. A.* **96**, 179–184 (1999).

204. Kraemer, B. C. *et al.* Neurodegeneration and defective neurotransmission in a Caenorhabditis elegans model of tauopathy. *Proc. Natl. Acad. Sci. U. S. A.* **100**, 9980–9985 (2003).

205. Fatouros, C. *et al.* Inhibition of Tau aggregation in a novel caenorhabditis elegans model of tauopathy mitigates proteotoxicity. *Hum. Mol. Genet.* **21**, 3587–3603 (2012).

206. Link, C., Fluet, A., Johnson, C. J., Van Doren, C. & Kim, S. Microarray analysis of gene expression in a transgenic Caenorhabditis elegans Alzheimer disease model. *Nat. Genet.* **23**, 58–58 (1999).

207. Link, C. D. *et al.* Gene expression analysis in a transgenic Caenorhabditis elegans Alzheimer's disease model. *Neurobiol. Aging* **24**, 397–413 (2003).

208. McColl, G. *et al.* Utility of an improved model of amyloid-beta (A β 1-42) toxicity in Caenorhabditis elegans for drug screening for Alzheimer ' s disease. 1–9 (2012).

209. Wu, Y. *et al.* Amyloid-β-induced pathological behaviors are suppressed by Ginkgo biloba extract EGB 761 and ginkgolides in transgenic Caenorhabditis elegans. *J. Neurosci.* **26**, 13102–13113 (2006).

210. Regitz, C., Fitzenberger, E., Mahn, F. L., Du??ling, L. M. & Wenzel, U. Resveratrol reduces amyloid-beta (Aβ1-42)-induced paralysis through targeting proteostasis in an Alzheimer model of Caenorhabditis elegans. *Eur. J. Nutr.* (2015). doi:10.1007/s00394-015-0894-1

211. McColl, G. *et al.* The Caenorhabditis elegans Aβ (1 – 42) Model of Alzheimer Disease Predominantly Expresses Aβ (3 – 42). **284**, 22697–22702 (2009).

212. Fong, S. *et al.* Energy crisis precedes global metabolic failure in a novel Caenorhabditis elegans Alzheimer Disease model. *Sci. Rep.* **6**, 1–9 (2016).

213. Ochiishi, T. *et al.* Development of new fusion proteins for visualizing amyloid-β oligomers in vivo. *Sci. Rep.* **6**, 1–15 (2016).

214. Treusch, S. *et al.* Functional Links Between Abeta Toxicity, Endocytic Trafficing, and Alzheimer's Disease Risk Factors in Yeast. *Science (80-.).* **334**, 1241–1245 (2011).

215. Hammarlund, M., Hobert, O., Miller, D. M. & Sestan, N. The CeNGEN Project: The Complete Gene Expression Map of an Entire Nervous System. *Neuron* **99**, 430–433 (2018).

216. Taylor, S. R. *et al.* Expression profiling of the mature C. elegans nervous system by single-cell RNA-Sequencing. *bioRxiv* 737577 (2019). doi:10.1101/737577

217. Butkevich, E. *et al.* Drebrin-like protein DBN-1 is a sarcomere component that stabilizes actin filaments during muscle contraction. *Nat. Commun.* **6**, 7523 (2015).

218. Shi, X. *et al.* WIP-1 and DBN-1 promote scission of endocytic vesicles by bridging actin and Dynamin-1 in the C. elegans intestine. *J. Cell Sci.* **132**, (2019).

219. Esbjörner, E. K. *et al.* Direct observations of amyloid β Self-assembly in live cells provide insights into differences in the kinetics of Aβ(1-40) and Aβ(1-42) aggregation. *Chem. Biol.* **21**, 732–742 (2014).

220. Kaminski, G. S., Bertoncini, C. W. & Chan, F. T. S. A FRET Sensor for Non-Invasive Imaging of Amyloid Formation in Vivo. **12**, 673–680 (2011).

221. Link, C. *et al.* Visualization of fibrillar amyloid deposits in living, transgenic Caenorhabditis elegans animals using the sensitive amyloid dye, X-34. *Neurobiol. Aging* **22**, 217–226 (2001).

222. Link, C. D. Expression of human β-amyloid peptide in transgenic Caenorhabditis elegans. *Proc. Natl. Acad. Sci. U. S. A.* **92**, 9368–9372 (1995).

223. VASSAR, P. S. & CULLING, C. F. Fluorescent stains, with special reference to amyloid and connective tissues. *Arch. Pathol.* **68**, 487–498 (1959).

224. Becker, W. Fluorescence lifetime imaging - techniques and applications. *J. Microsc.* **247**, 119–136 (2012).

225. Bindels, D. S. *et al.* mScarlet : a bright monomeric red fluorescent protein for cellular imaging. *Nat. Publ. Gr.* **14**, 53–56 (2016).

226. Ben-Zvi, A., Miller, E. A. & Morimoto, R. I. Collapse of proteostasis represents an early molecular event in Caenorhabditis elegans aging. *Proc. Natl. Acad. Sci. U. S. A.* **106**, 14914–14919 (2009).

227. Labbadia, J. & Morimoto, R. I. Repression of the Heat Shock Response Is a Programmed Event at the Onset of Reproduction. *Mol. Cell* **59**, 639–650 (2015).

228. Young, L. J., Kaminski Schierle, G. S. & Kaminski, C. F. Imaging Aβ(1-42) fibril elongation reveals strongly polarised growth and growth incompetent states. *Phys. Chem. Chem. Phys.* **19**, 27987–27996 (2017).

229. Huang, C. *et al.* Intrinsically aggregation-prone proteins form amyloid-like aggregates and contribute to tissue aging in caenorhabditis elegans. *Elife* **8**, (2019).

230. David, D. C. *et al.* Widespread protein aggregation as an inherent part of aging in C. elegans. *PLoS Biol.* **8**, 47–48 (2010).

231. Dosanjh, L. E., Brown, M. K., Rao, G., Link, C. D. & Luo, Y. Behavioral phenotyping of a transgenic caenorhabditis elegans expressing neuronal amyloid-β. *J. Alzheimer's Dis.* **19**, 681–690 (2010).

232. Kirstein-Miles, J., Scior, A., Deuerling, E. & Morimoto, R. I. The nascent polypeptide-associated complex is a key regulator of proteostasis. *EMBO J.* **32**, 1451–1468 (2013).

233. Fares, H. & Grant, B. Deciphering endocytosis in Caenorhabditis elegans. *Traffic* **3**, 11–19 (2002).

234. Bargmann, C. I. & Leon, A. Chapter 10 Laser Killing of Cells in Caenorhabditis elegans. in *Methods in Cell Biology* 225–250 (1995). doi:https://doi.org/10.1016/S0091-679X(08)61390-4

235. Kim, K. & Li, C. Expression and regulation of an FMRFamide-related neuropeptide gene family in Caenorhabditis elegans. *J. Comp. Neurol.* **475**, 540–550 (2004).

236. Peden, E. M. & Barr, M. M. The KLP-6 Kinesin Is Required for Male Mating Behaviors and Polycystin Localization in Caenorhabditis elegans. *Curr. Biol.* **15**, 394–404 (2005).

237. Pujol, N. *et al.* A reverse genetic analysis of components of the Toll signaling pathway in Caenorhabditis elegans. *Curr. Biol.* **11**, 809–821 (2001).

238. Bargmann, C. I., Hartwieg, E. & Horvitz, H. R. Odorant-selective genes and neurons mediate olfaction in C. elegans. *Cell* **74**, 515–527 (1993).

239. Kim, S. T., Lim, D. S., Canman, C. E. & Kastan, M. B. Substrate specificities and identification of putative substrates of ATM kinase family members. *J. Biol. Chem.* **274**, 37538–37543 (1999).

240. Massaad, C. A. & Klann, E. Reactive oxygen species in the regulation of synaptic plasticity and memory. *Antioxidants Redox Signal.* **14**, 2013–2054 (2011).

241. Fron, E. *et al.* Revealing the excited-state dynamics of the fluorescent protein dendra2. *J. Phys. Chem. B* **117**, 2300–2313 (2013).

242. Pinotsi, D. *et al.* Direct observation of heterogeneous amyloid fibril growth kinetics via two-color super-resolution microscopy. *Nano Lett.* **14**, 339–345 (2014).

243. Kaufman, R. J., Murtha, P. & Davies, M. V. Translational efficiency of polycistronic mRNAs and their utilization to express heterologous genes in mammalian cells. *EMBO J.* **6**, 187–193 (1987).

244. Li, D., Wang, M. & Animal, N. Construction of a bicistronic vector for the using a newly identi fi ed IRES. (2012). doi:10.2144/000113821

245. Klaips, C. L., Jayaraj, G. G. & Hartl, F. U. Pathways of cellular proteostasis in aging and disease. *Journal of Cell Biology* (2018). doi:10.1083/jcb.201709072

246. Min, J.-N. *et al.* CHIP Deficiency Decreases Longevity, with Accelerated Aging Phenotypes Accompanied by Altered Protein Quality Control. *Mol. Cell. Biol.* **28**, 4018–4025 (2008).

247. Sala, A. J., Bott, L. C., Brielmann, R. M. & Morimoto, R. I. Embryo integrity regulates maternal proteostasis and stress resilience. *Genes Dev.* 1–10 (2020). doi:10.1101/gad.335422.119

248. Kobro-Flatmoen, A., Nagelhus, A. & Witter, M. P. Reelin-immunoreactive neurons in entorhinal cortex layer II selectively express intracellular amyloid in early Alzheimer's disease. *Neurobiol. Dis.* **93**, 172–183 (2016).

249. Nixon, R. A. *et al.* Extensive involvement of autophagy in Alzheimer disease: An immuno-electron microscopy study. *J. Neuropathol. Exp. Neurol.* **64**, 113–122 (2005).

250. Sandhof, C. A. *et al.* Reducing INS-IGF1 signaling protects against non-cell autonomous vesicle rupture caused by SNCA spreading. *Autophagy* 1–22 (2019). doi:10.1080/15548627.2019.1643657

251. Denver, D. R., Morris, K., Lynch, M. & Thomas, W. K. High mutation rate and predominance of insertions in the Caenohabditis elegans nuclear genome. *Nature* **430**, 679–682 (2004).

252. Lipinski, K. J. *et al.* High spontaneous rate of gene duplication in Caenorhabditis elegans. *Curr. Biol.* **21**, 306–310 (2011).

253. Nei, M. The new mutation theory of phenotypic evolution. *Proc. Natl. Acad. Sci. U. S. A.* **104**, 12235–12242 (2007).

254. Chung, Y. J., Robert, C., Gough, S. M., Rassool, F. V. & Aplan, P. D. Oxidative stress leads to increased mutation frequency in a murine model of myelodysplastic syndrome. *Leuk. Res.* **38**, 95–102 (2014).

255. Rossman, T. G. & Goncharova, E. I. Spontaneous mutagenesis in mammalian cells is caused mainly by oxidative events and can be blocked by antioxidants and metallothionein. *Mutat. Res. - Fundam. Mol. Mech. Mutagen.* **402**, 103–110 (1998).

256. Shor, E., Fox, C. A. & Broach, J. R. The Yeast Environmental Stress Response Regulates Mutagenesis Induced by Proteotoxic Stress. *PLoS Genet.* **9**, (2013).

257. Brignull, H. R., Moore, F. E., Tang, S. J. & Morimoto, R. I. Polyglutamine proteins at the pathogenic threshold display neuron-specific aggregation in a pan-neuronal Caenorhabditis elegans model. *J. Neurosci.* **26**, 7597–7606 (2006).

258. Lee, H. *et al.* Nictation, a dispersal behavior of the nematode Caenorhabditis elegans, is regulated by IL2 neurons. *Nat. Neurosci.* **15**, 107–112 (2012).

259. Burket, C. T., Higgins, C. E., Hull, L. C., Berninsone, P. M. & Ryder, E. F. The C. elegans gene dig-1 encodes a giant member of the immunoglobulin superfamily that promotes fasciculation of neuronal processes. *Dev. Biol.* **299**, 193–205 (2006).

260. Wang, J., Schwartz, H. T. & Barr, M. M. Functional specialization of sensory cilia by an RFX transcription factor isoform. *Genetics* **186**, 1295–1307 (2010).

261. Coates, J. C. & De Bono, M. Antagonistic pathways in neurons exposed to body fluid regulate social feeding in Caenorhabditis elegans. *Nature* **419**, 925–929 (2002).

262. Serrano-Saiz, E. *et al.* XModular control of glutamatergic neuronal identity in C. elegans by distinct homeodomain proteins. *Cell* **155**, 659 (2013).

263. Yassin, L. *et al.* Characterization of the DEG-3/DES-2 receptor: A nicotinic acetylcholine receptor that mutates to cause neuronal degeneration. *Mol. Cell. Neurosci.* **17**, 589–599 (2001).

264. Bowen, D. M., Smith, C. B., White, P. & Davison, A. N. Neurotransmitter-related enzymes and indices of hypoxia in senile dementia and other abiotrophies. *Brain* **99**, 459–496 (1976).

265. Davies, P. & Maloney, A. J. F. Selective Loss of Central Cholinergic Neurons in Alzheimer'S Disease. *Lancet* **308**, 1403 (1976).

266. Mesulam, M. M. & Van Hoesen, G. W. Acetylcholinesterase-rich projections from the basal forebrain of the rhesus monkey to neocortex. *Brain Res.* **109**, 152–157 (1976).

267. Whitehouse, P. J., Price, D. L., Clark, A. W., Coyle, J. T. & DeLong, M. R. Alzheimer disease: Evidence for selective loss of cholinergic neurons in the nucleus basalis. *Ann. Neurol.* **10**, 122–126 (1981).

268. Drachman, D. A. & Leavitt, J. Human Memory and the Cholinergic System: A Relationship to Aging? *Arch. Neurol.* **30**, 113–121 (1974).

269. Summers, W. K., Majovski, L. V., Marsh, G. M., Tachiki, K. & Kling, A. Oral Tetrahydroaminoacridine in Long-Term Treatment of Senile Dementia, Alzheimer Type. *N. Engl. J. Med.* **315**, 1241–1245 (1986).

270. Pereira, L. *et al.* A cellular and regulatory map of the cholinergic nervous system of C. Elegans. *Elife* **4**, 1–46 (2015).

271. Attems, J., Walker, L. & Jellinger, K. A. Olfactory bulb involvement in neurodegenerative diseases. *Acta Neuropathol.* **127**, 459–475 (2014).

272. Marigliano, V. *et al.* Olfactory deficit and hippocampal volume loss for early diagnosis of Alzheimer disease: A pilot study. *Alzheimer Dis. Assoc. Disord.* **28**, 194–197 (2014).

273. Velayudhan, L., Pritchard, M., Powell, J. F., Proitsi, P. & Lovestone, S. Smell identification function as a severity and progression marker in Alzheimer's disease. *Int. Psychogeriatrics* **25**, 1157–1166 (2013).

274. He, B. *et al.* Injected Amyloid Beta in the Olfactory Bulb Transfers to Other Brain Regions via Neural Connections in Mice. *Mol. Neurobiol.* **55**, 1703–1713 (2018).

275. Koo, E. H. *et al.* Precursor of amyloid protein in Alzheimer disease undergoes fast anterograde axonal transport. *Proc. Natl. Acad. Sci. U. S. A.* **87**, 1561–1565 (1990).

276. Poon, W. W. *et al.* β-Amyloid (Aβ) oligomers impair brain-derived neurotrophic factor retrograde trafficking by down-regulating ubiquitin C-terminal hydrolase, UCH-L1. *J. Biol. Chem.* **288**, 16937–16948 (2013).

277. Hickson, I. *et al.* Identification and characterization of a novel and specific inhibitor of the ataxia-telangiectasia mutated kinase ATM. *Cancer Res.* **64**, 9152–9159 (2004).

278. Guo, Z., Kozlov, S., Lavin, M. F., Person, M. D. & Paull, T. T. ATM activation by oxidative stress. *Science (80-.).* **330**, 517–521 (2010).

279. Ivanov, A., Esclapez, M., Pellegrino, C., Shirao, T. & Ferhat, L. Drebrin A regulates dendritic spine plasticity and synaptic function in mature cultured hippocampal neurons. *J. Cell Sci.* **122**, 524–34 (2009).

280. Jurado, S. *et al.* PTEN is recruited to the postsynaptic terminal for NMDA receptor-dependent long-term depression. *EMBO J.* **29**, 2827–2840 (2010).

281. Knafo, S. *et al.* PTEN recruitment controls synaptic and cognitive function in Alzheimer's models. *Nat. Neurosci.* **19**, 443–53 (2016).

282. Wilson, C. & González-Billault, C. Regulation of cytoskeletal dynamics by redox signaling and oxidative stress: Implications for neuronal development and trafficking. *Front. Cell. Neurosci.* **9**, (2015).

283. Hervera, A. *et al.* Reactive oxygen species regulate axonal regeneration through the release of exosomal NADPH oxidase 2 complexes into injured axons. *Nat. Cell Biol.* **20**, 307–319 (2018).

284. Kirstein, J. *et al.* Proteotoxic stress and ageing triggers the loss of redox homeostasis across cellular compartments. *EMBO J.* **34**, 2334–2349 (2015).

285. Ishizuka, Y. *et al.* Histone deacetylase mediates the decrease in drebrin cluster density induced by amyloid beta oligomers. *Neurochem. Int.* **76**, 114–121 (2014).

286. Julien, C. *et al.* Decreased drebrin mRNA expression in Alzheimer disease: Correlation with tau pathology. *J. Neurosci. Res.* **86**, 2292–2302 (2008).

287. Svitkina, T. The actin cytoskeleton and actin-based motility. *Cold Spring Harb. Perspect. Biol.* **10**, (2018).

288. Sekino, Y., Kojima, N. & Shirao, T. Role of actin cytoskeleton in dendritic spine morphogenesis. *Neurochem. Int.* **51**, 92–104 (2007).

289. Koganezawa, N., Hanamura, K., Sekino, Y. & Shirao, T. The role of drebrin in dendritic spines. *Mol. Cell. Neurosci.* **84**, 85–92 (2017).

290. Kommaddi, R. P. *et al.* Aβ mediates F-actin disassembly in dendritic spines leading to cognitive deficits in alzheimer's disease. *J. Neurosci.* **38**, 1085–1099 (2018).

291. Baglietto-Vargas, D. *et al.* Impaired AMPA signaling and cytoskeletal alterations induce early synaptic dysfunction in a mouse model of Alzheimer's disease. *Aging Cell* 1–14 (2018). doi:10.1111/acel.12791

292. Cáceres, A., Ye, B. & Dotti, C. G. Neuronal polarity: Demarcation, growth and commitment. *Curr. Opin. Cell Biol.* **24**, 547–553 (2012).

293. Wilson, C., Núñez, M. T. & González-Billault, C. Contribution of NADPH oxidase to the establishment of hippocampal neuronal polarity in culture. *J. Cell Sci.* **128**, 2989–2995 (2015).

294. Ruei-Jiun Hung, Chi W. Pak, J. R. T. Direct Redox Regulation of F-Actin. *Science (80-.).* **832**, 1710–1713 (2011).

295. Frémont, S. *et al.* Oxidation of F-actin controls the terminal steps of cytokinesis. *Nat. Commun.* **8**, (2017).

296. Vitali, T., Maffioli, E., Tedeschi, G. & Vanoni, M. A. Properties and catalytic activities of MICAL1, the flavoenzyme involved in cytoskeleton dynamics, and modulation by its CH, LIM and C-terminal domains. *Arch. Biochem. Biophys.* **593**, 24–37 (2016).

297. Shankar, G. M. *et al.* Natural oligomers of the Alzheimer amyloid-β protein induce reversible synapse loss by modulating an NMDA-type glutamate receptor-dependent signaling pathway. *J. Neurosci.* **27**, 2866–2875 (2007).

298. Woo, J. A. *et al.* RanBP9 at the intersection between cofilin and Aβ pathologies: Rescue of neurodegenerative changes by RanBP9 reduction. *Cell Death Dis.* **6**, (2015).

299. Minamide, L. S., Striegl, A. M., Boyle, J. A., Meberg, P. J. & Bamburg, J. R. Neurodegenerative stimuli induce persistent ADF/cofilin-actin rods that disrupt distal neurite function. *Nat. Cell Biol.* **2**, 628–636 (2000).

300. Warren, S. C. *et al.* Rapid global fitting of large fluorescence lifetime imaging microscopy datasets. *PLoS One* **8**, e70687 (2013).

301. Schindelin, J. *et al.* Fiji: an open-source platform for biological-image analysis. *Nat. Methods* **9**, 676–682 (2012).

302. Stauffer, W., Sheng, H. & Lim, H. N. EzColocalization: An ImageJ plugin for visualizing and measuring colocalization in cells and organisms. *Sci. Rep.* **8**, 1–13 (2018).

303. Nussbaum-Krammer, C. I., Neto, M. F., Brielmann, R. M., Pedersen, J. S. & Morimoto, R. I. Investigating the Spreading and Toxicity of Prion-like Proteins Using the Metazoan Model Organism C. elegans. *JoVE* e52321 (2015). doi:doi:10.3791/52321

304. Cong, L. *et al.* Multiplex genome engineering using CRISPR/Cas systems. *Science* **339**, 819–823 (2013).

305. Kisselev, A. F. & Goldberg, A. L. Monitoring activity and inhibition of 26S proteasomes with fluorogenic peptide substrates. *Methods Enzymol.* **398**, 364–378 (2005).

306. Vilchez, D. *et al.* Increased proteasome activity in human embryonic stem cells is regulated by PSMD11. *Nature* **489**, 304–308 (2012).

307. Lange, S., Sylvester, M., Schumann, M., Freund, C. & Krause, E. Identification of phosphorylation-dependent interaction partners of the adapter protein ADAP using quantitative mass spectrometry: SILAC vs (18)O-labeling. *J. Proteome Res.* **9**, 4113–4122 (2010).

308. Cox, J. *et al.* Accurate proteome-wide label-free quantification by delayed normalization and maximal peptide ratio extraction, termed MaxLFQ. *Mol. Cell. Proteomics* **13**, 2513–2526 (2014).

309. Margie, O., Palmer, C. & Chin-Sang, I. C. elegans Chemotaxis Assay. *J. Vis. Exp.* 1–6 (2013). doi:10.3791/50069

310. Aits, S. *et al.* Sensitive detection of lysosomal membrane permeabilization by lysosomal galectin puncta assay by lysosomal galectin puncta assay. **8627**, (2015).

311. Wilm, T., Demel, P., Koop, H. U., Schnabel, H. & Schnabel, R. Ballistic transformation of Caenorhabditis elegans. *Gene* **229**, 31–35 (1999).

Fiji-Scripts for Thrashing Assay

(1) Save every open image (after opening a *.lif archive file)

```
//get image IDs of all open images
dir = getDirectory("Choose a Directory");
ids=newArray(nImages);
for (i=0;i<nImages;i++) {
    selectImage(i+1);
    title = getTitle;
    print(title);
    ids[i]=getImageID;

    saveAs("tiff", dir+title);
}
close("*")
```

(2) Convert all images in a folder to 8-bit, remove background and apply threshold

```
path=getDirectory("Choose a Directory");
list=getFileList(path);
for(i=0;i<list.length;i++){
        open(path+list[i]);
        dir = getDirectory("image");
        name = getTitle;
        run("8-bit");
        run("Subtract Background...", "rolling=50 light stack");
        setAutoThreshold("Default");
        //run("Threshold...");
        setThreshold(0, 196);
        setOption("BlackBackground", false);
        run("Convert to Mask", "method=Default background=Light calculate");
        saveAs("avi",  dir + name);
        run("Close");
        }
```

(3) Run wrMTrck

```
//defining scales, according to settings used in this thesis
run("Set Scale...", "distance=098 known=1 pixel=1 unit=mm global");

path=getDirectory("Choose a Directory");
list=getFileList(path);

for(i=0;i<list.length;i++){

        open(path+list[i]);

        dir = getDirectory("image");
        name = getTitle;

        run("8-bit");
        //run("Threshold...");
        setAutoThreshold("Default");
        setOption("BlackBackground", false);
        run("Convert to Mask", "method=Default background=Light calculate");

        run("wrMTrck", "minsize=30 maxsize=4000 maxvelocity=30 maxareachange=40
mintracklength=20 bendthreshold=2 binsize=0 showpathlengths showlabels showpositions
showsummary smoothing rawdata=0 benddetect=1 fps=5 backsub=0 threshmode=Otsu fontsize=24");

        saveAs("results",  dir + name + ".csv");
        saveAs("avi",  dir + name);

        run("Close");
        run("Close");
}
```

Additional Information about JKM7

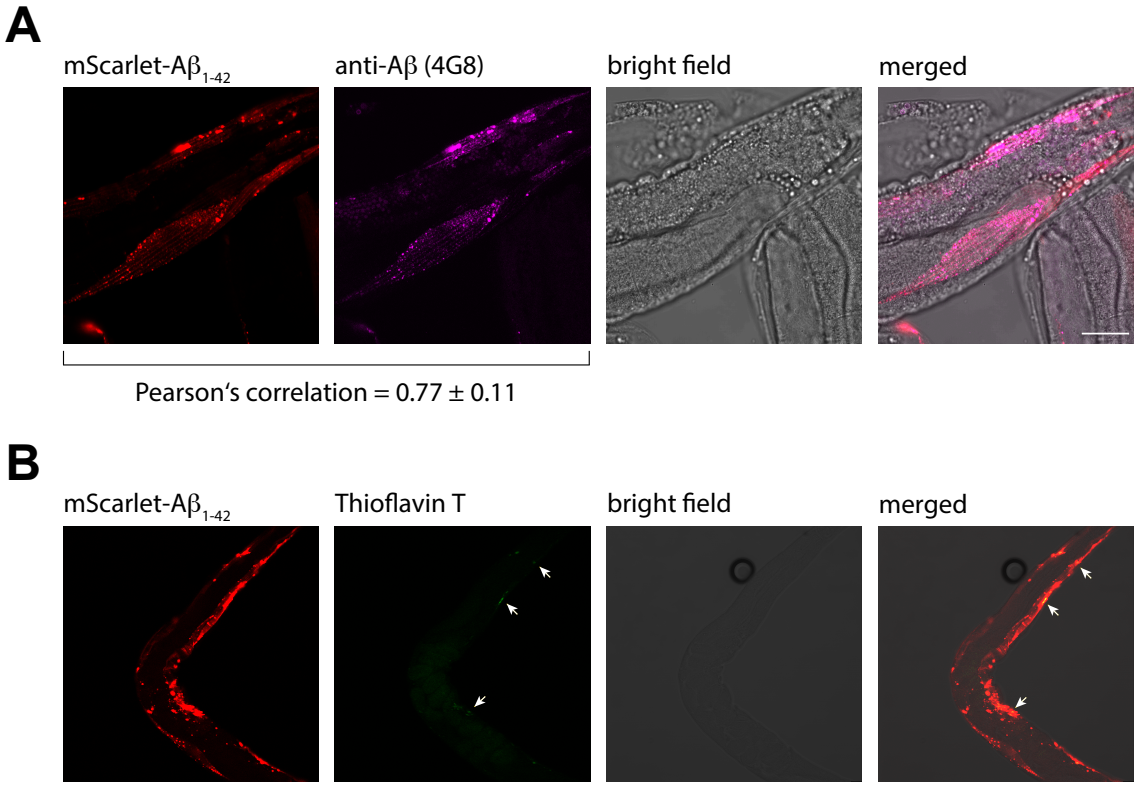

***Figure 7.1**: Aβ1-42 and wrmScarlet-Aβ1-42 are forming amyloids in strain JKM7*

(A) Representative confocal image of mAβ fixed with PFA and stained with anti-Aβ (6E10) + anti-mouse-IR680. Scale bar represents 20 µm. Colocalization of mScarlet fluorescence and IR680 fluorescence was analysed and Pearson's correlation coefficient was determined for all acquired images (n = 14), noted as mean ± SD. **(B)** Representative confocal image of mAβ, fixed and stained with ThT. ThT-positive foci are marked with white arrows. Scale bar is 20 µm.

Additional Information about JKM5

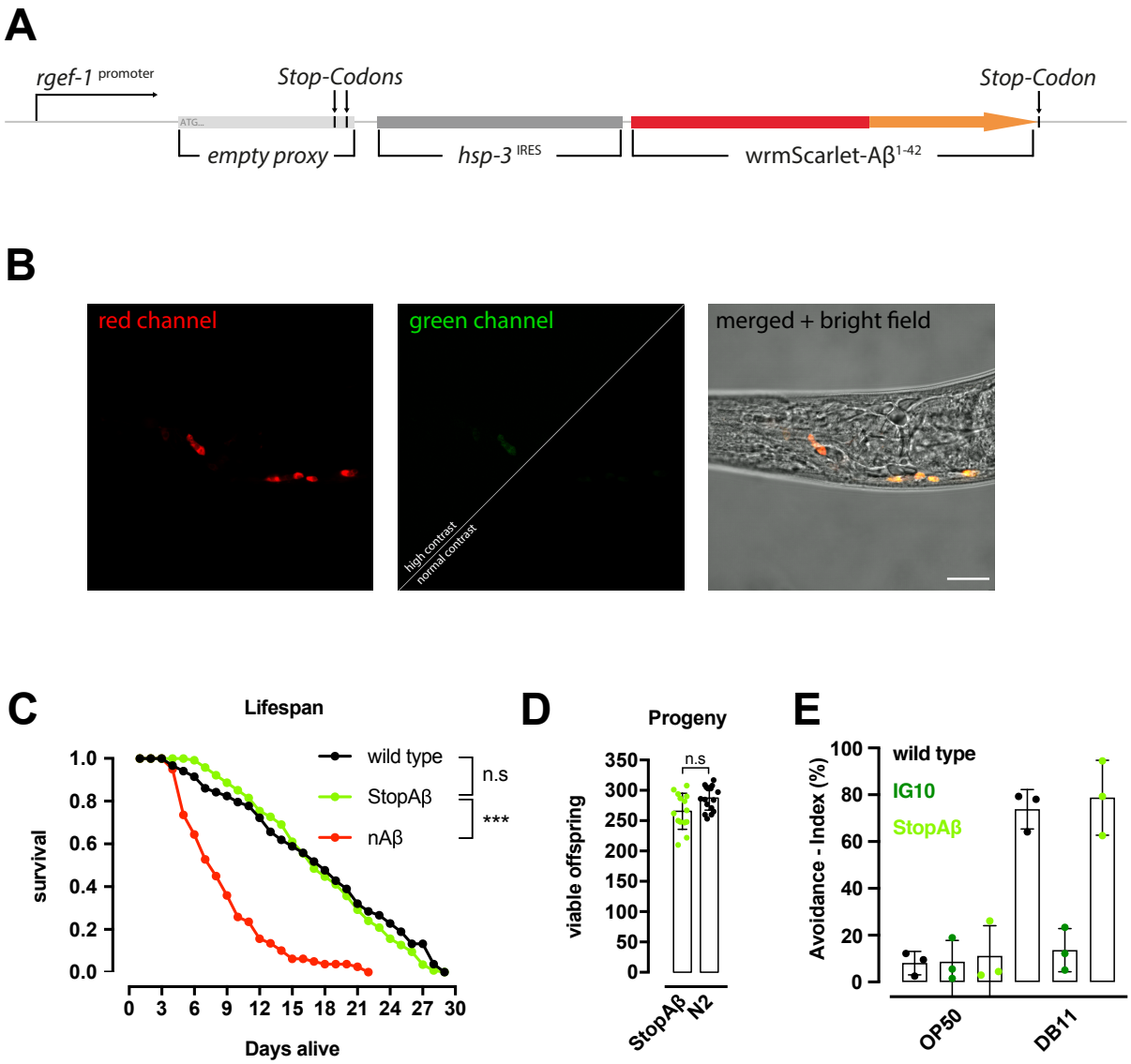

***Figure 7.2**: Characterization of StopAβ (JKM5)*

(A) Schematic depiction of the organisation of the transgene operon. The '*empty proxy*' is coding for the sequence: Met-Gly-Ala-Stop-Ala-Stop. **(B)** Representative confocal images of StopAβ stained with ThT. No ThT fluorescence was detected. Upon increasing the contrast, mScarlet auto fluorescence arises in the green channel. Scale bar is 20 µm. **(C)** Kaplan-Meier plot of the cumulative survival probability of nAβ (red), StopAβ (green) and wild type (black). Log-rank test was performed to test for significance (*** $p < 10^{-6}$). **(D)** Scatter-dot plot of viable offspring per nematode of StopAβ (green) and wild type (N2, black) nematodes. Depicted is mean ± SD. Analysed were three cohorts of 8 - 15 nematodes. **(E)** Scatter-dot plot of the avoidance index of StopAβ (green), IG10 (dark green) and wild type (black) nematodes. Three independent experiments with 3 - 5 cohorts of 10 - 15 individual nematodes were analysed (four times counted with 5 min breaks between counting). Depicted is mean ± SD. Pathogen-Avoidance-Assay was performed together with Manuel Iburg.

Aβ spreading to hypodermis

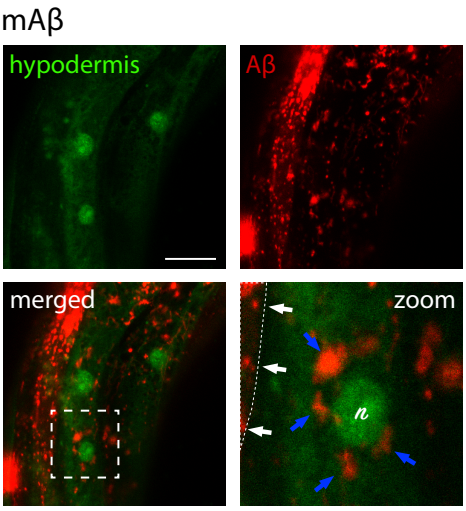

***Figure 7.3**: Aβ spreads from muscle cells to hypodermis*

Representative confocal image of JKM7×CS628 (hypodermal GFP marker) exhibits wrmScarlet-Aβ$_{1-42}$ derived fluorescence (white arrows) in body wall muscle cells (delimited by dashed, white line) as expected and wrmScarlet-Aβ$_{1-42}$ derived fluorescence colocalizing with GFP in hypodermis (blue arrows) around one hypodermal nucleus (n).

Aβ aggregation is independent of expression levels

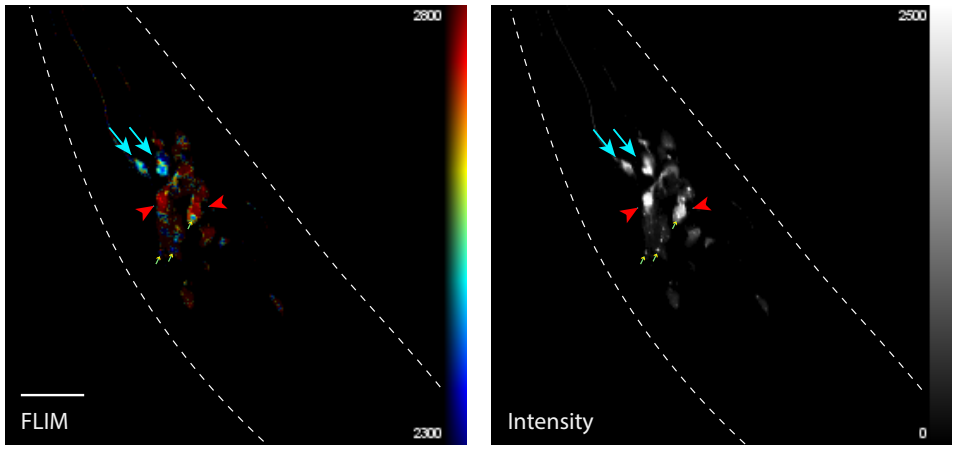

***Figure 7.4**: Aβ aggregates appear independent from strong accumulation*

Representative TCSPC-FLIM image and corresponding intensity map of nAβ. Cyan arrows mark IL2 neurons with the first aggregates on day 4 alive. Red arrow heads depict other neurons with equivalent or higher fluorescence intensity than IL2 neurons but no aggregates. Small yellow arrows depict randomly occurring small aggregates.

Short hairpin construct expression leads to cell-type specific knockdown

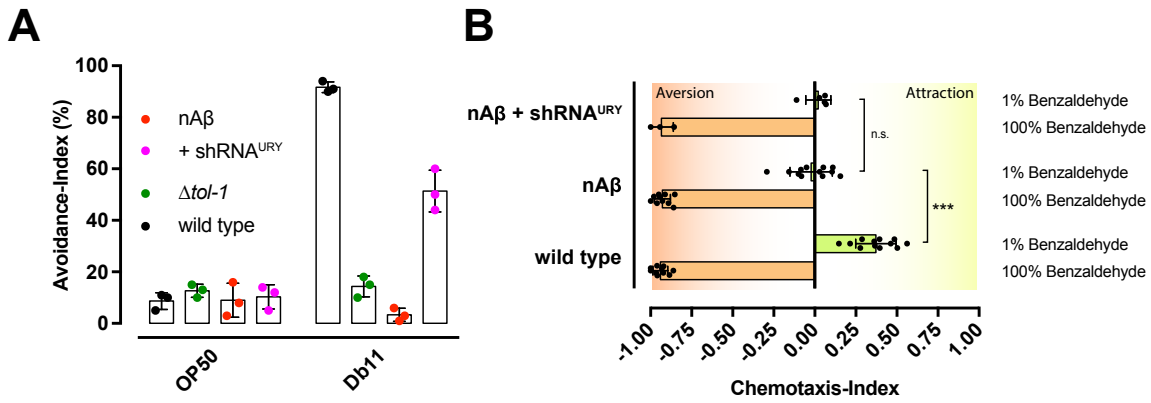

***Figure 7.5**: shRNA expression in URY neurons rescues pathogen avoidance but not chemotaxis*

(A) Scatter-dot plot of avoidance-index of nAβ (red), nAβ + shRNA^{URY} (pink), Δ*tol-1* (green), wild type (black) on *E. coli* OP50 or *S. marcescens* Db11 bacteria. Depicted is mean ± SD of three independent experiments with 3 – 5 cohorts of 10 – 15 nematodes each. Data acquired in cooperation with Manuel Iburg. **(B)** Scatter-dot plot of the Chemotaxis-Index of nAβ, nAβ + shRNA^{URY} and wild type tested against 1% Benzaldehyde and 100% Benzaldehyde. Two-way ANOVA plus Bonferroni post hoc test was employed to test significance (*** $p < 0.001$). Three independent experiments with 4 – 5 cohorts of 50 – 100 nematodes were conducted.

Abbreviations

°C	Degree Celsius
α7nACh	α7 Nicotinic Acetylcholine
AD	Alzheimer's Disease
AMC	7-amino-4-methylcoumarin
AMPA	α-amino-3-hydroxy-5-methyl-4-isoxazolepropionic acid
APP	Amyloid precursor protein
ATM	Ataxia telangiectasia mutated kinase
Aβ	Amyloid beta
bp	Base pairs
BSA	Bovine serum albumin
C. elegans	*Caenorhabditis elegans*
CGC	*Caenorhabditis* genetic center
CLEM	Correlative light-electron microscopy
daf-18	Abnormal dauer formation (gene) (human homolog: PTEN)
DAPI	4',6-Diamidin-2-phenylindol
DIC	Differential interference contrast
DMSO	Dimethyl sulfoxide
DNA	Deoxyribonucleic acid
Drebrin	Developmentally regulated brain protein (also: DBN)
DTT	Dithiothreitol
E. coli	*Escherichia coli*
ECL	Enhanced chemiluminescence
EDTA	Ethylenediaminetetraacetic acid
EM	Electron microscopy
ER	Endoplasmic reticulum
Ex	Extra-chromosomal array
FLIM	Fluorescence lifetime imaging
g	Gram *or* Gravitational force equivalent (x times 9.8 m/s^2)
GFP	Green fluorescent protein
GOI	Gene of interest
h	Hour
HEPES	4-(2-hydroxyethyl)-1-piperazineethanesulfonic acid
het	Heterozygous
hsp	Heat shock protein (gene), protein: HSP
Hz	Hertz
IHC	Immunohistochemistry
IL2	Inner labial sensilla 2 (set of six ciliated neurons)

IRES	Internal ribosome entry site
Is	Integrated strain
J	Joule
kb	Kilobase
kDa	Kilo Dalton
ko	Knockout
l	Litre
L1 – L4	Nematode larval stages 1 to 4
LSM	Laser scanning microscope
LTD	Long-term depression
LTP	Long-term potentiation
m	Meter
M	Molar
myo-3	Myosin heavy chain structural gene
NGM	Nematode growth medium
NMDA	N-methyl-D-aspartic acid
n.s.	Not significant
PBS	Phosphate buffered saline
PCR	Polymerase chain reaction
PMSF	Phenylmethylsulphonyl fluoride
POI	Protein of interest
PTEN	Phosphatase and Tensin homolog
PVDF	Polyvinylidene fluoride
PVP	Polyvinylpyrrolidone
RFP	Red fluorescent protein
rgef-1	Rap Guanine nucleotide Exchange Factor homolog (gene)
RNA	Ribonucleic acid
RNAi	RNA interference
ROS	Reactive oxygen species
rpm	Revolutions per minute
RT	Room temperature (approx. 20°C)
s / sec	Second
S. marcescens	*Serratia marcescens*
SDS	Sodium dodecyl sulphate
SDS-PAGE	SDS-polyacrylamide gel electrophoresis
siRNA	Small interfering RNA
STED	Stimulated emission depletion
TAE	Tris-acetate-EDTA
TBS	Tris buffered saline
TEMED	Tetramethyl ethylenediamine
ThT	Thioflavin T

Tris	Tris(hydroxymethyl)aminomethane
unc-119	Uncoordinated (gene)
UPS	Ubiquitin-Proteasome System
URY	Subset of sensory head neurons
UTR	Untranslated region
UV	Ultraviolet
v/v	Volume per volume
WB	Western blot
wt	Wild type
w/v	Weight per volume

SI prefixes

p	pico (10^{-12})	m	milli (10^{-3})
n	nano (10^{-9})	k	kilo (10^{3})
µ	micro (10^{-6})	M	mega (10^{6})

Amino acids – one letter / three letter code

Alanine	A	Ala	Leucine	L	Leu
Arginine	R	Arg	Lysine	K	Lys
Asparagine	N	Asn	Methionine	M	Met
Aspartate	D	Asp	Phenylalanine	F	Phe
Cysteine	C	Cys	Proline	P	Pro
Glutamine	Q	Gln	Serine	S	Ser
Glutamate	E	Glu	Threonine	T	Thr
Glycine	G	Gly	Tryptophan	W	Trp
Histidine	H	His	Tyrosine	Y	Tyr
Isoleucine	I	Ile	Valine	V	Val

List of tables and figures

List of publications

Gallrein C◊, Iburg M◊, Michelberger T, Koçak A, Puchkov D, Ayala Mariscal S, Kaminski Schierle G, Kirstein J. **A novel model of Amyloid-beta pathology in *C. elegans* reveals critically vulnerable neurons as seeds of pathogenicity**. (in preparation)

Pigazzini ML◊, Gallrein C◊, Iburg M◊, Kaminski Schierle G and Kirstein J. **Characterization of Amyloid Structures in Aging *C. elegans* using Fluorescence Lifetime Imaging**. *J. Vis. Exp.* 2020 Mar 27. DOI: 10.3791/61004.

Sandhof CA, Hoppe SO, Druffel-Augustin S, Gallrein C, Kirstein J, Voisine C and Nussbaum-Krammer C. **Reducing INS-IGF1 signaling protects against non-cell autonomous vesicle rupture caused by SNCA spreading**. *Autophagy*. 2019 Jul 29:1-22. DOI: 10.1080/15548627.2019.1643657.

Kreis P◊, Gallrein C◊, Rojas-Puente E◊, Mack TGA, Kroon C, Dinkel V, Willmes C, Murk K, Tom-Dieck S, Schuman EM, Kirstein J, Eickholt BJ. **ATM phosphorylation of the actin-binding protein drebrin controls oxidation stress-resistance in mammalian neurons and *C. elegans***. *Nat Commun*. 2019 Jan 30;10(1):486. DOI: 10.1038/s41467-019-08420-w.

◊ equal contribution

Affidavit

Hiermit erkläre ich gegenüber der Freien Universität Berlin, dass ich die vorliegende Dissertation selbständig und ohne Benutzung anderer als der angegebenen Quellen und Hilfsmittel angefertigt habe. Die vorliegende Arbeit ist frei von Plagiaten. Alle Ausführungen, die wörtlich oder inhaltlich aus anderen Schriften entnommen sind, habe ich als solche kenntlich gemacht.

Diese Arbeit wurde in gleicher oder ähnlicher Form bei keiner anderen Universität als Prüfungsleistung eingereicht.

Leipzig, den 20. Mai 2020 Christian Gallrein

Acknowledgement

First, I would like to thank Prof. Dr. Janine Kirstein for giving me the opportunity to join her team at the FMP Berlin and allowing me to carry out the here presented work. I am thankful for all support and advice from her during my time in her lab as well as the opportunity to spend some time abroad and to attend some excellent conferences.

I would like to thank Prof. Dr. Stephan Sigrist for accepting to be the second reviewer of my work.

A big thanks goes to all members of the Kristein lab. I appreciated the time spent with all of them and am grateful for all the support, vivid discussions and contribution.

I would like to thank Prof. Dr. Britta Eickholt and all members of here lab for the tight collaboration on the Drebrin project and for the opportunity to use their labs and equipment.

Furthermore, I would like to thank Prof. Dr. Gabriele Kaminski Schierle and all members of lab, as well as Chetan Poudel, for giving me the opportunity to visit here lab and learn FLIM microscopy techniques. Along, I acknowledge the Company of Biologist for funding my travel with a short term fellowship.

A big thanks goes to the FMP imaging facility, especially to Dr. Martin Lehmann, Dr. Dmytro Puchkov, Dr. Burkhard Wiesner, Dr. Christopher Schmied and Jenny Eichhorst for all the support and help regarding microscopy and image processing. Also, I would like to thank Dr. Fan Liu and the mass spectrometry facility for advice and processing of mass spectrometry analysis. I would like to thank Dr. Jörg Rösner and the NeuroCure imaging facility for access to the Leica SP5 FLIM microscope.

I would like to thank Prof. Dr. Marja Jäättelä for nematode strain BIJ34, Prof. Dr. Manuel Zimmer for the nematode strain ZIM1048 and Prof. Dr. Rick Morimoto for the nematode strain Q0 (YFP). I thank Prof. Dr. Erich Wanker for providing the $A\beta_{1-42}$ sequence for initial cloning. I appreciate the generosity of Prof. Dr. Niels Ringstad for *tol-1p* sequence, Prof. Dr. Oliver Hobert for the *klp-6p* sequence and Prof. Dr. Chris Li for the *flp-22p* sequence.

Finally, I would like to thank all my friends and family that supported me during my studies.